

UNIVERSITEIT ANTWERPEN

Faculteit Wetenschappen
Departement Fysica



Ab initio berekening van relativistische elektronenergieverliesspectra

The *ab initio* calculation of relativistic electron energy loss spectra

Proefschrift voorgelegd tot het behalen van de graad van Doctor in de Wetenschappen
aan de Universiteit Antwerpen te verdedigen door

This thesis is submitted for the degree of Doctor of Philosophy at the University of
Antwerp by

Kevin Jorissen

Antwerpen, 2007

Promotoren :
Supervisors :

Prof. Dirk van Dyck
Prof. Dirk Lamoen

1. MOTIVATION	4
1.A. OF GREEKS, ENGINEERS, AND BITS.....	4
1.B. THE FOCUS OF THIS DISSERTATION.....	6
2. NEDERLANDSE SAMENVATTING	9
3. GENERAL INTRODUCTION	13
3.A. CONTENT OF THIS DISSERTATION	13
3.B. ELECTRON ENERGY LOSS SPECTROSCOPY IN THE TRANSMISSION ELECTRON MICROSCOPE.....	15
3.b.1. <i>EELS as a key to the electronic structure</i>	15
3.b.2. <i>EELS compared to other techniques</i>	28
3.b.3. <i>Ab initio calculation of EELS</i>	30
3.C. DENSITY FUNCTIONAL THEORY	32
3.c.1. <i>The Kohn-Sham equations</i>	32
3.c.2. <i>Implementation in WIEN2k</i>	36
3.D. GREEN'S FUNCTION THEORY	37
3.d.1. <i>Multiple scattering formula for the cross section</i>	37
3.d.2. <i>Implementation in FEFF8</i>	40
3.d.2.1 The FEFF8 program.....	40
3.d.2.2 The final state rule.....	41
3.d.2.3 Potentials and Fermi energy	42
3.d.2.4 Self-Energy	43
3.d.2.5 Core hole.....	43
3.d.2.6 ELNES and EXELFS.....	44
3.d.2.7 Broadening.....	47
3.d.2.8 Orientation dependence.....	47
3.d.2.9 Non-dipole transitions	48
3.d.2.10 Debye-Waller factors	49
3.d.2.11 Density of States	51
4. RELATIVISTIC CALCULATIONS OF ELECTRON ENERGY LOSS SPECTRA	52
4.A. GENERAL RELATIVISTIC THEORY	53
4.B. THE DIPOLE APPROXIMATION	58
4.C. ANGULAR MOMENTUM EXPANDED FORMALISM	60
4.c.1. <i>General theory of the DDSCS in a l,m-representation</i>	60
4.c.2. <i>The dipole terms and correspondence to Schattschneider et al.</i>	63
4.c.3. <i>The cross terms</i>	66
4.c.4. <i>The monopole term</i>	67
4.c.5. <i>The quadrupole terms</i>	68
4.D. IMPLEMENTATION IN THE WIEN2K PROGRAM TELNES2.....	69
4.d.1. <i>The L/APW basis set and the l,m-decomposition</i>	70
4.d.2. <i>Integrating the cross-section over beam convergence and detector aperture</i>	73
4.d.3. <i>Broadening the spectrum</i>	76
4.E. IMPLEMENTATION IN THE FEFF PROGRAM	77
4.F. UNDERSTANDING AND SOLVING THE MAGIC ANGLE FIASCO	82
4.f.1. <i>Non-relativistic calculation of the magic angle</i>	82
4.f.2. <i>Experimental measurements of the magic angle</i>	86
4.f.3. <i>Improvements within the non-relativistic theory?</i>	90
4.f.3.1 Non-dipole contributions.....	90
4.f.3.2 Cross-terms.....	92
4.f.3.3 Beyond the small q approximation	93
4.f.3.4 Beyond the small angle approximation.....	94
4.f.3.5 Conclusion.....	94
4.f.4. <i>Relativistic calculation of the magic angle</i>	95
4.f.5. <i>FEFF and TELNES2 calculations of the magic angle</i>	98

5. CORE HOLE CALCULATIONS OF ELECTRON ENERGY LOSS SPECTROSCOPY WITHOUT THE SUPERCELL	107
5.A. INTRODUCTION	107
5.B. THE K-SPACE MULTIPLE SCATTERING FORMALISM	109
5.b.1. <i>Introducing the core hole</i>	111
5.b.2. <i>Monoatomic lattices</i>	112
5.b.3. <i>Calculation of the KKR structure factors</i>	112
5.C. IMPLEMENTATION IN THE FEFF8 PROGRAM	117
5.c.1. <i>Convergence of the k-space FEFF8 calculations</i>	118
5.D. VERIFICATION OF THE REAL SPACE FINITE CLUSTER APPROXIMATION	120
5.E. CORE HOLE EELS WITHOUT THE SUPERCELL	122
5.e.1. <i>Problems with the supercell core hole approach</i>	122
5.e.1.1 <i>Supercell size converge</i>	122
5.e.1.2 <i>Which core hole should one use?</i>	126
5.e.2. <i>Results using k-space FEFF8</i>	129
6. CONCLUSIONS	133
6.A. 'STATE OF THE SIMULATIONS' FOR TELNES2 AND FEFF	133
6.B. KEY RESULTS	135
6.C. OUTLOOK	136
7. ACKNOWLEDGMENTS	137
8. APPENDICES	139
8.A. BIBLIOGRAPHY	139
8.B. GLOSSARY	140
8.C. THE WIEN2K PROGRAM TELNES2	141
8.c.1. <i>Introduction</i>	141
8.c.2. <i>What is calculated?</i>	142
8.c.3. <i>Using the program</i>	142
8.c.4. <i>The master input file case.innes</i>	143
8.c.5. <i>Files used by the TELNES2 program</i>	148
8.c.6. <i>Practical considerations</i>	149
8.c.7. <i>Compatibility with TELNES</i>	150
8.c.8. <i>Major differences with respect to the previous release (i.e., TELNES)</i>	150
8.c.9. <i>Programmer's Guide</i>	152
8.c.9.1 <i>Style</i>	152
8.c.9.2 <i>Description of all program units</i>	152
8.D. THE FEFF8 EELS PROGRAM	153
8.E. THE FEFF8 K-SPACE PROGRAM	167
9. REFERENCES	173

1. Motivation

1.a. Of Greeks, engineers, and bits.

The motivational introduction to a dissertation is beyond doubt the most entertaining part for its writer to work on, for here he is allowed to be a little frivolous, while in the rest of his work he must abandon poetry in favor of the modest language of scientific writing. For now, though, we may indulge in a few pages of storytelling.

Science serves, of course, one major goal : to understand the world. This often means reducing the utterly vast amount of information of all that is and happens; it means distilling it into basic laws and unifying principles. Such analytic power also opens up ways to predict the natural world, and to control it.

That this approach has at all been successful, may well be called remarkable.

Physics is perhaps the field where the principle of reducing raw information to rules of logic and mathematics can be observed clearest. Of course science itself is built on a foundation of philosophy and reasoning, but the most basic building block within science, its most crucial assertion is that matter, in all its forms that we observe in the natural world, is made of atoms¹, and derives its complex behavior from the behavior of these atoms. This concept is commonly attributed to the Greek philosophers of the first millennium BC, who after all came up with the term “atom” (meaning “indivisible”, or, more literally, “uncuttable”). Through refinements based on observations in particle accelerators and telescopes, we have ended up with a handful of elementary particles and four forces. It is conceivable to think of all scientific knowledge as stemming from that standard model, linked to it by a path of increasing complexity. E.g., from the physical knowledge of basic interactions one can derive the chemical properties of molecules and their interactions, then move on to the properties of biological tissues and organisms ; in a next step up the ladder of complexity, psychoanalysis describes the workings of the mind, and higher up still, social sciences focus on interactions between beings. Each level of complexity is worthy of study, as it spawns new patterns and features that can be cast as laws. The current paradigm of scientific knowledge encompasses such concepts as the Big Bang, evolution and genetics, and the origin of language and speech.

Most of the examples given so far have focused on understanding –as indeed did the ancient Greek philosophers. (It has been pointed out that their science was based mostly on observation, and that experiments were few and far between.) As hinted at earlier, knowledge is power : it can be used to manipulate the natural world. Enter the engineers. From knowledge of biology they have developed genetically modified crops, and also hepatitis vaccinations. Psychoanalysis has led to therapy, social science to strategies for political campaigns. The chemical magic of oil is the basis for much of our economy.

And again, the physical science, in its incarnation in this dissertation, serves as another perfect example. For this text deals with materials science – the lore of understanding and designing materials, explaining and controlling their properties in terms of their atomic structure. The basic assertion of science – that complex behavior can be derived

from elementary interactions on an “atomic” level - is in a very literal way the driving force of materials science. This is clear both in the theory of materials science – where, e.g., the behavior of electrons in a lattice, or scattering properties (i.e., interactions) are studied – and also in its applications, which range from designing faster gates for computer transistors, to developing more efficient solar cells for energy production, to nanotechnology, to lighter composite materials for the construction of aircraft, ... All unified in one line of physics, the Schrödinger equation (or Dirac equation in the relativistic case).

The opportunity for specialization is dazzling. In this dissertation, I will focus on a particular technique used in materials science : electron microscopy. All observations require interaction of the observer and the observed object, and in electron microscopy, a beam of electrons is used to probe a sample, similarly to the use of light in a conventional light microscope. Surely the most spectacular feature of electron microscopy is its superior spatial resolution, which allows probing individual atom columns of a material. As the relevant scale of materials decreases (think nanotechnology), this is a big advantage.

Interactions can generally be divided into elastic interactions, where no energy is exchanged between probe and sample; and inelastic interactions, where a net energy transfer occurs between probe and sample. Electron energy loss spectroscopy, the focus of this work, belongs to the latter category. The sample’s properties are investigated by measuring how it absorbs energy from the beam.

Obviously, there are several ways one can study a given subject. Two options are theoretical work, and observations or experiments. A new, third pillar of research has emerged in the previous century. Since the number-crunching calculational power of computers reached a critical mass, they have been used to study problems in almost every field of science. Materials science, where the behavior of (mostly) electrons as described by solutions of the Dirac or Schrödinger equation determines material properties of interest, is again an excellent example. Computer calculations, both *ab initio* and using empirical information, have become more robust and powerful as computational resources and computational science steadily grew over the last few decades. The ability to obtain numerical solutions to problems for which analytical solutions or accurate measurements are hard or impossible to find, has significantly widened the scope of materials science. The calculations have not only served to make theoretical predictions (indeed, the often-quoted “design of materials” is still in its infancy), but has enjoyed massive application in interpreting experimental data. The wealth of information on electronic structure that is contained in an electron energy loss spectrum, for example, is hard to extract, and theoretical (i.e., computational) reference is often needed.

Apart from opening up otherwise inaccessible applications, numerical work also has the potential to validate our understanding of phenomena. In the words of R. P. Feynman, “If I can’t calculate it, I don’t understand it”.

In spite of the tremendous successes of computational science, one still encounters the occasional prejudice. Managing a hundred thousand lines of Fortran source code is, to some, less noble an endeavor than, say, fine-tuning the calibration of a microscope, or

counting Feynman diagrams. And the person who first conceived of the equations to be solved, inventing Density Functional Theory, say, is usually regarded as having higher scientific merit than the person who solves these equations by teasing its solutions out of a central processing unit. (As an aside, it is heartening to the computational scientist to learn that their conceptual fathers from the theoretical field do hold their computational colleagues in high regard.)

This dissertation is clearly a piece of computational science – but also aims to test the fundamental theory of EELS.

1.b. The focus of this dissertation

What is the theme of this dissertation? So far, I have descended into specialization as follows :

Physics, materials science, electron microscopy, electron energy loss spectroscopy, computational work.

Yet we need to decide more specifically where to focus my research work.

Let's situate this work by exploring a few lines of thought.

First, theories go through certain stages of growth. There are very new theories and techniques; state of the art, high-tech science that is still in a stage of conceptual development. It is in the hands of theoreticians, who study it on model systems, looking for proof of principle type applications.

On the other hand of the spectrum are theories that are so well understood and established that they can be readily applied by people who have only basic understanding of them ; they are typically integrated in black box type tools, that perhaps come pre-installed with some instrument; or they have completed the long migration from obscure journals into undergrad text books.

The theory of time dependent density functional theory (TDDFT), to name relevant examples, still seems to partly be in the developers' phase, with people spending much effort trying to find decent kernels. Ground-state density functional theory, on the other hand, is so well established and has been so widely tested that it is now used routinely by people who would be hard pressed to say what exactly a functional is.

In between are people who work with theories that are fairly well understood, and improve their methodology to make them more useful.

While rough black box and more acceptable "grey box" tools are certainly available to the scientific community, it is also clear that much improvement is still desired in electron energy loss simulation. It is in that middle field that I have therefore chosen to work. I did not wish to simply routinely apply black box tools to new materials ; nor did I want to spend my five years of doctoral research fiddling with a kernel for TDDFT that matches some uniform electron gas limit exactly. I want to do methodological, theoretical materials science work that doesn't consist of applications, but definitely has application in mind all along.

Not only the theory matures ; so do its applications. Much ink has been spent discussing the virtues of quantitative electron energy loss spectroscopy. The truth is, we still haven't seen too much truly quantitative EELS. Quantitative EELS requires two things : accurate and well characterized experiments, and solid interpretation of the measurements – probably involving accurate and precise ab initio calculations. The quality of measurements has surely undergone tremendous progress over time (although there's more to be said about quantitiveness than just the specs of the microscope) ; the calculations that we are concerned with in this dissertation have quite a way to go.

Focusing on the computational side, what type of studies are out there? With a little bit of humor (remember, we're still in the motivational chapter), but not meaning any real disrespect, I distinguish (at least) four kinds of studies :

1. "Look what I can do!" Sometimes, ab initio calculated EELS-spectra are published for interesting materials, just like that. In all fairness, I quote my own work here (Titantah et al.²).
2. "Excellent agreement!" In a large number of publications, a measured spectrum of a known structure is compared to a calculated spectrum, and excellent agreement, by some standard of excellence, is proclaimed. The system is not always completely known, and some information on it may be extracted by means of comparison to the calculations.
3. "Tell me something I don't know." Achieving some degree of excellent agreement for a known system is of course nice and all, but how exciting is that really? A useful technique must be able to deliver previously unknown or uncertain information.
4. "Pssst ... The universe is not face centered cubic! (It's dirty!)" Calculations are usually done for model systems, not taking into account the many irregularities of any real-life sample – its shape, contaminations, temperature, etc. We need to move towards modeling more realistic systems if we want to achieve true quantitative research.

If the state of the art of EELS simulation had to be summed up precisely, I would, in all fairness, admit that "we cannot really calculate an EELS spectrum". Is such harshness warranted? I claim that :

1/ Its fundamental theory and its implementation are still unsolved even for simple "toy models" ;

and, in line with our discussion above,

2/ The world is not a toy model.

While there's certainly no shortage of excellent theoretical EELS calculations, these successes are not consistent : there are too many systems for which the calculations don't work well. Issues such as many body and core hole effects have not fully been resolved yet. Theories based on the Dynamic Form Factor need to be generalized to the Mixed Dynamic Form Factor to account for interference effects. Multiplets need to be further incorporated into the calculations. Indeed, in Chapter 4 we will show how, just a few years ago, the whole formalism was based on the wrong (non-relativistic) theory. Despite the progress reported here and in other scientific literature, the calculations we are concerned with still have a long way to go.

Additionally, the improving quality of experiments keeps raising the bar for *ab initio* EELS calculations, as previously indiscernible discrepancies are revealed. Also, truly quantitative research demands high accuracy calculations, as “the peaks are in the right positions” is simply not good enough anymore.

Perhaps the state of computational EELS is characterized well by R. Nicholls who studied EELS of fullerene materials in³ :

“It might be thought that a straightforward approach would be to compare experimental EEL spectra with spectra simulated from model structures, and then to refine the model structure to improve the agreement. The recent scientific literature shows that it is very difficult to simulate EEL spectra with sufficient accuracy to enable a model refinement to be carried out in this way. The strategy employed in this study is to find features in the experimental EEL spectra which are significantly different for different fullerene materials, and then to explore which details of the model structures affect these significant features. This strategy involves relating changes in the spectra to changes in the model, rather than trying to reproduce the experimental data.”

While this is on some level a tribute to the usefulness of *ab initio* EELS, it also points out its deficiencies and limitations.

As will become more apparent from our discussion of the theory of electron energy loss spectroscopy in later chapters, the technique provides us with access to an overwhelming wealth of information – potentially the density matrix of a sample. To uncover that information in a truly quantitative EELS-experiment, we must then solve the two problems stated above :

- 1/ Learn how to correctly calculate the absorption spectrum of a sample ; and
- 2/ Learn how to do this calculation for a realistic sample.

This thesis focuses primarily on the former problem, although not without regard to the latter.

2. Nederlandse samenvatting

Elektronenergieverliesspectroscopie (EELS) is een waardevolle techniek **voor materiaalonderzoek op atomaire schaal**. EELS bestaat eruit een bundel van snelle elektronen (~ 100 keV) doorheen een sample te sturen en het energieverlies van de bundel met een spectrometer te registreren. Een fractie van de bundelelektronen interageert immers met het specimen, waarbij energie en impuls overgedragen kan worden. Een deel van de uittredende bundel heeft dus een andere energie en richting dan voor interactie met het sample. Men meet deze distributie van energieverliezen en verstrooiingshoeken op met een spectrometer en verkrijgt zo een EELS-spectrum.

Aangezien de energie-absorptie door het sample aangewezen is op de beschikbaarheid van onbezette elektronorbitalen met een excitatie-energie die overeenkomt met het energieverlies van de bundel, is het EELS-spectrum een ‘fingerprint’ van de lokale onbezette toestandsdichtheid, of korter, van de lokale elektronische structuur van het sample. In het bijzonder ‘edges’, signalen afkomstig van excitaties van een discreet kernniveau van een atoom in het sample (bv. 1s of 2p), geven aan welke elementen in het specimen aanwezig zijn en in welke hoeveelheid. De uitmuntende ruimtelijke resolutie en gevoeligheid van EELS, gekoppeld aan een steeds verbeterende energieresolutie, maken dat EELS een superieure techniek is voor metingen van de elektronische structuur op atomaire schaal. Die elektronische structuur is op zich verbonden met tal van materiaaleigenschappen die van belang zijn voor (technologische) toepassingen. De hoge ruimtelijke resolutie is duidelijk relevant in het tijdperk van de nanowetenschap en de nanotechnologie.

Om de schat aan informatie in het EELS-spectrum te kunnen ontsluiten, is het vaak onontbeerlijk om metingen te kunnen vergelijken met *ab initio* berekende spectra, aangezien de interpretatie van een spectrum (de link tussen spectrum en elektronische structuur of materiaaleigenschappen) niet triviaal is. Los daarvan is computationele materiaalfysica ook onontbeerlijk om theoretische inzichten te valideren en te verdiepen.

Deze thesis heeft tot doel de *ab initio* berekening van EELS-spectra te verbeteren.

Hoewel dergelijke berekeningen al met succes zijn uitgevoerd, blijven er teveel discrepanties tussen theorie en realiteit opdat men eenduidig kwantitatief EELS-onderzoek zou kunnen doen. De twee bijdragen geleverd in dit werk zijn ten eerste een relativistisch formalisme voor EELS, en ten tweede een strategie om “core hole” spectra te berekenen door middel van de “final state rule” zonder “supercel”. Deze begrippen worden hieronder verduidelijkt – laten we voorlopig opmerken dat het een verbetering betreft van een methode om meerdeeltjesinteracties in het excitatieproces te benaderen.

Deze twee sporen van vooruitgang zijn geïmplementeerd in twee veelgebruikte *ab initio* modules voor de berekening van EELS (**FEFF en WIEN2k+TELNES2**), en zijn dus beschikbaar voor de wetenschappelijke gemeenschap. FEFF berekent de elektronische structuur van een cluster atomen in de reële ruimte door het berekenen van de Greense functie. WIEN2k berekent de elektronische structuur van een oneindig periodisch rooster

van atomen (een kristal) in de reciproke ruimte door het berekenen van elektronorbitalen volgens dichtheidsfunctionaaltheorie of DFT. De twee methodes zijn complementair en het is dus nuttig om over beide te beschikken.

Hoofdstuk 3 is een algemene inleiding waarin de gebruikte begrippen en theorieën nader worden verklaard. De principes van EELS worden nader beschreven in hoofdstuk 3.b. Daarna wordt in hoofdstuk 3.c de dichtheidsfunctionaaltheorie bondig beschreven, waarop WIEN2k is gebaseerd. Tenslotte wordt in hoofdstuk 3.d de Greense functiemethode, basis voor FEFF, uit de doeken gedaan, met ruime illustraties aan het N K spectrum van GaN.

Het eerste onderzoeksonderwerp (hoofdstuk 4) betreft **relativistische berekening van EELS**. De bundelelektronen die gebruikt worden in het experiment hebben typisch een snelheid van 50-80% van de lichtsnelheid, ruim voldoende opdat een relativistische beschrijving van de interactie belangrijk zou zijn. Dergelijke effecten werden recent beschreven door Jouffrey et al.,⁴ die opmerkten dat er een contractie van het veld van het bundelelektron optreedt in de richting van voortbeweging, die beschreven kan worden alsof de impulsoverdracht proportioneel met het kwadraat van de snelheid contracteert langs dezelfde richting. Deze beschrijving liet hen toe de enorme discrepantie te verklaren tussen oudere, niet-relativistische berekeningen van de zogenaamde **magic angle** en de experimenteel gevonden magic angle. De magic angle is een bijzondere waarde van de apertuur van de EELS-detector waarbij de meting haar onafhankelijkheid van de orientatie van het sample ten opzichte van de bundel verliest. Dit is in eerste orde een materiaalafhankelijke grootheid, en daardoor een directe test van de onderliggende theorie van EELS. De magic angle is van praktisch nut omdat orientatieafhankelijkheid de interpretatie van experimenten erg kan bemoeilijken.

In deze thesis hebben we de relativistische theorie verder ontwikkeld. Jouffrey et al.⁴ maakten de benadering dat de overgedragen impuls klein is ; wij vermijden deze beperking en ontwikkelen een algemener formalisme, gedefinieerd in een ontwikkeling in bolfuncties l, m . Niet alleen is de theorie daarmee algemener, we vinden ook correcties van de orde 10% op de berekende waarde van de magic angle voor het C K spectrum van grafiet. Daarnaast berekenen we ook de werkzame doorsnede als functie van de verstrooiingshoek en vinden zeer goede overeenkomst met metingen (in tegenstelling tot niet-relativistische berekeningen).

Het algemene relativistische formalisme is geïmplementeerd in de DFT-code WIEN2k+TELNES2. Het benaderde relativistische formalisme (Jouffrey et al.⁴) is geïmplementeerd in zowel WIEN2k+TELNES2 alsook in de Multiple Scattering code FEFF.

Hoofdstuk 4 is georganiseerd als volgt. In hoofdstuk 4.a geven we een algemene afleiding van de werkzame doorsnede voor EELS vertrekkende van een relativistische Hamiltoniaan. In hoofdstuk 4.b bespreken we de zogenaamde dipoolbenadering, die de resultaten van Jouffrey et al. geeft. In hoofdstuk 4.c ontwikkelen we het algemenere relativistische formalisme dat voor willekeurige impulsoverdracht en ook voor niet-dipooltransities geldig is. We bespreken de implementatie van dit algemene formalisme

in de WIEN2k+TELNES2 code in hoofdstuk 4.d. We bespreken de implementatie van het benaderde dipoolformalisme in FEFF in hoofdstuk 4.e. Tenslotte bestuderen we de belangrijke toepassing van de ‘magic angle’ in hoofdstuk 4.f., toegepast op het C K spectrum van grafiet. We tonen experimentele metingen, bekijken het falen van de niet-relativistische theorie, en geven de relativistische resultaten van zowel analytische berekeningen als FEFF en WIEN2k berekeningen. We merken op dat het algemenere formalisme licht superieure resultaten geeft (~ 10%).

Het **tweede spoor** van de thesis heeft een volledig ander onderwerp (hoofdstuk 5). De excitatie van het sample tengevolge van energieuitwisseling met de bundel is in wezen een dynamisch proces. Nemen we als voorbeeld een grafietspecimen. Indien de bundel meer dan 284 eV aan energie overdraagt aan een koolstofatoom in het sample, kan het 1s elektron van dit atoom geexciteerd worden naar een onbezette toestand boven het Fermi-niveau. (De excitatieenergie van het 1s orbitaal is ongeveer 284 eV.) Tijdens die excitatie is er echter interactie tussen het 1s elektron en het “gat” of “core hole” dat het achterlaat in het 1s-orbitaal. De interactie beïnvloedt het EELS spectrum sterk. Deze “**core hole**” interactie is in principe een meerdeeltjeseffect. Omdat meerdeeltjesberekeningen echter veel moeilijker en CPU-intensiever zijn dan eendeeltjesberekeningen, is de standaard voor EELS-berekeningen op dit moment de zogenaamde “**Final State Rule**” of FSR, waarbij het core hole statisch berekend wordt door een geexciteerd atoom met core hole in het 1s-orbitaal als een onzuiverheid in het grafietskristal te plaatsen, en vervolgens het excitatiespectrum van dat atoom te berekenen in de eendeeltjesbenadering. Afgezien van het feit dat dit een benadering is, heeft dit bijkomende nadelen. Ten eerste kan de hoeveelheid lading die uit de 1s toestand wordt weggehaald, als een variabele screeningparameter gebruikt worden, hetgeen soms toelaat betere resultaten te bekomen, maar dit ten koste van (theoretische en praktische) eenduidigheid. Ten tweede werken bandstructuurmethodes zoals WIEN2k (en vele vergelijkbare codes, die de uitverkoren methode zijn om de elektronische structuur van kristallen te berekenen) met een ‘eenheidscel’ : een kleine bouwsteen die een oneindig aantal keren wordt herhaald om een perfect periodisch kristal te bekomen. De “core hole onzuiverheid” moet in een grotere **supercel** geplaatst worden om zinnige resultaten te bekomen, en de vereiste grootte van deze supercel kan alleen door een onvoorspelbare convergentiestudie bepaald worden. Voor methodes in de reële ruimte, zoals FEFF, is dit tweede probleem niet van toepassing – maar deze methodes benaderen dan weer het (quasi-) oneindige kristal door een eindige cluster van atomen, hetgeen opnieuw een benadering is die een convergentiestudie vereist (zij het een die doorgaans eenvoudiger is).

Samengevat zijn deze FSR + core hole + supercel-berekeningen geen routinewerk.

In deze thesis werd de FEFF-code, die traditioneel in de reële ruimte werkt, aangevuld met een formalisme dat op **KKR-theorie** gebaseerd is en met Greense functies in de reciproke ruimte werkt. Ten eerste maakt dit de Multiple Scattering methode eenvoudiger en correcter voor berekeningen aan periodische systemen. Ten tweede laat de beschikbaarheid van beide sporen – reële en reciproke ruimte, of “short range” en “long range” formalismes – toe om de gekende equivalentie van beiden voor het

beschrijven van periodische systemen zeer direct te verifiëren. Deze test hebben we succesvol uitgevoerd voor verschillende materialen, o.a. het Si K spectrum.

De belangrijkste winst is echter dat we nu binnen eenzelfde berekening kunnen overschakelen van reciproke naar reële ruimte, en daarmee het beste van beide werelden kunnen combineren. Het is dan ook mogelijk om de elektronische structuur van een perfect periodisch systeem (zeg het grafietkristal in de grondtoestand, zonder EELS-excitatie en core hole) zonder “short range” benadering in de reciproke ruimte te berekenen, en dan de overeenkomstige Greense functie in de reële ruimte te berekenen. Het “core hole” kan dan in de reële ruimte worden toegevoegd, waar er geen eenheidscellen of supercellen zijn, en een enkele onzuiverheid perfect kan worden berekend. Deze nieuwe strategie – **“FSR core hole EELS zonder de supercel”** is geïmplementeerd in de Multiple Scattering code FEFF. We hebben dergelijke berekeningen uitgevoerd voor de N K edge van GaN. We vinden zeer goede overeenkomst met het experiment, beter dan met andere methodes. We vergelijken bovendien met supercelberekeningen uitgevoerd met de DFT/bandstructuurcode WIEN2k+TELNES2, en we vinden dat de DFT-resultaten naar de “FSR core hole EELS zonder de supercel”-resultaten lijken te convergeren die we met FEFF hebben bekomen.

Hoofdstuk 5 is georganiseerd als volgt. In hoofdstuk 5.b beschrijven we de theorie voor Greense functiemethodes in de reciproke ruimte. In hoofdstuk 5.c bespreken we de implementatie ervan in FEFF en illustreren dergelijke berekeningen. In hoofdstuk 5.d testen we de equivalentie van beschrijvingen in reële en reciproke ruimte aan de hand van het Si K spectrum. In hoofdstuk 5.e tenslotte passen we de “FSR core hole EELS zonder de supercel” toe op het N K spectrum van GaN.

Hoewel de theorie en *ab initio* berekening van EELS duidelijk nog niet het eindpunt van zijn ontwikkeling heeft bereikt, heeft deze thesis daarmee twee zinvolle bijdragen geleverd, die toelaten betere EELS-spectra te berekenen, en die ook daadwerkelijk beschikbaar zijn voor elke wetenschapper, en die tenslotte licht werpen op ons theoretisch inzicht in EELS.

Noot : De appendices van deze thesis bevatten praktische en technische informatie over de FEFF en WIEN2k+TELNES2 programma's die van belang kan zijn voor gebruikers van deze relativistische *ab initio* programma's voor EELS.

3. General introduction

3.a. Content of this dissertation

In the previous chapter, I wrote that the theme of this dissertation is the improvement of calculations of electron energy loss spectroscopy (EELS). EELS is the study of material properties through measurement of its energy absorption from an electron beam. To solve all of the current challenges would be too ambitious for a one-man project, but I believe that the work presented in this thesis does make significant advances in the calculation of EELS.

I have focused primarily on improving the methodology of *ab initio* EELS, leading to higher quality of calculations. I have worked with relatively straightforward materials – say, graphite C, h-GaN, etc – as my focus is on methodology itself, rather than on specific material applications. I have paid less attention to building the bridge with experiment (and achieving fully quantitative EELS) by making our idealized “model systems” more realistic. Additionally, my dissertation focuses on so-called “core loss” spectra, which involve excitations of core electrons of the sample.

This paragraph provides a very concise summary of what follows.

Chapter 3.

The first major problem I’ve addressed concerns the fundamental theory of EELS. Until very recently, it was commonplace to describe the interaction of the microscope’s electron beam and the sample classically (i.e., non-relativistically). Suspicion starts to grow as soon as one realizes that beam energies of 300 keV (corresponding to $\beta = v/c = 0.77$) are commonly used. Ungrounded claims were sometimes made that up to such energies it is sufficient to make a few semi-relativistic changes to the theory, such as using a relativistic electron mass and wave vector. However, it has now been established that this is not true. Relativistic theory is needed to describe the scattering of the beam on the sample. The very core of EELS theory and calculations were, until very recently, fundamentally flawed.

I address this problem by developing a relativistic formalism, based on work by Schattschneider et al.⁵, to describe EELS. The relativistic theory gives significant corrections over the non-relativistic theory when applied to anisotropic samples. I have implemented this formalism into two important and complementary EELS codes, the real space multiple scattering program FEFF, and the density functional program WIEN2k. Both the small-q-approximated formalism of Schattschneider et al.⁵ and a formalism without such approximations are explored.

I find that the “magic angle paradox” (see chapter 4.f), the phenomenon that drew people’s attention to this basic problem in the first place, is solved quite well in both

approaches (as already shown for the small- q theory by Schattschneider et al.). I show an application to the graphite C K edge. The “full” formalism that I develop here gives modest but noticeable ($\sim 10\%$) corrections over the small- q formalism of Schattschneider et al.⁵.

Chapter 4.

The second problem that I have worked on, is of a more practical nature. It addresses the problems commonly encountered when using a supercell to calculate a core hole spectrum of a crystal within the final state rule. (These concepts will be explained below.)

It is quite obvious that the excitation of an electron of the sample from its core state into an unoccupied conduction state involves two particles : this excited electron, and the hole it leaves in the core state. In principle, the resulting core-hole interaction needs to be accounted for in a many-body theory. In practice, however, such theories prove much harder to solve computationally than corresponding one-particle approximations. Although progress is certainly being made on solving the many-body problem including core-hole interaction, it is very common to calculate EELS-spectra using the “final state rule”. This means that one places an excited atom in a host lattice of atoms in their ground state, calculates its electronic structure within an independent particle framework, and then calculates the EELS-spectrum. If the sample is a crystal, then one typically wants to do this calculation in reciprocal space, using a unit cell to describe the basic building block of the material. Supercells will then be necessary to accommodate the excited atom, in the same way that they are necessary for impurity calculations. Setting up these supercells, calculating their electronic structure, and converging the size of the supercell is sometimes easy, but is sometimes a tedious and cumbersome process requiring significant computational resources. Common challenges of the core hole calculations are discussed and illustrated with literature examples.

In this work, I present a workaround where the electronic structure of the unperturbed crystal is first calculated in reciprocal space using a formulation based on impurity KKR theory. In a second step, the excited atom (or “core hole atom”) is added in real space, avoiding the need to design a supercell and the danger of introducing artifacts. I have implemented this approach in the real space multiple scattering program FEFF (introduced in Sec. 3.d). Thanks to these improvements, FEFF is now able to give better results for the periodic systems that were not well described by a real space cluster. Additionally, we now have an approach to calculate core hole EELS without the need for a supercell. We also discuss the equivalence of long range and short range formulations of multiple scattering theory⁶, which is the formal justification for using a real space description for periodic systems. As applications, we look at GaN, graphite, Si, and diamond.

Appendices.

While this dissertation presents some new ideas and theoretical content, no doubt its most tangible legacy are the programs I’ve developed. I’ve developed new ELNES programs for both the DFT code WIEN2k⁷ and the Green’s function code FEFF⁸. Both are popular tools for *ab initio* calculation of ELNES^{9,10}.

The appendices gather technical information about these new programs. While these descriptions have no direct scientific value, they are included here for reference for users of these programs. Both the software structure and the usage of the programs are discussed.

The current chapter.

Before I move on to discuss my work, some concepts need introduction. In the following sections of this introductory chapter, I will describe electron energy loss spectroscopy, as well as the two formalisms underlying the two computational approaches featured in this dissertation : density functional theory, and Green's function theory.

3.b. Electron energy loss spectroscopy in the transmission electron microscope

3.b.1. EELS as a key to the electronic structure

Electron Energy Loss Spectroscopy (EELS) is, essentially, the interaction of a beam of electrons with a sample. It is a spectroscopic technique used in materials science to obtain structural, chemical and electronic information about a sample. EELS has been developed into a successful and reasonably well understood technique, and many good reference texts are now available to introduce the novice to EELS and give an overview of applications and limitations.^{11,12,13,14,15,16} Thanks to this availability of comprehensive resources, I feel justified in keeping this introduction concise, and referring the reader to one of the sources referenced above for a more exhaustive discussion of EELS. I will somewhat neglect, in favor of theory, the experimental part of the technique, in particular, as it is neither my area of expertise, nor the theme of this dissertation.

EELS is essentially the interaction of a beam of electrons with matter. The first EELS experiments were reflection experiments, in which a beam of electrons scatters off the surface of a sample.^{15,17,18} Such experiments probe the electronic properties of the surface. In this thesis, we describe the more conventional transmission EELS, in which the electron beam passes through the sample and its energy loss is measured. Transmission EELS probes the bulk properties of the sample (although one must note that samples tend to be so thin that the bulk character and the surface sensitivity of the experiment may be questionable).

Standalone, purpose built EELS spectrometers exist¹⁵, but most commonly, transmission EELS experiments are done in a transmission electron microscope (TEM).

This dissertation deals exclusively with EELS done in the TEM.

Some obvious advantages of using a TEM is, first of all, the ability to use very fine probes. Probes with a diameter of the order of ~ 1 Angstrom (\AA) can be focused on the sample, making the experiment very local, and therefore providing information on an atomic scale. The ability to use electromagnetic lenses to focus the electron beam, and, secondly, the strong Coulomb interaction between beam and sample which yields workable signal intensity even with very low beam currents, are crucial in making such incredible spatial resolution and sensitivity feasible. Although it would clearly be an exaggeration to say that EELS routinely allows to get information on the atomic scale, some experiments look very impressive indeed, e.g. Ref.¹⁹, where a signal was collected from single Gd atoms inside fullerenes encapsulated within single wall carbon nanotubes.

Let us have a closer look at what kind of information the EELS experiment gives.

The electrons entering the sample have been accelerated to very high energies (typically of the order 10^5 eV). Samples are typically less than 100nm thick, sometimes as thin as 20 nm. This is of the order of the mean free path (MFP) for plasmon excitations (typically ~ 100 nm).

Because the sample is so thin, and the beam electrons travel at such high velocity (e.g., a beam energy of 300 keV corresponds to $v = 0.8 c$), most of the beam electrons exit the sample without being scattered at all. Other electrons are scattered elastically, changing their direction but not their energy. Still other electrons scatter inelastically, losing energy to the sample and slightly changing direction. While the incoming beam was (in an idealized case) uniform in energy and direction, the outgoing beam's intensity is spread over a range of energies and scattering angles. While traditional TEM uses only the elastically scattered electrons, the EELS spectroscopist measures the distribution of inelastically scattered electrons, either as a function of energy loss and integrated over scattering angle, or as a function both of energy loss and of scattering angle. In practice, this is done by collecting the outgoing beam over a range of scattering angles, and using a magnetic prism to create energy dispersion.

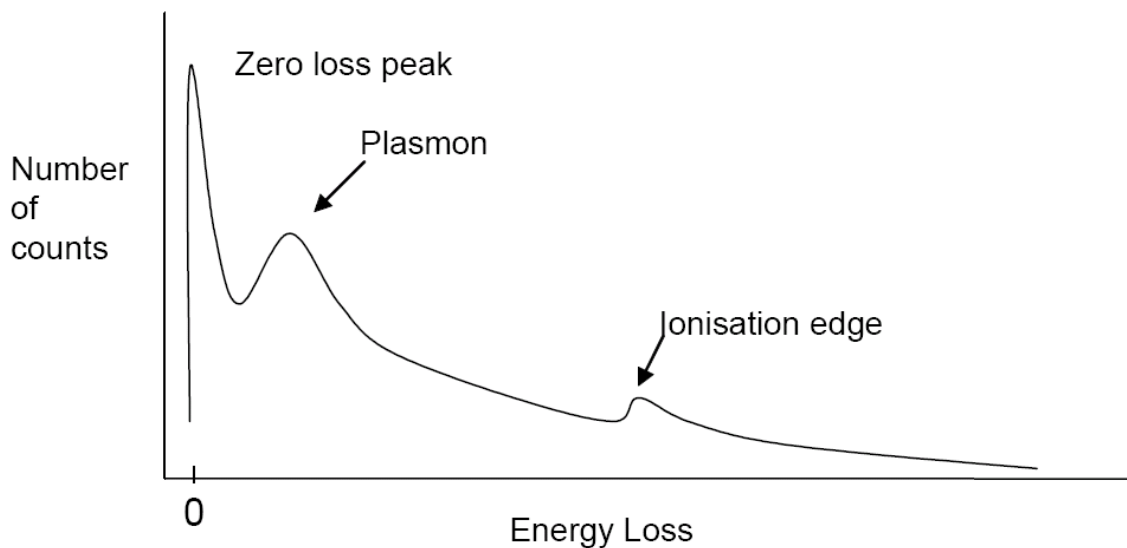


Figure 3-1 Cartoon version of a typical EELS spectrum.

Before we continue, it's worth noting that secondary particles partake in the experiment. The energy absorbed by the sample can lead to the emission of a photon (X-ray), or an Auger electron. These secondary signals can also be studied and give information on the sample, but this is not part of EELS. Figure 3-2 summarizes all processes that happen in the sample during an EELS experiment.

Figure 3-1 schematically shows an EELS spectrum. The largest signal occurs at energy loss zero : the zero loss peak (ZLP) contains all electrons that traversed the sample without losing any energy. The width of the ZLP is a good indicator of the energy resolution of the recorded spectrum, although this resolution does vary with energy loss. The fact that the ZLP has nonzero width is due to various broadening processes, but for a well operated microscope, it is mainly due to the imperfect monochromaticity of the electron source of the microscope. Modern instruments use cold field emission guns (FEG), which have energy widths of about 0.3 eV, or, more often, a Schottky FEG, with a resolution of about 0.6 eV. Microscopes equipped with a monochromator perform even better, obtaining energy resolution below 0.1 eV.²⁰

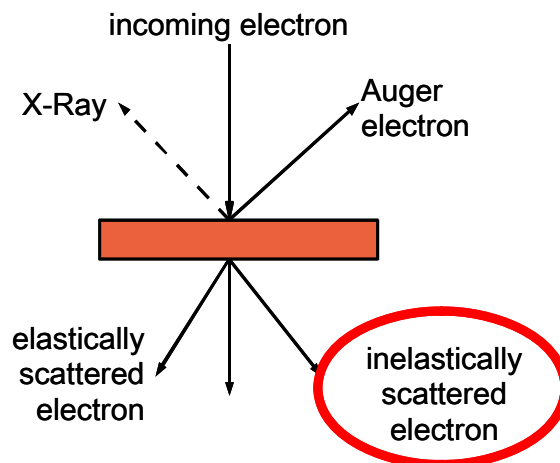


Figure 3-2 Processes occurring in the sample during an EELS experiment.

These numbers are of paramount importance. Modern 0.1 eV resolution microscopes allow scientists to extract much more information about the electronic structure of the sample than older microscopes with an energy resolution of 1-2 eV. We give an example for C70 C K edges (Nicholls³) in Figure 3-3.

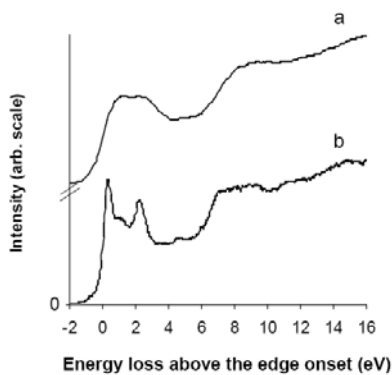


Figure 3-3 C K edge of C70 fullerene recorded on a JEOL 2010F (a) and the monochromated Delft Technai (b).³

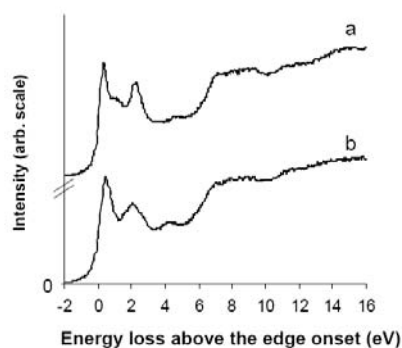


Figure 3-4 C K edge of C70 (a) and C60 (b) obtained on the monochromated Delft Technai.³

The upper spectrum was recorded on a JEOL 2010F (using a thermally assisted field emitter) ; the lower on the Delft monochromated FEI Technai, both operating at 120 kV. The difference in energy resolution is a factor of 10. Figure 3-4 shows the same C K edge, recorded on the Technai, of a C70 molecule (upper) and a C60 molecule (lower).

Clearly, in order to distinguish between the two fullerene molecules, the superior energy resolution is needed.

It is exciting to see that, with the development of modern high resolution microscopes, experimental EELS has in recent years reached the quality necessary for high precision measurements and true quantitative EELS.

Let us return to the description of the EELS spectrum (Figure 3-1). Apart from the ZLP, the spectrum is traditionally divided in two parts : the low loss region, and the core loss region. The separation between the two regions is fairly arbitrary and is typically taken to be at 50-100 eV energy loss.

The most intense feature in the low loss region, typically an order of magnitude less intense than the ZLP, is the plasmon peak. This is usually a fairly broad peak, situated at 5-50 eV energy loss, which corresponds to a collective excitation of electrons in the crystal by the beam. Intraband transitions can sometimes also be seen ; these are excitations of valence electrons into the conduction band. They are often superposed on the plasmon peak or the ZLP. If the sample is a semiconductor, then one can in principle measure the band gap from the low loss spectrum, as the onset of the EELS spectrum should be at the band gap energy. However, this information can be difficult to extract due to the ZLP.

The core loss region is characterized by atomic ionization, in which electrons are ejected from inner, or core, shells (e.g., K, L, M) of atoms in the specimen. This process requires that the core electron receives an energy greater than or equal to the critical excitation energy, E_c , which is a function of the specific atom and electron shell and is therefore uniquely defined. Characteristic signals termed “ionization edges” appear in the spectrum at energy losses corresponding to E_c , thus identifying the presence of specific elements in the spectrum. The mere presence of ionization edges at given energy loss in the spectrum therefore allows fingerprinting – qualitative identification of the chemical content of the sample. Quantification, i.e., analyzing the chemical composition of the sample is also possible, as the intensity of a given edge in the spectrum is proportional to the amount of the element present in the sample.

Edges are named by the corresponding element and shell, e.g., C K for the excitation of the carbon 1s shell. An overview of naming conventions is given in Figure 3-5.

Edge	Initial state	Initial state quantum numbers			Final state symmetry
		n	l	j	
K	$1s^{1/2}$	1	0	1/2	p
L ₁	$2s^{1/2}$	2	0	1/2	p
L ₂	$2p^{1/2}$	2	1	1/2	s or d
L ₃	$2p^{3/2}$	2	1	3/2	s or d
M ₁	$3s^{1/2}$	3	0	1/2	p
M ₂	$3p^{1/2}$	3	1	1/2	s or d
M ₃	$3p^{3/2}$	3	1	3/2	s or d
M ₄	$3d^{3/2}$	3	2	3/2	p or f
M ₅	$3d^{5/2}$	3	2	5/2	p or f
N ₁	$4s^{1/2}$	4	0	1/2	p
N ₂	$4p^{1/2}$	4	1	1/2	s or d
N ₃	$4p^{3/2}$	4	1	3/2	s or d
N ₄	$4d^{3/2}$	4	2	3/2	p or f
N ₅	$4d^{5/2}$	4	2	5/2	p or f
N ₆	$4f^{5/2}$	4	3	5/2	d
N ₇	$4f^{7/2}$	4	3	7/2	d
O ₂	$5p^{1/2}$	5	1	1/2	s or d
O ₃	$5p^{3/2}$	5	1	3/2	s or d
O ₄	$5d^{3/2}$	5	2	3/2	p or f
O ₅	$5d^{5/2}$	5	2	5/2	p or f

Figure 3-5 Nomenclature of EELS ionization edges.¹⁵

It's important to notice that the ionization edges are several orders of magnitude smaller than the ZLP, and are superimposed on a background consisting of the tails of the ZLP and previous inelastic peaks. The relative weakness of the core loss signal is one of the main challenges in EELS measurements and analysis.

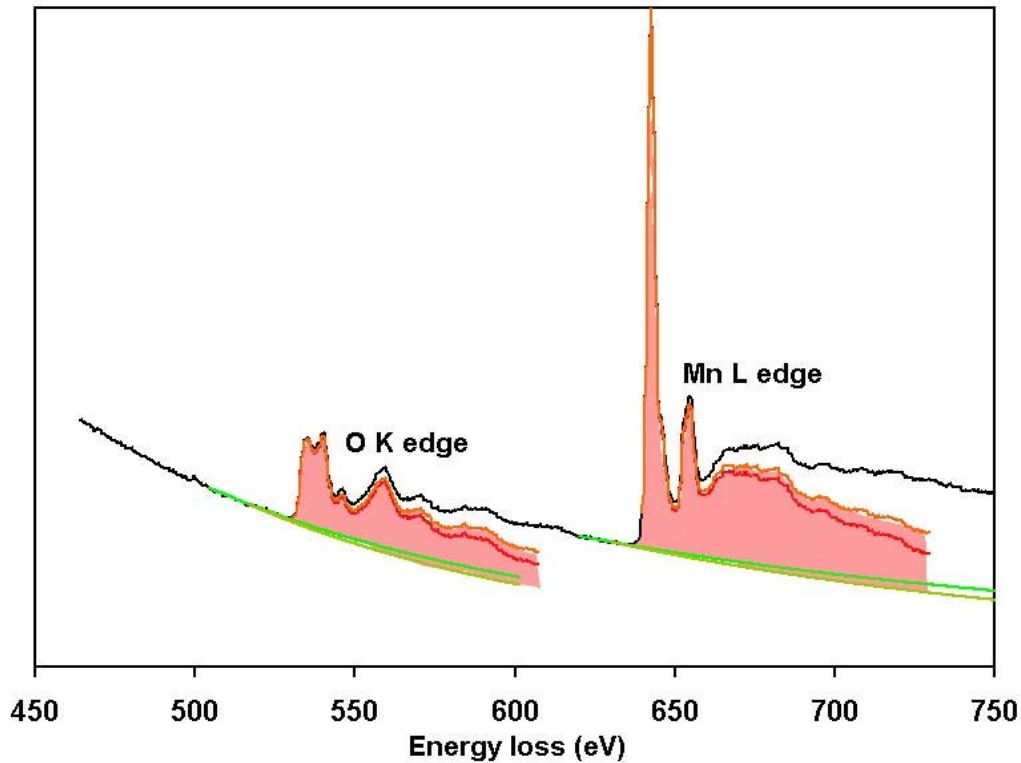


Figure 3-6 Background removal and plural scattering deconvolution of a MnO EELS spectrum.²¹ Total measured spectrum (black), 2 fits of the background (green), 2 corresponding background removed spectra (red and orange line), integrated cross section (red area under red curve).

In order to analyze the core loss EELS spectrum, it is customary to remove the background signal. This is usually done by fitting a smooth curve in the pre-edge region¹⁵, and removing it from the edge region by extrapolation, as can be seen in Figure 3-6 (green lines).²¹ As indicated in the figure, this technique usually introduces some uncertainties or artifacts.

Additionally, nothing keeps the inelastically scattered electron beam electrons from scattering again. The shape of the ionization edge will be complicated by signals from electrons that scattered inelastically off the core shell, and then underwent another energy loss event (typically, a plasmon excitation or other low loss excitation. It is very unlikely that an electron causes two core loss events.). This effect is called “plural scattering” and becomes more pronounced as the sample thickness increases. Plural scattering effects can be removed by Fourier deconvolution of the low loss spectrum^{22,23}, but as this numerical procedure of course introduces more uncertainty and artifacts, it is best to keep plural scattering to a minimum by working with thin samples, i.e., samples thinner than the mean free path of the plasmon excitation. An example is given in Figure 3-6 (red lines). The red area inscribed by the final curves is the measured cross section of the ionization edge, and can be used to determine the chemical composition of the sample, by comparing the measured cross-section to a known reference (measured or calculated). Usually, relative compositions are measured, as this eliminates many hard to quantify parameters (e.g., sample thickness) from the equations.

Model-based quantification procedures^{24,25,26} have been developed to address some of the problems associated with the somewhat *ad hoc* background and plural scattering removal described above.

In the rest of this dissertation, we focus on the ionization edges in the core loss spectrum. We also work with the background removed, plural scattering removed spectra, such as those shown in Figure 3-3 - Figure 3-6.

The ionization edges have intensity fluctuations above the edge onset. This is called the fine structure, and it is sensitive to the details of the local atomic environment such as coordination, valence, and the type of bonding. Measurement of such fine structure, and understanding how it is related to the electronic structure and ultimately to materials properties, can provide solutions to some otherwise unsolvable materials problems, particularly those where changes in bonding occur over small length scales.

The fine structure is again divided in two regions (Figure 3-7), called Energy Loss Near Edge Structure (ELNES) and EXtended Energy Loss Fine Structure (EXELFS). Typically, the first 30-50 eV above threshold is considered ELNES, and any discernible structure above that (50-500 eV above threshold) is considered EXELFS, but this distinction is fairly arbitrary. It can be motivated by the different interpretations of these regions. ELNES is typically seen as a signature of the local electronic structure of the probed atom. It is interpreted in terms of the local symmetry-projected density of states (DOS), giving information about bonding, configuration, charge transfer, valence, etc. EXELFS, on the other hand, is usually understood in terms of multiple scattering (MS) theory, where the excited electron is seen as a wave that propagates outward from the excited atom, interfering with waves backscattered from neighboring atoms, leading to oscillations in the fine structure. By extracting these oscillations from the fine structure, one can retrieve the Fourier transform of a radial distribution function, leading to information about interatomic distances and coordination numbers.^{27,28,29} The advantage over working with a diffraction pattern (which would be easier to measure accurately) is that the EXELFS information is element specific.

Both interpretations are equally valid for the whole ionization edge; the distinction is a matter of convenience only. As the cross section decreases rapidly with increasing energy loss, but the fine structure becomes easier to understand at higher energy losses, ELNES is easier to measure but harder to analyze, while EXELFS is harder to measure but easier to analyze.

While EXAFS, the X-ray equivalent of EXELFS, is a very popular technique, EXELFS studies are quite rare. Most EELS experiments focus either on the low loss region, or on the ELNES of ionization edges in the core loss region. This dissertation focuses on ELNES.

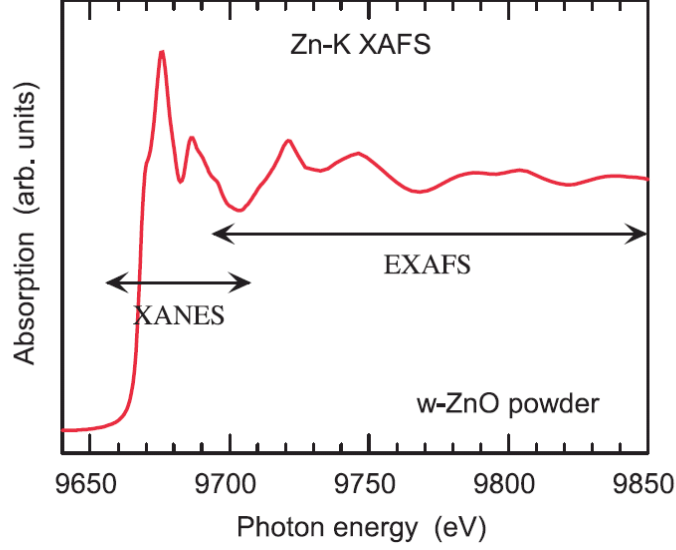


Figure 3-7 Experimental Zn K edge of wurtzite ZnO measured by XAS. Near edge and extended regions of the ionization edge are indicated as XANES and EXAFS.³⁰

In order to gain further understanding of EELS, let us turn to a (non-relativistic) quantum mechanical description of the absorption process. We refer to literature for more background to our intuitive description.^{13,31,18} We calculate the double differential scattering cross section (DDSCS), which is the probability of a beam electron being scattered into a direction described by a solid angle Ω , and transferring energy E and impulse \mathbf{q} to the sample. At the same time, the sample is excited and transitions from an initial state into a final state. Using Fermi's golden rule (derived from time dependent perturbation theory) to calculate the probability of such a transition, the DDSCS is given by³¹

$$\frac{\partial^2 \sigma}{\partial E \partial \Omega}(E, \mathbf{q}) = \zeta \sum_{I, F} \frac{k_F}{k_I} \left| \langle I k_I | V | k_F F \rangle \right|^2 \delta(E_I - E_F - E) \quad (3.2.1)$$

where V is the interaction potential between probe and sample, I and F are initial and final states of the sample of energy E_I and E_F , k_I and k_F are initial and final states of the probe, E is the energy loss, and ζ is a prefactor.

Although it is possible to measure the DDSCS (3.2.1), it is more common to measure a differential cross section

$$\frac{\partial \sigma}{\partial E}(E; \alpha, \beta) = \int_{\alpha, \beta} d\mathbf{q} \zeta \sum_{I, F} \frac{k_F}{k_I} \left| \langle I k_I | V | k_F F \rangle \right|^2 \delta(E_I - E_F - E) \quad (3.2.2)$$

which is (3.2.1) integrated over a range of impulse transfers selected by the microscope settings, here represented by the parameters α and β . The parameter α is the convergence semi-angle describing the width of the beam. The parameter β is the collection semi-angle describing the opening of the EELS spectrometer (Figure 3-8). (For simplicity, we assume here that the beam is incoherent and that the detector is placed on the optical axis.) The EELS spectrum depends significantly on the impulse transfer³², and hence it is important to account for α and β when interpreting experimental results. Typical values are of the order mrad.

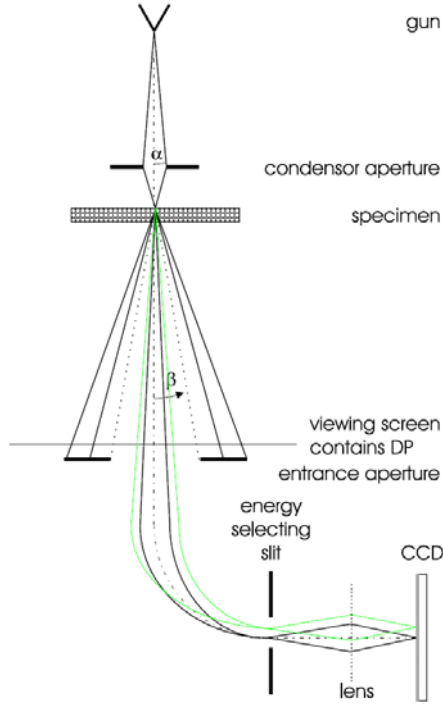


Figure 3-8 Convergence (α) and collection (β) semi-angle in an EELS experiment.¹⁵

In (3.2.1), the initial and final states of the probe are usually taken to be plane waves of wave vector \mathbf{k}_I resp. \mathbf{k}_F . (This implies that diffraction or channeling effects due to periodicity of crystals are neglected. To include these effects, a more general treatment using the Mixed Dynamic Form Factor would be required.³³) Furthermore, the interaction potential is the Coulomb potential. Exchange effects between probe and sample can be neglected because of the very high kinetic energy of the probe electron (it is extremely unlikely that the sample would emit an electron with kinetic energy of the order 10^5 eV). Coulomb interaction with the nucleus does not contribute for inelastic scattering (ignoring phonon excitations), and the nuclear positions can safely be assumed fixed during the excitation (this is the Born Oppenheimer approximation). The sample states I and F are then states of the electrons in the sample. Eq. (3.2.1) can now be updated^{31,18,13} to

$$\frac{\partial^2 \sigma}{\partial E \partial \Omega}(E, \mathbf{q}) = \frac{4\gamma^2 k_F}{a_0^2 k_I q^4} \sum_{I,F} \left| \left\langle I \left| \sum_{j=1}^N e^{i\mathbf{q} \cdot (\mathbf{r} - \mathbf{r}_j)} \right| F \right\rangle \right|^2 \delta(E_I - E_F - E) \quad (3.2.3)$$

where the constant ζ has been specified explicitly, and there are N sample electrons with position vector \mathbf{r}_j interacting with the beam electron at \mathbf{r} .

At this point, the sample states I and F in (3.2.3) are still N -electron states (N being the number of electrons in the sample). For practical purposes (e.g., calculations) these are often assumed to be products of one-electron states, of which only one changes during the scattering event. In that case, the equation can be simplified such that the states I and

F are now the one-electron orbitals occupied by the excited sample electron before resp. after the scattering. See Fuggle¹⁸ or Nelhiebel³¹ for details. I is then a one-electron core orbital, and F a one-electron unoccupied state.

$$\frac{\partial^2 \sigma}{\partial E \partial \Omega}(E, \mathbf{q}) = \frac{4\gamma^2}{a_0^2} \frac{k_F}{k_I} \frac{1}{q^4} \sum_{I,F} \left| \langle I | e^{i\mathbf{q}\cdot\mathbf{r}} | F \rangle \right|^2 \delta(E_I - E_F - E) \quad (3.2.4)$$

Eq. (3.2.4) can now be recast in terms of the unoccupied density of states (DOS) $\chi(E)$. With some approximation³⁴, we can write

$$\frac{\partial^2 \sigma}{\partial E \partial \Omega}(E, \mathbf{q}) = \sum_{l_F} \left| M_{l_F}(\mathbf{q}, E) \right|^2 \chi_{l_F}(E) \quad (3.2.5)$$

which is a sum of transitions to final states of l_F – character (s, p, d, ...), each given by the density $\chi_{l_F}(E)$ of available states of l_F – character multiplied by a matrix element $M_{l_F}(\mathbf{q}, E)$ which is a smooth and slowly decaying function of energy.

This is the expression for the DDSCS most often encountered in literature, although it is not strictly valid in all cases. For low symmetry materials, so-called cross-terms can contribute to the cross section (see Nelhiebel³⁴).

The impulse transfer \mathbf{q} in EELS tends to be small compared to the beam momentum \mathbf{k}_I , \mathbf{k}_F as the scattering is strongly forward oriented and the beam energy is much higher than the energy transfer. Additionally, the matrix element in (3.2.4) is confined to the region where the initial state I is nonzero. Typically, this is a deeply bound core state that extends only over distances comparable to the Bohr radius a_0 , but due to delocalization, the core state can be larger (\sim nm). The exponential interaction operator can therefore be approximated by the leading terms of its Taylor expansion,

$$e^{i\mathbf{q}\cdot\mathbf{r}} = 1 + i\mathbf{q}\cdot\mathbf{r} + (i\mathbf{q}\cdot\mathbf{r})^2 + \dots \approx 1 + i\mathbf{q}\cdot\mathbf{r} \quad (3.2.6)$$

After dropping the first term due to orthogonality of initial and final states, the leading term is the linear term. Retaining only this term is called the dipole approximation. Its effect is that only final states for which the orbital momentum quantum number obeys

$$l_F = l_I \pm 1 \quad (3.2.7)$$

can contribute to the cross-section (3.2.4). This reduces (3.2.5) to one term (initial state is a s-state) or two terms (other initial states).

Violations of the dipole transition rule have been observed^{15,35,30} but are rare in ELNES.

We have now established a useful interpretation of ELNES : apart from a smooth matrix element $M_l(E)$, it is a fingerprint of the local symmetry-selected unoccupied density of states. Local, because there needs to be overlap between initial and final states. Symmetry-selected, because of the dipole selection rule.

As an example, we show the Si L_{23} -edge in Figure 3-9.

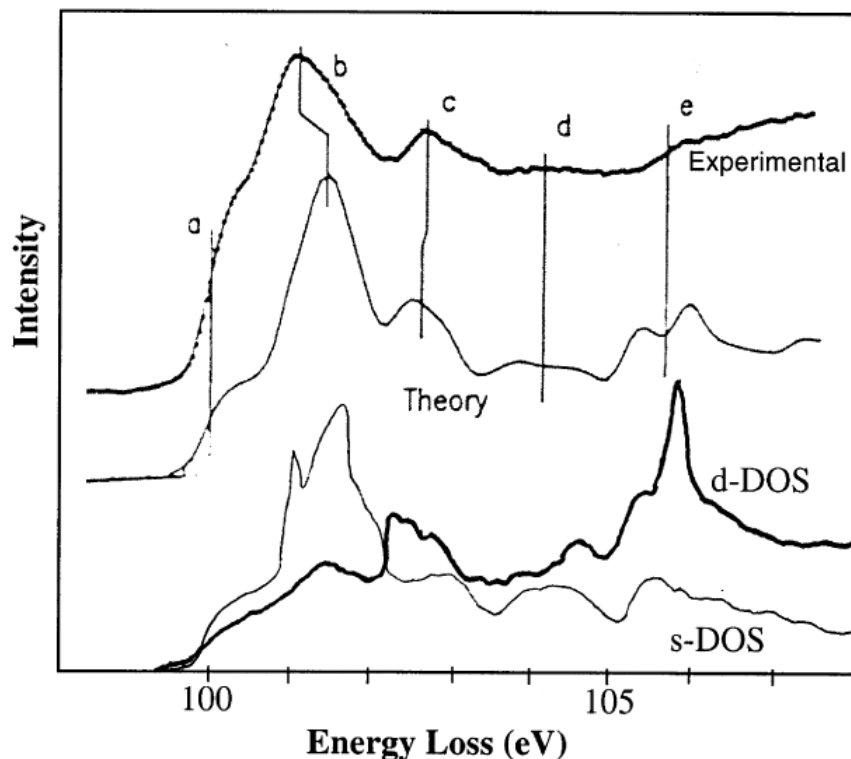


Figure 3-9 Si L_{23} -edge (initial state is the 2p-orbital). Experimental and theoretical spectrum compared with the local s-DOS and d-DOS. The spectrum can be seen to be the sum of a s-contribution and a d-contribution, in agreement with the dipole selection rule. Taken from Weng et al.³⁶

Given the DOS interpretation, it is now easy to understand that the same element in different materials will have a different EELS spectrum. An example is given for the C K edge in Figure 3-10. Of particular interest are the differences in fine structure, the appearance of a π^* peak in the materials that have sp^2 bonding but not in the materials that only have sp^3 bonding, and small variations in the edge onset (corresponding to small variations in the binding energy of the 1s state) known as chemical shifts. All these can be explained as differences in the local electronic structure.

A final warning needs to be given about the interpretation in terms of one-electron orbitals and DOS. The excitation of the core electron is a dynamic process, meaning that, as the electron is excited from one state to another, the “core hole” it leaves behind in the core state alters the local potential, and also alters the final state the electron transitions into. This can be understood in terms of timescales. A 200 keV electron has velocity $v = 2.7 \cdot 10^8$ m/s. Keast et al.¹¹ estimate that, given a diameter of ca. 0.01 nm for the O K shell, the value of the excitation timescale is only 10^{-19} to 10^{-20} s. (This argument ignores delocalization of the core shell and the possibility of an excitation occurring while the fast electron is some distance away from the atom, which is a less than compelling assumption. Arguably, the excitation timescale could be significantly ($\sim 10^2$) larger.) In comparison, the lifetime of the resultant excited state is typically much longer, owing to the slow core hole decay process (typically 10^{-14} to 10^{-15} s). This relatively slow decay

rate implies that the excited state should be influenced by the presence of the core hole. Generally, the core hole makes the final state “see” a larger than normal positive nuclear charge. The resulting attractive core hole potential tends to bind outer electronic states more strongly, making them contract spatially and lowering their binding energy, i.e., pulling them inward (in space) and downward (in energy). The core hole tends to shift transition probability down towards the edge threshold. If states get pulled below the onset, one speaks of core excitons.

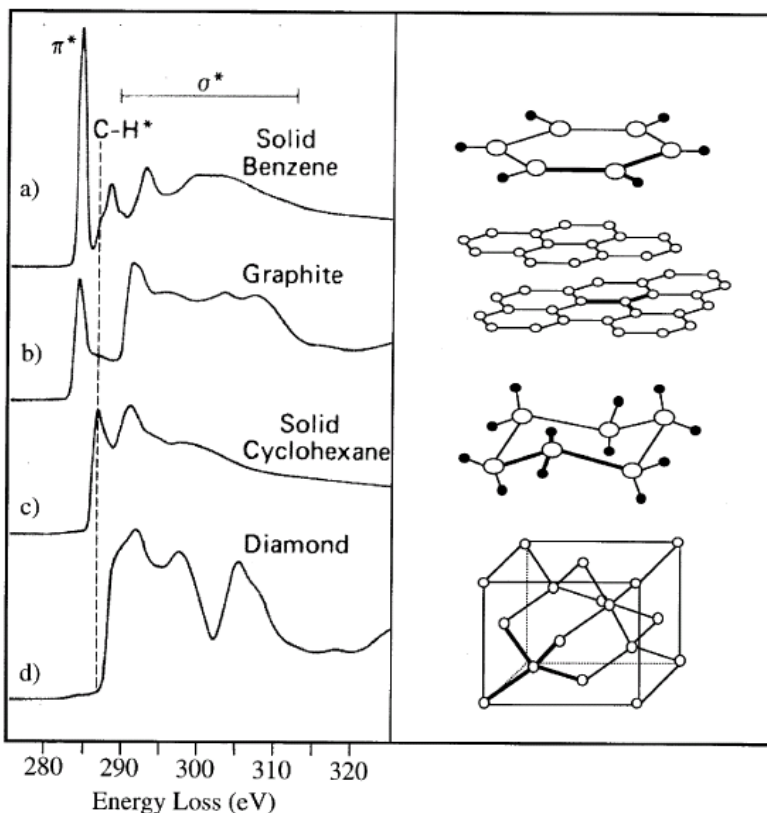


Figure 3-10 C K edge of carbon in different structures : benzene, graphite, cyclohexane, and diamond. The differences in local electronic structure and bonding are reflected in the EELS spectra, which show chemical shifts and different fine structure. Taken from Stohr.³⁷

The core hole may be shielded or screened by other electrons in the solid (e.g., mobile valence electrons) which will lessen its influence on more outlying electron states. Screening is expected to be stronger in metals, where such mobile valence electrons are more easily available, and weaker in insulators, where the core hole effect thus ought to be stronger. This generally appears to be the case.^{11,38}

A (theoretical) illustration of the core hole effect is given in Figure 3-11.

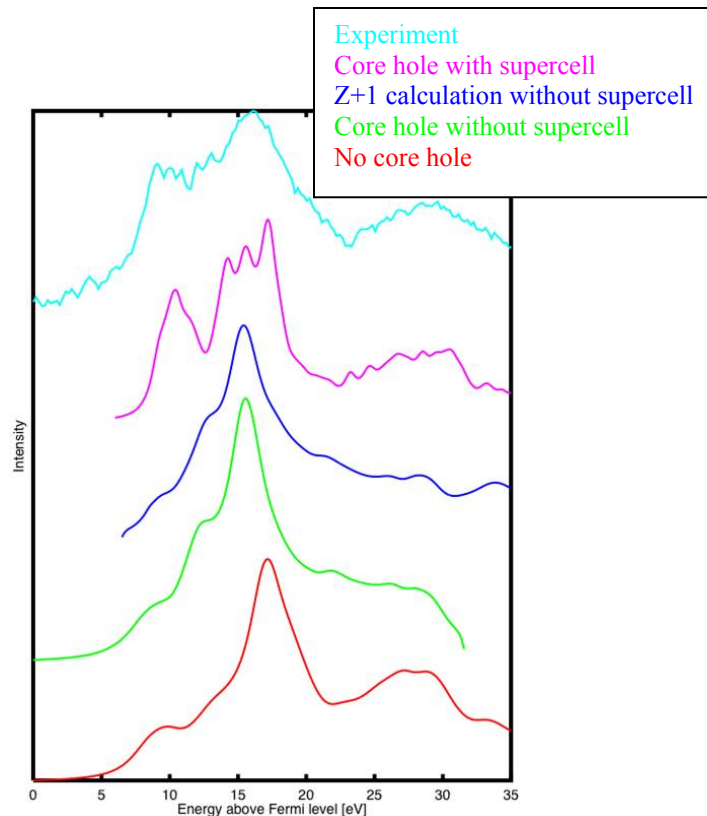


Figure 3-11 Mg K edge of MgO. Experiment is shown in light blue (top), ground-state calculation without core hole is shown for MgO (red, bottom). It fails to reproduce the experiment. A core hole calculation (pink, second curve from the top) matches the experimental spectrum fairly well.³⁹ The Z+1 approximation is also shown (dark blue). The green spectrum is an unconverged core hole spectrum.

3.b.2. EELS compared to other techniques.

Of course EELS isn't the only available technique for the study of the electronic structure of materials. First of all, we point out the difference between absorption techniques, which probe unoccupied electron states of the sample, and emission techniques, which probe occupied electron states.

Secondly, one can choose which primary particle to work with. In EELS, an electron probe is used to interact with the sample. Other possibilities are x-rays (photons) and neutrons. Electrons have the advantage that electromagnetic lenses make manipulation of the beam easy, and in particular it is possible to create Å-sized probes. At the same time, the strong Coulomb electron-electron interaction produces sufficient signal even at the low currents characteristic of these small probes. (Drawbacks of the strong interaction is that samples need to be very thin in order to have sufficient transparency, and that samples can easily suffer from beam damage.³)

Currently, only electrons can probe matter on the nanoscale (X-ray experiments typically have resolutions of up to $\sim \mu\text{m}$, although this can nowadays be improved to $\sim 10 \text{ nm}$ using zone plates. Neutron experiments have far worse spatial resolution.). This makes EELS a method of choice for studies of materials on the atomic scale.

The energy resolution of EELS used to be much worse than that of X-ray experiments (~ 1 eV for EELS, ~ 10 meV for X-rays), making X-rays the preferred primary particle for studies of bulk materials, but recent Schottky FEG + monochromator microscopes are getting energy resolution below ~ 100 meV, and it seems the gap is being closed.³

Third, instead of measuring the transmitted electron beam (EELS), one can also measure secondary particles such as X-rays (EDX) or Auger electrons (AES). These techniques yield comparable information to EELS, although not with the same spatial resolution and sensitivity.

Having established that EELS is a preferred technique for study of the electronic structure on the atomic scale, we refer to Tanaka³⁰, Keast¹¹, Egerton¹⁵ and references therein for many examples of EELS experiments on nanostructures, including interfaces, defects, dislocations, nanoparticles, ...

We now discuss the relation between XAS and EELS.

The X-ray equivalent of EELS is called X-ray Absorption Spectroscopy (XAS). Here, a beam of photons is used to excite core electrons into an unoccupied electron state, and similar spectra and ionization edges are measured as in EELS. The equivalent of ELNES is called X-ray Absorption Near Edge Structure (XANES), and the equivalent of EXELFS is Extended X-ray Absorption Fine Structure (EXAFS).

Formally, EELS and XAS are very similar.

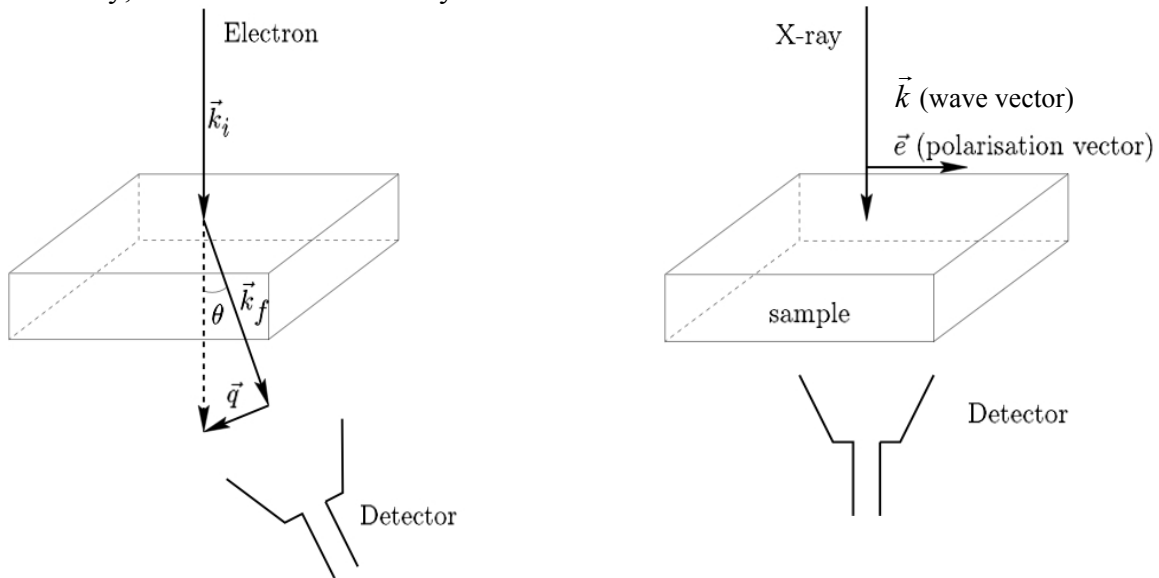


Figure 3-12 Schematic representation of EELS (left) and XAS (right).

The processes are represented schematically in Figure 3-12. The cross-sections are given by^{13,40}

$$\left. \frac{\partial^2 \sigma}{\partial E \partial \Omega} \right|_{EELS} \propto \sum_{I,F} |\langle I | e^{iq \cdot r} | F \rangle|^2 \quad (3.2.8)$$

$$\left. \frac{\partial \sigma}{\partial E} \right|_{XAS} \propto \sum_{I,F} |\langle I | e^{i\mathbf{k}\cdot\mathbf{r}} \boldsymbol{\varepsilon}\cdot\mathbf{r} | F \rangle|^2 \quad (3.2.9)$$

However, making the dipole approximation (3.2.6), (3.2.8) and (3.2.9) become equivalent

$$\left. \frac{\partial^2 \sigma}{\partial E \partial \Omega} \right|_{EELS} \propto \sum_{I,F} |\langle I | \mathbf{q}\cdot\mathbf{r} | F \rangle|^2 \quad (3.2.10)$$

$$\left. \frac{\partial \sigma}{\partial E} \right|_{XAS} \propto \sum_{I,F} |\langle I | \boldsymbol{\varepsilon}\cdot\mathbf{r} | F \rangle|^2 \quad (3.2.11)$$

with the polarization vector $\boldsymbol{\varepsilon}$ of the photon beam in XAS being formally equivalent to the impulse transfer vector \mathbf{q} in EELS. The omitted prefactors are different, leading to a faster decay of EELS with increasing energy loss.

3.b.3. *Ab initio* calculation of EELS.

As has been pointed out before, it's often useful to have *ab initio* calculations of EELS in order to help analyze experimental results. Straightforward examples include

- Calculation of an EELS cross-section used for quantification of the chemical composition of a sample
- Validation and refinement of a structural model by comparing calculated EELS to experimental results
- Improving understanding of an experimental EELS spectrum by using calculations to correlate peaks in the spectrum with features of the density of states or band structure, ... of the material

One needs to solve eq. (3.2.1) or an equivalent (see, e.g., the multiple scattering formulation in Sec. 3.d). Classifications of EELS calculations go back quite a ways^{41,42}. The different types of calculations essentially come down to different strategies used to calculate the electronic structure of excited states. Here, we distinguish three types of EELS calculations.

The first is the Multiple Scattering (MS) theory.^{43,44,45} In this approach, the excited electron in its final state is considered as a wave scattering off the atoms in the sample. This scattering process is described using Green's functions. It can be formulated both in real space (RSMS), which makes the method applicable to arbitrary, nonperiodic systems; or in reciprocal space, e.g. Kohn-Korringa-Rostoker theory (KKR).^{46,47}

The second approach are band structure calculations, which are, as the name implies, normally formulated in reciprocal space using infinite, periodic lattices. Eigenstates are solved for in reciprocal space, often using some basis set, such as plane waves (often coupled to the use of pseudopotentials⁴⁸]; or (Linearized) Augmented Plane Waves ((L)APW),⁴⁹ which use atomic spheres; or orthogonalized linear combinations of atomic orbitals (OLCAO).³⁰

The third approach is the atomic multiplet theory. In this very simple but successful approach, all multiplets are calculated and added in a simple approach that is mostly atomic, in which the solid state effects are summarized by the space group and some crystal field parameters.⁵⁰ Recently, multiplets have also been combined with band structure calculations.³⁰

A second divider (at least for the first two categories) is whether one works in an independent particle picture, or in a many-body picture. One can use a one-particle Green's function (e.g., the formalism developed below) or a two-particle Green's function (e.g., the Bethe-Salpeter theory (BSE))^{51,52} which can describe electron-hole interaction. One can use DFT (e.g., the section about DFT below), or time dependent density functional theory (TDDFT)⁵³.

It has been shown⁵⁴ that the independent particle (final state rule with core hole) calculations are incapable of describing certain many-body effects, such as deviations of the L_{23} branching ratio (the ratio of intensities of the $L_2:L_3$ white lines) from the statistical ratio of 1:2 in transition metals (Figure 3-13). It is not yet clear what is needed precisely to address this and other issues. E.g., Tanaka et al.³⁰ reports good results for white line ratios using one-electron band structure calculations combined with multiplets. Such calculations are more tractable than full many-body solutions such as GW + BSE.

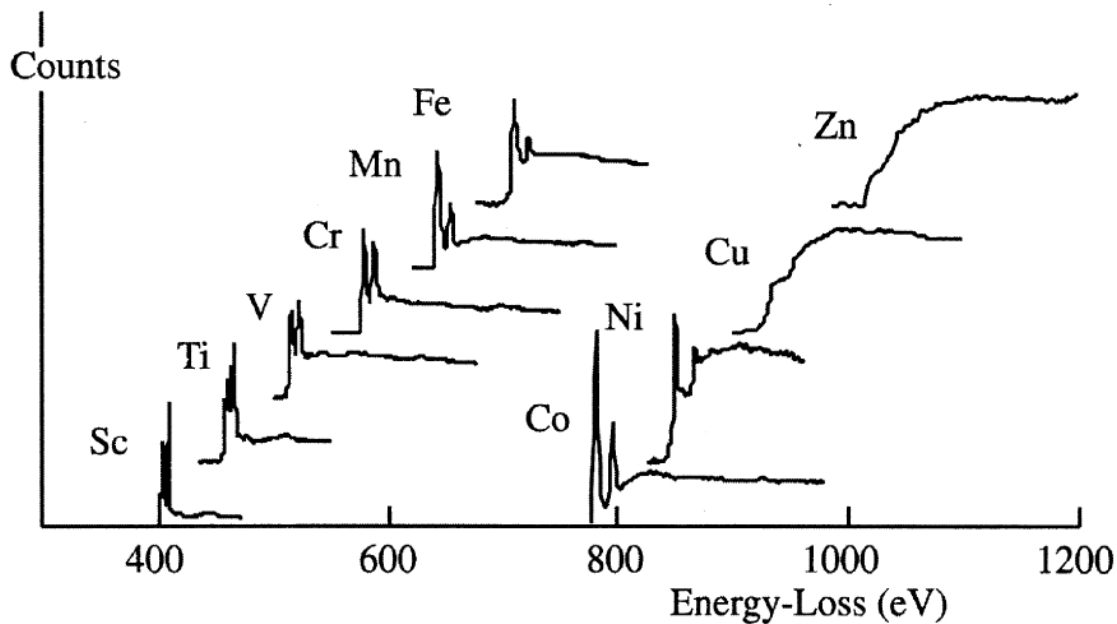


Figure 3-13 L_{23} edges for the transition metals. The sharp lines just above the edge onset are due to transitions to the unoccupied part of the narrow d-band. The intensity of these lines decreases as the atomic number increases across the spectrum and the d-band fills. The L_{23} white line ratio (see text) is generally different from the statistical 1:2 ratio and varies widely across the series.⁵⁵

The work in this dissertation is done either with multiple scattering theory (as implemented in the FEFF8 program⁸), or with band structure methods (as implemented in the WIEN2k program⁷). Each has its particular advantages. E.g., MS/FEFF8 is applicable to nonperiodic systems, is fast, can be used for large energy regions of 100's of eV above the edge threshold, easily takes temperature effects into account using Debye-Waller factors, and has some useful features for describing excited states, such as the self energy and TDDFT. On the downside, it uses spherical muffin tin potentials, and there can be finite cluster effects when describing solids. BS/WIEN2k, on the other hand, is slower and only applicable to periodic systems, and only useful in the near edge region, but it is Full Potential (FP), describes the electronic structure more accurately, and can be used for structural optimization.

3.c. Density functional theory

3.c.1. The Kohn-Sham equations

Whereas many approaches (e.g., Hartree-Fock) solve the Schrödinger equation in terms of wave functions, density functional theory (DFT) is formulated in terms of the electron charge density. This has obvious advantages, such as limiting the number of dimensions to 3, compared to 3N for a wave function of a N-particle system. Optimistically, one might say that density functional theory limits itself to useful information (the charge density), as, in the end, we are not interested in wave functions but in physical observables. According to DFT, these can be retrieved from the charge density.

DFT is based on two theorems known as the Hohenberg-Kohn theorems. The first theorem states that there is a one-to-one correspondence between the ground state electron density $n(\mathbf{r})$ of a many-electron system and the external potential acting on it.^{56,57} This is equivalent to the external potential being expressed as a functional of the electron density. The ground state wave function, $\psi(\mathbf{r}_1, \dots, \mathbf{r}_N)$, is a functional of the external potential and, therefore, also of the density.

The energy of a system is given by

$$E = \langle \psi [n(r)] | \hat{H} | \psi [n(r)] \rangle \quad (3.3.1)$$

where H is the Hamiltonian for the system, and so the energy is also a functional of the density. The Hamiltonian can be split into contributions from the kinetic energy (T), the interaction energy for the electron-electron interactions (U) and the external potential (V), which includes the electron-ion interactions, so that the energy becomes

$$E[n(r)] = \langle \psi [n(r)] | \hat{T} + \hat{U} + \hat{V} | \psi [n(r)] \rangle \quad (3.3.2)$$

The second of the Hohenberg-Kohn theorems states that for $E[n(r)]$ to be a minimum, the ground state wave function and therefore the ground state density must be used in

equation (3.3.2). This means that if $E[n(r)]$ is minimized with respect to the density, the ground state density and energy have been obtained.

To make this theory practical, the Kohn-Sham approach is followed.⁵⁸ The essence of this approach is to map the interacting system onto a system of non-interacting electrons that has the same total energy and ground-state electron density. Solutions for this non-interacting system can be obtained numerically. $n(r)$ is expanded as a sum of independent orthonormal orbital contributions

$$n(r) = \sum_{i=1}^N \phi_i^*(r) \phi_i(r) \quad (3.3.3)$$

These wave functions do not have a physical meaning. The Hamiltonian is then written as a sum of several contributions

$$\hat{H} = -\frac{\hbar^2 \nabla^2}{2m} + \hat{U}_{ion}(r) + \hat{U}_{Coulomb}(r) + \hat{U}_{xc}(r) \quad (3.3.4)$$

where the first term is the operator corresponding to the kinetic energy of a system of non-interacting electrons, U_{ion} is the nuclear potential, $U_{Coulomb}$ is the potential corresponding to the Hartree energy (the interaction energy between a single electron and the charge density made up from all the other electrons) and $U_{xc}(r)$ is known as the exchange-correlation potential. It is formally defined as

$$U_{xc}(r) = \frac{\delta E_{xc}[n(r)]}{\delta n(r)} \quad (3.3.5)$$

where $E_{xc}[n(r)]$ is the exchange-correlation energy. This energy is the sum of (i) the difference between the real kinetic energy and that of a system of non-interacting electrons and (ii) the difference between the real interaction energy between the electrons and the Hartree energy. A series of single particle equations, known as the Kohn-Sham equations, can now be obtained using the wave functions used to construct the density

$$\hat{H} \phi_i(r) = \varepsilon_i \phi_i(r) \quad (3.3.6)$$

The problem has now been reduced to a series of single particle Schrödinger equations which can be solved and used to construct the ground state electron density and to obtain the ground state energy. The terms in the Hamiltonian are dependent on the density, which is in turn dependent on the wave functions that are being sought. This means that a self-consistent cycle must be used to converge the wave functions.

The only difficulty remaining is that the exact form of the exchange correlation potential is unknown.

Exchange and correlation are defined separately :

$$E_{xc}(n) = E_x(n) + E_c(n) \quad (3.3.7)$$

Exchange energy is defined as the difference of the expectation value of the interaction potential U for the Kohn Sham wave function, and the Hartree energy :

$$E_x(\rho) = \langle \psi[n] | \hat{U} | \psi[n] \rangle - \hat{U}_H(n) \quad (3.3.8)$$

If the wave function is a simple Slater determinant, the exchange energy is given by the well known expression :

$$E_X = -1/2 \sum_{i \neq j} \int d^3r \int d^3r' \frac{\phi_i^*(\mathbf{r})\phi_j^*(\mathbf{r}')\phi_i(\mathbf{r}')\phi_j(\mathbf{r})}{|\mathbf{r} - \mathbf{r}'|} \quad (3.3.9)$$

(Note that (3.3.9) is not the density functional itself, since the equation is expressed in terms of orbitals and not in terms of the density).

The correlation energy is the remaining part. It is always negative.

$$E_C(n) = [T(n) - T_s(n)] + [V_{ee}(n) - U(n) - E_X(n)] \quad (3.3.10)$$

The correlation energy is the difference between interacting and non-interacting kinetic energy, plus the mistake introduced by evaluation E_X for the Kohn-Sham wave function instead of the exact wave function.

Adding correlation and exchange is advantageous because functionals often perform better for the sum than for the separate terms, due to cancellation of errors.

The exchange correlation potential can be approximated in several ways.

The simplest approach is to use a functional which depends only on the local density, the Local Density Approximation (LDA) functional.^{59,60}

$$E_{XC}^{LDA} [n_\uparrow, n_\downarrow] = \int d^3r n \varepsilon_{XC}^{LDA}(n_\uparrow, n_\downarrow) \quad (3.3.11)$$

where ε is the LDA exchange correlation kernel.⁶¹ Essentially, the system is treated as a homogeneous free electron gas, making it plausible that LDA work best for fairly homogenous systems.

The LDA is beyond any doubt the most often used functional, and although its failures are many, it has been quite successful, far more so than one would suspect, given its crudeness. Roughly speaking, one can make the following statements.⁶¹ For atoms and molecules, the exchange energy is underestimated by 10%, and the correlation energy is overestimated by a factor of 2 – 3, leading to a total exchange correlation energy underestimated by 7%. LDA gives fairly good charge densities, but less good exchange-correlation potentials, which can lead to ionization potentials being unreliable. The results are better for solids, where the correct band structure is found. However, the band gap is underestimated by up to a factor of two. Sometimes, semiconductors are falsely predicted to be metals. Atomization energies and cohesive energies of solids are typically 1.3 eV too large, far more than what's called "chemical accuracy" (ca. $\sim 10^{-2}$ eV or ~ 1 kcal/mole compare to $kT = 0.025$ eV at room temperature; or the latent heat of ice, 1.5 kcal/mole.). Bond lengths tend to be reliable. Lattice parameters are typically underestimated by a few percent.

For strongly correlated systems, there are problems (e.g., weakly bonded H_2). LDA is notorious for predicting that the ground state of iron is nonmagnetic. Magnetism generally isn't LDA's strongest side.

Generally speaking, LDA tends to make systems more homogeneous than they really are. That shouldn't come as a surprise : the underlying philosophy of LDA is homogeneity, after all.⁶¹

The generalized gradient approximation (GGA)⁶² additionally takes into account the gradient of the charge density, making it a semi-local approach :

$$E_{XC}^{GGA} [n_\uparrow, n_\downarrow] = \int d^3r f(n_\downarrow, n_\uparrow, \nabla n_\downarrow, \nabla n_\uparrow) \quad (3.3.12)$$

Although GGA is formally superior to LDA, in practice it doesn't always lead to better results. We again make some general statements.⁶¹

GGA's yield better total energies than LDA (important for structure optimization). The errors in exchange energies and in correlation energies are smaller than in LDA. The artificial overbonding of s-states relative to p (and p relative to d, etc.) of LDA is much improved in GGA. GGA also treats molecules and atoms on more equal footing. This leads to better binding energies than LDA, better dissociation energies, atomization energies, energy barriers, etc. GGA also gives weaker and less localized bonds than LDA, and as a result, GGA tends to find larger bond lengths than LDA, which has a tendency to overbind – but sometimes GGA overcorrects.⁶¹ Lattice parameters are slightly larger than in LDA and tend to be very accurate. GGA is much better at predicting the correct magnetic ground state than LDA, but the magnetic moments can be unrealistically large.

There are many newer and more advanced functionals. To give an overview would be beyond the scope of this introductory chapter, as the DFT results in this dissertation were all calculated using a GGA exchange-correlation potential.

We have remarked in the section on EELS that the core hole effect can have an important influence on the spectrum. In DFT calculations, it can be accounted for in different ways.⁶³

- Forced-excitation or ionization method: An electron (or part of an electron) is removed from the core state. This electron may be put into the valence band in a forced excitation, or completely removed in a complete ionization. If half of the core electron is excited, the state is known as Slater's transition state.⁶³ This method is only possible for DFT codes which include the core electrons.
- Z+1 method: The excited atom is treated as a defect, and substituted by the heavier following atom in the periodic table.

Both of these methods are static methods, i.e. they do not include the response of the electrons to the change in potential. Many argue that they are comparable.⁶⁴ However, the Z+1 approximation is more crude in that it uses the same core hole potential no matter which shell the core hole is in. The Z+1 approximation is not used much anymore. More advanced treatments are available which are based on Green's Functions methods.

We conclude this section by making a final remark about applying DFT results to EELS calculations, which involve excited states.

DFT can be used to calculate the ground state electronic configuration of a system. This is made up of the single particle eigenvalues. It is possible to continue the eigenvalue spectrum above the Fermi level and obtain an "unoccupied" density of states. Theoretically, the eigenvalues and eigenstates obtained from DFT are only meaningful in describing ground state properties and so there is no formal justification for interpreting

the unoccupied eigenvalues as the unoccupied DOS. It has, however, been found to describe experimental data well, and so is often used in this way.^{16,41,65}

3.c.2. Implementation in WIEN2k

Solving the Kohn-Sham equations normally involves finding the coefficients c_{ip} needed to express $\phi_i(\mathbf{r})$ in terms of a given basis set $\phi_p(\mathbf{r})$

$$\phi_i(\mathbf{r}) = \sum_{p=1}^P c_p^i \phi_p(\mathbf{r}) \quad (3.3.13)$$

In principle, P is infinite, but in practice a value of P is chosen to generate a basis which produces a function close to $\phi_i(\mathbf{r})$. The difficulty is to produce a basis set which contains few basis functions and is therefore computationally efficient, but describes many different situations well.

WIEN2k⁷ uses the linearized augmented plane wave (LAPW) method⁴⁹ to produce the basis set. This approach works by dividing the unit cell into non-overlapping atomic spheres (S) which are centered on the atomic sites, and an interstitial region (I). Inside the atomic spheres, a linear combination of radial wave functions multiplied by spherical harmonics is used. Additional functions are added to linearize the basis set⁴⁹ and increase its flexibility to describe states of different eigenenergies. In the interstitial region a plane wave expansion is used. We give an expression for the wave function

$$\begin{aligned} \phi_i(\mathbf{r}) &= \Omega^{-1/2} \sum_{\mathbf{G}} c_{\mathbf{G}} e^{i(\mathbf{G}+\mathbf{k})\cdot\mathbf{r}} & \mathbf{r} \in I \\ &= \sum_{lm} [A_{lm} u_l(r) + B_{lm} u_l'(r)] Y_{lm}(\theta, \phi) & \mathbf{r} \in S \end{aligned} \quad (3.3.14)$$

to give the reader a feeling of what the basis set looks like. More details can be found on this method in the literature.^{49,66}

The key fact about the WIEN2k L/APW basis is that it has the flexibility to describe free-electron-like states in the interstitial, and atomic-like states near the nuclei. Therefore, WIEN2k can be “all electron”. This means it calculates all electron states explicitly, including the tightly bound, atomic-like deep core states. In pure plane wave codes, it is customary to represent these states by pseudopotentials and pseudo wave functions. Of course, this leads to faster calculations. On the other hand, it is a complication for EELS to have to reconstruct correct core wave functions.^{67,68}

WIEN2k offers several exchange-correlation potentials. The spectra in this dissertation were calculated using the PBE96 GGA exchange correlation potential.⁶⁹

EELS spectra can be simulated in WIEN2k using the older TELNES program³⁴, or its relativistic successor TELNES2, which will be described in Sec. 4.d.⁷⁰ An excellent overview of ELNES calculations using WIEN2k + TELNES is given in Hébert.¹⁰

3.d. Green's function theory

3.d.1. Multiple scattering formula for the cross section

The multiple scattering (MS) formalism was originally developed for x-ray scattering (XAS), and we will follow closely the discussion in chapter 2 of Ankudinov⁷¹, which also contains many more references.

Using Fermi's golden rule for the XAS transition rate, the total XAS absorption cross section is given by

$$\sigma_{tot}(\omega) = \frac{4\pi^2 e^2}{cm^2 \omega} \sum_{i,f} \left| \langle f | \mathbf{p} \cdot \boldsymbol{\varepsilon} e^{i\mathbf{k} \cdot \mathbf{r}} | i \rangle \right|^2 \delta(E_f - E_i - \hbar\omega) \quad (3.4.1)$$

where ω is the frequency of the x-rays (corresponding to energy loss in EELS) with wave vector \mathbf{k} and unit polarization vector $\boldsymbol{\varepsilon}$. \mathbf{p} is the impulse vector. Labels i and f stand for initial (occupied) and final (empty) states, with energies E_i and E_f .

In the band structure approach, one finds initial and final eigenstates and eigenvalues (i , E_i and f , E_f) and then evaluates (3.4.1). It's possible to use a different approach of multiple scattering theory, which is based on Green's function theory.

In single electron theory, the Green's function is defined as

$$G(r, r', E) = \langle r | G(E) | r' \rangle = \langle r | \frac{1}{E - H + i\eta} | r' \rangle = \sum_f \frac{\langle r | f \rangle \langle f | r' \rangle}{E - E_f + i\eta} \quad (3.4.2)$$

where H is the Hamiltonian, and η is infinitesimal and positive. The cross section can be rewritten in terms of the Green's function :

$$\sigma_{tot}(\omega) = -\frac{4\pi}{c\omega} \text{Im} \sum_i \langle i | d_{\boldsymbol{\varepsilon}}^* \hat{G}(\omega + E_i) d_{\boldsymbol{\varepsilon}} | i \rangle \theta(E_i - E_F + \hbar\omega) \quad (3.4.3)$$

with the operator

$$d_{\boldsymbol{\varepsilon}} = \mathbf{p} \cdot \boldsymbol{\varepsilon} e^{i\mathbf{k} \cdot \mathbf{r}} \quad (3.4.4)$$

for XAS. (For EELS, we use $d = q^{-2} e^{i\mathbf{q} \cdot \mathbf{r}}$. The prefactor also needs to be chosen differently.) The $\theta(E)$ Heavyside function cuts off poles of the Green's function below the Fermi energy E_F .

The one-particle Hamiltonian is split into two parts, a free electron Hamiltonian H_0 and a scattering potential V .

$$H = H_0 + V = \left(-\frac{1}{2} \nabla^2 + V_{mt} \right) + \left(\sum_i v_i \right) \quad (3.4.5)$$

where V_{mt} is a constant shift of the zero level, and V has been written as a sum of scatterers (which are, of course, the atoms of the sample).

We use the free particle Green's function

$$G^0(\mathbf{r}, \mathbf{r}', E) = \langle \mathbf{r} | G^0(E) | \mathbf{r}' \rangle = \langle \mathbf{r} | \frac{1}{E - H_0 + i\eta} | \mathbf{r}' \rangle = -\frac{2k}{4\pi k} \frac{e^{ik|\mathbf{r}-\mathbf{r}'|}}{|\mathbf{r}-\mathbf{r}'|} = 2k G^0(\boldsymbol{\rho} - \boldsymbol{\rho}') \quad (3.4.6)$$

where $\boldsymbol{\rho} = k \mathbf{r}$ and $k = (2(E - V_m))^{1/2}$. The full Green's function can be written using perturbation theory in V and the Dyson series expansion

$$G = G^0 + \sum_i G^0 t_i G^0 + \sum_{j \neq i} G^0 t_i G^0 t_j G^0 + \dots \quad (3.4.7)$$

with the t-matrix at each site linked to the scattering potential as

$$t_i = v_i + v_i G^0 t_i \quad (3.4.8)$$

For spherical (muffin tin) potentials, it can be expressed in terms of phase shifts

$$t_l^i = -\frac{e^{i\delta_l^i} \sin \delta_l^i}{2k} \quad (3.4.9)$$

For EELS or XAS spectra and (3.4.3), the Green's function must be evaluated for \mathbf{r} and \mathbf{r}' at the scattering site, or central site "c" (i.e., the atom that gets excited by the scattering event). It helps to write the "central atom contribution" separately

$$G_c = G^0 + G^0 t_c G^0 \quad (3.4.10)$$

$$G = G_c + G_c \left[\sum_{i \neq c} G^0 t_i G^0 + \sum_{c \neq j \neq i \neq c} G^0 t_i G^0 t_j G^0 + \dots \right] G_c \quad (3.4.11)$$

where no two consecutive scattering events take place at the same atom site. The central atom Green's function can be expressed through regular (R_l) and irregular (N_l) solutions of the Schrödinger equation in a potential V

$$G_c = -2k \sum_l [R_l(r_<, k) N_l(r_>, k) + i R_l(r, k) R_l(r', k)] \sum_m Y_{lm}^*(\hat{r}) Y_{lm}(\hat{r}') \quad (3.4.12)$$

Projection onto a site and angular momentum basis

$$1 = \sum_{L,i} |L, i\rangle \langle L, i| \quad \langle \mathbf{r} | L, i \rangle = i^l j_l(kr) Y_{lm}(\hat{r}) = j_L(\mathbf{r}) \quad (3.4.13)$$

transforms the equations into matrix equations. Here we use the standard notation of multiple scattering theory where $L \equiv l, m$. Using two-center expansions for the Green's functions, e.g.

$$G_0(\boldsymbol{\rho}, \boldsymbol{\rho}') = \sum_{L, L'} j_L(\boldsymbol{\rho} - \boldsymbol{\rho}_0) G_{LL'}^0(\boldsymbol{\rho}_0) j_{L'}^*(\boldsymbol{\rho}') \quad (3.4.14)$$

(3.4.3) becomes

$$\sigma_{tot}(\omega) = -\frac{8\pi c k}{\omega} \text{Im} \sum_{i, L, L'} \langle i | d_\varepsilon^* | R_L \rangle \left[-i\delta_{LL'} + e^{i(\delta_l + \delta_{l'})} G_{LL'}^{sc}(\omega + E_i) \right] \langle R_{L'} | d_\varepsilon | i \rangle \theta(E_i - E_f + \hbar\omega) \quad (3.4.15)$$

where $\langle \mathbf{r} | R_L \rangle = i^l R_l(r, k) Y_{lm}(\hat{r})$, and the Green's function matrix $G_{LL'}^{sc}$ is defined as

$$G_{LL'}^{sc} = \sum_N \sum_{r_1, \dots, r_N} \sum_{\{L_i\}} G_{LL_N}^0(\boldsymbol{\rho}_{N+1}) t_{L_N}^N \dots G_{L_2 L_1}^0(\boldsymbol{\rho}_2) t_{L_1}^1 G_{L_1 L'}^0(\boldsymbol{\rho}_1) \quad (3.4.16)$$

which is a sum over scattering paths of N scattering events at the sites \mathbf{r}_1 through \mathbf{r}_N , via angular momentum states L_i .

Remark that in the dipole limit the cross-section can also be expressed as

$$\sigma_{tot}(E) \sim \langle i | \mathbf{q} \cdot \mathbf{r} \rho(\mathbf{r}, \mathbf{r}') \mathbf{q} \cdot \mathbf{r} | i \rangle \sim \sum_{L, L'} M_L(E) \rho_{LL'}(E) M_{L'}(E) \quad (3.4.17)$$

where $M_L(E)$ are dipole matrix elements, and $\rho_{LL'}(E) = -1/\pi \text{Im } G_{LL'}$, is the one-electron density matrix.

Only three ingredients are needed for the calculation of the cross section : the matrix elements of the operator d , the two center matrix elements of the free propagator (3.4.14), and the scattering t-matrices (3.4.9). All of these can be obtained by solving the Dirac (or Schrödinger) equation for a central field potential for each scatterer in the problem.

In order to be able to use a high angular momentum cutoff L in (3.4.15), it is of tremendous importance to use a separable representation for the free-propagator two-center matrix elements, as introduced by Rehr and Albers.⁷² In order to analyze EXAFS, one needs to calculate the spectra up to several 100 eV above the threshold. Often, one needs Green's function matrix elements for L and L' up to $l_{max}=25$. Thanks to the Rehr-Albers decomposition,⁷³ only matrices of rank 6x6 need to be multiplied in the multiple scattering formula (3.4.16) instead of matrices of rank 1250x1250 (for $l_{max}=25$).

High above the edge onset (EXELFS or EXAFS), the Path Expansion (PE) (3.4.16) usually converges well with relatively short scattering paths (i.e., not too many scattering events per path, and only to scatterers fairly close to the central site "c"). However, for the energy region close to the edge (ELNES or XANES), (3.4.16) can give severe convergence problems, as very long scattering paths contribute significantly. The so-called "Full Multiple Scattering" (FMS) helps here. We can rewrite (3.4.16) as a matrix equation

$$G^{sc} = G^0 + G^0 T G^0 + G^0 T G^0 T G^0 + \dots \quad (3.4.18)$$

defined as $\langle L, i | G^0 | L', j \rangle = G_{LL'}^0 (\rho_i - \rho_j)$ for $i \neq j$ and $\langle L, i | G^0 | L', i \rangle = 0$ and $\langle L, i | T | L', j \rangle = \sum_k t_L^k \delta_{ik} \delta_{jk} \delta_{LL'}$. The geometric series (3.4.18) now gives

$$G^{sc} = (1 - G^0 T)^{-1} G^0 \quad (3.4.19)$$

which is the FMS equation.

In principle, (3.4.19) and (3.4.16) are completely equivalent. However, whereas convergence in terms of the number of scattering paths limits the applicability of the path expansion, the FMS equation is limited by the size of the matrix that needs to be inverted in (3.4.19), which shouldn't be bigger than 10^4 or smaller for conventional computer systems. Given that one typically needs a cluster of a few hundred atoms (100-500) to model a solid using FMS, the angular momentum needs to be truncated at $l_{max} = 3$ or 4 . This limits the applicability of (3.4.19) to the near edge region (ELNES, XANES), as higher l-values become increasingly important further above the threshold.^{74,38} Fortunately, PE and FMS overlap at the beginning of the extended structure (see Figure 3-17).

Another difference between PE and FMS is that one can accurately incorporate Debye-Waller factors into PE, whereas they can only approximately be accounted for in FMS.⁷¹

Generalization of the formulas presented above to include spin and to work in a relativistic basis are straightforward.⁷¹

Introducing a core hole in the theory presented so far, is easy. The core hole atom will have its own t-matrix, different from that of other atoms of the same element in the solid (the other C atoms in the diamond crystal, say). Additionally, the finite core hole lifetime will add an imaginary part to the potential ($V_{mt} \rightarrow V_{mt} - i\Gamma_{ch}/2$). All propagators decay exponentially, reducing contribution.

Finally, one last convention needs to be introduced. It is common practice in MS applications to speak of a background and fine structure. The absorption coefficient can be written as

$$\mu(E) = \mu_0(E)(1 + \chi(E)) \quad (3.4.20)$$

as is immediately clear by comparison to (3.4.15). The function μ_0 is called the *atomic background*. While it is a smooth function of energy, it does depend slightly on the environment of the absorbing atom, and therefore the epithet “atomic” is somewhat misleading. The *fine structure* χ is just that : it contains all the peaks and wiggles of the spectrum, and most of the sensitivity of the spectrum to the local environment.

3.d.2.Implementation in FEFF8

This chapter introduces some of the concepts typical to a Multiple Scattering study, and provides examples to the last section. All examples are taken from Moreno et al.⁹ We need to stress that FEFF8 as presented here refers to the version *prior* to the implementation of improvements for EELS calculation as described in the following chapters of this dissertation (Chapters 4.e and 5). Here, we illustrate the FEFF8 program as in Ankudinov et al.⁸, while the new developments described later are presented in Jorissen et al.⁷⁵ Many improvements have been introduced, such as a better approach to orientation sensitivity, relativistic formalism, accounting for collection and convergence semi-angles, etc. All these important aspects will not be discussed in the current chapter, but will be treated later.

3.d.2.1 The FEFF8 program

FEFF8 is an *ab initio* and largely parameter-free implementation of the Real Space Multiple Scattering (RSMS) method. The code does have a few adjustable parameters, though. These include corrections to the Fermi-energy, experimental broadening, and the

Debye temperature in Debye-Waller factor calculations. The calculations permit a quantitative interpretation of EELS based on self-consistent-field (SCF) calculations of both excited-state and ground-state electronic structure including electronic densities of states (DOS) and charge transfer.

FEFF8 considers a finite cluster of atoms, specified by their real-space coordinates. Infinite systems can be approximated by a finite cluster of sufficient size. Periodicity or symmetry is not used, and there is no need for the unit cell of band structure (BS) calculations. In the calculation, one representative atom in the cluster is singled out to absorb the energy lost by the microscope's electron beam. For crystals with more than one inequivalent crystallographic site, an experiment measures the sum of the spectra for each site with an appropriate weighting. The same must be done in the calculation. Because FEFF8 does not require or make use of crystal symmetry or periodicity, there are no restrictions on the shape of a cluster, therefore one can study aperiodic systems such as interfaces, nanometer sized precipitates, vacancies, impurities and other imperfect situations.

3.d.2.2 The final state rule

Unfortunately, the question of which independent-particle states to use in the calculation of (3.4.1) is not unambiguous. The RSMS approach (3.4.3) doesn't explicitly calculate the final states, but they are implicit in the final state Hamiltonian and hence the Green's function for the final state. Typically a Δ SCF approach (which refers to different Self Consistent Field (SCF) calculations in the initial and final states) is used in XAS and EELS calculations, based on the *final state rule* (FSR). This rule states that the calculation is done using Fermi's golden rule with final states calculated with a final state Hamiltonian including an appropriately screened core hole (i.e., as in the "delta-scf" approach), while the initial states should be those for the ground state. This has been shown to be nearly equivalent to core-level Bethe-Salpeter Equation theory (BSE).⁷⁶ However this FSR rule is implemented in different ways. Modern DFT/band-structure methods typically use real potentials and treat the core hole using a super-cell. In contrast, the RSMS approach in FEFF8 can be regarded as a *quasi-particle* approximation,⁷⁷ where the final state Hamiltonian $h' = p^2 / 2m + V'_{Coul} + \Sigma(E)$ includes a core hole in the Coulomb potential V'_{Coul} and an energy dependent *self-energy* $\Sigma(E)$. The self-energy is the analog of the exchange-correlation potential V_{xc} of ground-state Density Functional Theory (DFT). In the near edge region these two final-state Hamiltonians are comparable, i.e., $\Sigma(E) \approx V_{xc}$. However, the energy dependence of $\Sigma(E)$ and damping from its imaginary part (which gives the photoelectron a finite mean free path) are crucial at high energies (e.g., well above a typical plasmon energy or about 30 eV) and account for the *extrinsic losses* in the final state. In addition, the real part of $\Sigma(E)$ gives a systematic energy-dependent shift to the spectral features compared to those calculated with ground state DFT.

In principle the self-energy $\Sigma(E)$ can be calculated from first principles using the GW approximation of Hedin, but this procedure is usually too computationally demanding for routine calculations. In practice, local density approximations for $\Sigma(E)$ are commonly used. For example, FEFF8 uses by default the Hedin-Lundqvist (HL) model which is based on the plasmon-pole model for an electron gas.⁷⁸ This model is based on a dynamically screened exchange operator in an electron gas, and can be thought of as an extension of ground state DFT to excited states. Another model, which is an option in FEFF8, is the Dirac-Hara (DH) self-energy.⁷⁹ This model only includes the static exchange terms and is essentially the local density approximation to the Fock exchange operator. In practice HL exchange is usually preferable in solids, while DH is sometimes better for molecules. In addition, broadening from the core-hole lifetime can be added by adding an additional complex constant $-i\Gamma$ to the Hamiltonian h' .

The treatment of the core-hole potential is often problematic due to the variability of core-hole screening in the final state. Thus various approximations are currently used for XAS and EELS calculations. For example, FEFF8 uses a self-consistent, fully screened core-hole, while band-structure codes typically use a self-consistent supercell model. These approaches should be similar for a sufficiently large supercell. Both of these approximations are improvements on *ad hoc* approaches such as the “ $Z+I$ ” approximation. The Bethe-Salpeter equation (BSE) on the other hand is usually calculated with a RPA screened core hole, as implemented in FEFF,⁸⁰ in contrast with the fully screened core hole of the FSR.

Since the core-hole is attractive, its main effect is a shift of the spectra to lower energies.

However efforts are currently being made to improve the treatment of various many-body effects in FEFF8. For example, linear response screening (i.e. RPA) of the core-hole may yield an approximation that is closer to the treatment in the Bethe-Salpeter equation (BSE). In addition, time-dependent density functional theory (TDDFT) yields screening of the external electric field and hence modified transition matrix elements.⁸⁰ Also, the spectra can be extended to the optical region by replacing the sum over initial core levels by the valence density matrix. These developments are aimed at extending the FEFF8 program to the low-loss region. Finally it has recently been shown that relativistic modifications must be made to equation (3.4.1) for anisotropic materials.⁴ These corrections are taken into account in a forthcoming FEFF8 release (FEFF8.5).⁷⁵

3.d.2.3 Potentials and Fermi energy

FEFF8 approximates the total electronic potential for the initial and final states with spherically averaged muffin-tin (MT) potentials centered on each atom. In this approximation, the potential is constant in the interstitial region between the spheres. The potential, Fermi level (E_F) and charge transfer may also be calculated self-consistently.⁸ SCF potentials make near-edge calculations much more accurate, but are not necessarily needed for the fine structure at high energies.

3.d.2.4 Self-Energy

As discussed in Sec. 3.d.2.2, the self-energy $\Sigma(E)$ must be added to the final state Hamiltonian for calculations of the excited final states for EELS. One can choose a given model for the self-energy in FEFF8. The Hedin-Lundqvist self-energy is used by default and appears to be the best choice for most applications, especially for solids. In some cases (e.g., small molecular systems) the Dirac-Hara exchange-correlation potential, which is the local density approximation to the Fock exchange, can be preferable. We compare in Figure 3-14 the nitrogen K-edge of h-GaN calculated using both models. The Hedin-Lundqvist is clearly superior, though it tends to have excessive loss near the edge, i.e., the theory exhibits more broadening (i.e., smaller fine-structure) than the experiment.

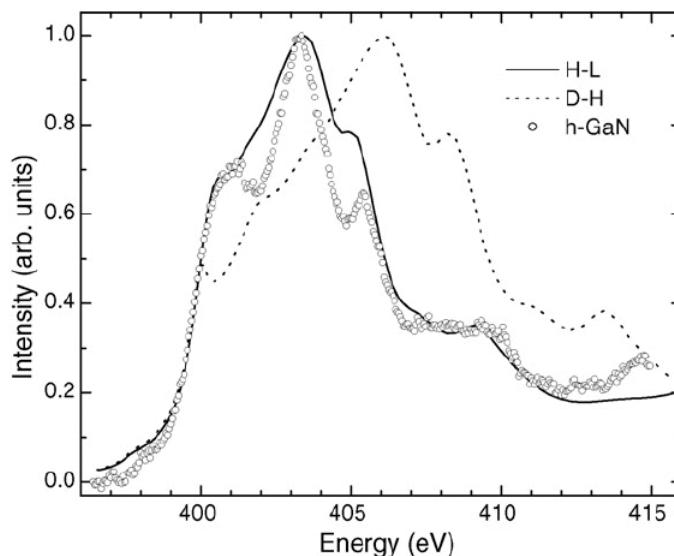


Figure 3-14 Spectrum of the nitrogen K-edge of h-GaN for two different models of the self-energy: Hedin-Lundqvist (H-L) and Dirac-Hara (D-H).⁹ A cluster of 158 atoms was used for FMS. Open circles are experimental data taken from Moreno et al.⁸¹

3.d.2.5 Core hole

It is widely thought that EELS directly measures the ground-state electronic structure through the LDOS. However, this interpretation is misleading because of the effects of the core hole and the self-energy on the spectra. The final state Green's function and hence the density matrix in Eq. (3.4.17) must be computed in the presence of a core hole, and is different from the unperturbed unoccupied states making up the ground state DOS. In addition EELS includes thermal effects of vibrations and disorder. All these final state

effects shift the spectra with respect to the ground state DOS. By default FEFF8 calculates the spectrum in the presence of a screened core hole according to the final-state rule. However FEFF8 can also do calculations without a core hole in order to assess its effect. We have found that the default screened core hole in FEFF8 can be comparable to that calculated with linear response (RPA screening), which is used in the Bethe-Salpeter equation approach. For insulators, a core hole is usually essential. On the other hand, there are cases where the effect of the core hole is almost completely screened out, e.g., in metals for soft x-ray edges of order 1000 eV and below. For these cases the mobile electrons of the metal completely ‘screen’ the core-hole potential. In such cases, the NOHOLE card can be used, which roughly simulates the effect of complete core-hole screening by causing FEFF8 to calculate potentials and phase shifts as if there were no core hole. For L_2 or L_3 edges, this often gives better prediction of white-line intensities of the transition metal series.⁸²

In Figure 3-15 we compare the calculated N K-ELNES of GaN with and without a core hole. Note that the effect of the core hole is to *red-shift* the spectrum, increasing the intensity close to the edge threshold and therefore sharpening the edge threshold. This is a general trend. For GaN, the default fully-screened core hole yields spectra in good agreement with experiment, while that without a core hole is significantly blue-shifted.

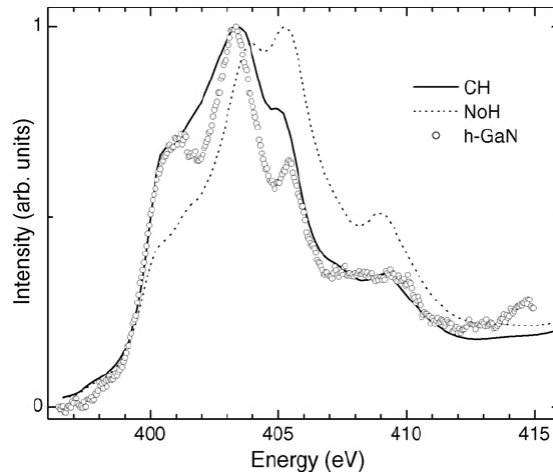


Figure 3-15 Spectra of the N K-edge calculated with (CH) and without (NoH) a core-hole. Open circles correspond to experiment.⁹

We remark that FEFF8 does not use periodical boundary conditions, and therefore only one core hole is used in the calculation of EELS from a given atom. Thus the unphysical core-hole – core-hole interactions and the related supercell size problems of band structure codes⁸³ are not present in the RSMS approach.

3.d.2.6 ELNES and EXELFS

Depending on the energy range of interest, FEFF8 uses one of two different methods for calculating the Green’s function and the EELS spectrum. These methods coincide with

the two regions of the spectrum often distinguished as the near-edge region (ELNES), and the extended region (EXELFS). The two methods generally overlap over a wide enough energy range that one can combine them into a full spectrum, from the threshold up to hundreds of eV (Figure 3-17).

For the calculation of near edge structure (ELNES) it is often preferable to use the Full Multiple Scattering (FMS) technique, since the multiple-scattering path expansion converges slowly or not at all near the edge. Within a finite sphere centered on the absorbing atom, all multiple-scattering paths are summed to infinite order by performing a matrix inversion.

One of the important tasks in any FEFF8 calculation of crystals is to ensure that the results are converged with respect to the size of the finite real space FMS cluster used to represent the crystal (Sec. 3.d.2.1). The calculation must be repeated with increasing cluster size until the details of the spectrum have converged to one's satisfaction. Typically, a converged ELNES calculation requires a cluster of about 150 atoms, depending on the core-hole lifetime. However bigger clusters (300-500 atoms) may be needed for some materials, e.g. for low Z materials like Si with shallow edges and long core-hole lifetimes.

An interesting advantage of that convergence process, and of the RSMS method in general, is the possibility of identifying peaks in the ELNES data with scattering events from particular shells in the cluster. In Figure 3-16 we show the effect of increasing the cluster size of the MS calculation of the N K -edge in h-GaN. The edge changes for each additional N shell. Convergence in terms of the number of peaks in the fine structure appears to be reached after the inclusion of eight shells. When compared with a calculation for a cluster of 42 shells (about 480 atoms), we can see that the fine structure is still changing, but such changes can only be checked by using high resolution EELS data.

A comparison with the LDOS allows the assignment of spectral peaks to electronic transitions between specific states.

FMS calculations are not usually accurate beyond $k = 6 \text{ \AA}^{-1}$ (100 eV) due to the usual computational limit on the angular-momentum basis to $l_{max} = 3 - 4$. For the calculation of extended fine structure (EXELFS), the Path Expansion must be used instead. (See Figure 3-17). The scattering contributions of all paths up to a maximal path length are summed. The spectrum needs to be converged with respect to the maximal path length by doing several calculations and comparing the results.

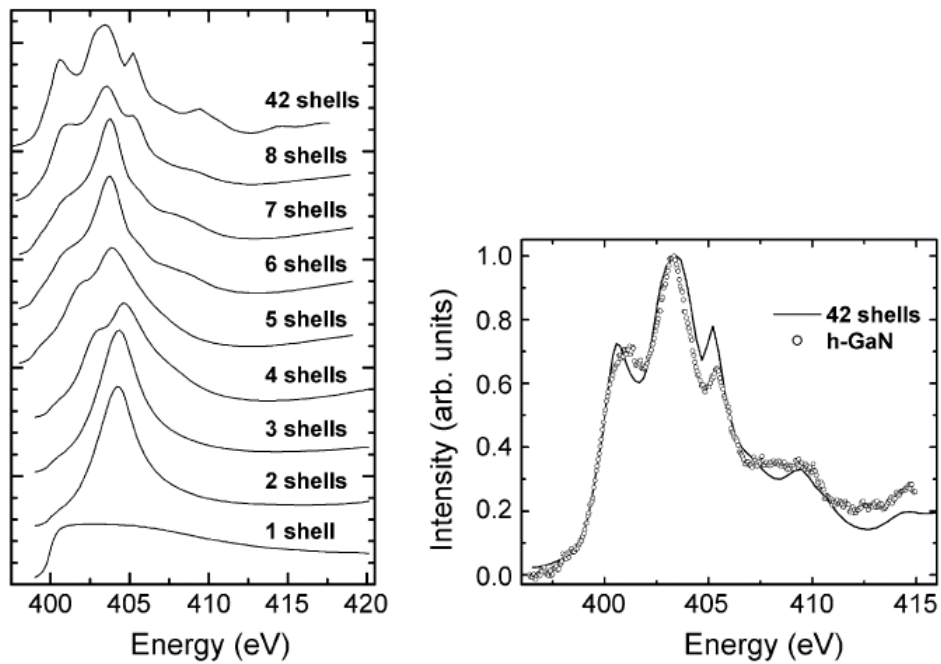


Figure 3-16 Effect of increasing the number of scattering shells for the FMS calculation of the nitrogen *K*-ELNES of h-GaN (left panel). Comparison between experiment (open circles) and calculation using 42 shells (right panel).⁹

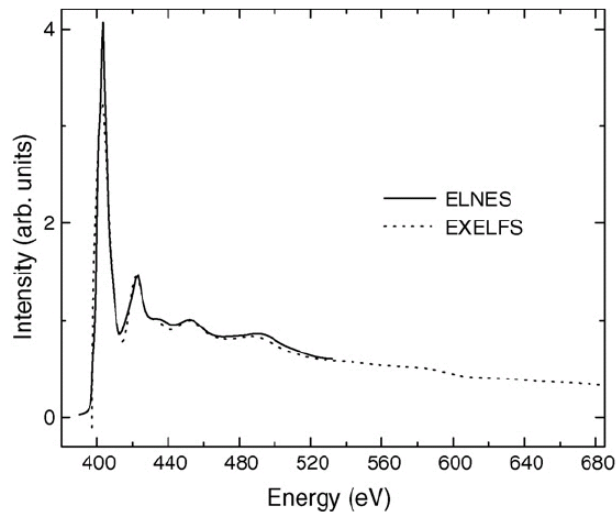


Figure 3-17 Near -edge (ELNES) and extended (EXELFS) spectrum of the N *K*-edge of GaN. ELNES is calculated using the FMS technique, while EXELFS is treated using the path expansion. The two simulations overlap smoothly at about 50 eV above threshold, a typical value.⁹

3.d.2.7 Broadening

Experimental spectra are broadened by at least three different mechanisms⁸⁴ : the lifetime of the initial (core) state, the lifetime of the final (conduction) state, and instrumental broadening. The first two are taken care of automatically by FEFF8, the last can be set by the user. FEFF8 by default includes values for the core-hole lifetime. These core-hole lifetimes are taken from tabulated values for each edge and element.⁸⁵ Broadening due to the lifetime of the final-state, and its energy dependence, is contained in the imaginary part of the self-energy.

3.d.2.8 Orientation dependence

Generally, an EELS experiment is sensitive to the relative orientation of the sample with respect to the beam, so rotating the sample alters the observed spectrum. One can specify the direction of the polarization vector in FEFF8. In EELS calculations, this corresponds to the direction of incidence of the electron beam in dipole approximation (see Sec. 3.b.2). In absence of polarization information, FEFF8 simply calculates a spectrum averaged over all directions of polarization.

In Figure 3-18 we show the orientation dependence of the nitrogen K-edge of h-GaN. The calculation reproduces the experimental energy scale well. Discrepancies with experiment may be due to the collection and convergence semi-angle (about 0.4 and 0.3 mrad, respectively) not accounted for in the calculation, as the intensities of the peaks have been shown to be sensitive to these parameters.⁸⁶ This effect is more important for the beam // 001, due to the conditions of the experiment.⁸¹

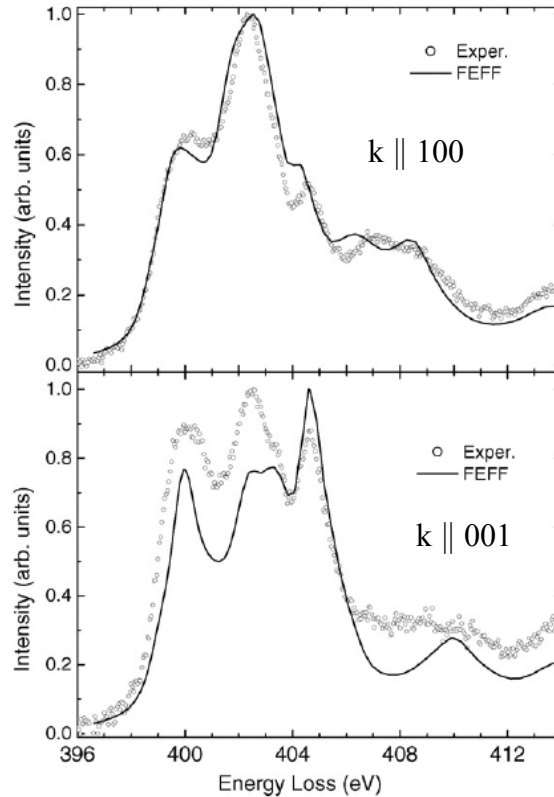


Figure 3-18 Experimental (open circles) and calculated (solid line) spectra for the N K-edge of the hexagonal phase, for two different main directions of the electron beam k . In the upper picture, the beam enters and exits the sample along its 100 direction. In the lower picture, the beam hits the sample along the 001 direction.⁹

We remark that in reality there is also orientation dependence due to channeling effects in periodic systems (crystals in zone axis orientation). Such effects are not included in our calculations.

3.d.2.9 Non-dipole transitions

In many cases, EELS experiments are entirely dominated by dipole transitions, and therefore FEFF8 calculates the dipole-selected spectrum by default. Sometimes, though, quadrupole contributions may be unavoidable, e.g. at large scattering angles or when no final states of dipole allowed character are available. They may even be the quantity of interest. In FEFF8 one can add quadrupole or magnetic-dipole contributions, or select only the $L \rightarrow L-1$ (e.g. $p \rightarrow s$) or the $L \rightarrow L+1$ (e.g. $p \rightarrow d$) dipole transition.

In Figure 3-19 (upper panel) we show the Ga L_3 -edge for h-GaN and its $L-1$ and $L+1$ components. In the lower panel we compare the quadrupole contribution to the Ga d-DOS. It follows the d-DOS closely. The quadrupole contribution has been scaled for convenience; it contributes less than 1% to the total spectrum in the upper panel.

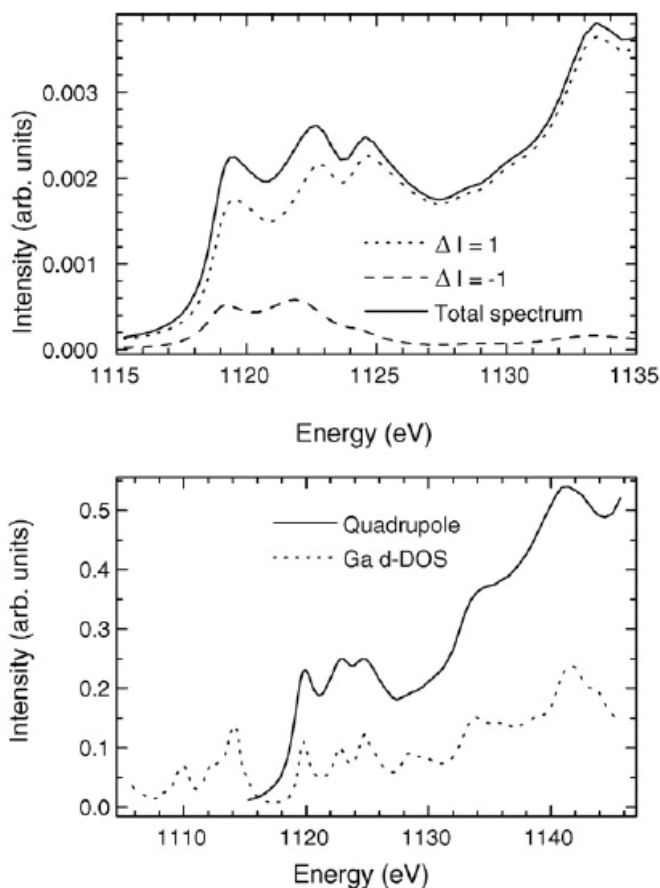


Figure 3-19 The Gallium L₃-edge of h-GaN and its L-1 and L+1 dipole contributions (upper panel). The quadrupole term of the L₃-edge is compared to the Ga d-DOS (lower panel).⁹ It has been scaled by a factor of 10⁵ for comparison to the DOS, so it contributes less than 1% to the total spectrum.

3.d.2.10 Debye-Waller factors

EELS experiments are performed at finite temperature. FEFF8 incorporates temperature effects by including Debye-Waller (DW) factors in the calculation. It calculates correlated-Debye-model DW factors for each path when using the Path Expansion for EXELFS, or multiplies each free-electron propagator by a single-scattering DW factor when using Full Multiple Scattering for ELNES. DW factors add extra broadening to the spectrum and wash out the details, increasingly as one goes further away from the edge threshold. The effect of DW factors on ELNES tends to be fairly small, as we can see in Figure 3-20. At higher energies, however, temperature effects become very important and obscure many details (see Figure 3-21). This can be intuitively understood in terms of the radial distribution function, which gets smeared out by vibrations of atoms around their lattice positions, and is related to the Fourier transform of the EXELFS fine structure.

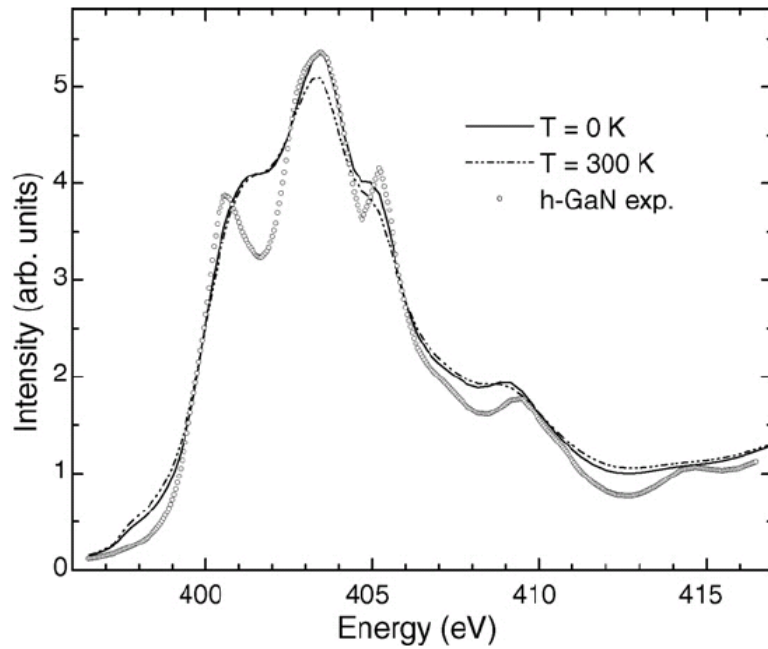


Figure 3-20 The N K-edge of GaN calculated with Debye-Waller factors at 0K, and with Debye-Waller factors at room temperature (300K). The Debye temperature of GaN is 600K.⁹

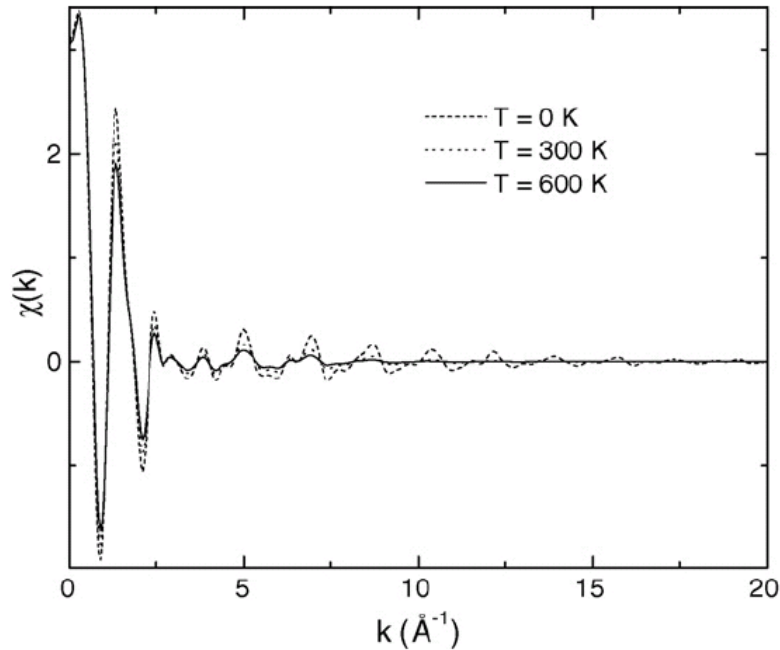


Figure 3-21 The fine structure $\chi(k)$ of the N K-edge of GaN. On the x-axis is $k = \sqrt{E - E_{fermi}}$ ($\chi = \mu / \mu_0 - 1$, where μ is the absorption spectrum and μ_0 is the atomic background). As temperature increases from zero up, thermal vibrations are seen to wash out the details of the spectrum, smearing out the spectrum into a smooth background.⁹

3.d.2.11 Density of States

Comparison of the site- and symmetry-projected DOS and ELNES data helps one to connect spectral features to transitions to particular states. In FEFF8, the angular-momentum-projected local density of states is calculated for each distinguishable atom in the system using Full Multiple Scattering. The energy resolution of the calculated DOS is limited by broadening due to the cluster size.

In Figure 3-22 we compare the experimental spectrum of h-GaN to the spectrum and the N p-DOS calculated by FEFF8. The spectrum follows closely the N p-DOS, as expected according to the dipole approximation.

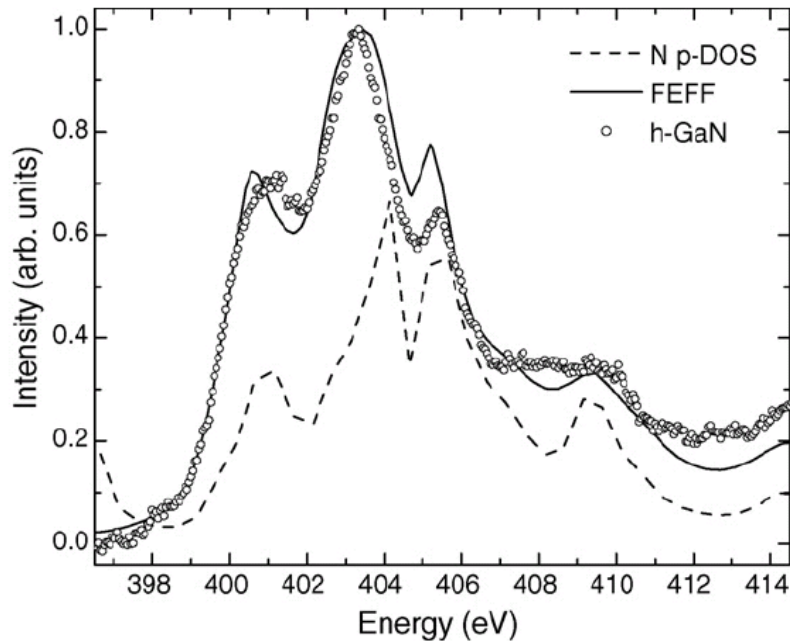


Figure 3-22 Comparison of the experimental h-GaN N K-edge (open circles), and the spectrum (full line) and N p-DOS (dashes) calculated by FEFF8. The spectrum clearly corresponds to the N p-DOS.⁹

4. Relativistic calculations of electron energy loss spectra

One may be surprised to find a whole chapter in the “results” section of a dissertation devoted to the basic theory of a well-established technique. However, the real surprise is that Electron Energy Loss Spectroscopy theory and calculations have indeed been based on a deficient theory for a long time. It was always assumed that a relativistic treatment of electron scattering is unnecessary. Given that electrons in an EELS-experiment are routinely accelerated to kinetic energies of 300 keV, corresponding to a velocity $v = 0.8 c$, it is surprising that such a bold assumption has never been the object of much scrutiny. Instead, it was believed that it was sufficient to use the relativistic relations between the beam electron’s energy and its mass and wave vector.^{31,87} This leads to an overall factor that does not change the shape of the spectrum.

Some work on relativistic atomic cross-sections is mentioned in Egerton¹⁵ and Dwyer⁸⁸.

Recently, it became apparent through the work of Jouffrey et al.⁴ and Schattschneider et al.⁵ that the non-relativistic description is only valid for isotropic experiments. In anisotropic situations (which are sometimes desired and sometimes unavoidable), significant mistakes are introduced. In particular, a material-independent property of the EELS-experiment, the so-called magic angle, exposed these flaws. The theoretically predicted value of this magic angle, which is a value of the spectrometer aperture for which the orientation dependence of the spectrum cancels out due to integration over momentum transfer, turns out to be off by a factor of four for the graphite C K edge (at a beam energy of 300 keV). Such errors – hardly a small correction – have significance for the interpretation of experiments, which depend strongly on the collection and convergence semi-angles.

Although the take-home message – that relativistic effects significantly alter anisotropic EELS spectra and are responsible for discrepancies such as the magic angle – was discovered and published by Jouffrey et al. and Schattschneider et al., more work needed to be done, and that work is presented in this chapter.

First of all, I present a theoretical derivation that is more rigorous than that of Schattschneider et al.⁵. Secondly, Schattschneider et al. only considered the small impulse transfer – dipole approximation. Here, we give expressions that are valid for any order of the interaction potential and are valid for arbitrary impulse transfer. Finally, writing down a formula does not mean the EELS community is now ready to use it. I have implemented two flavors of relativistic EELS in the *ab initio* codes FEFF8 and WIEN2k, and these codes and their results are discussed, revisiting in particular the magic angle of graphite.

4.a. General relativistic theory

In this section, we derive a general relativistic formula for the EELS cross section, as given in Sorini et al.^{89,70}

We consider a probe electron which scatters off of a macroscopic sample of condensed matter. Very similar problems have been solved long ago using both a semi-classical approach⁹⁰, and also using a fully quantum-mechanical approach.^{91,92,93} The fully quantum-mechanical and fully relativistic case of scattering two plane-wave electrons has long been a textbook problem.^{94,95} This old problem was revived recently in two interesting papers by Jouffrey et al.⁴ and Schattschneider et al.⁵ in which a flaw in the standard theory is pointed out. The flaw is simply that, in a classic paper⁹², Fano argues that the so-called "longitudinal" and "transverse" matrix elements for the scattering process may be summed incoherently. In fact, this is only true if the sample considered possesses certain symmetries. In a later review article⁹³, Fano states this approximation explicitly; his formula for the cross-section is only applicable to systems of high symmetry. This caveat which is only mentioned clearly in Fano's later review article seems to have been ignored by many, and indeed turns out to have been the source of the magic angle mystery. Schattschneider et al. showed that if one correctly sums and squares the transition matrix elements then, in the dipole approximation, one finds the correct relativistic magic angle.

We consider electron scattering within the formalism of Coulomb gauge QED and will reproduce the results of Jouffrey et al. and the theory of Schattschneider et al. up to a simple correction of order E/mc^2 , where E is the energy loss.

One very nice aspect of the formalism of Schattschneider et al. is its surprising simplicity. They follow the semi-classical approach of Møller⁹⁰, but with the added simplification of working with a probe and sample described by the Schrödinger equation rather than the Dirac equation. They also find that the theory is simplified by choosing to work in the Lorentz gauge.

Unfortunately, the theory of Møller is somewhat *ad hoc* in that a classical calculation in the Lorentz gauge is modified by replacing the product of two classical charge densities by the product of four different wave functions in order to obtain a transition matrix element. This procedure is justified by the fact that it reproduces the correct result, but appears to be slightly logically inconsistent. We feel that it will be useful to derive the result of Jouffrey et al. from a more fundamental starting point and see if anything interesting turns up. As it turns out, the theory of Schattschneider et al. is slightly incorrect, but only in such a way that can be easily explained via single particle quantum mechanics; although Schattschneider et al. work explicitly in the Lorentz gauge, they also make the assumption that

$$\mathbf{p} \cdot \mathbf{A}(\mathbf{r}) = \mathbf{A}(\mathbf{r}) \cdot \mathbf{p} \quad (4.1.1)$$

which, of course, is only true in the Coulomb gauge. In the end, this mistake only effects the final results at order ω/mc^2 where ω is the energy-loss of the probe. Thus the effect is negligible in many cases. Even so, we still believe it is useful to present a fully quantum-mechanical treatment along the lines of Fano⁹³, but without the assumption of high symmetry of the sample. That is, our treatment is as general as that of Schattschneider et al. as far as the symmetry of the sample is concerned. But, beyond the treatment of Schattschneider et al. and Møller, we take as our starting point the many-particle Hamiltonian of QED.

The basic starting point of the theory is the Hamiltonian in Coulomb gauge⁹⁴:

$$H = H_{el} + H_{int} + H_{rad} \quad (4.1.2)$$

where the Hamiltonian has been split into three parts:

The unperturbed electron part:

$$H_{el} = \int dx \psi^\dagger(\mathbf{x}) (c \alpha \cdot \mathbf{p} + \beta mc^2) \psi(\mathbf{x}) \quad (4.1.3)$$

where $\psi(\mathbf{x})$ is the second-quantized Dirac field, α_i and β are the usual Dirac matrices, m is the electron mass, and c is the speed of light.

The unperturbed (transverse) radiation part:

$$H_{rad} = \sum_k \sum_{\alpha=1}^2 a_{k,\alpha}^\dagger a_{k,\alpha} \hbar \omega_k \quad (4.1.4)$$

where $a_{\mathbf{k},\alpha}$ destroys a photon of momentum \mathbf{k} , polarization $\varepsilon^{(\alpha)}(\mathbf{k})$, and energy $\hbar\omega_k$. And the interaction part:

$$H_{int} = e \int dx \psi^\dagger(\mathbf{x}) \alpha \cdot \mathbf{A}(\mathbf{x}) \psi(\mathbf{x}) + \frac{e^2}{2} \int dx dy \frac{\psi^\dagger(\mathbf{x}) \psi(\mathbf{x}) \psi^\dagger(\mathbf{y}) \psi(\mathbf{y})}{|\mathbf{x} - \mathbf{y}|} \quad (4.1.5)$$

where

$$\mathbf{A}(\mathbf{x}) = \sum_{k\alpha} \sqrt{\frac{2\pi\hbar c^2}{V\omega_k}} (a_{k\alpha} \varepsilon_{k\alpha} e^{ik\cdot x} + a_{k\alpha}^\dagger \varepsilon_{k\alpha}^* e^{-ik\cdot x}) \quad (4.1.6)$$

and e is the charge of the proton. Also, we work in a box of volume V .

Let us next specialize to the case of a fixed number ($N+1$) of electrons where the $N+1$ -th electron is singled out as the “probe” and the remaining N electrons make up the sample. We also introduce a lattice or cluster of ion-cores which will be treated classically and

which gives rise to a potential $v_{e-core}(\mathbf{x}) = \sum_{i=1}^{N/Z} \frac{-Ze^2}{|\mathbf{x} - \mathbf{R}_i|}$ as seen by the electrons.

In this case our Hamiltonian becomes:

$$H = \left(c \alpha \cdot \left(\mathbf{p} + \frac{e}{c} \mathbf{A}(\mathbf{r}) \right) + \beta mc^2 \right) + \sum_{i=1}^N \left(c \alpha^{(i)} \cdot \left(\mathbf{p}^{(i)} + \frac{e}{c} \mathbf{A}(\mathbf{r}^{(i)}) \right) + \beta^{(i)} mc^2 \right) \quad (4.1.7)$$

$$+ v_{e-core}(\mathbf{r}) + e^2 \sum_{i=1}^N \frac{1}{|\mathbf{r} - \mathbf{r}^{(i)}|} + \frac{e^2}{2} \sum_{1=i \neq j=1}^N \frac{1}{|\mathbf{r}^{(i)} - \mathbf{r}^{(j)}|} + \sum_{i=1}^N v_{e-core}(\mathbf{r}^{(i)}) + v_{core-core} + H_{rad}$$

where the coordinates which are not labeled by an index refer to the probe electron. $v_{core-core}$ is the interaction between ion cores which is a constant and will be dropped henceforth.

Next, the interaction of the sample electrons among themselves and with the potential of the ion cores may be taken into account by a single-particle self-consistent potential $v(x)$ which includes both $v_{e\text{-core}}(x)$ and exchange-correlation effects. The interaction of the probe electron with the effective single electron of the sample will be considered explicitly. The difference between this interaction and the actual interaction between the probe and sample can be accounted for by introducing another potential $v_0(x)$ which is not necessarily the same as $v(x)$; $v_0(x)$ should be “closer” to the pure $v_{e\text{-core}}(x)$ potential than $v(x)$. The potential $v_0(x)$ leads to diffraction of the probe electron which will not be considered here in order that we can make contact with the theory of Schattschneider et al. It is also for this reason that we have introduced the single-particle picture of the sample (along with the fact that we would eventually like to apply this theory to real condensed matter systems in a practical way).

With the single-particle approximation for the sample, we have

$$H = \left(c \alpha \cdot \left(\mathbf{p} + \frac{e}{c} \mathbf{A}(\mathbf{r}) \right) + \beta mc^2 \right) + \left(c \alpha_s \cdot \left(\mathbf{p}_s + \frac{e}{c} \mathbf{A}(\mathbf{r}_s) \right) + \beta_s mc^2 \right) + v'(\mathbf{r}) + \frac{e^2}{|\mathbf{r} - \mathbf{r}_s|} + v(\mathbf{r}_s) + H_\gamma \quad (4.1.8)$$

As stated above, in the remainder of this derivation we will set $v' \rightarrow 0$, but generalization of the theory to include diffraction should not be difficult.

As it turns out, we may start from a Schrödinger treatment of the probe and sample rather than a Dirac treatment. Again, this facilitates contact with the theory of Schattschneider et al. We will indicate later how the results change if we retain a Dirac treatment of the electrons. Thus we may start with the Hamiltonian:

$$H = \frac{\left(\mathbf{p} + \frac{e}{c} \mathbf{A}(\mathbf{r}) \right)^2}{2m} + \frac{\left(\mathbf{p}_s + \frac{e}{c} \mathbf{A}(\mathbf{r}_s) \right)^2}{2m} + \frac{e^2}{|\mathbf{r} - \mathbf{r}_s|} + v(\mathbf{r}_s) + H_\gamma \quad (4.1.9)$$

$$= H_0 + \frac{e}{mc} \mathbf{p} \cdot \mathbf{A}(\mathbf{r}) + \frac{e}{mc} \mathbf{p}_s \cdot \mathbf{A}(\mathbf{r}_s) + \frac{e^2}{|\mathbf{r}_p - \mathbf{r}_s|} + O(A^2)$$

In our theory the unperturbed states are then direct products of unperturbed sample electron states, unperturbed probe electron states (plane-waves, ignoring diffraction) and the free (transverse) photon states. Also, from now on we ignore the interaction terms which are $O(A^2)$. Thus our perturbation is:

$$U = \frac{e^2}{|\mathbf{r} - \mathbf{r}_s|} + \frac{e}{mc} \mathbf{p} \cdot \mathbf{A}(\mathbf{r}) + \frac{e}{mc} \mathbf{p}_s \cdot \mathbf{A}(\mathbf{r}_s) \quad (4.1.10)$$

and we are interested in matrix elements of

$$U + UG_0U + \dots \quad (4.1.11)$$

where

$$G_0(E) = \frac{1}{E - H_0 + i\delta} \quad (4.1.12)$$

and δ is a positive infinitesimal.

The matrix elements are taken between states (ordered as: probe, sample, photon)

$$|k_i\rangle|i\rangle|0\rangle \quad (4.1.13)$$

and

$$|k_f\rangle|f\rangle|0\rangle \quad (4.1.14)$$

To lowest order (e^2) there will be a “longitudinal” (instantaneous Coulomb) contribution to the matrix element, and a “transverse” (photon mediated) contribution. See Figure 4-1 for diagrams of these processes.

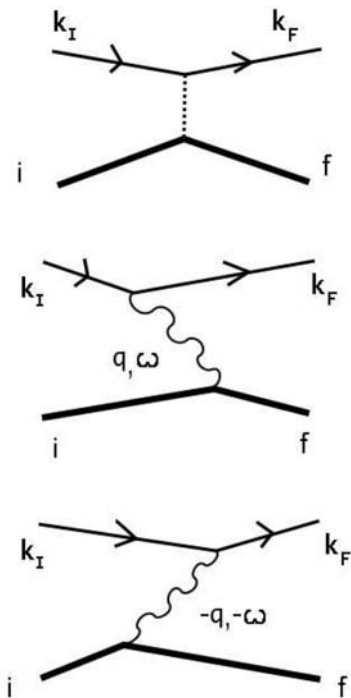


Figure 4-1 The lines labelled by momenta k_i and k_f represent the probe particle. The lines labelled by the letters i and f represent the sample particle. The dashed line is the instantaneous Coulomb interaction. The wiggly lines are photons. Time flows to the right.

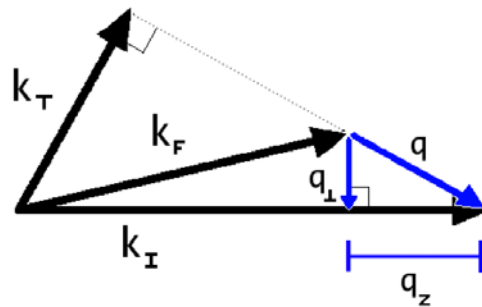


Figure 4-2 The four relevant momenta: k_i is the initial momentum of the probe particle, k_f is the final momentum of the probe particle, q is the momentum transfer $k_i - k_f$ and k_τ is the part of either the initial or final momenta which is perpendicular to the momentum transfer.

Instead of going through all the tedious details of the perturbation theory, we will simply write down the matrix element:

$$M = \frac{4\pi e^2}{V} \left\{ \frac{1}{q^2} \langle f | e^{i\mathbf{q}\cdot\mathbf{r}} | i \rangle + \frac{1}{\omega^2 - c^2 q^2} \frac{k_T^j}{m} \left\langle f \left| \frac{p_s^j}{m} e^{i\mathbf{q}\cdot\mathbf{r}} \right| i \right\rangle \right\} \quad (4.1.15)$$

where \mathbf{k}_T (see Figure 4-2) is the part of the initial (or final) momentum which is perpendicular to the momentum transfer \mathbf{q} :

$$k_T^j = \left(\delta_{ij} - \frac{q_i q_j}{q^2} \right) k_f^l = \left(\delta_{ij} - \frac{q_i q_j}{q^2} \right) k_i^l \quad (4.1.16)$$

The result of Eq. (4.1.15) is easy to understand diagrammatically. For example, to each wiggly line of momentum q and energy ω we may assign a value

$$\frac{1}{\omega - cq} \left(\delta_{ij} - \frac{q_i q_j}{q^2} \right) \frac{2\pi \hbar c}{Vq} \quad (4.1.17)$$

The other parts of the diagrams are similar.

At this point we note that the relativistic version of Eq. (4.1.15) can be obtained by making the replacement $\frac{\mathbf{p}}{m} \rightarrow c\boldsymbol{\alpha}$.

Eq. (4.1.15) is equivalent to Eq. (12) of Fano⁹³ which does not include any offending “incoherent” approximation. The offending equation is given as Eq. (16) of Fano⁹³ in which the matrix elements have been summed incoherently.

Before continuing on to the dipole approximation it will be useful to rewrite (4.1.15) by using the definition

$$\mathbf{k}_T = \mathbf{k}_0 - \mathbf{q} \frac{\mathbf{q} \cdot \mathbf{k}_0}{q^2} \quad (4.1.18)$$

to eliminate \mathbf{k}_T in favor of \mathbf{k}_0 (or equivalently \mathbf{v}_0). Making this replacement we arrive at

$$M = \frac{4\pi e^2}{V} \left\{ \frac{1}{q^2} \langle f | e^{i\mathbf{q}\cdot\mathbf{r}} | i \rangle - \frac{\mathbf{q} \cdot \mathbf{v}_0}{q^2} \frac{\langle f | \mathbf{q} \cdot \mathbf{p} / m | i \rangle}{\omega^2 - c^2 q^2} + \frac{\langle f | \mathbf{v}_0 \cdot \mathbf{p} / m e^{i\mathbf{q}\cdot\mathbf{r}} | i \rangle}{\omega^2 - c^2 q^2} \right\} \quad (4.1.19)$$

which can be rewritten as:

$$M = \frac{4\pi e^2}{V} \frac{1}{q^2 - \omega^2 / c^2} \left\langle f \left| e^{i\mathbf{q}\cdot\mathbf{r}} \left(1 - \frac{\mathbf{v}_0 \cdot \mathbf{p}}{mc^2} - \frac{\omega^2}{q^2 c^2} \left(1 - \frac{\mathbf{q} \cdot \mathbf{p}}{m\omega} \right) \right) \right| i \right\rangle \quad (4.1.20)$$

where we have made use of $\mathbf{q} \cdot \mathbf{v}_0 = \omega$ in order to cancel certain terms which appear after commuting the exponential through to the far left. Also, we have removed the label s from the position and momentum of the sample electron.

Eq. (4.1.20) looks just like Eq. (6) of Schattschneider et al.⁵ except for the “extra” term

$$\left\langle f \left| e^{i\mathbf{q}\cdot\mathbf{r}} \left(1 - \frac{\mathbf{q} \cdot \mathbf{p}}{m\omega} \right) \right| i \right\rangle \quad (4.1.21)$$

Fortunately, this term may be greatly simplified by considering the commutator

$$\left[e^{i\mathbf{q}\cdot\mathbf{r}}, H_0 \right] = \left[e^{i\mathbf{q}\cdot\mathbf{r}}, \frac{p^2}{2m} \right] = e^{i\mathbf{q}\cdot\mathbf{r}} \left(-\frac{\mathbf{p} \cdot \mathbf{q}}{m} - \frac{q^2}{2m} \right) \quad (4.1.22)$$

where the first equals sign follows from the fact that $e^{i\mathbf{q}\cdot\mathbf{r}}$ commutes with everything in H_0 except for the kinetic term of the sample electron. Then, using the fact that

$$\langle f | [anything, H_0] | i \rangle = \langle f | anything | i \rangle (E_i - E_f) = \langle f | anything | i \rangle (-\omega) \quad (4.1.23)$$

we have

$$\langle f | e^{iq \cdot r} | i \rangle (-\omega) = \left\langle f \left| e^{iq \cdot r} \left(-\frac{\mathbf{p} \cdot \mathbf{q}}{m} - \frac{q^2}{2m} \right) \right| i \right\rangle \quad (4.1.24)$$

and thus

$$\left\langle f \left| e^{iq \cdot r} \left(1 - \frac{\mathbf{p} \cdot \mathbf{q}}{m} \right) \right| i \right\rangle = \left\langle f \left| e^{iq \cdot r} \frac{q^2}{2m\omega} \right| i \right\rangle \quad (4.1.25)$$

Making the above replacement in Eq. (4.1.20) we find

$$M = \frac{4\pi e^2}{V} \frac{1}{q^2 - \omega^2/c^2} \left\langle f \left| e^{iq \cdot r} \left(1 - \frac{\mathbf{v}_0 \cdot \mathbf{p}}{mc^2} - \frac{\omega^2}{q^2 c^2} \frac{q^2}{2m\omega} \right) \right| i \right\rangle \quad (4.1.26)$$

and we see that the “extra” term only changes the result by order ω/mc^2 ;

$$\begin{aligned} M &= \frac{4\pi e^2}{V} \frac{1}{q^2 - \omega^2/c^2} \left\langle f \left| e^{iq \cdot r} \left(1 - \frac{\mathbf{v}_0 \cdot \mathbf{p}}{mc^2} - \frac{\omega}{2mc^2} \right) \right| i \right\rangle \\ &= \frac{4\pi e^2}{V} \frac{1}{q^2 - \omega^2/c^2} \left\langle f \left| e^{iq \cdot r} \left(1 - \frac{\mathbf{v}_0 \cdot (\mathbf{p} + \frac{\mathbf{q}}{2})}{mc^2} \right) \right| i \right\rangle \end{aligned} \quad (4.1.27)$$

which is exactly what Schattschneider et al. would have obtained if they hadn't neglected their commutator $[\mathbf{p}, \mathbf{A}]$. It is especially instructive to judge the term they neglected from the top line of Eq. (4.1.27) : in a typical EELS experiment, $\omega = 0-2000$ eV, while the electron rest mass corresponds to 500 000 eV. It is therefore not a problem to neglect the effect of the commutator in normal EELS applications.

4.b. The Dipole Approximation

The dipole approximation features rather prominently in this work, as it does in the EELS community overall. While there is general agreement that the approximation is valid when the impulse transfer is small, and that it simplifies EELS by selecting only a limited number of final states $|f\rangle$ to contribute to the cross section (hence the alternative name “dipole selection rule”), the resulting formalism depends somewhat on how exactly one conceives the impulse transfer to be small. “Dipole approximation” may refer to any of the following :

- * linear in impulse transfer
- * approximating the exponential factor in the matrix element by the linear term of its Taylor expansion
- * only “ $\Delta l=1$ ” states can contribute (meaning that the orbital quantum number of the final state should be exactly 1 larger or smaller than that of the initial state)
- * first order in the interaction potential
- * ...

These statements may or may not be equivalent depending on the formalism and the calculation that it is applied to. A clear example of this will be given when we discuss the magic angle later on.

As the angular momentum quantum number l has a clear physical meaning, I will use it to define monopole, dipole, quadrupole, octopole, ... transitions as those for which $|l - l_i| = 0, 1, 2, 3, \dots$ where the index i labels the initial (core) state. So, unless reference is made to another definition, I will mean by dipole terms of the cross section those transitions for which $\Delta l = \pm 1$.

For now, we will choose another particular “dipole approximation”, essentially following Schattschneider⁵ and applying the Taylor expansion to the exponential factor, and truncating it after the first order term. In this dipole approximation Eq. (4.1.27) reduces to

$$M = \frac{4\pi e^2}{V} \frac{1}{q^2 - \omega^2/c^2} \left\langle f \left| \left(-\frac{\mathbf{v}_0 \cdot \mathbf{p}}{mc^2} + i \mathbf{q} \cdot \mathbf{r} \right) \right| i \right\rangle \quad (4.2.1)$$

The term $\left(1 - \frac{\mathbf{v}_0 \cdot \mathbf{q}}{2mc^2} \right)$ doesn't contribute because the initial and final state are orthogonal.

Now, we apply Eq. (4.3.32) and make use of the replacement $\frac{\mathbf{p}}{m} \rightarrow i\omega \mathbf{r}$ which is appropriate within the matrix element to find

$$M = \frac{4\pi e^2}{V} \frac{i}{q^2 - \omega^2/c^2} \left\langle f \left| \left(\mathbf{q} - \frac{\mathbf{v}_0 (\mathbf{q} \cdot \mathbf{v}_0)}{c^2} \right) \cdot \mathbf{r} \right| i \right\rangle \quad (4.2.2)$$

For a velocity \mathbf{v}_0 in the z-direction we see that relativistic effects have modified the impulse transfer as

$$q_z \rightarrow q_z (1 - \beta^2) ; q_x, q_y \text{ unchanged} \quad (4.2.3)$$

which is the same “shortened q-vector” that appears in Eq. (15) of Schattschneider et al. and Eq. (2) of Jouffrey et al. Here, $\beta = v_0/c$.

This description ought to be valid whenever the argument of the Taylor expansion, $\mathbf{q} \cdot \mathbf{r}$, is small. We can assume that the initial state, which is, for core loss spectra, tightly bound to the atom nucleus, limits the radial integral of the matrix element. Therefore, r is often taken to be limited to something of the order of the Bohr radius, although the initial state may be significantly larger due to delocalization. The magnitude of the impulse transfer depends on the beam energy, energy loss and scattering angle at which measurements are made. For the C K edge measured around 300 eV energy loss with a beam energy of 300 keV with a collection angle of the order mrad, impulse transfer values of up to 1-2 inverse Bohr radius contribute to the cross section. It is not immediately clear to me, then, that one could assume that q is small for the calculation of the matrix element.

Neither is the opposite line of reasoning clear : even when q is larger, the overlap of initial and final state can make the matrix element very small for certain states, and thus suppress quadrupole and higher transitions.

The chapter on the magic angle will prove that the “dipole selection rule” is valid but the “small q approximation” is not (or more poorly than usually assumed) for the C K edge.

4.c. Angular momentum expanded formalism

In this chapter, we go back to the general formulation we’ve developed so far (parallel to Schattschneider et al.⁵), but we avoid making the assumption that q is small enough to make the small q or dipole approximation. By expanding the double differential scattering cross section (DDSCS) in spherical harmonics, we thus develop a formalism that describes arbitrary transitions (monopole, dipole, quadrupole, etc.) for arbitrary momentum transfer (although we still require the impulse transfer to be small compared to the beam momentum – which is always the case in EELS-experiments in the TEM – since otherwise the commutator corrections of (4.1.27) become important). We also achieve a formalism that can readily be implemented in an *ab initio* EELS code. Our present work is to be seen as the relativistic generalization of Nelhiebel et al.³⁴, where a similar formalism was developed neglecting relativity.

4.c.1. General theory of the DDSCS in a l, m -representation.

The relativistic EELS double differential cross section is given by (Sec. 4.a or Ref.⁵):

$$\frac{\partial^2 \sigma}{\partial E \partial \Omega} = \left[\frac{4\gamma^2 a_0^{-2}}{q^2 - (E/\hbar c)^2} \right]^2 \frac{k_f}{k_i} \sum_{i,f} \left| \left\langle f \left| e^{iq \cdot r} \left(1 - \frac{\mathbf{v}_0 \cdot \mathbf{p}}{m_e c^2} \right) \right| i \right\rangle \right|^2 \delta(E_f - E_i - E) \quad (4.3.1)$$

The exponential factor can be expanded using the Rayleigh formula :

$$e^{iq \cdot r} = 4\pi \sum_{\lambda=0}^{+\infty} \sum_{\mu=-\lambda}^{\lambda} i^\lambda Y_{\lambda\mu}^*(\Omega_q) Y_{\lambda\mu}(\Omega_r) j_\lambda(qr) \quad (4.3.2)$$

We assume the initial state i to be a core state of the following simple form

$$i(\mathbf{r}) = u_i(r) Y_{l_i m_i}(\Omega) \quad (4.3.3)$$

and the summation over initial states to reduce to a spin factor of 2 and a summation over m_i . This is a reasonable description for a tightly bound “core state”. For low-loss EELS, where the initial state is a valence state, the initial state needs to be described as the final state below, and the formalism would look different (i.e., contain a “JDOS” or Joint Density of States).

The impulse operator is given by

$$\mathbf{p} = -i\hbar \nabla \quad (4.3.4)$$

In spherical coordinates (r, θ, ϕ) , the Nabla operator is of the form

$$\nabla = \frac{\partial}{\partial r} \mathbf{e}_r + \frac{1}{r} \frac{\partial}{\partial \theta} \mathbf{e}_\theta + \frac{1}{r \sin \theta} \frac{\partial}{\partial \phi} \mathbf{e}_\phi \quad (4.3.5)$$

where \mathbf{e} are normalized basis vectors.

Introducing spherical harmonics Y_{lm}

$$|lm\rangle = Y_{lm}(\theta, \phi) = \sqrt{\frac{2l+1}{4\pi} \frac{(l-m)!}{(l+m)!}} P_{lm}(\cos \theta) e^{im\phi} = (-1)^m Y_{l,-m}^*(\theta, \phi) \quad (4.3.6)$$

which are orthonormal and form a complete basis set for $[0, \pi] \times [0, 2\pi]$, and using

$$\frac{dY_{lm}(\Omega)}{d\theta} = m \cot(\theta) Y_{lm}(\Omega) + \sqrt{(l-m)(l+m+1)} e^{-i\phi} Y_{l, m+1}(\Omega) \quad (4.3.7)$$

we can express (4.3.5) in a basis of spherical harmonics :

$$\nabla = \sum_{lm} \left[|lm\rangle \mathbf{e}_r \frac{\partial}{\partial r} + \frac{im}{r \sin \theta} |lm\rangle \mathbf{e}_\phi + m \frac{\cot \theta}{r} |lm\rangle \mathbf{e}_\theta + \frac{e^{-i\phi}}{r} \sqrt{(l-m)(l+m+1)} |lm+1\rangle \mathbf{e}_\theta \right] \langle lm| \quad (4.3.8)$$

As $\frac{\partial}{\partial z} = \cos \theta \frac{\partial}{\partial r} - \frac{\sin \theta}{r} \frac{\partial}{\partial \theta}$, we know that

$$\nabla_z = \cos \theta \nabla_r - \sin \theta \nabla_\theta \quad (4.3.9)$$

This is useful since we now choose \mathbf{v}_0 along the z -axis, and therefore only the z -component of \mathbf{p} is applied to the initial state i . It is important to remember that our formalism is thus developed in the ‘‘laboratory frame’’, with its z -axis defined by the electron beam and not by the crystallographic axes of the sample.

$$\mathbf{v}_0 \cdot \mathbf{p} = -i\hbar v_0 \sum_{lm} \left[\cos \theta |lm\rangle \frac{\partial}{\partial r} - m \frac{\cos \theta}{r} |lm\rangle - \sin \theta \frac{e^{-i\phi}}{r} \sqrt{(l-m)(l+m+1)} |lm+1\rangle \right] \langle lm| \quad (4.3.10)$$

Finally, we use

$$1 = \sum_{lm} |lm\rangle \langle lm| \quad (4.3.11)$$

Now

$$\begin{aligned} \left\langle f \left| e^{iq \cdot r} \left(1 - \frac{\mathbf{v}_0 \cdot \mathbf{p}}{mc^2} \right) \right| i \right\rangle &= 4\pi \sum_{\lambda\mu} \sum_{lm} i^\lambda d_{lm}^{f*} Y_{\lambda\mu}^*(\Omega_q) \int_0^{+\infty} r^2 dr u_l(r) j_\lambda(qr) * \\ &\int_{4\pi} d\Omega Y_{lm}^*(\Omega) Y_{\lambda\mu}(\Omega) * \left[Y_{l, m_i}(\Omega) u_i(r) + \frac{i\hbar v_0}{m_e c^2} \left\{ \cos \theta Y_{l, m_i}(\Omega) \left(\frac{\partial u_i}{\partial r} - \frac{m_i}{r} u_i(r) \right) \right. \right. \\ &\left. \left. - \sin \theta \frac{e^{-i\phi}}{r} \sqrt{(l_i - m_i)(l_i + m_i + 1)} Y_{l, m_i+1}(\Omega) u_i(r) \right\} \right] \end{aligned} \quad (4.3.12)$$

where we have chosen to expand the final state f as

$$\langle lm|f\rangle = d_{lm}^f u_l(r) \quad (4.3.13)$$

and u_l are normalized functions (e.g., the APW basis functions of WIEN2k) and the d coefficients will, when summed over all final states, form the density of states.

We can write the cosine and sine functions as spherical harmonics of first order,

$$\begin{aligned}\cos \theta &= \sqrt{4\pi/3} Y_{10}(\theta, \phi) \\ \sin \theta &= \sqrt{8\pi/3} e^{i\phi} Y_{1-1}(\theta, \phi)\end{aligned}\quad (4.3.14)$$

and then use the formula

$$Y_{l_1 m_1} Y_{l_2 m_2} = \sum_{l=0}^{+\infty} \sum_{m=-l}^l (-1)^{l-m} \sqrt{\frac{[l_1 l_2 l]}{4\pi}} Y_{lm} \begin{pmatrix} l & l_1 & l_2 \\ -m & m_1 & m_2 \end{pmatrix} \begin{pmatrix} l & l_1 & l_2 \\ 0 & 0 & 0 \end{pmatrix} \quad (4.3.15)$$

we get three- Y_{lm} -integrals after all, at the expense of more Wigner 3j coefficients : as (say) $l_2=1$, (4.3.15) has only 2 (simple) nonzero terms. The symbols in round brackets are Wigner 3j-coefficients, as defined by the Racah formula.⁹⁶

We recall that

$$\int d\Omega Y_{l_1 m_1}^* Y_{l_2 m_2} Y_{l_3 m_3} = (-1)^{m_1} \sqrt{\frac{[l_1 l_2 l_3]}{4\pi}} \begin{pmatrix} l_1 & l_2 & l_3 \\ -m_1 & m_2 & m_3 \end{pmatrix} \begin{pmatrix} l_1 & l_2 & l_3 \\ 0 & 0 & 0 \end{pmatrix} =: \left\{ \begin{matrix} l_1 & l_2 & l_3 \\ -m_1 & m_2 & m_3 \end{matrix} \right\} \quad (4.3.16)$$

where $[n] = 2n + 1$.

Eq. (4.3.15) with $l_2=1$ then becomes

$$Y_{l_1 m_1} Y_{1 m_2} = Y_{l_1+1, m_1+m_2} \begin{Bmatrix} l_1+1 & l_1 & 1 \\ -m_1-m_2 & m_1 & m_2 \end{Bmatrix} + Y_{l_1-1, m_1+m_2} \begin{Bmatrix} l_1-1 & l_1 & 1 \\ -m_1-m_2 & m_1 & m_2 \end{Bmatrix} \quad (4.3.17)$$

and therefore

$$\begin{aligned}\int_{4\pi} d\Omega Y_{l_1 m_1}^* Y_{l_2 m_2} Y_{l_3 m_3} Y_{1 m_4} &= \begin{Bmatrix} l_3+1 & l_3 & 1 \\ -m_3-m_4 & m_3 & m_4 \end{Bmatrix} \begin{Bmatrix} l_1 & l_2 & l_3+1 \\ -m_1 & m_2 & m_3+m_4 \end{Bmatrix} \\ &+ \begin{Bmatrix} l_3-1 & l_3 & 1 \\ -m_3-m_4 & m_3 & m_4 \end{Bmatrix} \begin{Bmatrix} l_1 & l_2 & l_3-1 \\ -m_1 & m_2 & m_3+m_4 \end{Bmatrix}\end{aligned}\quad (4.3.18)$$

This leads to

$$\begin{aligned}\langle i|V|f\rangle &= 4\pi \sum_{\lambda\mu} \sum_{lm} i^\lambda d_{lm}^{f*} Y_{\lambda\mu}^*(\Omega_q) \left[t_1 + i \sum_{a=2}^5 t_a \right] \\ &= 4\pi \sum_{\lambda\mu} \sum_{lm} i^\lambda d_{lm}^{f*} Y_{\lambda\mu}^*(\Omega_q) \left\{ \begin{Bmatrix} l & \lambda & l_i \\ -m & \mu & m_i \end{Bmatrix} \int j_\lambda u_l u_i + \frac{i\hbar v_0}{m_e c^2} \sqrt{\frac{4\pi}{3}} \int j_\lambda u_l \left(\frac{\partial u_i}{\partial r} - \frac{m_i}{r} u_i \right) \right. \\ &\left[\begin{Bmatrix} l_i+1 & l_i & 1 \\ -m_i & m_i & 0 \end{Bmatrix} \begin{Bmatrix} l & \lambda & l_i+1 \\ -m & \mu & m_i \end{Bmatrix} + \begin{Bmatrix} l_i-1 & l_i & 1 \\ -m_i & m_i & 0 \end{Bmatrix} \begin{Bmatrix} l & \lambda & l_i-1 \\ -m & \mu & m_i \end{Bmatrix} \right] \\ &- \frac{i\hbar v_0}{m_e c^2} \sqrt{\frac{8\pi}{3}} \sqrt{(l_i-m_i)(l_i+m_i+1)} \int j_\lambda u_l \frac{u_i}{r} \\ &\left. \left[\begin{Bmatrix} l_i+1 & l_i & 1 \\ -m_i & m_i+1 & -1 \end{Bmatrix} \begin{Bmatrix} l & \lambda & l_i+1 \\ -m & \mu & m_i \end{Bmatrix} + \begin{Bmatrix} l_i-1 & l_i & 1 \\ -m_i & m_i+1 & -1 \end{Bmatrix} \begin{Bmatrix} l & \lambda & l_i-1 \\ -m & \mu & m_i \end{Bmatrix} \right] \right\}\end{aligned}\quad (4.3.19)$$

The terms t_a are defined by the second equality of (4.3.19) and depend on all indices of the expansion, but for brevity these are hidden. Term t_1 is the non-relativistic term and terms t_2 - t_5 are relativistic, making it very trivial to reduce our results to the non-

relativistic limit : c goes to infinity, terms 2-5 disappear. Each term has its own selection rule given by the 3j elements. The importance of the relativistic terms is seen to depend directly on the velocity v_0 of the beam electrons.

Now (4.3.1) becomes

$$\frac{\partial^2 \sigma}{\partial E \partial \Omega} = \left[\frac{4\gamma^2 a_0^{-2}}{q^2 - (E/\hbar c)^2} \right]^2 \frac{k_f}{k_i} 2 \sum_{m_i} \sum_{lm} \sum_{l'm'} \sum_{\lambda\mu} \sum_{\lambda'\mu'} \text{dos}(E + E_i; lm, l' m') (4\pi)^2 i^{\lambda-\lambda'} \quad (4.3.20)$$

$$Y_{\lambda'\mu'}(\Omega_q) Y_{\lambda\mu}^*(\Omega_q) \left[t_1 t_1' + \left(\sum_{a=2}^5 t_a \right) \left(\sum_{a=2}^5 t_a' \right) + i \left(t_1' \sum_{a=2}^5 t_a - t_1 \sum_{a=2}^5 t_a' \right) \right]$$

The factor 2 outside the summations is the spin factor. We have defined the density of states (dos) as

$$\text{dos}(E; lm, l' m') = \sum_{f=kv} d_{lm}^f d_{l'm'}^{f*} \delta(E_f - E) \quad (4.3.21)$$

In some materials of high symmetry, the DOS has no cross-terms, meaning that only terms with $l=l'$ and $m=m'$ will contribute. We will look at this in more detail in Sec. 4.c.3.

4.c.2. The dipole terms and correspondence to Schattschneider et al.

We have already remarked that the “dipole approximation” is an ill defined term. It is essentially an approximation made for small q ; however, this approximation can be made in different ways. The most common way is to use a first order Taylor expansion for the interaction potential :

$$e^{iq \cdot r} \approx 1 + iq \cdot r \quad (4.3.22)$$

Retaining terms of first order after multiplication with the relativistic interaction term, one obtains the most celebrated aspect of the dipole approximation : the dipole selection rule, that allows only transitions to states with orbital quantum number +1 or -1, and forbids all other transitions.

It is not immediately clear how to do the same thing starting from (4.3.19). Here, we gather all terms corresponding to transitions into $l+1$ or $l-1$ states. This can be done without assuming that q is small.

It will be instructive to see which additional approximations are necessary to recover the results achieved earlier by using the Taylor expansion.

We will consider the graphite C K-edge, that is, a transition from an initial carbon 1s-state. This simplifies the notations ; generalization to another edge would be trivial but make all the formulas twice as long. As most ELNES experiments obey this, we will calculate the p -spectrum, i.e., the transitions to a final state of p -character. Expressing this in angular momentum indices,

$$l_i = m_i = 0 ; l = l' = 1 ; m = m' \quad (4.3.23)$$

The “dipole” matrix element (4.3.19) can now be expressed as :

$$\begin{aligned} \langle f|V|i\rangle &= 4\pi \sum_{\lambda\mu} \sum_m i^\lambda d_{lm}^{f*} Y_{\lambda\mu}(\Omega_q) \{ \dots \} \\ &= 4\pi \sum_m d_{lm}^{f*} \left\{ \frac{j_{11}^{(1)}}{\sqrt{4\pi}} Y_{1m}(\Omega_q) + \frac{\hbar v_0}{m_e c^2 \sqrt{3}} \left(\frac{j_{01}^{(2)}}{4\pi} \delta_{m0} - \frac{j_{21}^{(2)}}{\sqrt{4\pi} \sqrt{5\pi}} Y_{2m}(\Omega_q) \left(\delta_{m0} + \frac{\sqrt{3}}{2} (\delta_{m1} + \delta_{m-1}) \right) \right) \right\} \end{aligned} \quad (4.3.24)$$

where we have introduced compact notations for the radial integrals :

$$\varepsilon = \frac{\hbar v_0}{m_e c^2} \sqrt{\frac{4\pi}{3}} \quad (4.3.25)$$

$$j_{\lambda l}^{(1)} = \int j_\lambda(qr) u_l(r) u_l(r)$$

$$j_{\lambda l}^{(2)} = \int j_\lambda(qr) \frac{\partial u_l(r)}{\partial r} u_l(r) \quad (4.3.26)$$

$$j_{\lambda l}^{(3)} = \int j_\lambda(qr) \frac{u_l(r)}{r} u_l(r)$$

The radial integral of type (1) is the non-relativistic radial integral ; the other two are relativistic contributions.

We now notice that the integral $j_{21}^{(2)}$ is actually of second order in q . It can be shown numerically to be tiny compared to the other terms in (4.3.24), and it can be safely ignored for our purpose here.

The total cross-section can be obtained similar to how we obtained Eq. (4.3.20):

$$\begin{aligned} \frac{\partial^2 \sigma}{\partial E \partial \Omega}(E, \mathbf{q}) &= \frac{4\gamma^2 a_0^{-2}}{\left(q^2 - \left(\frac{E}{\hbar c} \right)^2 \right)^2} \frac{k'}{k} 2(4\pi)^2 \left\{ D_\pi \left[\sqrt{\frac{3}{4\pi}} \cos \theta_q \frac{j_{11}^{(1)}}{\sqrt{4\pi}} + \frac{\hbar v_0}{m c^2} \frac{j_{01}^{(2)}}{\sqrt{3}(4\pi)} \right]^2 \right. \\ &+ \left(D_\sigma - 2 \operatorname{Re} \left(D_{11}^{1-1} e^{2i\phi_q} \right) \right) \left[\sqrt{\frac{3}{8\pi}} \sin \theta_q \frac{j_{11}^{(1)}}{\sqrt{4\pi}} \right]^2 \\ &+ \left. 2 \operatorname{Re} \left(D_{1-1}^{10} e^{-i\phi_q} - D_{11}^{10} e^{i\phi_q} \right) \left[\sqrt{\frac{3}{8\pi}} \sin \theta_q \frac{j_{11}^{(1)}}{\sqrt{4\pi}} \right] \left[\sqrt{\frac{3}{4\pi}} \cos \theta_q \frac{j_{11}^{(1)}}{\sqrt{4\pi}} + \frac{\hbar v_0}{m c^2} \frac{j_{01}^{(2)}}{\sqrt{3}(4\pi)} \right] \right\} \end{aligned} \quad (4.3.27)$$

where the π and σ density of states have been introduced :

$$D_\pi = d_{10}^f d_{10}^{f*} ; D_\sigma = d_{11}^f d_{11}^{f*} + d_{1-1}^f d_{1-1}^{f*} \quad (4.3.28)$$

The cross section has been split into a π contribution, a σ contribution, and a contribution consisting of “cross-terms”. The angles have received a subscript “ q ” to indicate that they are the spherical coordinates of the impulse transfer vector, which is generally not

the same as the scattering angle (which is the angle between the incoming and outgoing electron beam).

It is clear that (4.3.27) is not (4.2.3). This is a clear indication that the transition selection rule ($l=l_i \pm 1$) is not the same as the small q approximation. Let us now make the additional assumption that q is small.

We remark that for small q (and let us from now on assume that we are working in this approximation) the spherical Bessel function can be approximated as :

$$\begin{aligned} j_0(x) &= \frac{\sin x}{x} \approx 1 \\ j_1(x) &= \frac{\sin x}{x^2} - \frac{\cos x}{x} \approx \frac{x}{3} \\ j_2(x) &= \left(\frac{3}{x^3} - \frac{1}{x} \right) \sin x - \frac{3}{x^2} \cos x \approx \frac{x^2}{15} \end{aligned} \quad (4.3.29)$$

Now, writing

$$\frac{\partial}{\partial r} = \nabla_r = \frac{m_e v_r}{-i\hbar} \quad (4.3.30)$$

and using that

$$\int u_i v u_l = i \omega \int u_i r u_l \quad \omega = \hbar^{-1} (E_f - E_i) \quad (4.3.31)$$

and knowing from theory [Eq. (12) in Schattschneider⁵] that

$$\omega = v_0 q \cos \theta_q \quad (4.3.32)$$

we see that

$$j_{01}^{(2)} = \frac{-3v_0 m \cos \theta_q}{\hbar} j_{11}^{(1)} \quad (4.3.33)$$

Using this result, (4.3.27) becomes

$$\begin{aligned} \frac{\partial^2 \sigma}{\partial E \partial \Omega} &= \left[\frac{4\gamma^2 a_0^{-2}}{q^2 - (E/\hbar c)^2} \right]^2 \frac{k_f}{k_i} 6 (j_{11}^{(1)})^2 \left[\frac{D_\sigma - 2 \operatorname{Re}(D_{11}^{1-1} e^{2i\phi_q})}{2} \sin^2 \theta_q + D_{10} \cos^2 \theta_q (1 - \beta^2)^2 \right. \\ &\quad \left. + \sqrt{2} \operatorname{Re}(D_{1-1}^{10} e^{-i\phi_q} - D_{11}^{10} e^{i\phi_q}) \sin \theta_q \cos \theta_q (1 - \beta^2) \right] \end{aligned} \quad (4.3.34)$$

with $\beta = v_0 / c$.

For interpretation, let us consider what would happen if we were to change a vector \mathbf{q} into another vector \mathbf{q}' by shrinking its z-component by a factor $(1 - \beta^2)$ whilst leaving the x and y components unaltered.

$$\begin{aligned}
q' &= q \sqrt{1 - \beta^2 \cos^2 \theta_q (2 - \beta^2)} \\
\cos \theta_q' &= \cos \theta_q \frac{1 - \beta^2}{\sqrt{1 - \beta^2 \cos^2 \theta_q (2 - \beta^2)}} \quad \text{or} \quad q' \cos \theta' = q (1 - \beta^2) \cos \theta \quad (4.3.35) \\
\sin \theta_q' &= \sin \theta_q \frac{1}{\sqrt{1 - \beta^2 \cos^2 \theta_q (2 - \beta^2)}} \quad \text{or} \quad q' \sin \theta' = q \sin \theta
\end{aligned}$$

In our small q approximation, $j_{11}^{(1)}$ is linear in q . We see now that in (4.3.34) the \mathbf{q} -dependence of the dipole cross section deviates in two ways from the non-relativistic theory of Nelhiebel³⁴:

* the prefactor in square brackets has a modified \mathbf{q} -dependence and becomes larger for high energy losses

* the remaining part (similar to the dynamic form factor or DFF) behaves as if the impulse transfer has diminished by a factor $(1 - \beta^2)$ in the direction parallel to the electron beam.

These are exactly the observations made in Jouffrey et al.⁴, and (4.3.34) is identical to his “dipole approximation” results (except that he does not discuss cross-terms). This confirms that our formulae (at least the part relevant for the dipole approximation) are correct and in agreement with other work.

We have also demonstrated how the term “dipole approximation” may be ambiguous and may involve different levels of approximation.

4.c.3. The cross terms.

Cross-terms in the cross-section are those terms containing a “cross density of states”, that is, a factor $d_{lm}^{f*} d_{l'm'}^f$, for which either $l \neq l'$ or $m \neq m'$. They are often neglected in published formulae. This is valid if the crystal under investigation is of sufficiently high symmetry, and/or if the DOS is defined in a coordinate frame that coincides with the axes of symmetry.

Let us investigate when the cross terms will disappear. Nelhiebel³¹ describes this, but works ‘backwards’: terms ‘must’ disappear. Let us work ‘forwards’. The procedure can be as follows. The point group of a site does not give the symmetry of the wave function, but it does give that of the potential and the charge density. The charge density is the square modulus of the wave function, which can be expanded in spherical harmonics (see Eq. (4.3.13)). Thus we get an expression featuring our $d_{lm}^{f*} d_{l'm'}^f$, which will in this section be abbreviated as D_{lm}^{LM} coefficients. Now the application of a symmetry operation on the spatial coordinate has to be expressed in spherical coordinates, and then one has to work out how this transforms the spherical harmonics. In order for this symmetry

transformation to leave the charge density invariant, the D coefficients will have to obey certain rules. We list a few simple examples :

symmetry	coord transf	Y_{lm} transformation	properties of D	remarks
m_x	$\phi \rightarrow \pi - \phi$	$Y_{lm}(\theta, \pi - \phi) = Y_{l-m}(\theta, \phi)$	$D_{lm}^{LM} = D_{l-m}^{L-M}$	D_{lm}^{L-m} is real
m_y	$\phi \rightarrow -\phi$	$Y_{lm}(\theta, -\phi) = (-1)^m Y_{l-m}(\theta, \phi)$	$D_{lm}^{LM} = (-1)^{m-M} D_{l-m}^{L-M}$	
m_z	$\theta \rightarrow \pi - \theta$	$Y_{lm}(\pi - \theta, \phi) = (-1)^l Y_{lm}(\theta, \phi)$	$D_{lm}^{LM} = (-1)^{m-M+l-L} D_{lm}^{L-M}$	$l-L+m-M$ even
C2 z	$\phi \rightarrow \pi + \phi$	$Y_{lm}(\theta, \pi + \phi) = (-1)^m Y_{lm}(\theta, \phi)$	$D_{lm}^{LM} = (-1)^{m-M} D_{lm}^{LM}$	$m-M$ must be even
C3 z	$\phi \rightarrow \frac{2}{3} \pi + \phi$	$Y_{lm}(\theta, \pi + \phi) = i^{4m/3} Y_{lm}(\theta, \phi)$	$D_{lm}^{LM} = i^{4/3(m-M)} D_{lm}^{LM}$	$(m-M)/3$ integer
C4 z	$\phi \rightarrow \frac{1}{2} \pi + \phi$	$Y_{lm}(\theta, \pi + \phi) = i^m Y_{lm}(\theta, \phi)$	$D_{lm}^{LM} = i^{m-M} D_{lm}^{LM}$	$(m-M)/4$ integer
C6 z	$\phi \rightarrow \frac{1}{6} \pi + \phi$	$Y_{lm}(\theta, \pi + \phi) = i^{2m/3} Y_{lm}(\theta, \phi)$	$D_{lm}^{LM} = i^{2/3(m-M)} D_{lm}^{LM}$	$(m-M)/6$ integer
inversion	$\theta \rightarrow \pi - \theta$ $\phi \rightarrow \pi + \phi$? = C2 z + m_z	$m-M$ must be even	$l+L$ must be even

Any D symbol not meeting the requirement in the last column of the table (except for the first line – this is a property, not a requirement) is zero.

We see that e.g. C4 ||z will kill all cross terms in (4.3.27).

Diamond is of such high symmetry that its cross-terms cancel in any coordinate frame. Generally speaking, this is true for all crystals with orthorhombic or higher symmetry.³¹ Graphite, however, has lower symmetry. Its cross-terms are zero if the coordinate frame is chosen correctly (z-axis defining the spherical harmonics is perpendicular to the graphene sheets), but they give an important contribution if the axes are chosen differently.

4.c.4. The monopole term.

The monopole term contains the transitions of order 0 in the interaction potential, or equivalently, the transitions for which $l = l_i$. Its only contribution is similar to that in non-relativistic theory, except for the Coulombic prefactor :

$$M = \frac{4 a_0^{-2}}{(q^2 - (E/\hbar c)^2)^2} \frac{k_f}{k_i} D_{00} \int r^2 j_0(qr) u_{l_s}(r) u_{l=0}(r) dr \quad (4.3.36)$$

for a K-edge where u_{l_s} is the radial part of the core state wave function, and $u_{l=0}$ is the radial part of the final state of s-character (replace the u – functions by their appropriate relatives for other edges). In the small q limit, this reduces to

$$M = \frac{4 a_0^{-2}}{(q^2 - (E/\hbar c)^2)^2} \frac{k_f}{k_i} D_{00} \int r^2 u_{l_s}(r) u_{l=0}(r) dr \quad (4.3.37)$$

Just like in the dipole transition, the monopole DFF M works as if the impulse transfer were shortened – but in the most trivial way : by simply not depending on it. The monopole usually doesn't contribute to the spectrum. This is unrelated to the impulse transfer being small or not, but is entirely due to the small overlap of the wave functions in (4.3.37).

4.c.5. The quadrupole terms.

We define the quadrupole terms q as those for which $l = l_i \pm 2$. We calculate its direct terms q_{lm} for the K edge.

$$q_{22} = (4\pi)^{-2} \frac{15}{8} \sin^4 \theta j_{220}^2 \quad (4.3.38)$$

$$q_{2-2} = q_{22} \quad (4.3.39)$$

$$q_{21} = (4\pi)^{-2} \frac{\sin^2 \theta}{2} \left[\sqrt{15} \cos \theta j_{220} + \varepsilon \sqrt{3/5} (j_{120}^{(0)'} + 3j_{120}'') \right]^2 \quad (4.3.40)$$

$$q_{2-1} = q_{21} \quad (4.3.41)$$

$$q_{20} = (4\pi)^{-2} \left[\sqrt{5/4} (3 \cos^2 \theta - 1) j_{220} + \varepsilon \cos \theta (\sqrt{4/5} j_{120}' + \sqrt{36/5} j_{120}'') \right]^2 \quad (4.3.42)$$

which gives for the total direct quadrupole cross section

$$q = (4\pi)^{-2} \alpha \left\{ \left[\sqrt{5/4} (3 \cos^2 \theta - 1) j_{220} + \varepsilon \cos \theta (\sqrt{4/5} j_{120}' + \sqrt{36/5} j_{120}'') \right]^2 D_{20} + \frac{\sin^2 \theta}{2} \left[\sqrt{15} \cos \theta j_{220} + \varepsilon \sqrt{3/5} (j_{120}^{(0)'} + 3j_{120}'') \right]^2 (D_{21} + D_{2-1}) + \frac{15}{8} \sin^4 \theta j_{220}^2 (D_{22} + D_{2-2}) \right\} \quad (4.3.43)$$

where $\varepsilon = \frac{\hbar v_0}{m_e c^2}$. It is now worthwhile to evaluate this expression in the small q limit

and see whether we again find a non-relativistic DFF formula with relativistically shortened q -vector.

$$j_{220} \approx \frac{q^2}{15} \int r^4 u_{1s} u_{l=2}$$

$$j_{120}'' \approx \frac{q}{3} \int r^2 u_{1s} u_{l=2} \quad (4.3.44)$$

$$j_{120}^{(0)'} \approx -5 \frac{m_e v_0}{\hbar} \cos \theta j_{220}$$

As an additional approximation, j_{120}'' may be assumed zero due to orthogonality of initial and final states. We get

$$q \approx (4\pi)^{-2} \alpha j_{220}^2 \left\{ \left[\sqrt{5/4} (3 \cos^2 \theta - 1) - \cos^2 \theta \sqrt{20} \beta^2 \right]^2 D_{20} + \frac{15}{2} \sin^2 \theta \cos^2 \theta (1 - \beta^2)^2 (D_{21} + D_{2-1}) + \frac{15}{8} \sin^4 \theta (D_{22} + D_{2-2}) \right\} \quad (4.3.45)$$

It is now obvious from the different behavior of the two terms involving $\cos \theta$ that there is no simple geometrical interpretation of the relativistic changes to the quadrupole term.

The last open question is how the $l=2, m \neq m'$ cross terms behave. We derive

$$q_{2m}^{2m'} = Y_{2m} Y_{2m'}^* (4\pi)^{-1} \left[j_{220} + i\varepsilon \sqrt{4\pi/3} \left(j_{120}^{(m)} \begin{Bmatrix} 1 & 2 & 1 \\ -m & m & 0 \end{Bmatrix} - \sqrt{2(2-m)(3+m)} j_{120} \begin{Bmatrix} 1 & 2 & 1 \\ -m & m+1 & -1 \end{Bmatrix} \right) \right] \quad (4.3.46)$$

$$\left[j_{220} - i\varepsilon \sqrt{4\pi/3} \left(j_{120}^{(m')} \begin{Bmatrix} 1 & 2 & 1 \\ -m' & m' & 0 \end{Bmatrix} - \sqrt{2(2-m')(3+m')} j_{120} \begin{Bmatrix} 1 & 2 & 1 \\ -m' & m'+1 & -1 \end{Bmatrix} \right) \right]$$

In particular,

$$q_{22}^{2-2} = \frac{15}{2} (4\pi)^{-2} \sin^4 \theta e^{4i\phi} (j_{220})^2 = (q_{2-2}^{22})^* \quad (4.3.47)$$

$$q_{00}^{22} = \varepsilon \sqrt{\frac{15}{2}} (4\pi)^{-2} \cos \theta \sin^2 \theta e^{-2i\phi} j_{100}^{(0)} j_{220} = (q_{22}^{00})^* = (q_{00}^{2-2})^* = q_{2-2}^{00} \quad (4.3.48)$$

Additionally, there are cross terms for which m or m' equals 1.

Quadrupole terms are generally very small. They contribute only in “extraordinary” circumstances, such as

- very high scattering angles
- pre-peak signals (in the “dipole band gap”)^{30,97}
- due to diffraction effects³⁵
- in certain materials^{98,99}

Also, it’s possible that the relativistic formalism has stronger quadrupole signals in some situations. This requires further investigation.

The angular momentum expansion (4.3.20) doesn’t stop at second order – but this manuscript does. Octopole and higher orders can be treated analogously to cases already discussed.

4.d. Implementation in the WIEN2k program TELNES2

The WIEN2k program⁷ is a benchmark ab initio band structure code based on the L/APW formalism⁴⁹ within the Density Functional Theory framework⁵⁶. It calculates the electronic structure of the ground state of a periodic system self-consistently in reciprocal

space by constructing and diagonalizing its Kohn-Sham Hamiltonian. It works with a L/APW basis set briefly described below.

I have developed a program (TELNES2⁷⁰) that calculates ELNES spectra from WIEN2k's Kohn-Sham electronic structure. The double differential ELNES cross section is calculated by evaluation of Eq. (4.3.19)-(4.3.20).

Two further points merit discussion. The first concerns the basis set used in WIEN2k and how to generate from it the angular expansion coefficients for the final states. The second addresses the integration of the double differential cross section over impulse transfer (or, equivalently, scattering angle) to obtain the differential cross section which is measured in experiment.

4.d.1. The L/APW basis set and the l,m -decomposition

Although a detailed description of the ab initio DFT band structure code WIEN2k would be out of place in this dissertation, and indeed redundant as it is readily available elsewhere,⁶⁶ we must briefly remark on the basis set used to describe wave functions of a crystal.

Space is divided into two regions : a set of non-overlapping spheres (S) centred around each atom in the crystal, and the remaining interstitial space (I) (Figure 4-3).

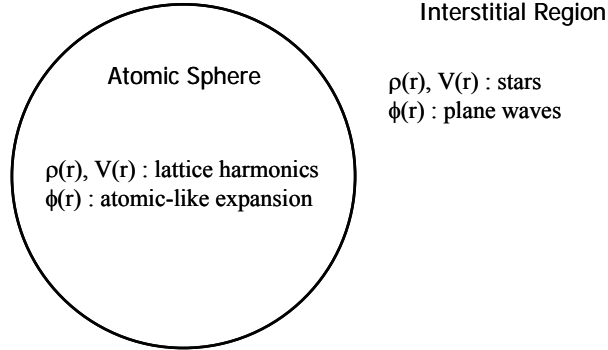


Figure 4-3 Space is divided into atomic spheres and an interstitial region, each with its own basis set for the wave functions and the electron density and potential.⁴⁹

In the interstitial region, electrons are assumed to be delocalized and free-electron like, and their wave function is expanded in plane waves. Within the atomic spheres, the electron wave function is assumed to be more atomic-like, and it is expanded in a local basis :

$$\begin{aligned} \phi(\mathbf{r}) &= \Omega^{-1/2} \sum_{\mathbf{G}} c_{\mathbf{G}} e^{i(\mathbf{G}+\mathbf{k})\cdot\mathbf{r}} & \mathbf{r} \in I \\ &= \sum_{lm} \left[A_{lm} u_l(\mathbf{r}) + B_{lm} u'_l(\mathbf{r}) \right] Y_{lm}(\theta, \phi) & \mathbf{r} \in S \end{aligned} \quad (4.4.1)$$

where the function u is given by

$$\left\{ -\frac{d^2}{dr^2} + \frac{l(l+1)}{r^2} + V(r) - E_l \right\} r u_l'(r) = r u_l(r) \quad (4.4.2)$$

where V is the Kohn-Sham potential of the crystal. u' is the derivative with respect to energy of u , which allows a small basis set of u -functions calculated at a small number of “linearization energies” E_l (usually taken at energies close to the middle of a band) to be linearized to make the basis applicable to a sufficiently large energy range to describe all relevant electron states.⁴⁹ To allow for even more flexibility and to describe semicore states, so-called Local Orbitals are added to the basis :

$$\phi_{LO}(\mathbf{r}) = \begin{cases} \left[A_{lm}^{\alpha,LO} u_{1l}^{\alpha}(r) + B_{lm}^{\alpha,LO} u_{1l}^{\alpha}(r) + C_{lm}^{\alpha,LO} u_{2l}^{\alpha}(r) \right] Y_{lm}(\theta, \phi) & \text{for } r \in R_{\alpha} \\ 0 & \text{for } r \notin R_{\alpha} \end{cases} \quad (4.4.3)$$

or

$$\phi_{lo}(\mathbf{r}) = \begin{cases} \left[A_{lm}^{\alpha,lo} u_{1l}^{\alpha}(r) + B_{lm}^{\alpha,lo} u_{1l}^{\alpha}(r) \right] Y_{lm}(\theta, \phi) & \text{for } r \in R_{\alpha} \\ 0 & \text{for } r \notin R_{\alpha} \end{cases} \quad (4.4.4)$$

These notations must be less than clear to the reader ; he is referred to more specialized texts⁶⁶ for a better description of the WIEN2k L/APW+LO/lo basis set. The point we make in this section is simple enough that more detailed description does not seem warranted.

An alternative basis set, called APW, is

$$\begin{aligned} \phi(\mathbf{r}) &= \Omega^{-1/2} \sum_{\mathbf{G}} c_{\mathbf{G}} e^{i(\mathbf{G}+\mathbf{k})\cdot\mathbf{r}} & \mathbf{r} \in I \\ &= \sum_{lm} d_{lm} u_l(r) Y_{lm}(\theta, \phi) & \mathbf{r} \in S \end{aligned} \quad (4.4.5)$$

This is simpler, but because no energy linearization is used, nor any local orbitals, it is necessary to have a basis function u for every eigenenergy, leading to a large basis set which is not practical for SCF calculations.⁴⁹

We will now assume that, due to the strong localization of the initial state wave function, a description of the final state is only needed within the atomic spheres, and the interstitial plane wave expansion can be ignored from now on, as the initial state does not extend into the interstitial region. WIEN2k calculations check that this is the case and protest if the initial core state is not fully (say, 99.99%) confined within the atomic sphere. (It is possible to perform the calculation anyway – and sometimes strange, unphysical results will follow.) For all but the most shallow core edges this will never pose any real problems.

It is very convenient to write the double differential cross section in such a way that it is separated into a matrix element (M) and a local partial density of states (DOS) :

$$\frac{d^2\sigma}{d\Omega dE} = \sum_l \rho_l(E) M_l(E) \quad (4.4.6)$$

This is essentially the way we have developed our EELS formalism until now. However, it is not possible in every theoretical framework.

Let's look again at the basic expression for the cross section in the first Born, single scattering, independent particle approximation for an incoming plane wave :

$$\frac{d^2\sigma}{d\Omega dE} = \alpha \sum_{i,f} \left| \langle i|V|f \rangle \right|^2 \delta(E - E_{if}) \quad (4.4.7)$$

Now we expand the final state wave function

$$|f \rangle = \sum_{lm} \sum_{a_l} c_{lma_l}^f |lm(\Omega)\rangle |a_l(r)\rangle \quad (4.4.8)$$

This expression is valid for APW and LAPW basis sets within the atomic sphere. The ket $|lm\rangle$ denotes a spherical harmonic, the ket $|a_l\rangle$ denotes a radial basis function. For APW, there is just one; for LAPW, there are at least two, and often three.

I repeat the definition of the local partial density of states :

$$\rho_{lm}(E) = \sum_f \left| \langle f|\lambda\mu \rangle \right|^2 \delta(E_f - E) \quad |\lambda\mu\rangle = \sum_{a_l} |a_l\rangle |lm\rangle \quad (4.4.9)$$

$$\rho_{lm}(E) = \sum_f \delta(E_f - E) \sum_{a_l} \sum_{A_L} c_{lma_l}^f c_{lmA_L}^{f*} \quad (4.4.10)$$

This definition is easily generalized to cross-DOS ($lm \neq LM$).

Combining (4.4.8) and (4.4.7) yields

$$\frac{d^2\sigma}{d\Omega dE} = \alpha \sum_{if} \sum_{lm} \sum_{a_l} \sum_{LM} \sum_{A_L} c_{LMA_L}^{f*} c_{lma_l}^f \langle i|V|lma_l\rangle \langle LMA_L|V|i\rangle \delta(E - E_{if}) \quad (4.4.11)$$

Only if the summation over a,A disappears (APW basis set) it is possible to decompose the spectrum into l,m -terms of matrix element times partial density of states.

For APW :

$$\begin{aligned} \frac{d^2\sigma}{d\Omega dE} &= \alpha \sum_{if} \sum_{lm} \sum_{LM} c_{LM}^{f*} c_{lm}^f \langle i|V|lma_l\rangle \langle LMA_L|V|i\rangle \delta(E - E_{if}) \\ &= \alpha \sum_i \sum_{lm} \sum_{LM} \langle i|V|lma_l\rangle \langle LMA_L|V|i\rangle \rho_{lm}^{LM}(E) \end{aligned} \quad (4.4.12)$$

If there are no cross terms :

$$\frac{d^2\sigma}{d\Omega dE} = \alpha \sum_i \sum_{lm} \left| \langle i|V|lma_l\rangle \right|^2 \rho_{lm}(E) \quad (4.4.13)$$

If we consider only one initial state " l_c " and if the (dipole) selection rules only allow for a transition to l_c+1 , and if we integrate over the orientation of the beam with respect to the crystal, then (4.4.13) simplifies even further :

$$\frac{d^2\sigma}{d\Omega dE} = \alpha \rho_{(l_c+1)}(E) \left| M_{l_c \rightarrow l_c+1}(E) \right|^2 \quad (4.4.14)$$

For the LAPW basis set, which WIEN2k uses to construct and diagonalize the Hamiltonian of the crystal and find its electronic structure, it is not possible to write(4.4.12). The only solution is to perform a basis transformation from the L/APW to the APW basis :

$$d_{l'm'}^{(kv)} u_{l'}^{(E_{kv})}(r) = A_{l'm'}^{(kv)} u_{l'}^{(E_1)}(r) + B_{l'm'}^{(kv)} u_{l'}^{(E_2)}(r) + C_{l'm'}^{(kv)} u_{l'}^{(E_2)}(r) \quad (4.4.15)$$

As (4.4.15) does not guarantee that $d_{l'm'}$ is independent of r , it is made so by averaging

$$\frac{1}{d_{l_1, m_1}, d_{l_2, m_2}^*} = \frac{\int dr d_{l_1, m_1}, d_{l_2, m_2}^* u_{l_1}^{(E_{kv})}(r) u_{l_2}^{(E_{kv})}(r)}{\int dr u_{l_1}^{(E_{kv})}(r) u_{l_2}^{(E_{kv})}(r)} \quad (4.4.16)$$

This averaging procedure in principle introduces inaccuracies in the $d_{l,m}$ -coefficients, but in practice these turn out to be insignificant.

4.d.2. Integrating the cross-section over beam convergence and detector aperture.

So far, we have concerned ourselves with the double differential scattering cross-section (DDSCS), which describes scattering of a plane wave (fast beam electron) \mathbf{k} into a plane wave \mathbf{k}' by interaction with the crystal. It gives the probability of capturing an electron that has lost an energy $[E, E+dE]$ and is scattered into a solid angle $[\Omega, \Omega+d\Omega]$. The DDSCS is directly related to the Dynamic Form Factor DFF.

Let us introduce a more compact notation for the DDSCS :

$$dd(\mathbf{k}, \mathbf{k}') := \frac{\partial^2 \sigma}{\partial E \partial \Omega}(\mathbf{k}, \mathbf{k}') \equiv \frac{\partial^2 \sigma}{\partial E \partial \Omega}(E, \mathbf{q}) \quad (4.4.17)$$

dd is determined by the properties of the crystal and the setup of the experiment.

In an EELS-experiment, we resolve the spectrum with respect to \mathbf{k}' : we measure intensity as a function of the energy of the outgoing electron ($E' \equiv k'$) and of its position in the two-dimensional plane of the detector, corresponding to the angle of exit ($d\Omega' \equiv (d\theta', d\phi')$). We do not distinguish between electrons with different incoming wave vector. So, what we really measure is an intensity:

$$I(\mathbf{k}') = \int dd(\mathbf{k}, \mathbf{k}') f_\alpha(\mathbf{k}) d\mathbf{k} \quad (4.4.18)$$

where f_α describes the beam that hits the sample, characterized by a parameter α . We sum incoherently over incoming wave vector. In reality, the beam has coherence, and this is not correct ; however, we do not treat coherence in this text.

A popular expression for the profile of the incoming beam is the simple circular envelope

$$f_\alpha(\mathbf{k}) = \frac{I_0}{\pi\alpha^2} \Theta\left(\frac{\theta}{\alpha}\right) \delta(k - k_0) \quad ; \quad \Theta(x) = 0 \text{ unless } x \leq 1 \quad (4.4.19)$$

which is monochromatic, centered around $\theta = 0$, and has a total intensity of I_0 . In this case, the parameter α is readily identified as the convergence semi-angle of the microscope (Figure 3-8). Of course, in reality beams will always have some distortions from this perfect profile.

Now we approximate the DDSCS dd by imposing that it depends only on the scattering vector \mathbf{q} and not on \mathbf{k} and \mathbf{k}' separately in the context of evaluating the integral. That is, it depends on the sample to beam orientation on a scale of degrees, but it doesn't depend on the orientation on the scale of mrad on which we are integrating.

$$\begin{aligned} \mathbf{q} &= \mathbf{k} - \mathbf{k}' \\ dd(\mathbf{k}, \mathbf{k}') &\equiv dd(\mathbf{q}) \end{aligned} \quad (4.4.20)$$

This is in a trivial way not correct : it is the DFF that depends only on \mathbf{q} ; dd contains a prefactor k'/k . Apart from this, we can motivate our approximation by remarking that the scattering angles in EELS are of the order of millirad, and that a tilt of the crystal with respect to the beam of a few millirad does not alter the scattering process : the (M)DFF is invariant to such a small tilt – unless one works in or near zone axis conditions. In the latter case, channeling/diffraction effects must be taken into account when calculating the cross section, and the precise orientation of the crystal is crucial. However, we here assume that we are not working in zone axis conditions, and there are no diffraction effects. Then only the difference in wave vectors matters, not their very precise orientation. We may now write

$$I(\mathbf{k}') = \int dd(\mathbf{k} - \mathbf{k}') f_\alpha(\mathbf{k}) d\mathbf{k} \quad (4.4.21)$$

Usually we do not use the intensity I of just one pixel of the detector, but we integrate over the signal collected in the detector. This integral turns the double differential cross section into a differential cross section, with the energy loss the only remaining variable. (In reality, one integrates over a certain energy window as well, determined by the energy resolution of the experiment.) This may be expressed by

$$d(k') = \int_\beta d\Omega' \int dd(\mathbf{q}) f_\alpha(\mathbf{k}) d\mathbf{k} = \int d\mathbf{q} dd(\mathbf{q}) \int_\beta f_\alpha(\mathbf{k}' + \mathbf{q}) d\Omega' = \int d\mathbf{q} dd(\mathbf{q}) g^{\alpha\beta}(k', \mathbf{q}) \quad (4.4.22)$$

where the weight function g is defined by the last equality of (4.4.22). We assume that the aperture of the detector can be characterized by a parameter β , the collection semi-angle (Figure 3-8).

In practice, we will approximate the integral over the impulse transfer by a sum over a finite number of values for which we calculate the DDSCS :

$$d(k') \approx \sum_i w_i dd(\mathbf{q}_i) g^{\alpha\beta}(k', \mathbf{q}_i) \quad (4.4.23)$$

w_i is a weight originating in the approximation of the integral over \mathbf{q} by a sum and depends only on the choice of sampling. If the mesh of n_q \mathbf{q} -vectors is chosen uniformly, it is

$$w_i = \frac{\pi(\alpha + \beta)^2}{n_q} \quad (4.4.24)$$

Using (4.4.19) for f_α yields

$$\begin{aligned} g^{\alpha\beta}(k', \mathbf{q}_i) &= \int_\beta d\theta' \sin \theta \int d\phi' \frac{I_0}{\pi\alpha^2} \Theta_\alpha(\alpha \cos(\theta_i)) \\ \cos \theta_i &= \frac{q_i \cos \theta_{q_i} + k' \cos \theta'}{\sqrt{q_i^2 + k'^2 + 2q_i k' (\cos \theta_{q_i} \cos \theta' + \sin \theta_{q_i} \sin \theta' \cos(\phi_{q_i} - \phi')}} \end{aligned} \quad (4.4.25)$$

To avoid confusion over the notations used, we list explicitly the components of all vectors used :

$$\begin{aligned} \mathbf{k} &= (k, \Omega) = (k, \theta, \phi) \\ \mathbf{k}' &= (k', \Omega') = (k', \theta', \phi') \\ \mathbf{q}_i &= (q_i, \Omega_{q_i}) = (q_i, \theta_{q_i}, \phi_{q_i}) \end{aligned} \quad (4.4.26)$$

The integral in (4.4.25) must be performed over a solid angle of radius β around a central spot (θ_0, ϕ_0) ¹. For a spectrum recorded in the usual forward direction, the central spot corresponds to the 000-spot and is characterized by $\theta_0 = 0$. We assume $\theta_0 = 0$ in the rest of this paragraph, as other scenarios are easy enough to understand but complicate notations.

Equation (4.4.25) is an integral of a constant function, so it is the area of a surface defined by two conditions on Ω' . One is expressed by f_α and the other by the boundaries of the integral (β). Symbolically we can write

$$\Omega' \in \Omega_\beta \quad \text{and} \quad \Omega_{q_i+k'} \in \Omega_\alpha \equiv \Omega' \in (\Omega_\alpha - \mathbf{q}_i) \quad (4.4.27)$$

$$g^{\alpha\beta}(k', \mathbf{q}_i) = \frac{I_0}{\pi\alpha^2} \Omega_\beta \cap (\Omega_\alpha - \mathbf{q}_i) \quad (4.4.28)$$

The weight of vector \mathbf{q}_i is the overlap of two solid angles with a different radius, one of which is shifted by the transverse component of the impulse transfer vector (i.e., \mathbf{q}_i projected onto the detector plane), and the other one by a vector defined by (θ_0, ϕ_0) . More realistic functions for f_α will not lead to such a clear interpretation of the weight coefficients $g^{\alpha\beta}$.

I now give explicit expressions for the overlap of two circles, which is of course nothing but elementary geometry. We calculate the overlap of two circles, one with radius α and the other with radius β . The center of the second sphere is at position $(\theta, 0)$ in a Cartesian frame (the first circle has center $(0, 0)$). For sufficiently small values of θ the circles cross at two points with x-coordinate

$$p = \frac{\theta^2 + \alpha^2 - \beta^2}{2\theta} \quad (4.4.29)$$

The area of overlap now consists of two segments, one defined by an arc of radius α on the interval $[p, \alpha]$ and another arc of radius β on the interval $[\theta - \beta, p]$. These can be integrated, and one obtains the overlap area as :

$$\begin{aligned} \alpha + \beta \leq \theta &\Rightarrow \Omega_\beta \cap (\Omega_\alpha - \mathbf{q}_i) = 0 \\ |\alpha - \beta| \leq \theta \leq \alpha + \beta &\Rightarrow \Omega_\beta \cap (\Omega_\alpha - \mathbf{q}_i) = \frac{\pi}{2} (\alpha^2 + \beta^2) - p\sqrt{\alpha^2 - p^2} - (\theta - p)\sqrt{\beta^2 - (\theta - p)^2} \\ &\quad - \beta^2 \operatorname{asin}\left(\frac{\theta - p}{\beta}\right) - \alpha^2 \operatorname{asin}\left(\frac{p}{\alpha}\right) \\ \theta \leq |\alpha - \beta| &\Rightarrow \Omega_\beta \cap (\Omega_\alpha - \mathbf{q}_i) = \pi \min(\alpha, \beta)^2 \end{aligned} \quad (4.4.30)$$

If we include the prefactor $I_0/\pi\alpha^2$, it becomes clear that, contrary to what is sometimes believed, collection and convergence angle are not equivalent. This is readily illustrated by looking at the case of forward scattering

$$g^{\alpha\beta}(k', \mathbf{q} \parallel \mathbf{k} \parallel \mathbf{k}') = \frac{I_0}{\pi\alpha^2} \Omega_\beta \cap \Omega_\alpha = I_0 \frac{\min(\alpha, \beta)^2}{\alpha^2} \quad (4.4.31)$$

¹ Relative to the center of the incoming beam, which we chose earlier to have $\theta = 0$.

For a given collection angle, increasing the convergence angle from zero will not change the intensity up to a given value, when the intensity will start to decrease quadratically. This can be understood by considering a simple function for $S(\mathbf{Q})$ and smearing it out by convolution with f_α . For large values of α , intensity will be transferred to angles outside of the detector aperture.

Given the assumptions we've made here, exchanging α and β only multiplies the total differential cross section by a constant factor (i.e., independent of energy loss).

WIEN2k.

Eqs. (4.4.22) - (4.4.25), (4.4.30) are used in the TELNES2 program of the WIEN2k code. As an alternative to Eq. (4.4.24), one also has the option of using an exponential grid for sampling \mathbf{q} instead of a uniform grid. This can be useful when the collection and convergence angles are large and one wants best accuracy at small scattering angles, where the transition probability is largest. Additionally, a one-dimensional line grid can be chosen. This is obviously of no use for calculating the differential cross-section, but is meant for studying the angular behaviour of the double differential cross section.

Finally, it is also possible to integrate over energy loss, and output a differential cross section which is differential with respect to scattering angle instead of energy loss. This can be useful when comparing to experiments with large energy windows.

4.d.3. Broadening the spectrum.

Experimental spectra are never perfectly sharp functions of energy loss, and in order to compare theoretical calculations to experimental data, the calculated spectra need to be broadened. This is done by convolution with a broadening function. Usually, three different broadening steps are distinguished⁸⁴ :

- * Lorentzian broadening due to the initial state lifetime.
- * Lorentzian broadening due to the final state lifetime.
- * Gaussian broadening to account for “experimental broadening”

The width of the initial state is taken from atomic tables.⁸⁵ When calculating edges such as L23 (corresponding to initial $p_{1/2}$ and $p_{3/2}$ states), it can be significantly different for its L2 and L3 component.

The width of the final states is not well known, and is impossible to calculate in an independent-particle DFT code. It is known to be energy dependent. In TELNES2/WIEN2k, one has several options : constant width, width linear with energy loss above threshold, width quadratic with energy loss, or a somewhat more sophisticated approach recently published by Moreau¹⁰⁰. The first three options are described in more detail in Hébert¹⁰.

The “experimental broadening” is a vague term that can be used to represent such things as the energy resolution of the electron beam and the spectrometer, thermal effects, ... The width of the measured Zero Loss Peak (ZLP) is often used as an estimate for the width of the Gaussian broadening function, but it is equally common to simply choose the broadening that matches the experimental spectrum best.

4.e. Implementation in the FEFF program

So far, we have developed a clear and intuitive picture of EELS in this chapter. The spectrum is calculated *ab initio* by summing transitions between initial and final states. While the description of the scattering mechanism seems unambiguous enough, it is also obvious that the quality of the results heavily depends on one’s ability to calculate accurate initial and final states. As nobody can solve the many-body problem exactly for any system of practical interest, approximations will compromise the accuracy of *ab initio* calculations. This motivates our goal to have more than one method to calculate EELS. The WIEN2k program⁷, based on the ground state theory of DFT, was never really designed to provide accurate unoccupied (final) states for EELS.

FEFF⁸ is a different *ab initio* code, based on the Green’s function method outlined in Chapter 3.d.1. It is sufficiently different from WIEN2k that it is a valuable alternative. We refer to Chapter 3.d.2 for more details.

FEFF has been used extensively in the X-ray Absorption Spectroscopy (XAS) community, where it is routinely applied to the interpretation of experimental XANES and EXAFS measurements. Because XAS and EELS are formally identical in the non-relativistic dipole approximation (apart from a prefactor, and identifying the impulse transfer in EELS with the polarization vector in XAS – see Sec. 3.b.2), FEFF-XAS has also been applied to EELS research. An extensive overview of how to use FEFF-XAS for EELS with applications to GaN ELNES has been published in Moreno et al.⁹ and discussed in Sec. 3.d.2.

However, we have now firmly established that the relativistic nature of EELS makes it different from XAS, even in the dipole approximation. Additionally, variables such as the collection and convergence angle of the microscope really influence the fine structure of the spectrum. These variables were not accounted for in FEFF-XAS, and although it is possible to compensate for this by hand, mistakes were undoubtedly made. To remedy these problems, we have developed a new code, FEFF8.5 or FEFF-EELS,⁷⁵ which incorporates all the advantages of the older FEFF8.4 or FEFF-XAS (including the use of advanced codes such as TDLDA in the calculations⁸⁰ which account for corrections to the independent electron approximation ; the use of Debye-Waller factors to approximately account for temperature effects ; etc.), but features dramatic improvements for the *ab initio* calculation of EELS. From now on, we will refer to FEFF-EELS simply as FEFF. The novelty of the new code consists of the shortened q-vector relativistic formalism of Sec. 4.b in terms of a cross-section tensor as outlined in this Section below, and the

treatment of the impulse transfer and collection or convergence angle as described in Sec. 4.d.2 . More technical information on FEF(-EELS) can be found in the Appendix (App. 8.d).

FEFF calculates the relativistic dipole EELS spectrum using the shortened \mathbf{q} -vector formalism as described in Section 3b and Schattschneider et al.⁵ We will recast that formalism in terms of a cross section tensor (CST).⁷⁵

The cross section is calculated as

$$\frac{\partial^2 \sigma(\mathbf{q}, E)}{\partial E \partial \Omega} = \left(\frac{\partial \sigma}{\partial \Omega} \right)_{Th} S(\mathbf{q}', E) \quad (4.5.1)$$

the product of the Thompson cross-section and the Dynamic Form Factor S :

$$\left(\frac{\partial \sigma}{\partial \Omega} \right)_{Th} = \frac{4a_0^{-2} k'}{\left(q^2 - \left(\frac{E}{\hbar c} \right)^2 \right)^2 k} \quad (4.5.2)$$

$$S(\mathbf{q}', E) = \sum_{i,f} \left| \langle f | \mathbf{q}' \cdot \mathbf{r} | i \rangle \right|^2 \delta(E_f - E_i - E) \quad (4.5.3)$$

The impulse transfer vector is relativistically contracted in the direction of propagation :

$$\mathbf{q}' = \mathbf{q} - \beta^2 q_z \mathbf{e}_z \quad ; \quad \mathbf{q} = \mathbf{k} - \mathbf{k}' \quad ; \quad \beta = v_0 / c \quad (4.5.4)$$

where v_0 is the beam velocity.

This equation is very similar to the description of XAS in the dipole limit, with the impulse transfer \mathbf{q} playing the role of the polarization vector $\boldsymbol{\varepsilon}$ in x-ray scattering matrix elements. However, for relativistic EELS there is an extra \mathbf{q} -dependent contribution along the direction of propagation \mathbf{e}_z .

In general the DDCS can always be separated into a probe-dependent part containing the \mathbf{q} -dependence, and a sample-dependent part which is independent of \mathbf{q} . Since the theory is bi-linear in \mathbf{q} the sample-dependent term transforms as a tensor, i.e.,

$$S(\mathbf{q}', E) = \sum_{i,j=1}^3 q'_i q'_j \sigma_{ij}(E) \quad (4.5.5)$$

$$\sigma_{ij}(E) = \sum_{i,f} \langle f | x_i | i \rangle \langle i | x_j | f \rangle \delta(E_f - E_i - E) \quad (4.5.6)$$

The cross-section tensor σ_{ij} (CST) can therefore describe all possible transitions of the sample. However, experimental conditions determine which impulse transfers occur and therefore the weight of each component of the cross-section tensor that contributes to the total cross section. This can be illustrated clearly by considering the sample to beam orientation of an EELS experiment. Rotation of the sample is equivalent to a rotation of \mathbf{q} , thus changing the weights of the σ_{ij} components in Eq.(4.5.5).

The relativistic character of the formalism is also obvious: the field of the beam electron contracts in its propagation direction, resulting in the evaluation of (4.5.5) using a contracted impulse transfer vector as in Eq.(4.5.4), denoted by a prime.

Formally the CST is a symmetric tensor with at most six independent components. As such, it can always be diagonalized. However, only in symmetric materials, where its

principal axes are given by the physical symmetry of the crystal itself, is a priori knowledge of the diagonal representation available, and will one set of coordinates diagonalize the tensor for all energies. In the general case of a low symmetry sample, or in a situation where a non-symmetric coordinate system is desirable, the cross terms $i \neq j$ in Eq.(4.5.5) are important contributions to the cross section which cannot be neglected. We give an example of this below.

First, we point out a valuable advantage of explicitly separating probe and sample information in the calculation. Recalculating the spectrum for different experimental conditions is extremely fast. Once the CST has been stored, a fraction of a second suffices to obtain the spectrum for given sample to beam orientation, collection angle, or convergence angle. This is clearly illustrated by writing (4.4.22) in CST formulation :

$$\frac{\partial \sigma(E)}{\partial E} = \sum_{i,j=1}^3 \sigma_{ij}(E) \int_{\alpha,\beta} q'_i q'_j \frac{4a_0^{-2}}{\left(q^2 - \left(\frac{E}{\hbar c}\right)^2\right)^2} \frac{k'}{k} d\mathbf{q} \quad (4.5.7)$$

As the CST depends only on the sample, only integrals of functions of \mathbf{q} need to be calculated. These integrals are approximated by a sum over a finite set of impulse transfer vectors \mathbf{q} . This has already been discussed in Section 4.d.2.

The calculation of the cross section tensor for EELS is done in real space, analogous to the case of XAS calculations². For the near edge region (ELNES or XANES), the Full Multiple Scattering technique (FMS) is used, in which all scattering paths within a sphere of limited radius are summed implicitly by matrix inversion. For the extended region (EXELFS or EXAFS), the path expansion approach is taken, in which the scattering from a selected number of paths of limited length is summed explicitly. This is done for each of the six independent components of the sigma tensor.

Combining the ELNES and EXELFS calculations, one can calculate spectra over hundreds of eV, far beyond the limitations of most band-structure codes.

Experimental parameters included in our calculations are : the microscope's collection and convergence semi-angle, the electron beam energy, the sample to beam orientation, and the position of the EELS detector in the scattering plane. FEFF8 calculations always include core hole broadening ; additional broadening can easily be included.

We illustrate the concept of the CST on the C K edge ELNES of graphite, which has its threshold at ca. 285 eV. We also show that its diagonal components are generally not sufficient to calculate the EELS spectrum.

Therefore, we show the different components of the cross section tensor calculated in two different coordinate systems. System 1 is symmetrical : its z-axis is perpendicular to the graphene sheets of the sample, x and y are in-plane. System 2 is non-symmetrical : it is

² Additional information is available in the FEFF documentation, at <http://leonardo.phys.washington.edu/feff/> .

obtained from system 1 by a rotation of 35° around the x-axis of system 1. We work in a Cartesian representation and refer to the components i,j of σ as x,y,z .

In Figure 4-4, we see that in symmetric coordinates the σ_{zz} spectrum contains the so-called π -transitions, corresponding to transitions into final states formed by the graphite π states, with a strong peak at ca. 285 eV. The σ_{xx} and σ_{yy} are identical and contain the σ -transitions, corresponding to the final states of σ character. Their threshold is higher than the π threshold, at ca. 289 eV. All off-diagonal components are zero (which can be explained by symmetry, i.e., equivalence of x and $-x$, y and $-y$, and z and $-z$).

Figure 4-5 shows that in the rotated system, σ_{xx} is equal to that in the symmetric frame, but σ_{yy} and σ_{zz} have mixed and are of mixed π , σ - character. Additionally, the decrease in symmetry allows y,z cross terms to exist. (The x , $-x$ symmetry has been preserved, suppressing xz , zx , xy and yx components. A more general rotation of the coordinates would make all off-diagonal elements nonzero.)

Finally, Figure 4-6 shows the resulting ELNES spectrum. In system 1, calculation of the direct components of σ is sufficient. To calculate the same spectrum in system 2, however, the off diagonal components (yz and zy in this example) make a very important contribution.

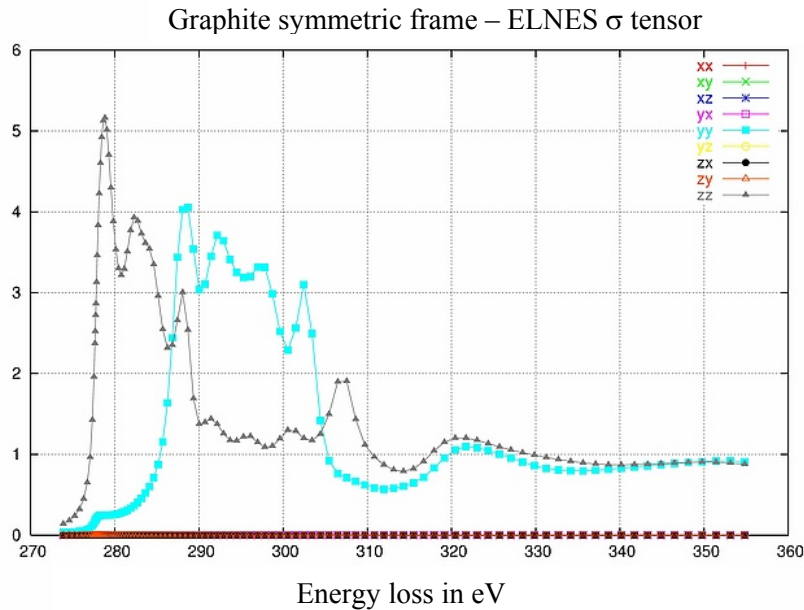


Figure 4-4 Components of the CST of graphite in symmetric coordinates.⁷⁵

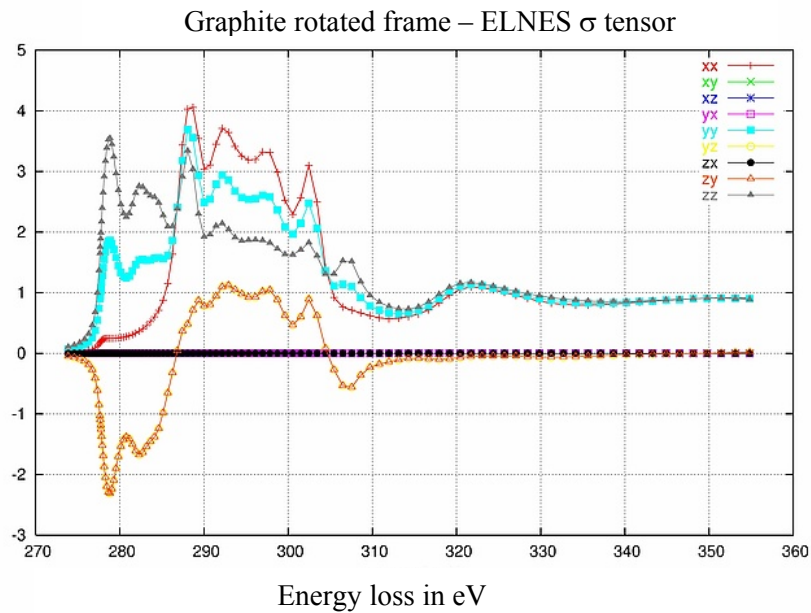


Figure 4-5 Components of the CST of graphite in nonsymmetric coordinates, tilted 35° around the symmetric x-axis.⁷⁵

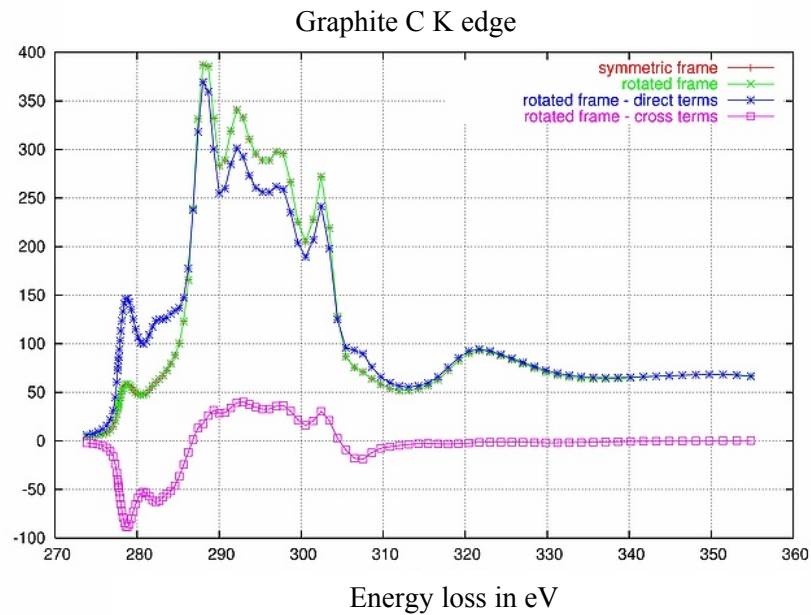


Figure 4-6 C K edge of graphite calculated in coordinate systems 1 and 2 (see text). The beam is perpendicular to the graphene sheets, the beam energy is 300 keV, $\alpha = 10$ mrad, $\beta = 0$ mrad.⁷⁵

4.f. Understanding and solving the magic angle fiasco

The magic angle is a special value of the collection semi-angle (the aperture of the EELS detector, see Figure 3-8 and Sec. 4.d.2) for which the spectrum does not depend on the sample to beam orientation. This may sound rather exotic, but the magic angle is an interesting quantity for at least two reasons :

- * It allows one to avoid the complication of orientation dependence from measurements of an anisotropic sample, greatly simplifying interpretation.
- * It is a quantity that is independent of any material properties, but is fully determined by the fundamentals of the inelastic scattering process. As such, it provides great insight into scattering fundamentals, and makes an excellent test for scattering calculations, as one cannot hide behind the usual deficiencies in the description of excited electron states.

In fact, the magic angle depends only on the beam energy, the energy loss, and the convergence semi-angle.

In this chapter, we explore several questions :

- * What is the classic, non-relativistic treatment of the magic angle? (Sec. 4.f.1)
- * How do experiments compare? (Sec. 4.f.2)
- * What improvements can be considered within the non-relativistic theory? (Sec. 4.f.3)
- * What is the relativistic treatment of the magic angle? (Sec. 4.f.4)
- * Can TELNES2 and FEFF reproduce the correct magic angle? (Sec. 4.f.5)

As a system of interest, we choose again the carbon K edge of graphite, perhaps the most well known anisotropic system. We will work at a convergence angle α of 0 mrad. It is trivial to generalize this to nonzero values in computer calculations, but complicates the algebra tremendously, providing very little illumination in return.

4.f.1. Non-relativistic calculation of the magic angle.

We work at zero convergence angle (i.e., parallel illumination). We use the formalism described by Nelhiebel et al.³⁴ Within the dipole selection rule, the double differential cross section of a K edge is given by

$$\frac{d^2\sigma}{d\Omega'dE}(\mathbf{q}) = \frac{4\gamma^2}{a_0^2} \frac{k'}{k} 8\pi q^{-4} \sum_{\mu,\mu'=-1}^{+1} (-1)^{\mu-\mu'} Y_{1\mu}^*(\Omega) Y_{1\mu'}(\Omega) \langle j_1(q) \rangle_{01}^2 dos_{1\mu'}^{1\mu'}(E) \quad (4.6.1)$$

where γ is the relativistic factor, a_0 the Bohr radius, Y_{lm} the spherical harmonics, j_l the spherical Bessel functions of the first kind, the notation between brackets the matrix element between initial and (part of the) final state, dos the generalized partial density of states (dependent on the sample to beam orientation), (q, Ω) the coordinates of \mathbf{q} , and

(k', Ω) and (k, Ω_k) the coordinates of \mathbf{k}' and \mathbf{k} in the laboratory frame. \mathbf{q} is the impulse transfer, and $\langle j_l \rangle$ the matrix element. For the sake of clarity, we ignore cross-terms in the DOS. This approximation does not affect our results in any substantial way. This reduces (4.6.1) to

$$\frac{d^2\sigma}{d\Omega' dE}(\mathbf{q}) = \varepsilon q^{-4} \sum_{\mu=-1}^{+1} |Y_{1\mu}(\Omega)|^2 \langle j_1(q) \rangle_{01}^2 dos_{1\mu}(E) \quad (4.6.2)$$

where dos is now the regular partial density of states. Now assuming the matrix element to be linear in q (i.e., approximating j_1 by a linear function), and writing the spherical harmonics explicitly, we get

$$\frac{d^2\sigma}{d\Omega' dE}(\mathbf{q}) = \varepsilon q^{-2} \left((dos_{11} + dos_{1-1}) \frac{3}{8\pi} \sin^2 \theta + dos_{10} \frac{3}{4\pi} \cos^2 \theta \right) \quad (4.6.3)$$

We follow the convention where the spherical harmonics are normalized. We now choose the z-axis of our coordinate system parallel to the incoming beam, that is, $\Omega_k = (0,0)$. By definition $\mathbf{q} = \mathbf{k} - \mathbf{k}'$, and therefore

$$\begin{aligned} q^2 &= k^2 + k'^2 - 2kk' \cos \theta' \\ \cos \theta &= \frac{k - k' \cos \theta'}{q} & \sin \theta &= \frac{k' \sin \theta'}{q} \end{aligned} \quad (4.6.4)$$

In practise, the signal is integrated over the detector plane to yield a total cross section $I(E)$:

$$\begin{aligned} I_\beta(E) &= \int_0^{2\pi} d\phi' \int_0^\beta d\theta' \sin \theta' \frac{d^2\sigma}{d\Omega' dE}(\mathbf{q}) \\ &= \varepsilon \int_0^\beta d\theta' \sin \theta' q^{-2} \left(D_\sigma \frac{3}{8\pi} \frac{k'^2 \sin^2 \theta'}{q^2} + D_\pi \frac{3}{4\pi} \frac{(k - k' \cos \theta')^2}{q^2} \right) \end{aligned} \quad (4.6.5)$$

The notations σ (sum of 11 and 1-1 component) and π (10 component) simply refer to a decomposition of the density of states in spherical harmonics in the laboratory frame ; they do not coincide with our intuitive understanding of these terms, as the graphite crystal may be tilted relative to the lab frame. Both the D functions and q itself depend on the energy E.

As all angles are small (\sim mrad), we can make approximations :

$$\begin{aligned} q^2 &\approx k^2 (\theta_E^2 + \theta_{sc}^2) & \sin \theta' &\approx \theta' & \sin^2 \theta' &\approx \theta'^2 \\ \cos \theta' &\approx 1 - \theta'^2 / 2 & \cos^2 \theta' &\approx 1 - \theta'^2 \end{aligned} \quad (4.6.6)$$

In our setup, the scattering angle θ_{sc} is equal to θ' . The characteristic scattering angle θ_E is defined as

$$\theta_E = \frac{\Delta E}{E} \frac{E + m_0 c^2}{E + 2m_0 c^2} \approx \frac{\Delta E}{2E} \quad (m_0 c^2 = 511060 eV) \quad (4.6.7)$$

The approximation in the last term of (4.6.7) is not very accurate and is in general undesirable. For the experiment we will describe later, $E=300$ keV and $\Delta E=295$ eV,

$$\theta_E = 0.5 \text{ mrad (nonrelativistic)} ; \theta_E = 0.6 \text{ mrad (relativistic)} \quad (4.6.8)$$

However, making the approximation (4.6.6) implies that we are actually using the value

$$\theta_E^2 \approx \left(\frac{z-1}{z} \right)^2 \left(1 + \frac{\theta^2 z}{z-1} \right) \Rightarrow \theta_E \approx \left(\frac{z-1}{z} \right) = \frac{\Delta E}{E} \left(1 - \frac{k'}{k+k'} \right) \approx \frac{\Delta E}{2E} \quad ; \quad z = \frac{k}{k'} \quad (4.6.9)$$

So, we have implicitly resigned to the non-relativistic approximation for the characteristic angle. This is important, as we will obtain a result for the magic angle in units of the characteristic angle, and we need to be able to convert it to hard numbers. Near the threshold of the C K edge at 300 keV beam energy, $z \approx 1.0005$.

Now let us specify the crystal to beam orientation by the parameter γ and add it as a label to the partial DOS.

Equation (4.6.5) now becomes

$$I_\beta(E) = \varepsilon \int_0^\beta d\theta' \theta' (\theta_E^2 + \theta_{sc}^2)^{-2} (D_\sigma(\gamma) k'^2 \theta'^2 + 2D_\pi(\gamma) (q^2 - k'^2 \theta'^2)) \quad (4.6.10)$$

We calculate two integrals

$$\begin{aligned} \int_0^b \frac{x dx}{(x^2 + a^2)} &= \frac{1}{2} \ln \left(\frac{a^2 + b^2}{a^2} \right) \\ \int_0^b \frac{x^3 dx}{(x^2 + a^2)^2} &= \frac{1}{2} \ln \left(\frac{a^2 + b^2}{a^2} \right) - \frac{b^2}{2(a^2 + b^2)} \end{aligned} \quad (4.6.11)$$

and therefore

$$\begin{aligned} I_\beta(E) &= D_\pi(\gamma) \pi_\beta + D_\sigma(\gamma) \sigma_\beta \\ \sigma_\beta &= \frac{k'^2}{2} \left[\ln \left(\frac{\theta_E^2 + \beta^2}{\theta_E^2} \right) - \frac{\beta^2}{\theta_E^2 + \beta^2} \right] \quad \pi_\beta = k'^2 \ln \left(\frac{\theta_E^2 + \beta^2}{\theta_E^2} \right) - 2\sigma_\beta \end{aligned} \quad (4.6.12)$$

Finally, we must have a closer look at the orientation dependence of the experiment by introducing a set of Euler angles $\boldsymbol{\gamma} = (\gamma_1, \gamma_2, \gamma_3)$ giving the transformation between two Cartesian frames, one related to the laboratory coordinate system, the other related to the crystal coordinate system. The partial DOS in the crystal frame has a natural and intuitive meaning in that π and σ mean what they usually mean.

The spherical harmonics of first order ($l = 1$) transform as follows :

$$\begin{pmatrix} Y_{1-1} \\ Y_{10} \\ Y_{11} \end{pmatrix} = \begin{pmatrix} e^{-i(\gamma_1 + \gamma_3)} (1 + \cos \gamma_2) / 2 & -e^{-i\gamma_1} \sin \gamma_2 / \sqrt{2} & e^{i(\gamma_3 - \gamma_1)} (1 - \cos \gamma_2) / 2 \\ e^{-i\gamma_3} \sin \gamma_2 / \sqrt{2} & \cos \gamma_2 & -e^{i\gamma_3} \sin \gamma_2 / \sqrt{2} \\ e^{-i(\gamma_3 - \gamma_1)} (1 - \cos \gamma_2) / 2 & e^{i\gamma_1} \sin \gamma_2 / \sqrt{2} & e^{i(\gamma_1 + \gamma_3)} (1 + \cos \gamma_2) / 2 \end{pmatrix} \begin{pmatrix} Y_{1-1}(\boldsymbol{\gamma}) \\ Y_{10}(\boldsymbol{\gamma}) \\ Y_{11}(\boldsymbol{\gamma}) \end{pmatrix} \quad (4.6.13)$$

where the left hand array is the crystal frame, and the right hand array is the lab frame. The coefficients of an expansion into spherical harmonics transform the opposite way (i.e., using the inverse of the matrix in (4.6.13)), and the partial DOS is a product of two such coefficients. Therefore, the direct DOS-terms transform as

$$\begin{aligned} D_\pi(\boldsymbol{\gamma}) &= |C_{10}(\boldsymbol{\gamma})|^2 = \frac{\sin^2 \gamma_2}{2} D_\sigma + \cos^2 \gamma_2 D_\pi + \sqrt{2} \sin \gamma_2 \cos \gamma_2 \operatorname{Re} \left[e^{i\gamma_3} (C_{10}^* C_{11} + C_{10} C_{1-1}^*) \right] \\ &\quad - \sin^2 \gamma_2 \operatorname{Re} \left[e^{2i\gamma_3} C_{11}^* C_{1-1} \right] \end{aligned} \quad (4.6.14)$$

$$\begin{aligned} D_\sigma(\boldsymbol{\gamma}) &= |C_{1-1}(\boldsymbol{\gamma})|^2 + |C_{11}(\boldsymbol{\gamma})|^2 = \sin^2 \gamma_2 D_\pi + \frac{1 + \cos^2 \gamma_2}{2} D_\sigma + \sin^2 \gamma_2 \operatorname{Re} \left[e^{2i\gamma_3} C_{11} C_{1-1}^* \right] \\ &\quad - \sqrt{2} \sin \gamma_2 \cos \gamma_2 \operatorname{Re} \left[e^{i\gamma_3} (-C_{10}^* C_{11} + C_{10} C_{1-1}^*) \right] \end{aligned}$$

We remark that graphite has sufficiently high enough symmetry that the cross-terms would cancel in the crystal frame, simplifying (4.6.14). Cross-terms in the lab frame, which we have not calculated here, would definitely be non-zero for graphite.

We also remark that the first and third Euler angle simply add phase factors to the cross terms.

At last, we can complete equation (4.6.12) :

$$\begin{aligned}
I_{\beta}(E) &= D_{\pi}(\gamma)\pi_{\beta} + D_{\sigma}(\gamma)\sigma_{\beta} \\
&= D_{\pi}(\pi_{\beta} \cos^2\gamma_2 + \sigma_{\beta} \sin^2\gamma_2) + D_{\sigma} \left(\frac{\pi_{\beta} \sin^2\gamma_2 + \sigma_{\beta}(1 + \cos^2\gamma_2)}{2} \right) \\
&\quad + \left(-\sqrt{2} \sin\gamma_2 \cos\gamma_2 \operatorname{Re} \left(e^{i\gamma_3} (C_{10}^* C_{11} + C_{10} C_{1-1}^*) \right) + \sin^2\gamma_2 \operatorname{Re} \left(e^{2i\gamma_3} C_{11}^* C_{1-1} \right) \right) (\sigma_{\beta} - \pi_{\beta})
\end{aligned} \tag{4.6.15}$$

At the magic angle β^* , the spectrum $I(E)$ should be independent of the orientation of the sample, that is, independent of γ . Eq. (4.6.15) shows how to achieve this. We demand

$$\sigma_{\beta} = \pi_{\beta} \tag{4.6.16}$$

Using (4.6.12) and approximating $k = k'$ (the energy loss is much smaller than the beam energy), we quickly find

$$\frac{3x^2}{1+x^2} = \ln(1+x^2) \quad (x = \beta^* / \theta_E) \tag{4.6.17}$$

This equation has exactly one solution at x approximately equal to 3.975. At this solution, for a 300 keV beam and 295 eV energy loss, (4.6.15) reduces to

$$I_{\beta^*}(E) = (D_{\pi} + D_{\sigma} / 2) 1.887 k^2 \tag{4.6.18}$$

Remark that the magic angle does not depend on any material property. It is fully defined by the energy of the probe and the energy loss.

In reality, we never measure the ELNES signal of one atom, but the integrated intensity from a lot of atoms, e.g. in a crystal. This total measured signal is simply the sum of every atom's individual ELNES spectrum. These spectra differ in the partial DOS – either because atoms are intrinsically different (e.g., different element, or (as in graphite) inequivalent atoms of the same species), or because they are oriented differently with respect to the electron beam. Nevertheless, every one of them is orientation insensitive at the magic angle condition (4.6.16) and therefore the sum of their spectra is also. In the case of graphite, the measured signal will consist of four terms like (4.6.18) which are equal two by two.

The theoretical "x=4" result of this chapter has been published by several authors^{32,101,102}. (Note : the last reference contains a trivial mistake in the derivation, which corrects the reported x=1.36 to the x=4 found above.)

4.f.2. Experimental measurements of the magic angle.

Experimental measurements tend to disagree with the theoretical prediction $x = 4$, and the discrepancies are far from subtle. Daniels et al.¹⁰³ measured a magic angle for BN, graphite and MgB₂ at 200 keV beam energy and found it to be close to $x = 2.1$. (In the same paper, they present a non-relativistic theoretical derivation arriving at the same result, but it is nonsensical and should be ignored.)

For the C K edge, Hébert measured a magic angle of $x = 1.46$ at 200 keV beam energy, and a magic angle of $x = 2.04$ at 120 keV beam energy.¹⁰⁴

We present experimental results by Radtke et al.¹⁰⁵ for the magic angle of graphite at 300 keV beam energy. Experiments are performed on a Jeol 3000F operating at 300kV with a GIF 2000 EELS spectrometer operating in diffraction mode. The sample consists of a HOPG polycrystalline graphitic sample. Single crystalline grains are selected by the electron beam. Almost parallel illumination was chosen (convergence angle < 0.2 mrad) to avoid the combined effect of collection and convergence angle.

The experiment consists of collecting the C-K ELNES for different collection angles and for zone axis and out of zone axis orientation. By definition the ELNES spectra for both orientations should be the same when the collection angle approaches the magic angle.

Figure 4-7 presents the results of this experiment for zone axis orientation and for approximately 30° away from zone axis. The spectra are background removed and deconvoluted with the low loss spectrum to remove the effect of plural scattering. Figure 4-7 shows clearly the effect of orientation and collection angle on the fine structure details of the C-K edge. It also shows that there is a certain range of collection angles where the fine structure is almost independent on orientation.

For this experiment, the magic angle is approached for camera lengths close to 80 cm and a GIF entrance aperture of 3mm. This can be converted into a collection angle making use of a calibration table. The magic angle is then found to be close to 0.68 mrad.

These results agree with the detailed experiments of Daniels et al.¹⁰³ and Hébert¹⁰⁴ in the sense that the magic angle is much smaller than the expected $4 \theta_E$.

The weak point of this experiment lies in the fact that the results depend on calibration, which may be unreliable, and in the fact that we get very little information about the reason for the discrepancy between theory and experiment. The same is true for the experiments by Daniels and Hébert referenced earlier.

A second experiment is performed to investigate the details of the discrepancy between the theoretical and experimental magic angle.¹⁰⁵ A series of energy filtered diffraction

patterns is recorded with a energy selecting slit of approximately 2 eV over an energy range covering the C K-edge in increments of 2eV. The obtained series of inelastic diffraction patterns allows a detailed study of the angular dependence of scattering of the different energy regions of the C K-edge. The series was background subtracted to obtain an approximation of the angular distribution of the C K-excitation without background. Figure 4-8 shows 4 selected diffraction patterns from the series. Figure 4-8A shows the angular distribution in the background preceding the C K-edge, Figure 4-8B shows the angular distribution of the π^* feature in the background subtracted fine structure, Figure 4-8C shows the angular distribution in the $\pi^*+\sigma^*$ region and Figure 4-8D shows the distribution in a region of the tail of the edge. Fig 3 also shows the radial distribution around the centre of the patterns. The observed patterns fit qualitatively with the expectation that before the edge and far way from the onset of the edge, the pattern should be a simple Lorentzian while for the π^* feature a more forward scattered distribution is expected and the $\pi^*+\sigma^*$ region is expected to show a ring-like scattering pattern due to the presence of the σ^* contribution. Simulations show that when the sample is tilted, the ring like pattern in the $\pi^*+\sigma^*$ region becomes asymmetric in qualitative agreement with experiment.

Analytical expressions for the scattering behaviour in the different regions can be obtained from dipole scattering theory for a single carbon atom. These theoretical curves are also shown in Figure 4-8 and lead to the conclusion that there is a quantitative discrepancy between the experimental curves and the theoretical curves.¹⁰⁵ If the calibration is chosen in a way that the Lorentzian profile agrees with observed profile before and after the edge, one sees that the observed π^* feature is much more confined to smaller angles than expected from theory. The observed discrepancy is at least a factor of 1.6.

Multiple scattering could cause the Lorentzian parts to be broader than expected but the effect should be small since the angular distribution of e.g. a plasmon is very small.

It seems that this experiment demonstrates a fundamental problem between the simple scattering theory and the experiment which could be of importance for simulation of EELS spectra in general.

It is important to note that this last experiment can not be explained away by calibration problems unlike the first experiment, which is important since calibration problems would be a possible source of a discrepancy between experiment and theory in the determination of the magic angle.

In conclusion of the experimental part, two observations are important:

1. The observed magic angle in EELS is $\sim 1 \theta_E$ in contrast to the predicted $4 \theta_E$.
2. The observed scattering angles in the π^* feature of the C K-edge are considerably smaller than predicted.

The second observation contains already a powerful hint towards the reason for this discrepancy since angular distributions are a more direct result of theory as compared to the magic angle.

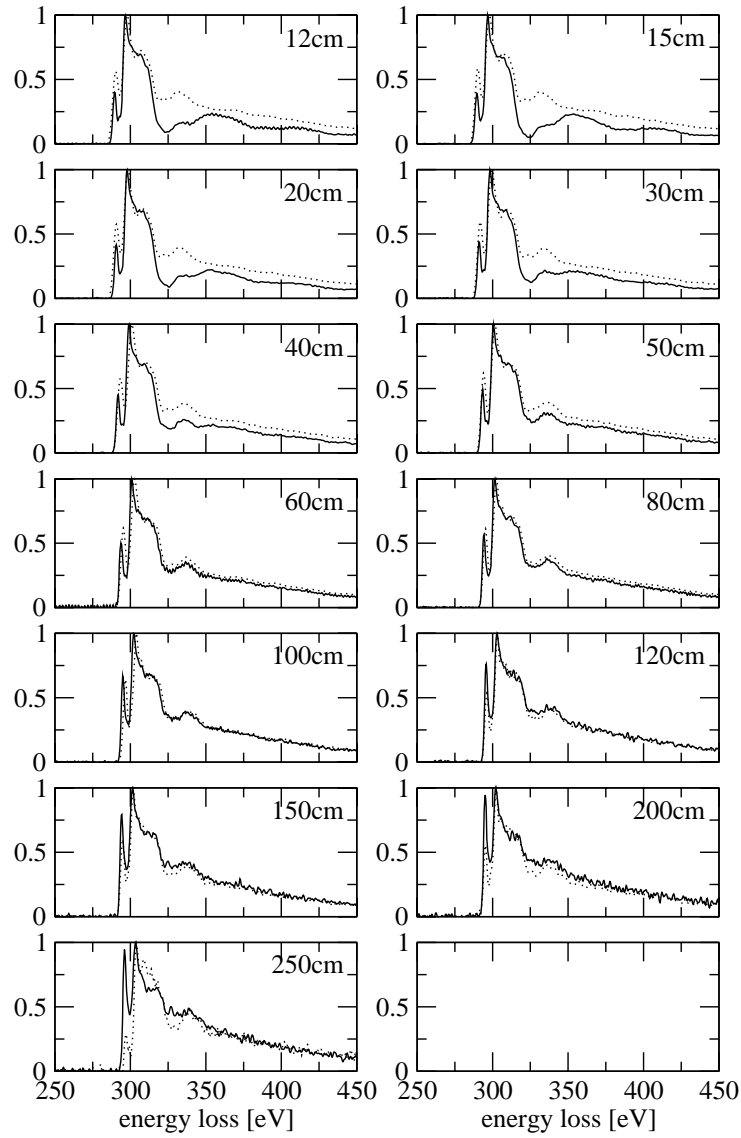


Figure 4-7: C K-ELNES for zone axis conditions (full line) and tilted approx. 30 degrees away (dashed) for 13 different nominal camera lengths (12 cm – 250 cm). The magic angle occurs around 80 cm camera length which translates into a collection angle of 0.68 mrad which is close to $1 \theta_E$. Radtke et al.¹⁰⁵

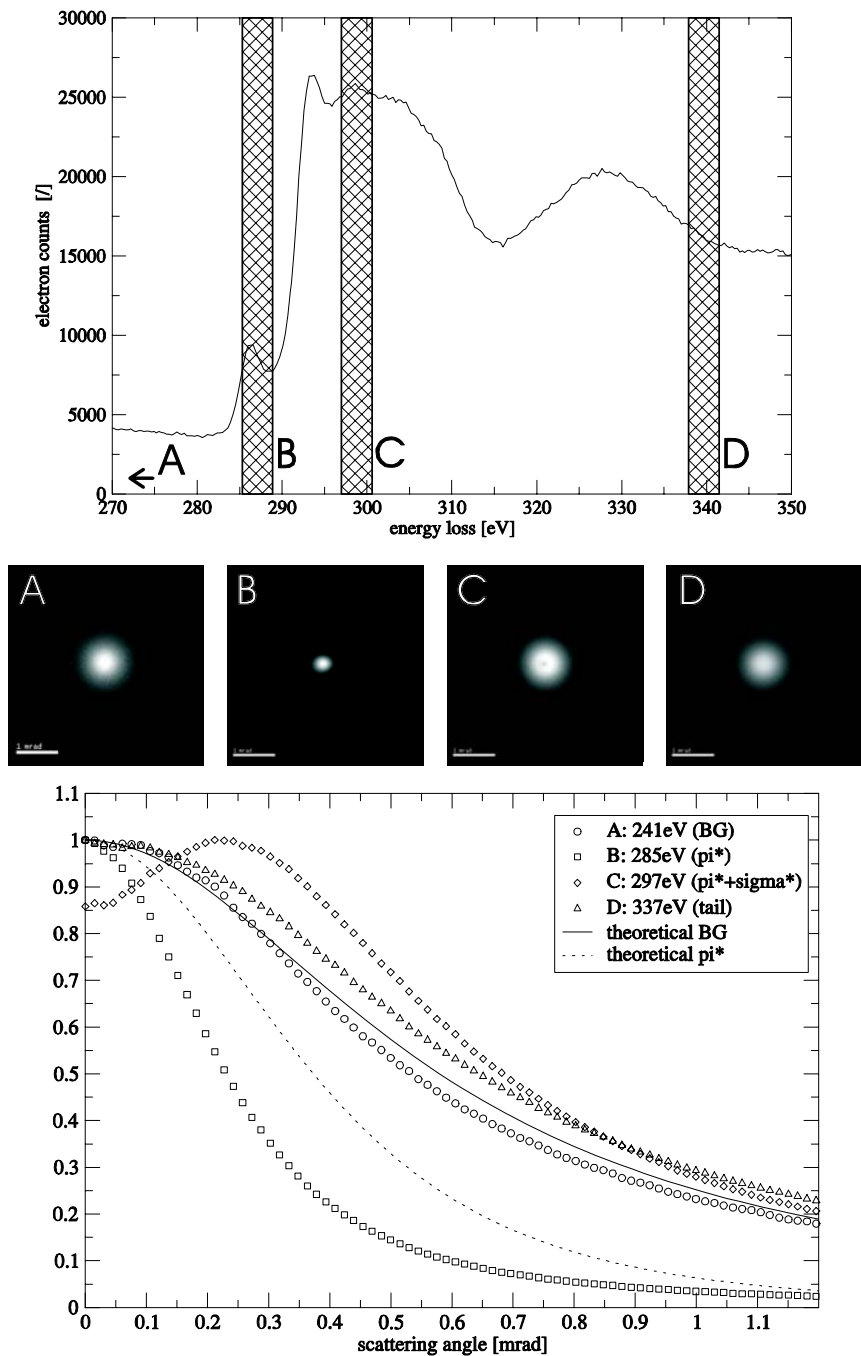


Figure 4-8 Angular distribution of inelastic scattering at different energies in the carbon K edge of HOPG graphite, from Radtke et al.¹⁰⁵

4.f.3. Improvements within the non-relativistic theory?

Of course, we have already discussed the importance of relativistic corrections to rectify the magic angle fiasco. However, it is worthwhile reviewing a few approximations made in 4.f.1 and investigating their impact on the (non-relativistic) magic angle. This way, we eliminate possible sources of errors in the theoretical prediction of the magic angle.

4.f.3.1 Non-dipole contributions.

The dipole selection rule is not a dogma. It can be violated.

Let us look first at *monopole contributions*. To take these into account, an additional term must be inserted into (4.6.3) :

$$\text{monopole term} = \varepsilon q^{-4} \frac{2}{4\pi} \text{dos}_{00} \langle j_0(q) \rangle_{00}^2 \quad (4.6.19)$$

where ε contains all unwritten prefactors. Obviously, the s-DOS dos_{00} is rotation invariant, and therefore cannot contribute to the magic angle. We can safely ignore term monopole contributions when it comes to the magic angle.

Let us move on to *quadrupole transitions*. They are absolutely negligible in numerical simulations of the C K edge. To better understand the (un)importance of quadrupole transitions to the spectrum, we compare the matrix elements and final state DOS of quadrupole and dipole transitions in Figure 4-9.

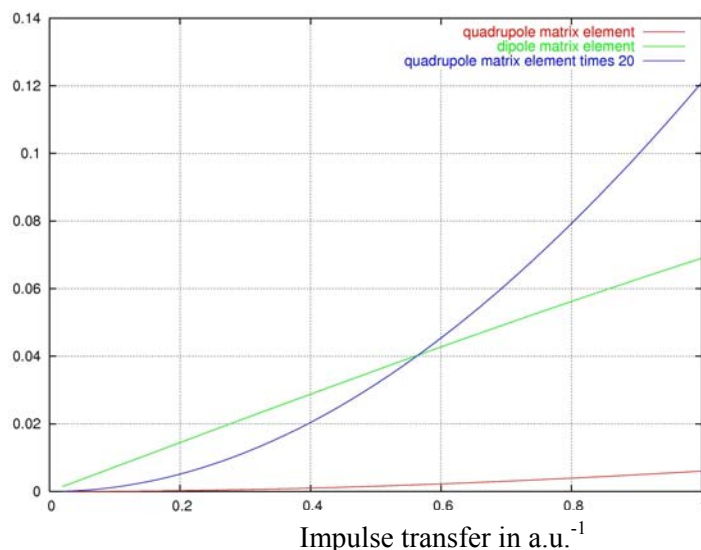


Figure 4-9 Matrix elements of the graphite C K edge as defined by the top integral in Eq. (4.3.26) (See also text). Dipole matrix element in green, quadrupole matrix element in red, and quadrupole matrix element multiplied by a factor of 20 shown in blue.

It is important to realize that the matrix element shown here is simply the radial integral of the initial and final state wave functions and the spherical Bessel function (first integral of Eq. (4.3.26)). It needs to be multiplied by the Coulombic prefactor of q^{-4} and the DOS in order to build the cross-section.

Only for a very large aperture/collection angle will the quadrupole matrix element become comparable to the dipole matrix element. If we assume $\alpha+\beta = 3$ mrad at 300 keV beam energy and 300 eV energy loss, q is about 0.3 au^{-1} , and the quadrupole matrix element is at least 20 times smaller than the dipole matrix element. The Coulombic prefactor q^{-4} makes the small q region, where the difference is even far larger, dominant in the cross section. This leads to a total suppression of quadrupole signal in the cross-section, unless one moves the detector away from the 000-spot. Quadrupole transitions are of no importance for the study of the magic angle in graphite.

In the π region, there is hardly any d-DOS (Figure 4-10). The d-DOS (which corresponds to quadrupole transitions from the 1s core state) closely follows the s-DOS and can, in the σ region, be approximated very roughly as half the s-DOS.

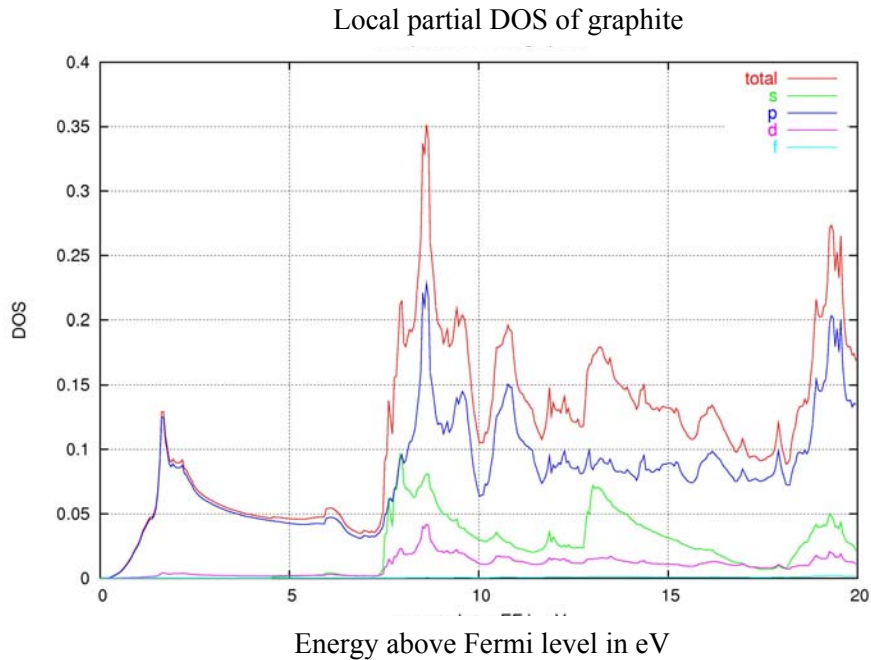


Figure 4-10 Local partial DOS of graphite : s-DOS (green), p-DOS (dark blue), d-DOS (pink), f-DOS (light blue) and total local DOS (red).

If we still wanted to study quadrupole contributions, Eq. (4.6.2) can be generalized to

$$\frac{d^2\sigma}{d\Omega'dE}(\mathbf{q}) = \varepsilon q^{-4} \sum_l \sum_{\mu=-l}^{+l} |Y_{l\mu}(\Omega)|^2 \langle j_l(q) \rangle_{0l}^2 dos_{l\mu}(E) \quad (4.6.20)$$

The terms we have investigated before correspond to $l = 0$ (monopole or s term) and $l = 1$ (dipole or p term); $l = 2$ describes the quadrupole or d term transition. Knowing that

$$j_2(x) = \left(\frac{3}{x^3} - \frac{1}{x} \right) \sin(x) - \frac{3}{x^2} \cos(x) \quad (4.6.21)$$

$$\lim_{x \rightarrow 0} j_2(x) = a x^2$$

as can be seen from a Taylor expansion of $\sin x$ and $\cos x$, the factor q^{-4} cancels from (4.6.20) and the angular behaviour of the quadrupole term is determined uniquely by the spherical harmonics (in the range of q where the quadratic description is appropriate). Naming the quadrupole contribution Q , we find

$$Q = \varepsilon \left[\frac{15}{32\pi} \sin^4 \theta_q (dos_{2-2} + dos_{22}) + \frac{15}{8\pi} \sin^2 \theta_q \cos^2 \theta_q (dos_{2-1} + dos_{21}) + \frac{5}{16\pi} (9 \cos^4 \theta_q - 6 \cos^2 \theta_q + 1) dos_{20} \right] \quad (4.6.22)$$

where, similarly to section 1, the D are defined in a frame fixed to the beam and not to the sample (in other words, they are orientation dependent), and θ_q is the coordinate of the scattering vector \mathbf{q} , and not the scattering angle.

Now one can proceed as we have done for the dipole terms – rotating the partial DOS and integrating the goniometric functions up to the collection angle β . The algebra is tedious and not instructive. It is quite clear from the results, which I will not show here, that the occurrence of significant quadrupole character in the spectrum would prohibit the existence of a magic angle. There is no way of integrating the cross section over impulse transfer that would cancel out the more complex orientation dependence of the quadrupole terms. If quadrupole terms contributed to the cross section at all, there most likely wouldn't be a magic angle at any value of the collection semi-angle.

4.f.3.2 Cross-terms.

Cross terms corresponding to generalized cross DOS also contribute to the spectrum – indeed, (4.6.1) certainly allows them. Cross terms are terms for which either l and l' or μ and μ' are different. However, these terms will depend on the angle ϕ as

$$e^{i(\mu-\mu')\phi} \quad (4.6.23)$$

When calculating a differential cross-section, we integrate this factor over ϕ as in(4.6.5), so a condition for cross terms to contribute is

$$\mu - \mu' = 0 \quad l \neq l' \quad (4.6.24)$$

(if the second condition were not fulfilled, the term would be direct). If $\alpha > 0$ and $\phi = \phi'$ no longer holds, this argument no longer strictly holds.

In the case of graphite and parallel illumination, only the ($l=0, \mu=0, l'=1, \mu'=0$) cross term still has to be considered. Investigating its angular behaviour, one can see that it would destroy the magic angle if it contributed significantly. However, numerical simulations again show this cross-term to be negligible (less than 10^{-3} of the total spectrum) for the experiment we are investigating.

It is worth remembering that cross-terms may be bigger in other materials, and that their amplitude may depend on orientation.

4.f.3.3 Beyond the small q approximation.

In Sec. 4.f.1, we just assumed linearity in q of the matrix element containing the initial state and final state radial wave functions and the spherical Bessel function. We repeat the definition of the matrix element :

$$\langle j_\lambda(q) \rangle_{0\lambda}^E = \int_0^{+\infty} dr u_{1s}(r) u_\lambda^E(r) j_\lambda(rq) r^2 \quad (4.6.25)$$

containing in the integral from left to right: the 1s radial wave function, the radial (valence) basis function of orbital quantum number λ of energy E above threshold (Sec. 4.d.1), and the spherical Bessel function of order λ .

In the figure below we show the matrix element for $\lambda = 1$ as a function of q (in au^{-1}).

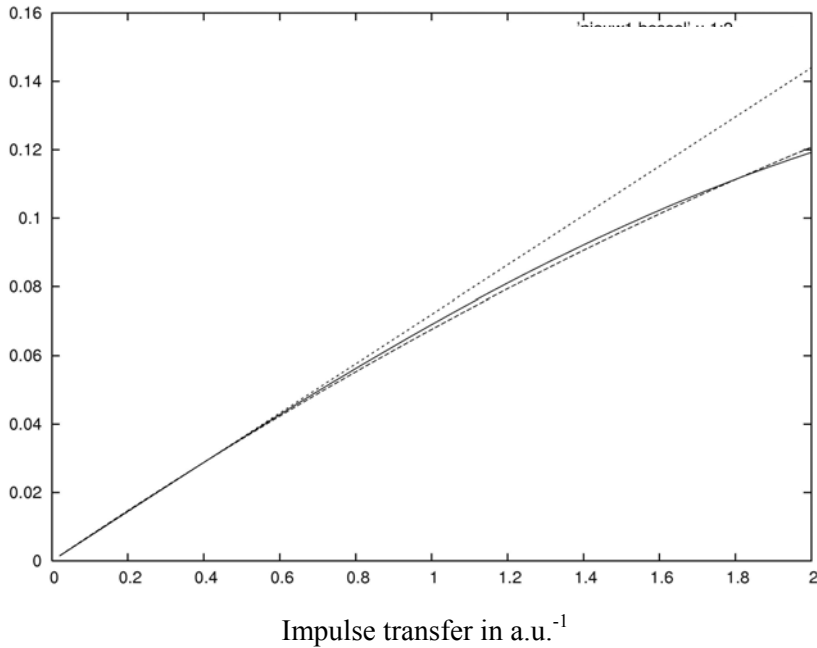


Figure 4-11 Dipole matrix element (full line) of the graphite C K edge as a function of impulse transfer in a.u.^{-1} , and a linear (dots) and a quadratic (dash) fit

In Figure 4-11, the matrix element for 2 eV above threshold is fitted both to a linear and a quadratic function. Up to about 0.8 au^{-1} , the linear approximation holds rather well. Up to 2 au^{-1} , the quadratic fit is good. The fitting coefficients depend on energy.

Repeating the calculations of Sec. 4.f.1 using a quadratic approximation for the matrix element :

$$\langle j_1(q) \rangle_{01} \sim q + aq^2 \quad (4.6.26)$$

Eq. (4.6.10) is now replaced by

$$I_\beta(E) = \varepsilon \int_0^\beta \theta' \left[(\theta_E^2 + \theta_{sc}^2)^{-2} + 2ak(\theta_E^2 + \theta_{sc}^2)^{-3/2} + a^2k^2(\theta_E^2 + \theta_{sc}^2)^{-1} \right] \\ \left(D_\sigma(\gamma)k'^2 \theta'^2 + 2D_\pi(\gamma)(q^2 - k'^2 \theta'^2) \right) d\theta' \quad (4.6.27)$$

Collecting all terms, and proceeding exactly as in Sec. 4.f.1 (i.e., writing the total spectrum as a sum of π and σ component – only the coefficients have changed), we again write (4.6.16), which now gets more complicated.

$$\ln(1+x^2)(1-3(ak\theta_E)^2) = \frac{3x^2}{1+x^2} - x^2(ak\theta_E)^2 + 16ak\theta_E - 4ak\theta_E \frac{(x^2+4)}{\sqrt{1+x^2}} \quad (4.6.28)$$

For $a=0$, (4.6.28) reduces to (4.6.17). The value of a depends on the fitting region; e.g. for graphite in the interval [0.1:0.5] we find the best fit for $a=-0.0391$, somewhat varying with energy loss. In this study we limit the scattering angle to about 3 mrad, which implies q does not increase above 0.52 au^{-1} . In this region, the linear approximation is quite good, and the small a -coefficient results in a small correction to the magic angle.

The solution of (4.6.28) is in $x = 4.010$ for our current case, a correction of less than 1% of the previous results.

For cross sections involving larger q , the corrections to the small q approximation become larger. However, for the non-relativistic magic angle this is not an issue.

4.f.3.4 Beyond the small angle approximation.

In all previous sections, small angles approximations were made (see (4.6.6)). Instead of evaluating Eq. (4.6.10), we now calculate the exact integral (4.6.5). The final equation is now

$$(z^2-3)(1+tg^2(\beta/2))((z+1)^2tg^2(\beta/2)+(z-1)^2) \ln \left(\frac{((z+1)^2tg^2(\beta/2)+(z-1)^2)}{(z-1)^2(1+tg^2(\beta/2))} \right) \\ = -12z tg^2(\beta/2) (z^2+1+tg^2(\beta/2)(z+1)^2) \quad ; \quad z = k/k' \quad (4.6.29)$$

At 15 eV above the graphite K threshold, $c = 1.0005$. We find $\beta^* = 1.991 \text{ mrad}$, i.e., $x \approx 4$ (considering that we used the non-relativistic characteristic angle in f.1). The correction we found by going beyond the small angle approximation is virtually zero.

4.f.3.5 Conclusion.

All of the approximations we looked at – non-dipole transitions, cross terms, the small angle approximation, and the small q approximation – have close to no impact on the theoretical non-relativistic magic angle. They offer no explanation whatsoever for the observed discrepancies between experiment and theory.

4.f.4. Relativistic calculation of the magic angle.

In this section, we will generalize section 4.f.1 by including relativistic theory. That is, we replace (4.6.1) by (4.3.27), which we repeat here for convenience :

$$\begin{aligned}
\frac{\partial^2 \sigma}{\partial E \partial \Omega}(E, \mathbf{q}) = & \frac{4\gamma^2 a_0^{-2}}{\left(q^2 - (E/\hbar c)^2\right)^2} \frac{k'}{k} 2(4\pi)^2 \left\{ D_\pi \left[\sqrt{\frac{3}{4\pi}} \cos \theta_q \frac{j_{11}^{(1)}}{\sqrt{4\pi}} + \frac{\hbar v_0}{mc^2} \frac{j_{01}^{(2)}}{\sqrt{3}(4\pi)} \right]^2 \right. \\
& + \left(D_\sigma - 2 \operatorname{Re} \left(D_{11}^{1-1} e^{2i\phi_q} \right) \right) \left[\sqrt{\frac{3}{8\pi}} \sin \theta_q \frac{j_{11}^{(1)}}{\sqrt{4\pi}} \right]^2 \\
& \left. + 2 \operatorname{Re} \left(D_{1-1}^{10} e^{-i\phi_q} - D_{11}^{10} e^{i\phi_q} \right) \left[\sqrt{\frac{3}{8\pi}} \sin \theta_q \frac{j_{11}^{(1)}}{\sqrt{4\pi}} \right] \left[\sqrt{\frac{3}{4\pi}} \cos \theta_q \frac{j_{11}^{(1)}}{\sqrt{4\pi}} + \frac{\hbar v_0}{mc^2} \frac{j_{01}^{(2)}}{\sqrt{3}(4\pi)} \right] \right\}
\end{aligned} \tag{4.6.30}$$

Now, we have to rotate the DOS in this expression, integrate the cross section over the collection angle of the microscope, and then impose orientation invariance.

For the rotation of the DOS, we can still use (4.6.14). The relativistic version of (4.6.16), (4.6.12) is now given by

$$\frac{\left(j_{11}^{(1)}\right)^2}{2} \int_{\beta} d\Omega' \frac{\sin^2 \theta_q}{\left(q^2 - (E/\hbar c)^2\right)^2} = \int_{\beta} d\Omega' \frac{\left(j_{11}^{(1)} \cos \theta_q + \frac{\hbar v_0}{3mc^2} j_{01}^{(2)}\right)^2}{\left(q^2 - (E/\hbar c)^2\right)^2} \tag{4.6.31}$$

Rewriting in terms of the scattering angle θ (4.6.4) (we drop the ') and using $E/\hbar c = \beta q \cos \theta_q$ and $v_0 q \cos \theta_q = \omega$ and writing $q \tilde{j}_{11}^{(1)} = j_{11}^{(1)}$ this can be reworked into

$$\frac{1}{2} \int_0^{\beta} d\theta \frac{k'^2 \sin^3 \theta}{q^4 \left(1 - \frac{\beta^2}{q^2} (k - k' \cos \theta)^2\right)^2} = \int_0^{\beta} d\theta \frac{\sin \theta (k - k' \cos \theta)^2 \left(1 + \frac{\hbar v_0^2}{3mc^2 \omega} \frac{j_{01}^{(2)}}{\tilde{j}_{11}^{(1)}}\right)^2}{q^4 \left(1 - \frac{\beta^2}{q^2} (k - k' \cos \theta)^2\right)^2} \tag{4.6.32}$$

Let's now make the small angle approximation (4.6.6), and add a slightly modified version of (4.3.33)

$$\frac{j_{01}^{(2)}}{j_{11}^{(1)}} = -3 \frac{m\omega}{\hbar} f \quad (4.6.33)$$

where f goes to 1 as q goes to 0 and the small q approximation becomes more accurate. f , a number that measures how valid the small q approximation is, can be evaluated numerically by calculating the radial integrals in (4.6.33) explicitly and evaluating their ratio. This can be done using TELNES2. As these radial integrals contain radial functions which are material dependent, some material dependence affects the magic angle beyond the small q approximation through f . In principle f depends on the energy loss E and the impulse transfer q , but for the example studied here, we found this dependence to be negligible.

We can now write for the magic angle β

$$\frac{k'^2}{2} \int_0^\beta d\theta \frac{\theta^3}{(\theta^2 + \theta_E^2)^2 \left(1 - \beta^2 \frac{(k - k' + k'\theta/2)^2}{(\theta^2 + \theta_E^2)} \right)^2} = (1 - f\beta^2)^2 \int_0^\beta d\theta \frac{\theta (k - k' + k'\theta/2)^2}{(\theta^2 + \theta_E^2)^2 \left(1 - \beta^2 \frac{(k - k' + k'\theta/2)^2}{(\theta^2 + \theta_E^2)} \right)^2} \quad (4.6.34)$$

Numerical solutions to (4.6.34) (calculated in Maple) are illustrated in Figure 4-12.

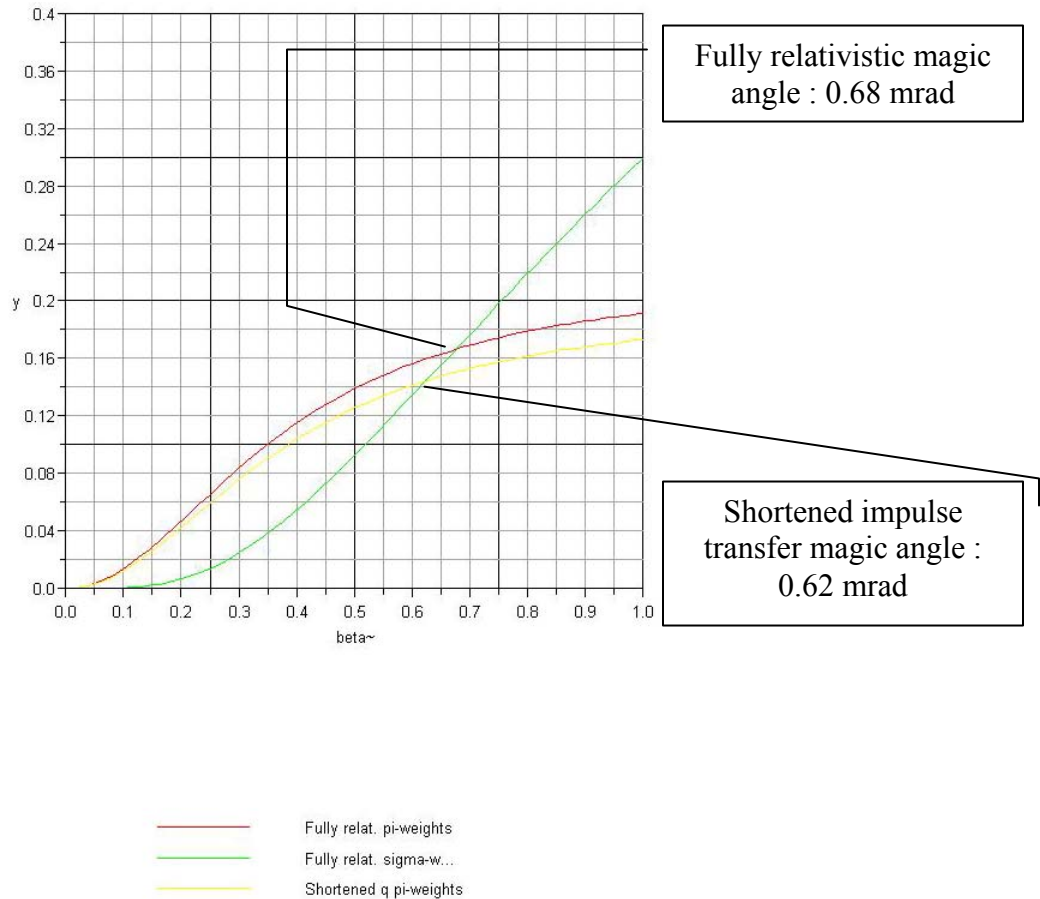


Figure 4-12 Numerical/analytical solution of the magic angle of the graphite C K edge for a 300 keV beam and 295 eV loss. The convergence angle is 0 mrad. The π -weight is the right-hand side of eq. (4.6.34), and the σ -weight is the left-hand side. The magic angle is at the collection angle value (on horizontal scale in mrad) for which they cross. Note that the full formalism gives a different π -curve (red) and hence a different magic angle as compared to the small q approximated “shortened q vector” approach (yellow) of Schattschneider et al. The crucial step is eq. (4.6.33), where $f=1$ recovers the results of Schattschneider et al. However, in the full formalism, f is slightly different from 1. The σ -curves are the same in both approaches (green).

As before, we study a graphite C K edge at 300 keV beam energy and 295 eV energy loss. The magic angle is found where π and σ integrals are equal. Note that Figure 4-12 gives two different π curves. One is calculated assuming that the small q-approximation is valid and $f = 1$, and gives a magic angle of about 0.62 mrad. This corresponds to the work of Schattschneider et al.⁵ or Section 4.b. The other (red) curve uses a correct value for the parameter f of (4.6.33), $f = 0.966$. This value was obtained numerically from TELNES2 calculations, as will be explained in Section 4.f.5. It leads to a magic angle of about 0.68 mrad. The experimental value we found in Section 4.f.2 was ... 0.68 mrad. The non-relativistic theoretical value was 1.99 mrad.

It is now clear that the relativistic EELS theory corrects the prediction of the magic angle and makes it roughly equal to the experimental value. The small q-approximation is

somewhat inaccurate (~10%) even in very common situations – a C K edge at small scattering angles, where the more general l,m formalism we developed here gets the experimental value almost exactly right.

4.f.5. FEFF and TELNES2 calculations of the magic angle.

The ab initio ELNES programs FEFF⁷⁵ and WIEN2k/TELNES2⁷⁰ don't solve (4.6.34), of course ; they calculate the double differential cross section. It would be rather tedious to plot spectra for two sample tilts and for a whole series of collection angles, in analogy with the experiments presented in Sec.4.f.2. Rather, we will calculate the scattering cross section, evaluated at a single energy loss value of 295 eV, integrated up to a collection angle, and then we plot this spectrum as a function of the collection angle for various sample tilts. The magic angle is the collection angle for which all the sample tilts give the same spectrum.

This would be hard to visualize for the integral of the total spectrum, because the differences in the total spectrum between different tilts aren't very large at all values of the energy loss. Since partial spectra and functions of them must also be equal at the magic angle, we plot the π/σ ratio of the spectrum instead of the total spectrum. This ratio is given by the Y_{10} -component of the spectrum divided by the $Y_{11} + Y_{1-1}$ components in the laboratory frame. Equivalently, if working in Cartesian coordinates, it is given by the zz -component divided by the $xx+yy$ components. This quantity is of some interest because it can be linked to the sp^2/sp^3 content of a carbon system.¹⁰⁶

$$\frac{\pi}{\sigma} := \frac{\sigma_{zz}}{\sigma_{xx} + \sigma_{yy} + \sigma_{zz}} \quad (4.6.35)$$

First, we show the results of our FEFF calculations.

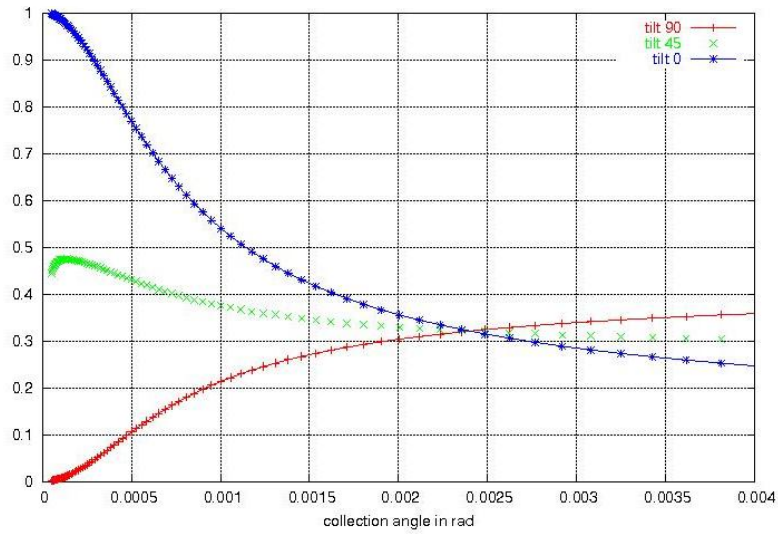


Figure 4-13 Non-relativistic calculation of the π/σ ratio (see text) of the graphite C K edge at 10 eV above threshold for a 300 keV beam and three sample to beam orientations. The magic angle is at the intersection of the three curves (ca. 2.3 mrad). The convergence angle is 0 mrad.

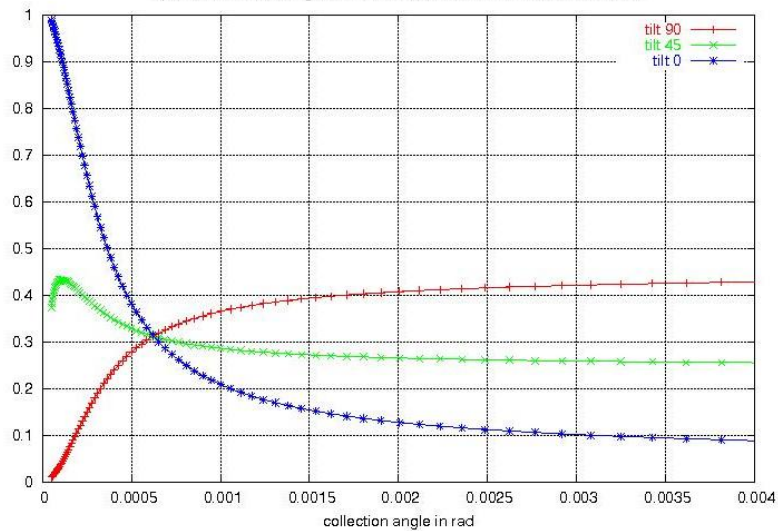


Figure 4-14 Relativistic calculation of the π/σ ratio (see text) of the graphite C K edge at 10 eV above threshold for a 300 keV beam and three sample to beam orientations. The magic angle is at the intersection of the three curves (ca. 0.63 mrad). The convergence angle is 0 mrad.

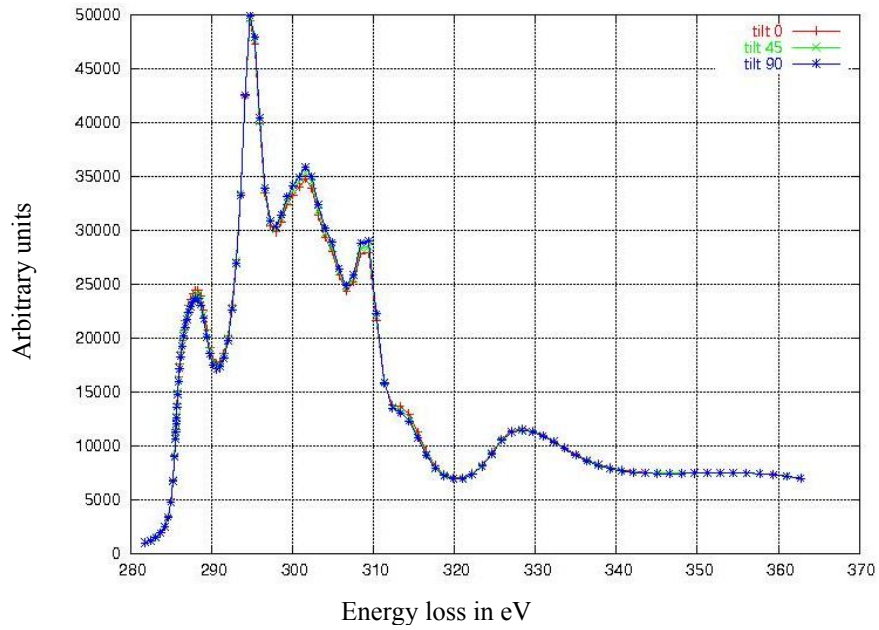


Figure 4-15 C K edge of graphite for 3 orientations, 300 keV beam energy, $\alpha = 0$ mrad, $\beta = 0.6$ mrad. Relativistic calculation.

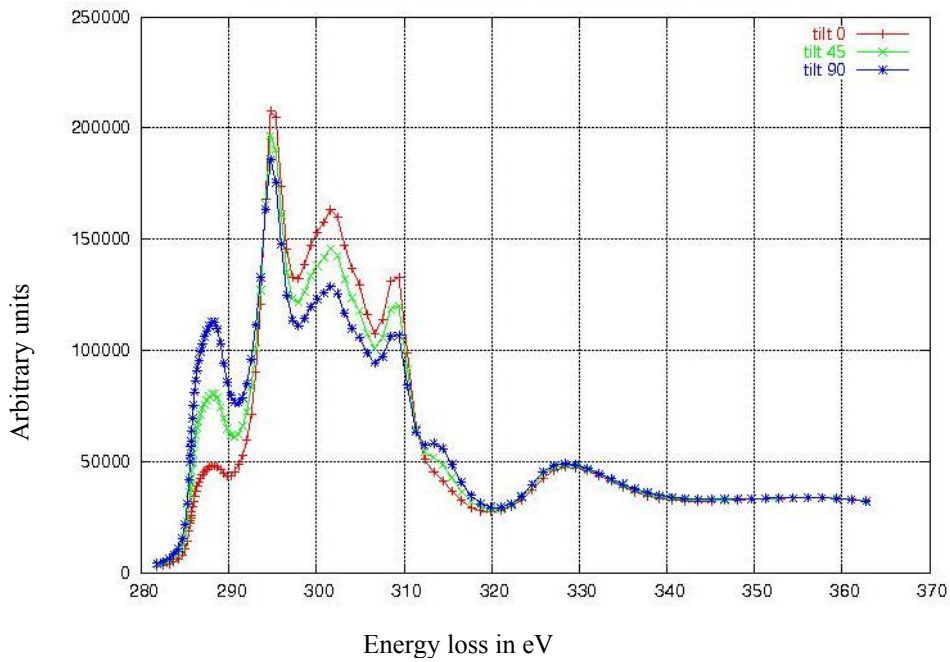


Figure 4-16 Carbon K edge of graphite for 3 orientations, 300 keV beam energy, $\alpha = 0$ mrad, $\beta = 2.4$ mrad. Relativistic calculation.

The FEFF results of Figure 4-13 and Figure 4-14 clearly reproduce our analytic findings of Sec. 4.f.4. The non-relativistic magic angle is about 2.3 mrad, and the relativistic magic angle is 0.63 mrad – quite close to the experimental result of 0.68 mrad.

Because EELS studies tend to work with cross sections as functions of energies rather than the more abstract π/σ ratios shown in Figure 4-13 and Figure 4-14, we also show the effect of relativistic corrections on the spectrum. In Figure 4-15, we show the total C K spectrum, calculated relativistically, at an almost magic collection angle of 0.6 mrad. Clearly, the orientation dependence of the spectrum is all but vanished so close to the magic angle (0.63 mrad for these calculations). In Figure 4-16, we show the same calculations evaluated at the non-relativistically predicted magic angle, and the relativistic calculations clearly show that the spectrum is strongly orientation dependent. If the interpretation of a measurement has been based on the assumption that the spectrum is rotation invariant at the non-relativistic magic angle, or on the assumption that the angle at which the spectrum is found to be rotation invariant equals the non-relativistic prediction, then it is most likely wrong.

We remark again that for isotropic measurements (i.e., experiments on an isotropic material, such as crystals of high symmetry or polycrystalline or amorphous samples, and experiments on anisotropic samples in which one averages over all sample to beam orientations) the errors of the non-relativistic theory are far less grave, as the relativistic correction to the difference in weighing of the π and σ spectra (as represented geometrically by the interpretation of the impulse vector contracted in the direction of beam propagation) is irrelevant to isotropic measurements, where the π and σ spectra are equivalent. However, the fact that relativistic theory makes the inelastic scattering much more forward peaked remains true, regardless of whether the sample is isotropic.

Now we show the results of the WIEN2k+TELNES2 calculations. TELNES2 can calculate all three formalisms we've discussed so far – the non-relativistic formalism of Nelhiebel et al.³⁴, the relativistic small q approximation with the contracted impulse transfer vector of Schattschneider et al.⁵, and the full relativistic l,m formalism presented in this dissertation and in Jorissen et al.⁷⁰

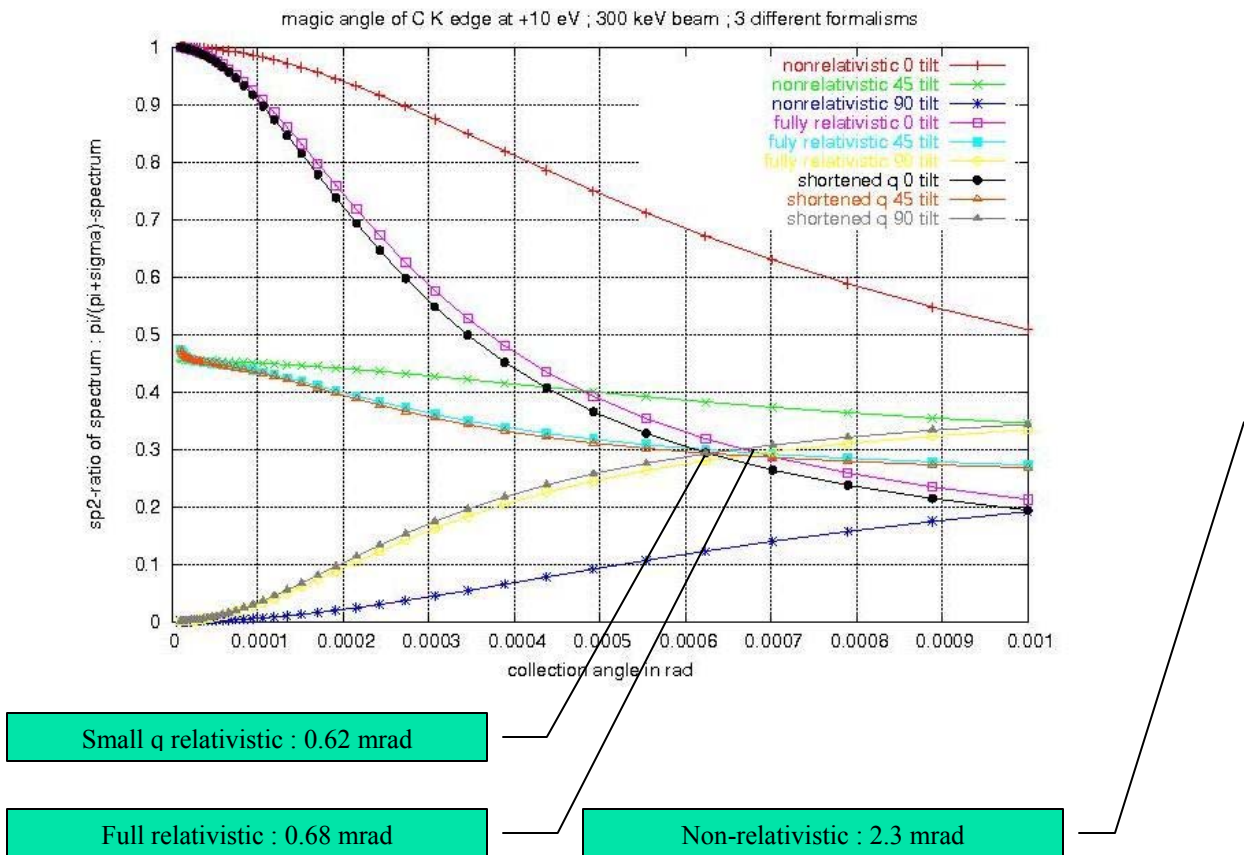


Figure 4-17 The π/σ ratio (see text) of the graphite C K edge at 295 eV loss, using a 300 keV beam and a 0 mrad convergence angle, as a function of the collection semi-angle (in rad). Three different orientations, represented by a tilt angle between the microscope beam and the c axis of the graphite crystal (perpendicular to the graphene sheets), are considered. The magic angle is the value of the collection angle for which the three orientations overlap, i.e., orientation dependence vanishes. Three sets of three such curves are calculated using the TELNES2 program : a non-relativistic calculation (red, green, dark blue), a small q approximated relativistic calculation (black, red, grey), and a full l,m relativistic calculation (pink, light blue, yellow). The non-relativistic magic angle is situated to the far right of the graph at ca. 0.0023 rad.

The results are shown in Figure 4-17 and in Figure 4-18, which is a detail of Figure 4-17. The non-relativistic calculation again gives a wildly inaccurate prediction of the magic angle at ca. 2.3 mrad, far from the experimental value of 0.68 mrad. The relativistic contracted q-vector gives a magic angle at about 0.63 mrad, clearly removing most of the discrepancy between non-relativistic theory and experiment. The full l,m relativistic calculations lead to a predicted value of about 0.68 mrad, which is about 10% larger than the small q vector approximation and coincides with the measured value.

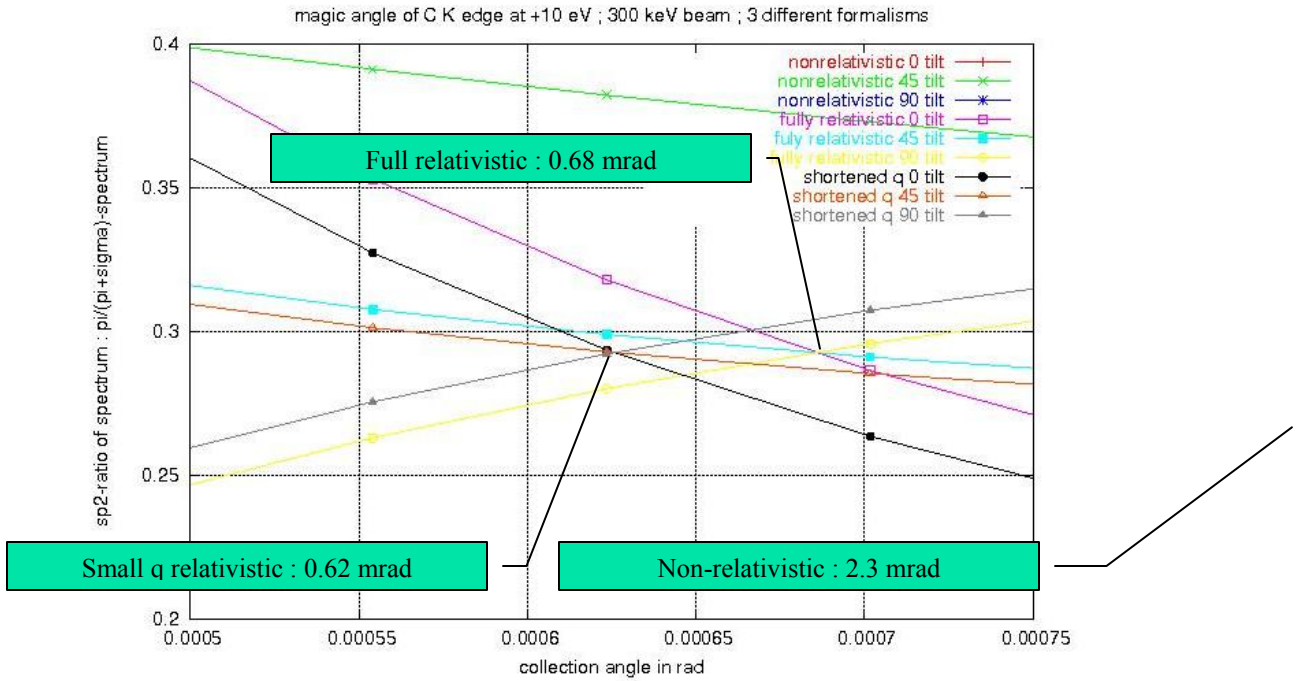


Figure 4-18 Detail of Figure 4-17.

We recall from the discussion in 4.f.4 that the crucial difference between the results of the full l,m and the small q approximated theory stems from the factor f in Eq. (4.6.33), in which an integral is approximated for small impulse transfer q , and Schattschneider's work corresponds to $f=1$. Of course, there is no way of knowing a more correct value for f without actually calculating the radial matrix elements. Using the ab initio EELS program TELNES2, we have evaluated these integrals as show in Figure 4-19.

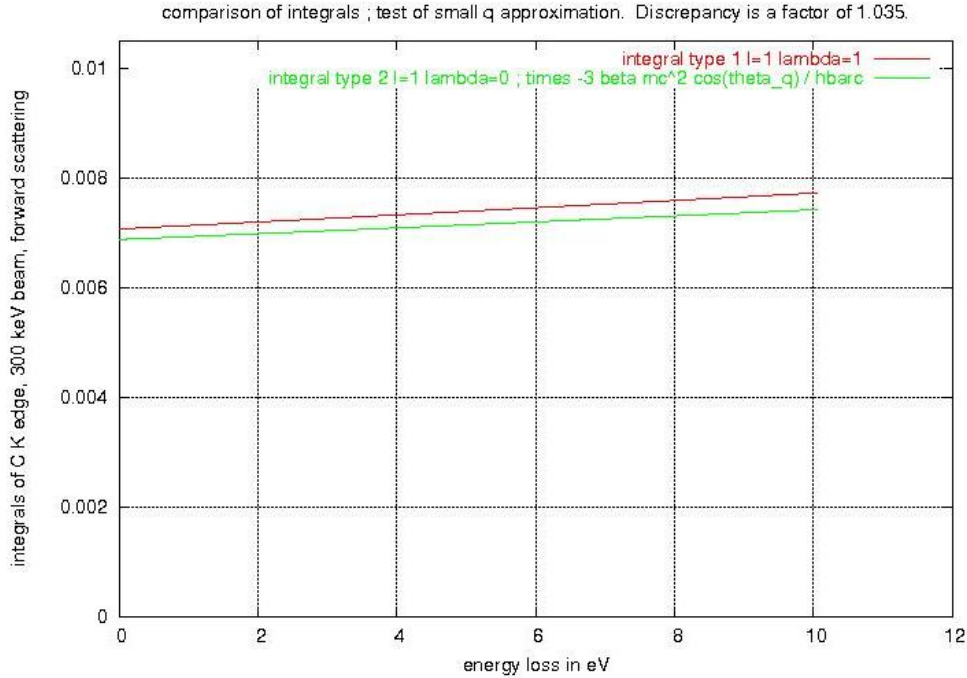


Figure 4-19 Comparison of the radial integrals of the small q approximation of eq. (4.6.33). The missing factor f in eq. (4.6.33) is seen to be $0.966 = 1/1.035$. All parameters for the TELNES2 calculation are as in previous simulations.

The factor $f=0.966$ used in Section f.4. was taken from this calculation. Surprisingly, this small correction leads to a $\sim 10\%$ change in the magic angle.

As an interesting side note, the factor f depends on the overlap between wave functions and is therefore material dependent. It turns out, then, that the magic angle is somewhat material dependent after all. Sorini et al.⁸⁹ discuss other ideas on this material dependence.

We remark that TELNES2 doesn't make any approximations to any of the integrals it needs, and therefore doesn't use this parameter f , which we have introduced only to illuminate the difference between both relativistic formalisms.

So far, we have shown integrated quantities. TELNES2 is also capable of outputting spectra (the DDSCS) as a function of scattering angle at a fixed energy loss (which we still fix at 295 eV). We show how the angular shape of the total spectrum (Figure 4-20) and its π and σ components (Figure 4-21) differs in the three formalisms. All experimental parameters are the same as above, but we study only the 0° tilt angle spectrum. For comparison, we also repeat the measurements of Figure 4-8D in Figure 4-22.

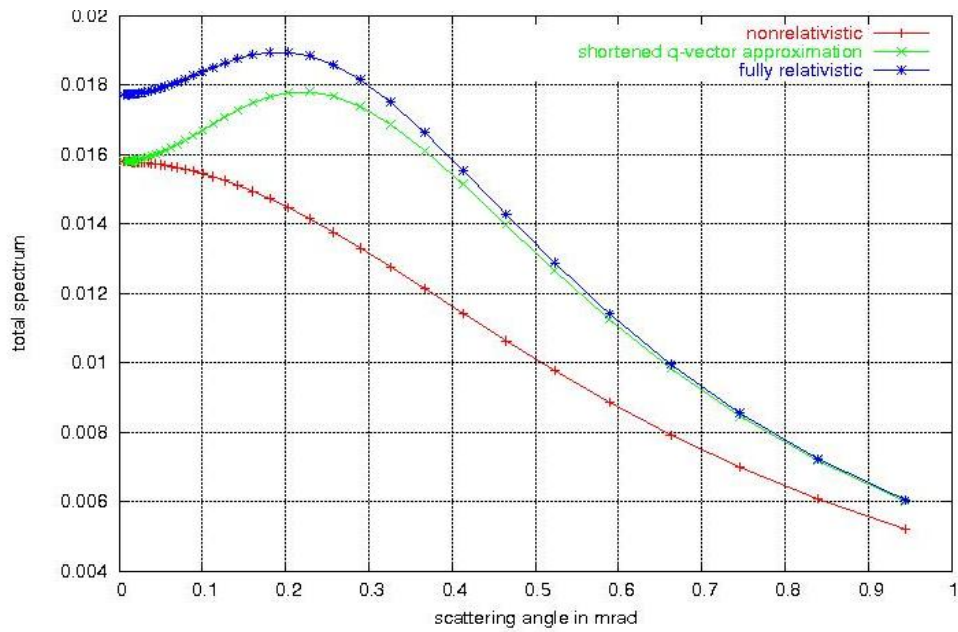


Figure 4-20 The double differential scattering cross section of the graphite C K edge at 295 eV loss for a 300 keV beam incident along the crystal c axis. DDSCS as a function of scattering angle calculated using TELNES2. The curves are not renormalized.

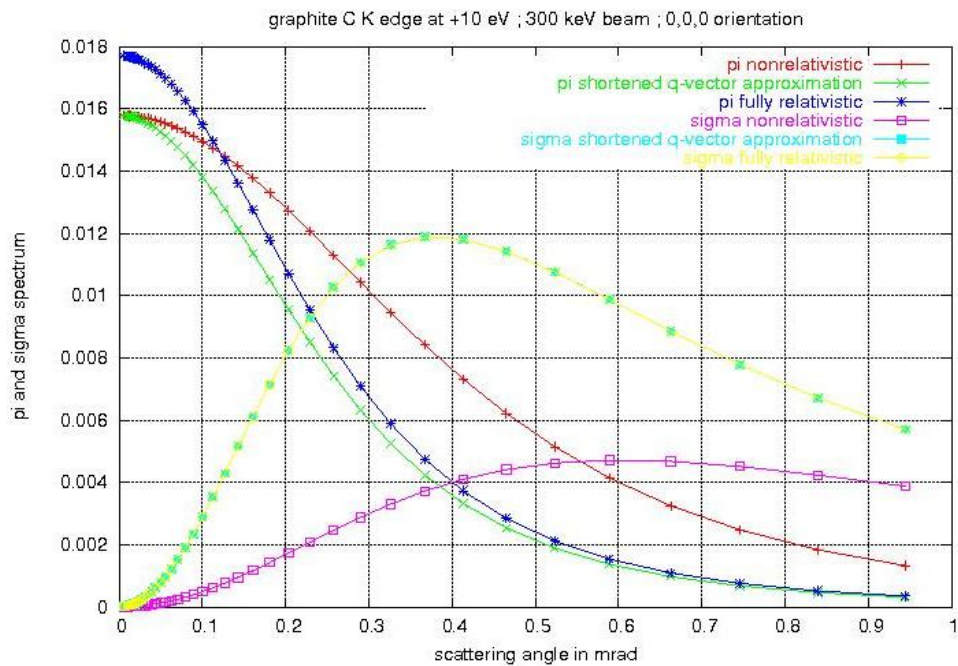


Figure 4-21 This figure shows the same calculation as Figure 4-20, only now the partial π and σ spectra are shown instead of the total spectrum. The curves are not renormalized.

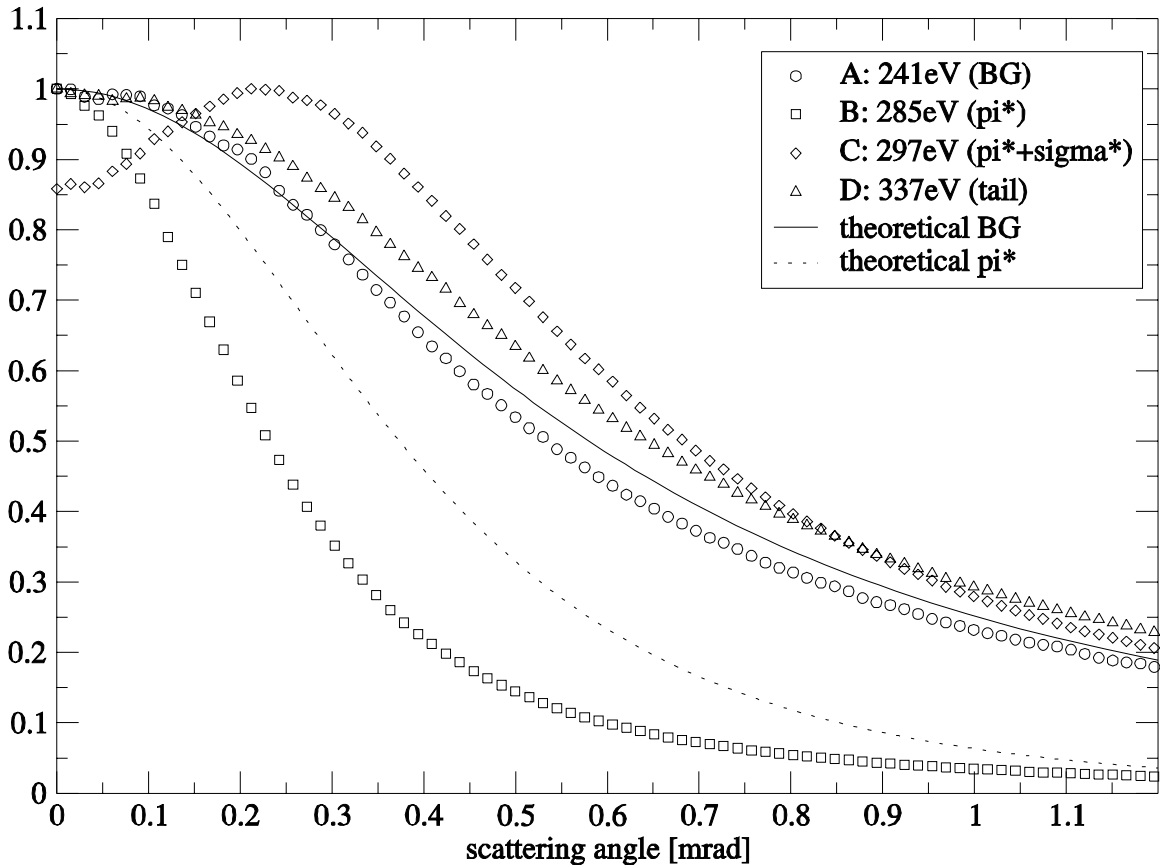


Figure 4-22 Angular distribution of the graphite C K edge, measured at 300 keV beam energy (see Sec. 4.f.2). Curve B is the π edge, and curve C is the total spectrum. The “theoretical” curves are non-relativistic analytical curves (a Lorentz function of width θ_E). All curves were normalized to have a maximum of 1 on the vertical scale. From Radtke et al.¹⁰⁵

Figure 4-21 shows that both the π and the σ cross sections are sharply contracted due to the relativistic interaction potential. This also leads to a different shape of the total cross-section in Figure 4-20, which now has a big bump due to the earlier occurrence of the σ signal. The only difference between the two relativistic formalisms we studied is the difference in overall intensity of the π spectrum.

Both the much narrower π peak and also the bump in the total cross section are clearly and accurately confirmed in the measured scattering profiles of Figure 4-22 .¹⁰⁵

If the study of the magic angle seemed somewhat esoteric, then surely these results must convince that the non-relativistic scattering theory is gravely flawed.

5. Core hole calculations of electron energy loss spectroscopy without the supercell

5.a. Introduction

In chapter 3.d we introduced Green's function multiple scattering theory as a formalism suitable for the calculation of electronic structure and of energy loss spectra in particular. We focused mostly on its real space variant, which is implemented in the FEFF8 code and has proven its qualities many times over.^{43,8,40} Particularly interesting features of the real space formalism are its very efficient treatment of the extended energy loss region (EXELFS, EXAFS) using the Path Expansion ; and its freedom from symmetry requirements. It is applicable to aperiodic, asymmetric system. This is of great help in the study of molecules, amorphous systems, impurities and defects in crystals, etc.

However, in many situations one is interested in the properties of infinite periodic systems or crystals. A reciprocal space formalism, such as the KKR theory^{47,46} described in the introduction, is clearly well suited to describe this crystal. The question arises whether it is possible and efficient to describe the infinite periodic system in a real space formalism, such as Real Space Multiple Scattering (RSMS).

The formal equivalence of the long range reciprocal space formalism and the short range real space formalism has been discussed before, at least as early as in Schaich⁶. Schaich points out that as the real space results for the electronic structure are taken to longer and longer range, they should converge to the reciprocal space results.

The question of efficiency of RSMS then depends on the "near-sightedness" of nature, which has often been remarked upon.¹⁰⁷ The extensive experience of the RSMS community shows that real space calculations of the electronic structure of crystals indeed converge as a larger cluster of representative atoms is taken into account. A XAS or EELS spectrum is often fairly converged for a cluster of about 150 atoms, and very well converged for a cluster of 300 atoms.^{108,8,9}

It may seem that this is all that is to be said. However, the rest of this chapter will be devoted to developing, implementing and discussing a reciprocal space multiple scattering formalism for the *ab initio* calculation of EELS and XAS (and electronic structure in general). The resulting formalism will be very close to impurity KKR, indeed fully equivalent to it, but tailored specifically to be used in connection with RSMS, and implemented in FEFF8.

Our motivations are the following :

- 1/ To improve the efficiency of FEFF8 calculations of periodic systems and remove the possibility of real space finite cluster size artifacts in the calculation.
- 2/ To investigate some of the notorious cases for which RSMS presently fails to give good results. We will look in particular at the diamond C K edge, which is very hard to converge with respect to cluster size ; and at the graphite C K edge, where RSMS calculations using FEFF8 do not describe the π bonds well.
- 3/ To verify the equivalence argued by Schaich⁶ numerically. We can now calculate real space and reciprocal space (short and long range) results within one formalism and then verify that the real space results indeed converge to the reciprocal space results.

There is a fourth motivation, arguably the most important and novel one for the calculation of XAS and EELS spectra of crystals.

- 4/ We aim to improve the reciprocal space calculations of EELS by eliminating the need to use a supercell to calculate core loss spectra. Hence we also eliminate the convergence and artifact problems that come with the supercell approach.

While reciprocal space formalisms such as DFT and KKR are perfectly adapted to calculation of the ground-state properties of a crystal due to their explicit use of periodic boundary conditions (PBC), these very PBC become a burden when calculating excitation spectra. Within independent particle theory, the excitation is often modeled by selecting one atom in the unit cell and placing one of its core electrons into the conduction band, leaving a so-called “core hole” in the core state. This effectively maps the excitation problem onto an impurity problem. As the PBC copy the excited atom into every neighboring unit cell and so on, unphysical core hole – core hole interactions will introduce artifacts into the calculation, unless a unit cell is chosen large enough that neighboring core hole atoms “do not see each other”.

In the real space approach, there is obviously no such problem, as there are no PBC. We will therefore propose a hybrid approach for the calculation of excitation spectra for crystals :

- (i) calculate the ground state of the perfect crystal in reciprocal space ;
- (ii) add the core hole and calculate the excitation spectra in real space.

In (i), the conventional unit cell is used, and in (ii) there is no unit cell. Therefore, any problem related to the use of supercells is avoided.

This hybrid approach is, in itself, not new. It goes back at least as far as Beeby^{109,110}, where a similar scheme was used in KKR-theory for calculations of the electronic properties of impurities. However, our application of the same scheme to core hole EELS and XAS spectroscopy is an innovation with much potential to improve final state rule EELS and XAS.

We remark that our new approach allows to study the effects of using a supercell in more detail, as there is now an alternative method without supercell to compare to.

5.b. The *k*-space multiple scattering formalism.

As we have seen in Chapter 3.d, RSMS and FEFF8 use a Green's function formalism. The Green's function of the electron G is calculated from the free propagator G^0 and the scattering matrix t .

In the RSMS theory, the EELS or XAS spectrum is calculated by evaluating matrix elements of the Green's function :

$$\mu(E) = cst \sum_i \text{Im} \langle i | G(E) | i \rangle \quad (5.2.1)$$

The Green's function is calculated by considering all possible scattering paths of the photoelectron of energy E :

$$G_{mn'} = G_{mn'}^0 + \sum_{n_2} G_{mn_2}^0 t_{n_2} G_{n_2n'}^0 + \sum_{n_2} \sum_{n_3} G_{mn_2}^0 t_{n_2} G_{n_2n_3}^0 t_{n_3} G_{n_3n'}^0 + \dots \quad (5.2.2)$$

where the n -indices label atoms in the solid, the t -matrices describe all scattering events, the G^0 are free propagators, and G on the left hand side of the equation is the full propagator, expressed in a site and angular momentum basis (see Sec. 3.d.1 ; the angular momentum indices are suppressed here for the sake of notational clarity). Eq. (5.2.2) is a sum containing an infinite number of terms involving a near infinite (of order Avogadro's number N_A) number of atoms. To calculate the absorption spectrum near edge thresholds, the Full Multiple Scattering (FMS) approach has been developed, in which one limits the number of atoms to a small cluster around the absorber (typically 100-300 atoms), but sums implicitly over all scattering paths within this cluster by casting (5.2.2) as a matrix inversion :

$$\begin{aligned} G &= G^0 + G^0 t G^0 + G^0 t G^0 t G^0 + \dots \\ &= G^0 [1 - t G^0]^{-1} = [1 - G^0 t]^{-1} G^0 \end{aligned} \quad (5.2.3)$$

For EXELFS or EXAFS, that is for energy losses more than 50 eV beyond the edge threshold, it is calculated by an explicit path expansion. This means that a limited set of paths (usually limited by path length and maximum number of scattering events) in a finite cluster of atoms is considered, as in the first line of (5.2.3). For ELNES or XANES, that is for energy losses up to 50 eV beyond the edge threshold, "Full Multiple Scattering" or FMS is used, meaning that within a finite cluster of atoms all paths are summed up to infinite order. This is done by the matrix inversion in the first line of (5.2.3).

Crystals are infinite systems, and therefore the matrices in (5.2.3) are of infinite rank. In real space calculations, one would (just as one does in practice for finite but rather big systems) truncate the matrices at some radius in real space. Sometimes it is hard to converge spectra in this respect. E.g. diamond requires at least 600 atoms in a FMS calculation. The periodicity of crystals makes it more elegant and advantageous to take the calculation to k -space. This way, it is possible to treat the 'full' crystal without introducing a cluster cut-off radius, as was first described in detail by Beeby.¹⁰⁹ We proceed analogously here.

We introduce the k -space KKR structure constants K as the lattice Fourier transform of the real space free propagator G_0 :

$$K_{\alpha\beta}(\mathbf{k}) = \lim_{N \rightarrow \infty} N^{-1} \sum_{\substack{i \neq j \\ \text{lattice vectors}}}^N e^{i\mathbf{k} \cdot \mathbf{r}_{ij}} G_{i\alpha, j\beta}^0 \quad G_{i\alpha, j\beta}^0 = G^0 \left((\mathbf{r}_i + \mathbf{a}_\alpha) - (\mathbf{r}_j + \mathbf{a}_\beta) \right) \quad (5.2.4)$$

where the lattice of the crystal consists of the vectors $\{\mathbf{r}_i\}$ (Roman indices ; these are integer linear combinations of the three basis vectors of the lattice), and vectors defining the position of atoms in the unit cell $\{\mathbf{a}_\alpha\}$ (Greek indices). Summations over Greek indices run from 1 to m , the number of atoms in the unit cell. Summations over Roman indices run over all $N \rightarrow \infty$ atoms in the crystal. The inverse transformation is

$$\Omega_{BZ}^{-1} \int_{BZ} d\mathbf{k} K_{\alpha\beta}(\mathbf{k}) e^{-i\mathbf{k} \cdot \mathbf{r}_{ij}} = G_{i\alpha, j\beta}^0 \quad (5.2.5)$$

Substituting (5.2.5) in (5.2.2) gives

$$\begin{aligned} G_{m'n'} &= G_{m'n'}^0 + \sum_{n_2} G_{m'n_2}^0 t_{n_2} G_{n_2 n'}^0 + \sum_{n_2} \sum_{n_3} G_{m'n_2}^0 t_{n_2} G_{n_2 n_3}^0 t_{n_3} G_{n_3 n'}^0 + \dots \\ &= \int_{BZ} d\mathbf{k} K_{\alpha\alpha'}(\mathbf{k}) e^{-i\mathbf{k} \cdot \mathbf{r}_{ii'}} + \sum_{i_2 \alpha_2} \int_{BZ} \int_{BZ} d\mathbf{k} d\mathbf{k}' K_{\alpha\alpha_2}(\mathbf{k}) t_{\alpha_2} K_{\alpha_2 \alpha'}(\mathbf{k}') e^{-i\mathbf{k} \cdot \mathbf{r}_{i_2 i'}} e^{-i\mathbf{k}' \cdot \mathbf{r}_{i_2 i'}} \\ &+ \sum_{i_3 \alpha_3} \sum_{i_2 \alpha_2} \int_{BZ} \int_{BZ} \int_{BZ} d\mathbf{k} d\mathbf{k}' d\mathbf{k}'' K_{\alpha\alpha_2}(\mathbf{k}) t_{\alpha_2} K_{\alpha_2 \alpha_3}(\mathbf{k}') t_{\alpha_3} K_{\alpha_3 \alpha'}(\mathbf{k}'') e^{-i\mathbf{k} \cdot \mathbf{r}_{i_2 i'}} e^{-i\mathbf{k}' \cdot \mathbf{r}_{i_2 i_3}} e^{-i\mathbf{k}'' \cdot \mathbf{r}_{i_3 i'}} \\ &+ \dots \end{aligned} \quad (5.2.6)$$

where we have used the notation $n=(i, \alpha)$, $n'=(i', \alpha')$. Now we can use the fact that the system under consideration is periodic, to simplify this expression. We treat the third term of (5.2.6) ; all others are treated similarly :

$$\begin{aligned} &\sum_{i_2} \sum_{i_3} e^{-i\mathbf{k} \cdot \mathbf{r}_{i_2 i'}} e^{-i\mathbf{k}' \cdot \mathbf{r}_{i_2 i_3}} e^{-i\mathbf{k}'' \cdot \mathbf{r}_{i_3 i'}} = e^{-i(\mathbf{k}+\mathbf{k}'+\mathbf{k}'') \cdot \mathbf{r}_{ii'}} \sum_{i_2} \sum_{i_3} e^{i\mathbf{k} \cdot \mathbf{r}_{i_2 i'}} e^{i\mathbf{k}' \cdot (\mathbf{r}_{i_2} + \mathbf{r}_{i_3 i'})} e^{i\mathbf{k}'' \cdot \mathbf{r}_{i_3 i'}} \\ &= e^{-i(\mathbf{k}+\mathbf{k}'+\mathbf{k}'') \cdot \mathbf{r}_{ii'}} \sum_{i_2} e^{i(\mathbf{k}' \cdot \mathbf{r}_{i_2} + \mathbf{k} \cdot \mathbf{r}_{i_2 i'})} \sum_{i_3} e^{i(\mathbf{k}' - \mathbf{k}'') \cdot \mathbf{r}_{i_3 i'}} e^{i\mathbf{k}'' \cdot \mathbf{r}_{i_3 i'}} \\ &= e^{-i(\mathbf{k}+\mathbf{k}'+\mathbf{k}'') \cdot \mathbf{r}_{ii'}} \sum_{i_2} e^{i(\mathbf{k}' \cdot \mathbf{r}_{i_2} + \mathbf{k} \cdot \mathbf{r}_{i_2 i'})} e^{i\mathbf{k}'' \cdot \mathbf{r}_{ii'}} \sum_{i_3} e^{i(\mathbf{k}' - \mathbf{k}'') \cdot \mathbf{r}_{i_3 i'}} \\ &= e^{-i(\mathbf{k}+\mathbf{k}') \cdot \mathbf{r}_{ii'}} \sum_{i_2} e^{i(\mathbf{k}' \cdot \mathbf{r}_{i_2} + \mathbf{k} \cdot \mathbf{r}_{i_2 i'})} \Omega_{BZ} \delta(\mathbf{k}' - \mathbf{k}'') \\ &= e^{-i\mathbf{k} \cdot \mathbf{r}_{ii'}} \Omega_{BZ} \delta(\mathbf{k}' - \mathbf{k}'') \Omega_{BZ} \delta(\mathbf{k} - \mathbf{k}') \end{aligned} \quad (5.2.7)$$

The Green's function is then given by

$$G_{m'n'} = \int_{BZ} d\mathbf{k} e^{-i\mathbf{k} \cdot \mathbf{r}_{ii'}} \left[K_{\alpha\alpha'}(\mathbf{k}) + \sum_{\alpha_2}^{\text{unitcell}} K_{\alpha\alpha_2}(\mathbf{k}) t_{\alpha_2} K_{\alpha_2 \alpha'}(\mathbf{k}) + \sum_{\alpha_2}^{\text{unitcell}} \sum_{\alpha_3}^{\text{unitcell}} K_{\alpha\alpha_2}(\mathbf{k}) t_{\alpha_2} K_{\alpha_2 \alpha_3}(\mathbf{k}) t_{\alpha_3} K_{\alpha_3 \alpha'}(\mathbf{k}) + \dots \right] \quad (5.2.8)$$

This can once more be cast as a matrix inversion,

$$G_{m'n'} = \int_{BZ} d\mathbf{k} e^{-i\mathbf{k} \cdot \mathbf{r}_{ii'}} \left[(1 - KT)^{-1} K \right]_{\alpha\alpha'} \quad T_{\alpha\alpha'} = t_{\alpha} \delta_{\alpha\alpha'} \quad (5.2.9)$$

Equation (5.2.9) yields the Green's function, and hence the electronic structure and excitation spectra, without any finite cluster approximations. The singularities of the integrand of (5.2.9) yield the band structure. This is formally equivalent to KKR

theory,^{47,46} where the band structure is obtained from the singularities of the scattering path operator

$$\tau(\mathbf{k}) = [K(\mathbf{k}) - t^{-1}]^{-1} \quad (5.2.10)$$

The indices n, n' on the left hand side of (5.2.9) number atoms in a real space lattice or cluster ; the indices α, α' on the right hand side label the corresponding sublattices and only run from 1 to m even in infinite crystals. Eq. (5.2.9) is a prescription for calculating in reciprocal space the real-space Green's function $G_{nn'}$.

5.b.1. Introducing the core hole.

Calculations of EELS or XAS spectra are naturally concerned with excited systems, not with systems in their ground state. Excitations are naturally multiparticle events ; however, they are conveniently modeled within one electron theory by considering a system containing a core hole. This is done by calculating the electronic structure of a system which contains one explicitly excited atom (with one electron transferred from a core state to the conduction band), much like an impurity calculation. In principle, this destroys the periodicity of the crystal, leading to all the problems of band structure methods discussed in Sec. 5.a.

However, adding the core hole to the formalism we've established here is almost trivial. It is situated entirely in real space, avoiding all the problems with PBC.

Assume that we have the (real space) solution G_p for the perfect crystal, calculated using (5.2.9). The system with core hole has the same KKR structure constants as the perfect system, and a scattering matrix T that is different only in one site block T_{cc} corresponding to the core hole atom. Its Green's function G is given by basic matrix algebra:

$$\begin{aligned} T &= T_{perfect} + T_{impurity} = T_p + T_i & G_p &= (1 - G^0 t_p)^{-1} G^0 \\ G &= (1 - G^0 T_p - G^0 T_i)^{-1} G^0 = (1 - G_p T_i)^{-1} G_p \end{aligned} \quad (5.2.11)$$

This follows from $(A+B)^{-1} = (1+A^{-1}B)^{-1} A^{-1}$. Equation (5.2.11) becomes particularly simple when T_i is nonzero in one block only (as for the core hole). In this case, the Green's function elements between sites n and n' is given by

$$G_{nn'} = (1 - \delta_{nc}) G_{nn'}^p + (\delta_{nc} 1 + (1 - \delta_{nc}) G_{nc}^p t_c^i) (1 - G_{cc}^p t_c^i)^{-1} G_{cn'}^p \quad (5.2.12)$$

where c is the index of the core hole (which we could set to one), and the indices p and i stand for perfect and with impurity, and 1 is the unit matrix. For the core hole atom, we get

$$G_{cc} = (1 - G_{cc}^p t_c^i)^{-1} G_{cc}^p \quad (5.2.13)$$

G_{cc} is needed for the calculation of an EELS or XAS spectrum.

The treatment of impurities is done in impurity KKR in precisely the same way.¹⁰⁹

5.b.2. Monoatomic lattices.

If the unit cell contains only one atom, the summations over a can be dropped from (5.2.4) and (5.2.9), simplifying the equations to

$$K(\mathbf{k}) = \lim_{N \rightarrow \infty} \sum_{\substack{j \neq 1 \\ \text{lattice vectors}}}^N e^{i\mathbf{k} \cdot \mathbf{r}_{1j}} G_{1,j}^0 \quad (5.2.14)$$

and

$$G_{mn} = \int_{BZ} d\mathbf{k} e^{-i\mathbf{k} \cdot \mathbf{r}_n} (1 - K(\mathbf{k})t)^{-1} K(\mathbf{k}) \quad (5.2.15)$$

This is the result of Schaich⁶ and Beeby¹⁰⁹.

5.b.3. Calculation of the KKR structure factors.

The most efficient scheme for the calculation of the KKR structure factors defined in Eq. (5.2.4) of the previous section, is the Ewald summation technique.¹¹¹ It is important to use the approach described in these references, as brute force numerical approaches are wasteful at best, and potentially problematic. The technique is described in a few more recent and more easily accessible papers.^{112,113} However, the theory is always described for monoatomic lattices. We here present the complete derivation of the Ewald summation of the KKR structure factors of “complex” crystals containing an arbitrary number of atoms in the unit cell.

We remember the definitions :

$$K_{\alpha\beta}(\mathbf{k}) := G_{\alpha\beta}^0(\mathbf{k}) := \lim_{N \rightarrow \infty} \frac{1}{N} \sum_{\substack{i \neq j \\ \text{lattice vectors}}}^N e^{i\mathbf{k} \cdot \mathbf{r}_{ij}} G_{i\alpha,j\beta}^0 \quad (5.2.16)$$

$$G_{i\alpha,j\beta}^0 = G^0\left(\left(\mathbf{r}_i + \mathbf{a}_\alpha\right) - \left(\mathbf{r}_j + \mathbf{a}_\beta\right)\right) \quad (5.2.17)$$

$$\Omega_{BZ}^{-1} \int_{BZ} d\mathbf{k} K_{\alpha\beta}(\mathbf{k}) e^{-i\mathbf{k} \cdot \mathbf{r}_{ij}} = N^{-1} \Omega_{BZ}^{-1} \sum_{l \neq p} G_{l\alpha,p\beta}^0 \int_{BZ} d\mathbf{k} e^{i\mathbf{k} \cdot (\mathbf{r}_p - \mathbf{r}_j)} = G_{i\alpha,j\beta}^0 \quad (5.2.18)$$

Calculating $K_{\alpha\beta}$ by use of (5.2.16) is very inefficient and can lead to convergence problems. What's more, we also need the structure factor expressed in an angular momentum basis L, L' ($L=l, m$). To achieve all this, we use a technique called Ewald summation.¹¹¹ We define a dummy function

$$G_{\alpha\beta}(\mathbf{R}) \text{ short for } G_{\alpha\beta}(\mathbf{r}, \mathbf{r}', p, \mathbf{k}) \quad p = \sqrt{E}, \quad \mathbf{R} = \mathbf{r} - \mathbf{r}' \quad (5.2.19)$$

The requirements for this function are :

$$\lim_{R \rightarrow 0} G_{\alpha\beta}(\mathbf{R}) = K_{\alpha\beta} \quad \text{and} \quad \lim_{G \rightarrow 0} G_{\alpha L, \beta L'}(\mathbf{R}) = K_{\alpha L, \beta L'} \quad (5.2.20)$$

and $G_{\alpha\beta}$ must be such that it's convenient to calculate.

A good choice is

$$G_{\alpha\beta}(\mathbf{R}) = -(4\pi)^{-1} \sum'_s \frac{e^{ip|\mathbf{R}-\mathbf{r}_s-\mathbf{a}_{\alpha\beta}|}}{|\mathbf{R}-\mathbf{r}_s-\mathbf{a}_{\alpha\beta}|} e^{ik \cdot \mathbf{r}_s} \quad (5.2.21)$$

where the prime on the summation symbol means that the sum runs over all lattice vectors excluding the term $\mathbf{r}_s=0$. The Fourier transform of $G_{\alpha\beta}$:

$$\int_{BZ} G_{\alpha\beta}(\mathbf{R}) e^{-ik \cdot \mathbf{r}_s} d\mathbf{k} = G^0(\mathbf{R} - (\mathbf{r}_s + \mathbf{a}_{\alpha\beta})) \quad \text{if } \mathbf{r}_s \in \text{lattice} ; = 0 \quad \text{otherwise} \quad (5.2.22)$$

where G^0 is the real-space free propagator (notice that this definition is not the Rehr-Albers normalization). It is now clear that (5.2.21) satisfies (5.2.20).

We use two identities proven by Ewald¹¹¹ almost a century ago :

$$\frac{e^{ip|\mathbf{R}-\mathbf{r}_s|}}{|\mathbf{R}-\mathbf{r}_s|} = \frac{2}{\sqrt{\pi}} \int_{0(C)}^{+\infty} e^{-(\mathbf{R}-\mathbf{r}_s)^2 \xi^2 + p^2 / 4\xi^2} d\xi \quad (5.2.23)$$

$$\sum'_s e^{-(\mathbf{R}-\mathbf{r}_s)^2 \xi^2 + ik \cdot (\mathbf{r}_s - \mathbf{R})} = \frac{\pi^{3/2}}{\tau} \xi^{-3} \sum_n e^{-\frac{(k+K_n)^2}{4\xi^2} + iK_n \cdot \mathbf{R}} \quad (5.2.24)$$

lattice reciprocal lattice

τ is the volume of the first BZ. Using (5.2.23), we now write (5.2.21) as

$$G_{\alpha\beta}(\mathbf{R}) = -(4\pi)^{-1} \frac{2}{\sqrt{\pi}} \sum'_s e^{ik \cdot \mathbf{r}_s} \left(\int_0^{\sqrt{\eta}/2} d\xi + \int_{\sqrt{\eta}/2}^{+\infty} d\xi \right) \left(e^{-\frac{(\mathbf{R}-\mathbf{r}_s-\mathbf{a}_{\alpha\beta})^2 \xi^2 + p^2}{4\xi^2}} \right) \quad (5.2.25)$$

The prime on the lattice sum means that the 0-term is omitted. The contour (C) of the integral is defined as follows. From 0 on, let $\arg \xi = \frac{\arg p - \pi/2}{2}$ for a while ; then, the

contour goes to the real axis by the time $\sqrt{\eta}/2$ is reached. After that, the contour just runs along the real axis. Now the first part of the integral will be transformed to reciprocal space by using (5.2.24) :

$$G_{\alpha\beta}(\mathbf{R}) = -(4\pi)^{-1} \frac{2}{\sqrt{\pi}} \left[\sum'_s e^{ik \cdot \mathbf{r}_s} \left(\int_{\sqrt{\eta}/2}^{+\infty} e^{-\frac{(\mathbf{R}-\mathbf{r}_s-\mathbf{a}_{\alpha\beta})^2 \xi^2 + p^2}{4\xi^2}} d\xi \right) + \frac{\pi^{3/2}}{\tau} \sum_n e^{i(k+K_n) \cdot (\mathbf{R}-\mathbf{a}_{\alpha\beta})} \int_0^{\sqrt{\eta}/2} \xi^{-3} e^{-\frac{(K_n+k)^2 - p^2}{4\xi^2}} d\xi - \int_0^{\sqrt{\eta}/2} e^{-R^2 \xi^2 + \frac{p^2}{4\xi^2}} d\xi + \right] \quad (5.2.26)$$

where the last term needs to be added because the lattice sum in (5.2.24) runs over all sites, whereas the $s=0$ term is excluded from (5.2.25). s numbers lattice vectors, whereas n numbers reciprocal lattice vectors. Now use

$$\int_0^b x^{-3} e^{-\frac{a}{x^2}} dx = \frac{2}{a} e^{-\frac{a}{b^2}} \quad (5.2.27)$$

to calculate the second term. This leads to

$$G_{\alpha\beta}(\mathbf{R}) = -(2\pi^{3/2})^{-1} \left[\sum_s' e^{i\mathbf{k}_s \cdot \mathbf{r}_s} \left(\int_{\sqrt{\eta}/2}^{+\infty} e^{-\frac{(\mathbf{R}-\mathbf{r}_s-\mathbf{a}_{\alpha\beta})^2 \xi^2 + \frac{p^2}{4\xi^2}}}{\xi^2} d\xi \right) \right. \\ \left. - \tau^{-1} \sum_n e^{i(\mathbf{K}_n+\mathbf{k}) \cdot (\mathbf{R}-\mathbf{a}_{\alpha\beta})} \frac{e^{-\frac{(\mathbf{K}_n+\mathbf{k})^2 - p^2}{\eta}}}{(\mathbf{K}_n+\mathbf{k})^2 - p^2} - \int_0^{\sqrt{\eta}/2} e^{-R^2 \xi^2 + \frac{p^2}{4\xi^2}} d\xi \right] \quad (5.2.28)$$

Now it is time to do the basis set expansion. In the end, we want an expression of the form

$$G_{\alpha\beta}(\mathbf{R} = \mathbf{r} - \mathbf{r}') = \sum_L \sum_{L'} \left[i^{l-l'} B_{\alpha L \beta L'} j_l(pr) j_{l'}(pr') + p \delta_{LL'} j_l(pr) n_l(pr') \right] Y_L(\mathbf{r}) Y_{L'}(\mathbf{r}') \quad (5.2.29)$$

However, as the Green's function is obviously a function of \mathbf{R} , it can also be expanded as

$$G_{\alpha\beta}(\mathbf{R}) = -(4\pi)^{-1} \frac{\cos(pR)}{R} + \sum_L i^l D_{\alpha\beta L} j_l(pR) Y_L(\mathbf{R}) \quad (5.2.30)$$

which is much simpler. The B coefficients can be recovered as

$$B_{\alpha L \beta L'} = 4\pi \sum_{\Lambda} D_{\alpha\beta \Lambda} C_{LL'}^{\Lambda} \quad (5.2.31)$$

where C are Wigner 3j symbols. The divergent terms in (5.2.29) and (5.2.30) are only needed for \mathbf{r} and \mathbf{r}' in the same cell. (Remember that FEFF8 has overlapping muffin tins, so even for $\mathbf{R}=0$ this is important.) Finally, the spherical harmonics in (5.2.29) and (5.2.30) are real (if one were to use complex spherical harmonics, one of them would carry a complex conjugate *).

We will now calculate $d_{\alpha\beta lm} = \int_{4\pi} G_{\alpha\beta}(\mathbf{R}) Y_{lm}^*(\mathbf{R}) d\Omega_R$. The D_{lm} will follow later by taking the limit \mathbf{R} to 0. Using the Rayleigh expansion

$$e^{i\mathbf{k} \cdot \mathbf{r}} = 4\pi \sum_L i^l j_l(kr) Y_L^*(\mathbf{k}) Y_L(\mathbf{r}) \quad (5.2.32)$$

where $Y_{lm}(\mathbf{k}) \equiv Y_{lm}(\theta_k, \phi_k)$

$$d_{\alpha\beta lm} = -\tau^{-1} \sum_n \frac{e^{-(k_n^2 - p^2)/\eta}}{(k_n^2 - p^2)} e^{-i\mathbf{k}_n \cdot \mathbf{a}_{\alpha\beta}} 4\pi i^l j_l(k_n R) Y_{lm}^*(\mathbf{k}_n) + (2\pi^{3/2})^{-1} \sqrt{4\pi} \delta_{l0} \delta_{m0} \int_0^{\sqrt{\eta}/2} e^{-R^2 \xi^2 + \frac{p^2}{4\xi^2}} d\xi \\ - (2\pi^{3/2})^{-1} \sum_s' e^{i\mathbf{k}_s \cdot \mathbf{r}_s} \int_{\sqrt{\eta}/2}^{+\infty} d\xi e^{\frac{p^2}{4\xi^2}} \int_{4\pi} e^{-\frac{(\mathbf{R}-\mathbf{r}_s-\mathbf{a}_{\alpha\beta})^2 \xi^2}} Y_{lm}^*(\mathbf{k}) d\Omega_R \quad (\mathbf{k}_n := \mathbf{k} + \mathbf{K}_n) \quad (5.2.33) \\ =: d_{\alpha\beta lm}^{(1)} + d_{\alpha\beta lm}^{(3)} + d_{\alpha\beta lm}^{(2)}$$

Splitting the sum in 3 terms is just a matter of convenience. τ is the volume of the BZ, as usual. Remarking that

$$e^{-(\mathbf{R}-\mathbf{r}_s-\mathbf{a}_{\alpha\beta})^2 \xi^2} = e^{-\left(R^2 + (\mathbf{r}_s + \mathbf{a}_{\alpha\beta})^2\right) \xi^2} e^{i(-2i\xi^2(\mathbf{r}_s + \mathbf{a}_{\alpha\beta})) \cdot \mathbf{R}} \quad (5.2.34)$$

one can again use (5.2.32) to calculate $d_{\alpha\beta lm}^{(2)}$:

$$\begin{aligned}
d_{\alpha\beta lm} = & -4\pi\tau^{-1} \sum_n \frac{e^{-(k_n^2 - p^2)/\eta}}{(k_n^2 - p^2)} e^{-ik_n \cdot \mathbf{a}_{\alpha\beta}} i^l j_l(k_n R) Y_{lm}^*(\mathbf{k}_n) + \pi^{-1} \delta_{l0} \delta_{m0} \int_0^{\sqrt{\eta}/2} e^{-R^2 \xi^2 + p^2/4\xi^2} d\xi \\
& - 2\pi^{-1/2} i^l \sum_s e^{ik_s \cdot \mathbf{r}_s} Y_{lm}^* \left(-i(\mathbf{r}_s + \mathbf{a}_{\alpha\beta}) \right) \int_{\sqrt{\eta}/2}^{+\infty} d\xi e^{-\left(R^2 + (\mathbf{r}_s + \mathbf{a}_{\alpha\beta})^2\right) \xi^2 + \frac{p^2}{4\xi^2}} j_l(-2i\xi^2 R |\mathbf{r}_s + \mathbf{a}_{\alpha\beta}|)
\end{aligned} \tag{5.2.35}$$

Now for small arguments ($R \rightarrow 0$), the spherical Bessel functions have the following property

$$j_l(ax) \approx \left(\frac{a}{b}\right)^l j_l(bx) \tag{5.2.36}$$

Therefore

$$\begin{aligned}
d_{\alpha\beta lm} = & -4\pi\tau^{-1} \sum_n \frac{e^{-(k_n^2 - p^2)/\eta}}{(k_n^2 - p^2)} e^{-ik_n \cdot \mathbf{a}_{\alpha\beta}} i^l \left(\frac{k_n}{p}\right)^l j_l(pR) Y_{lm}^*(\mathbf{k}_n) + \pi^{-1} \delta_{l0} \delta_{m0} \int_0^{\sqrt{\eta}/2} e^{-R^2 \xi^2 + p^2/4\xi^2} d\xi \\
& - 2\pi^{-1/2} i^l \sum_s e^{ik_s \cdot \mathbf{r}_s} Y_{lm}^* \left(-i(\mathbf{r}_s + \mathbf{a}_{\alpha\beta}) \right) \left(\frac{-2i|\mathbf{r}_s + \mathbf{a}_{\alpha\beta}|}{p}\right)^l \int_{\sqrt{\eta}/2}^{+\infty} d\xi e^{-\left(R^2 + (\mathbf{r}_s + \mathbf{a}_{\alpha\beta})^2\right) \xi^2 + \frac{p^2}{4\xi^2}} \xi^{2l} j_l(pR)
\end{aligned} \tag{5.2.37}$$

Comparison to (5.2.30) now allows to identify the D_{LM} :

$$\begin{aligned}
D_{\alpha\beta lm} = & -4\pi\tau^{-1} \sum_n \frac{e^{-(k_n^2 - p^2)/\eta}}{(k_n^2 - p^2)} e^{-ik_n \cdot \mathbf{a}_{\alpha\beta}} \left(\frac{k_n}{p}\right)^l Y_{lm}^*(\mathbf{k}_n) + (\pi j_0(pR))^{-1} \delta_{l0} \delta_{m0} \int_0^{\sqrt{\eta}/2} e^{-R^2 \xi^2 + p^2/4\xi^2} d\xi \\
& - 2\pi^{-1/2} \sum_s e^{ik_s \cdot \mathbf{r}_s} Y_{lm}^* \left(-i(\mathbf{r}_s + \mathbf{a}_{\alpha\beta}) \right) \left(\frac{-2i|\mathbf{r}_s + \mathbf{a}_{\alpha\beta}|}{p}\right)^l \int_{\sqrt{\eta}/2}^{+\infty} d\xi e^{-\left(R^2 + (\mathbf{r}_s + \mathbf{a}_{\alpha\beta})^2\right) \xi^2 + \frac{p^2}{4\xi^2}} \xi^{2l}
\end{aligned} \tag{5.2.38}$$

Then, taking the limit $R \rightarrow 0$ (as D_{lm} ought to be independent of R)

$$\begin{aligned}
D_{\alpha\beta lm} = & -4\pi\tau^{-1} \sum_n \frac{e^{-(k_n^2 - p^2)/\eta}}{(k_n^2 - p^2)} e^{-ik_n \cdot \mathbf{a}_{\alpha\beta}} \left(\frac{k_n}{p}\right)^l Y_{lm}^*(\mathbf{k}_n) + (\pi)^{-1} \delta_{l0} \delta_{m0} \int_0^{\sqrt{\eta}/2} e^{p^2/4\xi^2} d\xi \\
& - 2\pi^{-1/2} \sum_s e^{ik_s \cdot \mathbf{r}_s} Y_{lm}^* \left(-i(\mathbf{r}_s + \mathbf{a}_{\alpha\beta}) \right) \left(\frac{-2i|\mathbf{r}_s + \mathbf{a}_{\alpha\beta}|}{p}\right)^l \int_{\sqrt{\eta}/2}^{+\infty} d\xi e^{-\left(\mathbf{r}_s + \mathbf{a}_{\alpha\beta}\right)^2 \xi^2 + \frac{p^2}{4\xi^2}} \xi^{2l}
\end{aligned} \tag{5.2.39}$$

Eq. (5.2.39) is the main result of this paragraph.

The term $D_{LM}(3)$.

$$(\pi)^{-1} \int_0^{\sqrt{\eta}/2} e^{p^2/4\xi^2} d\xi = (\pi)^{-1} \sum_l \left(\frac{E}{4}\right)^l \frac{1}{l!} \int_0^{\sqrt{\eta}/2} \xi^{-2l} d\xi = -(\pi)^{-1} \sum_l \left(\frac{E}{4}\right)^l \frac{1}{l!(2l-1)} \left[\xi^{-2l+1}\right]_0^{\sqrt{\eta}/2} \tag{5.2.40}$$

Now it is important to remember the definition of the contour :

$$\arg \xi = \frac{\arg p - s\pi/2}{2} \Rightarrow \arg \left(\frac{p^2}{4\xi^2}\right) = \arg p + s\pi/2 \tag{5.2.41}$$

$$s = 1 \text{ for } 0 < \arg p < \pi \quad ; \quad s = -1 \text{ for } \pi < \arg p < 2\pi$$

This definition guarantees that

$$\cos \left(\arg \left(\frac{p^2}{4\xi^2} \right) \right) < 0 \tag{5.2.42}$$

This ensures that the integrand of (5.2.40) goes to zero as ξ goes to zero, and the integral exists. The final result is then

$$D_{lm}^{(3)} = \delta_{l0} \delta_{m0} \frac{-1}{2\pi} \sqrt{\eta} \sum_{l=0}^{+\infty} \left(\frac{E}{\eta} \right)^l \frac{1}{l!(2l-1)} \quad (5.2.43)$$

The term Dlm(2) :

The integral in Dlm(2) can be expressed in terms of incomplete Gamma functions :

$$\begin{aligned} \int_{\sqrt{\eta}/2}^{+\infty} d\xi e^{-\left(r_s + a_{\alpha\beta}\right)^2 \xi^2 + \frac{p^2}{4\xi^2}} \xi^{2l} &= \sum_n \left(\frac{p}{2} \right)^{2n} \frac{1}{n!} \int_{\sqrt{\eta}/2}^{+\infty} d\xi e^{-\left(r_s + a_{\alpha\beta}\right)^2 \xi^2} \xi^{2(l-n)} \\ &= \sum_n \left(\frac{p}{2} \right)^{2n} \frac{1}{n!} \frac{\left| r_s + a_{\alpha\beta} \right|^{2(n-l)-1}}{2} \Gamma \left(l-n + \frac{1}{2}, \frac{\eta}{4} \left| r_s + a_{\alpha\beta} \right|^2 \right) \end{aligned} \quad (5.2.44)$$

We can use the following representation of the incomplete Gamma function

$$\begin{aligned} \Gamma(a, z) &= z^a e^{-z} \frac{1}{z + \frac{1-a}{1 + \frac{1}{z + \frac{2-a}{1 + \frac{3-a}{z + \frac{3}{z + \dots}}}}}}} \quad \text{for } z \notin [-\infty, 0] \\ &= z^a e^{-z} f(a, x) \end{aligned} \quad (5.2.45)$$

where f is the continued fraction defined by (5.2.45). Combining (5.2.39), (5.2.44) and (5.2.45) gives

$$\begin{aligned} D_{lm}^{(2)} &= -2\pi^{-1/2} \sum_s e^{jk_r s} Y_{lm}^* \left(-i \left(r_s + a_{\alpha\beta} \right) \right) \left(\frac{-2i \left| r_s + a_{\alpha\beta} \right|}{p} \right)^l \int_{\sqrt{\eta}/2}^{+\infty} d\xi e^{-\left(r_s + a_{\alpha\beta}\right)^2 \xi^2 + \frac{p^2}{4\xi^2}} \xi^{2l} \\ &= -\sqrt{\frac{\eta}{4\pi}} \sum_s e^{jk_r s} Y_{lm}^* \left(-i \left(r_s + a_{\alpha\beta} \right) \right) \left(\frac{-i\eta \left| r_s + a_{\alpha\beta} \right|}{2p} \right)^l e^{\frac{\eta}{4} \left| r_s + a_{\alpha\beta} \right|^2} \sum_n \left(\frac{p^2}{\eta} \right)^n \frac{1}{n!} f \left(l-n + \frac{1}{2}, \frac{\eta}{4} \left| r_s + a_{\alpha\beta} \right|^2 \right) \end{aligned} \quad (5.2.46)$$

5.c. Implementation in the FEFF8 program

Eq. (5.2.9), (5.2.12) and (5.2.39) have been implemented in the RSMS *ab initio* program FEFF8.¹¹⁴ For the calculation of ELNES, FEFF8 now offers three approaches :

$$\begin{aligned}
 G &= G_0 + G_0 t G_0 + G_0 t G_0 t G_0 + \dots \\
 &= G_0 [1 - t G_0]^{-1} \\
 &= \int_{BZ} d\mathbf{k} G_0(\mathbf{k}) [1 - t G_0(\mathbf{k})]^{-1}
 \end{aligned}
 \tag{5.3.1}$$

being the Path Expansion (PE, first line of (5.3.1)) and the Full Multiple Scattering (FMS, second line) in real space (see Sec. 3.d), and the k-space approach (third line of (5.3.1)) of Sec. 5.b. In all three cases, the core hole is treated in real space. In the PE and FMS, it is simply one atom in the real space cluster used for the calculation. In the k-space approach, it is added in real space after evaluation of (5.3.1) :

$$G_{ch} = G [1 - \Delta t_{ch} G]^{-1} \tag{5.3.2}$$

All quantities in (5.3.1) and (5.3.2) are matrices in a site and angular momentum basis. The number of sites is given by the number of atoms in the cluster for real space calculations, and is given by the number of atoms in the unit cell for reciprocal space calculations. Similar angular momentum cutoffs are needed in real space and in reciprocal space.

As one typically needs a cluster of 100-300 atoms in real space calculations, the reciprocal space treatment becomes especially advantageous for crystals with small unit cells containing only a few atoms. The computational cost of the calculation is almost completely dominated by the matrix inversions in (5.3.1). In k-space calculations, one needs to one inversion for each k-vector needed to sample the Brillouin Zone integral of a small matrix (\sim number of atoms in the unit cell); compared to one inversion of a large (\sim number of atoms in the cluster) matrix for real space FMS. As the unit cell of a crystal becomes larger, fewer k-points are typically needed to calculate the BZ integral ; however, the calculations still become slower with increasing unit cell size.

For EXELFS or EXAFS, at energy losses more than 50-70 eV above threshold, the angular momentum cutoffs required for converged results gradually increase. At the same time, the Path Expansion formalism becomes increasingly more successful at describing the spectrum. It is therefore recommended to stick with the real space PE calculations for extended fine structure, even for crystals. (The potentials and t-matrices needed for the PE calculation can still be calculated in k-space.)

Reciprocal space calculations with FEFF8 have been automated and are easy to use. A more technical description is given in the Appendix 8.e. Here, we mention only a few major points.

The k-space modules of FEFF8 are activated simply by placing the “RECIPROCAL” keyword in the input file. The crystal structure can then be specified by giving the lattice

vectors in Cartesian coordinates, and by giving the basis in one of several choices of units. FEFF8 will generate a real space list of coordinates based on this information, which can be used for the Path Expansion. No further input is required, except for the number of k-vectors used to sample the Brillouin Zone. This is also an important parameter in other reciprocal space codes, e.g. band structure codes such as WIEN2k. It is up to the user to converge the calculations in terms of this k-vector mesh.

The KKR structure factors are calculated for every energy loss as explained in Section 5.b.3. The Green's function and the core hole effect are calculated as explained in Sections 5.b and 5.b.1.

Using the symmetry of the crystal.

Crystals are characterized by their space group, which describes the symmetry of the crystal. This symmetry simplifies the problem in two ways. First, the Green's function matrix exhibits symmetry in terms of sites or angular momentum components. Therefore, it is necessary to calculate only part of it – the rest of the matrix follows by symmetry requirements (e.g., related to another part by a unitary transformation ; or zero because of symmetry). FEFF8 currently does not use this symmetry at all.

Second, the reciprocal lattice inherits symmetry from the real space lattice. Therefore, the reciprocal space integral in (5.3.1) can be reduced and less k-vectors are needed to calculate it. It is possible to use this symmetry in FEFF8. However, it is important to understand precisely which quantities one needs. If only the trace of the Green's function matrix is needed, then it is sufficient to simply integrate over the Irreducible wedge of the Brillouin Zone (IBZ). However, if off-diagonal components are needed, then the whole Brillouin Zone (BZ) needs to be reconstructed from the IBZ by applying unitary transformations. The need for off-diagonal elements is less exotic than it might seem, as they are clearly needed in order to add the core hole according to (5.3.2). This reconstruction is possible in FEFF8, but some care is required in using symmetry.

5.c.1. Convergence of the k-space FEFF8 calculations.

In a k-space FEFF8 calculation, the Green's function is calculated by numerically evaluating the Brillouin Zone integral (5.2.9). The integral is approximated by a sum over a finite mesh of k-vectors. The number of k-vectors in this grid is the major convergence parameter of the calculation. Convergence depends on the band structure of a specific material, and also on the desired accuracy. E.g., to simulate a spectrum with large life time broadening, it is not necessary to converge small details in the Density of States.

Different methods for evaluating BZ-integrals have been proposed, most notably special k-point methods^{115,116} and tetrahedron integration.¹¹⁷ FEFF8 uses the latter approach as described in Bloechl et al.¹¹⁷

Below we show, as a first example, the C K edge of diamond calculated with FEFF8.

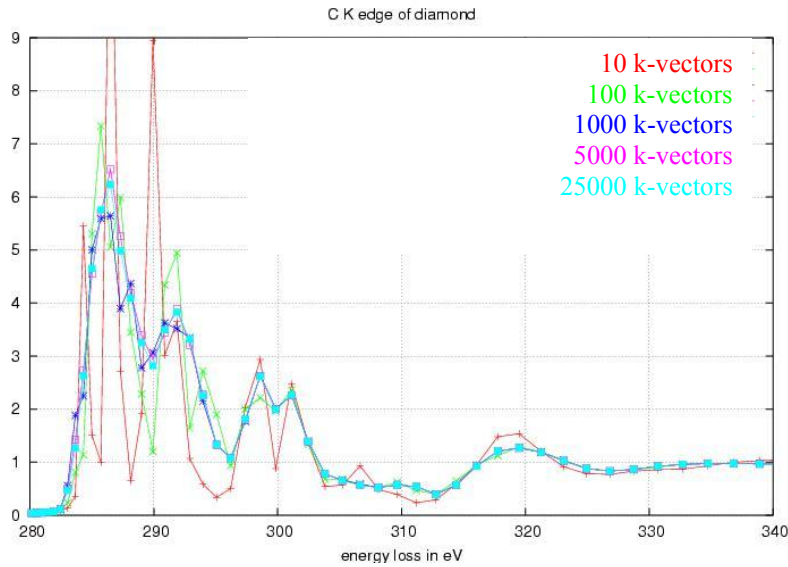


Figure 5-1 Convergence of the C K edge of diamond, calculated using FEFF8, with the number of k-vectors used for Brillouin Zone integration (10, 100, 1000, 5000 and 25000 k-vectors).

Reasonable convergence is achieved for 1000 k-vectors; good convergence for 5000 k-vectors. Even for 100 k-vectors, the peaks of the fine structure are in the right location, although the fine structure is clearly not converged.

As a second example, we calculate the Density of States of HOPG graphite.

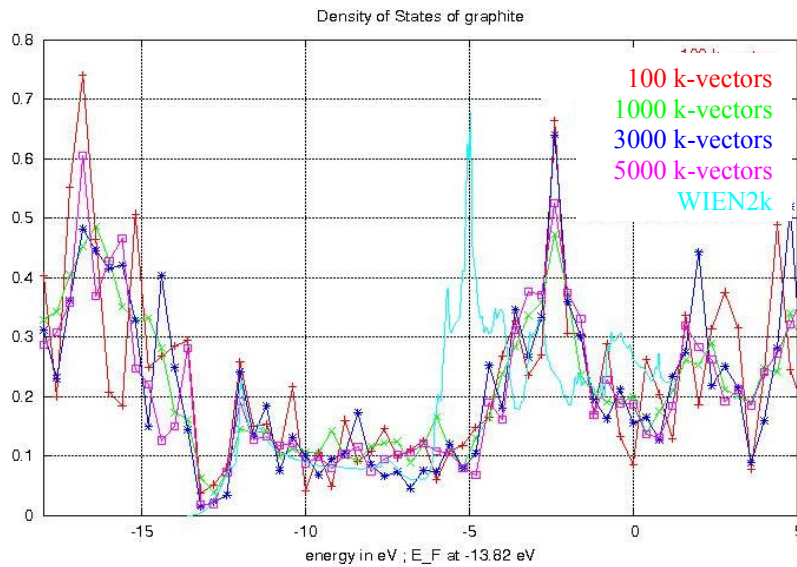


Figure 5-2 Total Density of States of graphite, calculated using FEFF8, and its convergence in terms of the number of k-vectors used for BZ integration. We show calculations using 100, 1000, 3000 and 5000 k-vectors in the full Brillouin Zone, compared to a converged WIEN2k calculation.

For the calculation of the unbroadened and much sharper DOS, convergence appears somewhat slower, and 5000 k-points are needed for a converged result. It is particularly interesting to look at the zero width band gap at the Fermi level (at -13.8 eV in the Fig.), which takes 3000 k-vectors to appear clearly.

For comparison, we show the DOS as calculated by the band structure code WIEN2k.⁷ We see that FEFF8 gets the essential features and fine structure of the π and σ bands right (as compared to WIEN2k), but that it overestimates the energy splitting between the two. We believe that this is a problem of the muffin tin potential, which approximates the potential by its spherical average. For anisotropic states such as the π bonds in graphite, this is a bad approximation. WIEN2k, on the other hand, is a full potential code. We expect that a generalization of FEFF8 to a full potential description will reduce this discrepancy between the two codes. Another important difference between WIEN2k and FEFF8 is that the latter uses a quasiparticle containing a self-energy, whereas the former doesn't include the self-energy.

The convergence of calculated properties with respect to the number of k-points used to evaluate Brillouin Zone integrals is typical of all methods that use a grid of k-points to sample such integrals. It's impossible to give a general recommendation for how many k-points to use, as the required number depends on the size of the Brillouin Zone (which is inversely proportional to the real-space unit cell) and on the complexity of the band structure. However, we find that in FEFF k-meshes of the order of 10^3 points are often sufficient to find good results for the systems (i.e., fairly small unit cells) studied in this work.

5.d. Verification of the real space finite cluster approximation

All the results that have been obtained using the Real Space Multiple Scattering method (e.g., the FEFF8 program⁸) for crystals rely on the assumption that one can calculate the spectrum of an atom in an infinite solid using its local electronic structure calculated in real space by replacing the solid with a finite cluster of atoms surrounding the probed atom.

It would be overly dramatic to say that the present work will prove or disprove the real space results for periodic structures. After all, people have previously observed that

1/ Typically, 100-300 atoms are sufficient in FEFF8 RSMS calculations to converge near-edge fine structure of XANES or ELNES.

2/ For many materials, one can obtain satisfactory agreement between RSMS calculations of spectra and actual experimental spectra.

3/ It has been theoretically motivated that the real space and reciprocal space treatments of multiple scattering Green's function theory ought to be equivalent.⁶

4/ For many materials, one can obtain satisfactory agreement between RSMS calculations of various material properties and other theoretical calculations that are based on periodic boundary conditions.⁸⁶

In the large majority of cases, the real space cluster approach to crystals has proven correct and efficient. However, there are cases where convergence in terms of cluster size is slow or elusive (e.g., the diamond C K edge).

Our new reciprocal space Green's function calculations provide an additional opportunity to validate the real space cluster approach. We can perform real and reciprocal space calculations within the exact same theoretical framework, with the exact same approximations and conventions. We can show that real space cluster calculations indeed converge to the same result as reciprocal space calculations, thereby effectively backing up the conclusions of Schaich⁶ numerically.

We show the Si K edge in Figure 5-3. We show the convergence in reciprocal space as a function of the number of k-vectors used for the BZ integration, and we show the convergence in real space as a function of the number of atoms used for the finite cluster FMS inversion. The t-matrices of (5.3.1) were calculated in k-space for k-space calculations, and in r-space for r-space calculations. One can clearly see that the two calculations converge to the same result.

We also provide comparison with experiment. Agreement is acceptable, but not excellent. It looks as if the core hole lacks strength in the calculations.

Similar results were seen in the calculation of other ionization edges as well.

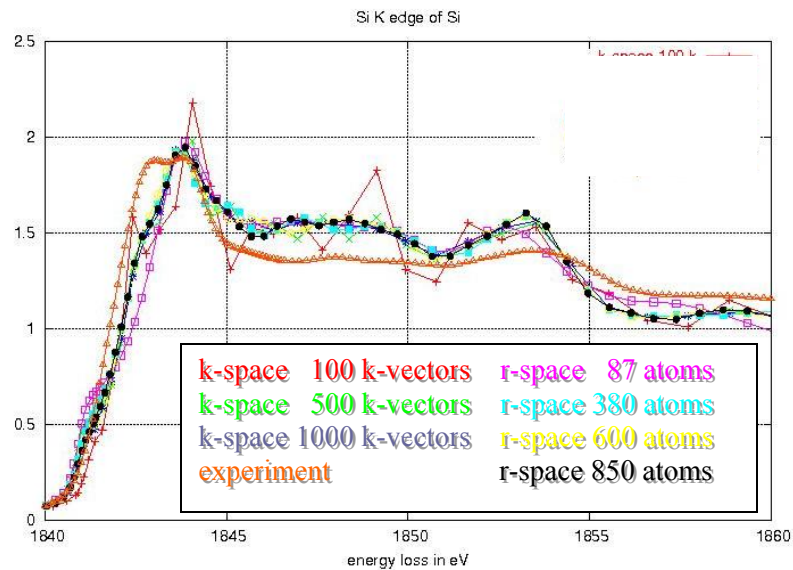


Figure 5-3 Convergence of the Si K edge as a function of cluster size in real space (short range) calculations, and as a function of Brillouin zone sampling in reciprocal space (long range). A measured spectrum is shown in red.

5.e. Core hole EELS without the supercell

5.e.1. Problems with the supercell core hole approach

We have already mentioned several times how the EELS excitation process is modeled in single particle theory by calculating the states of an ionized atom in a supercell. This approach is called the “Final State Rule” (FSR) because one calculates states in the ‘final’ picture of the EELS process (when the target atom is in its ionized state) and uses those to calculate a transition strength. This is a static model of a dynamic process, and so it would be unrealistic to expect it to be flawless.

Final state calculations are still commonplace, even though progress is steadily being made on more dynamic descriptions of the energy loss process. FSR calculations often yield good results, providing dramatic improvements in many cases over simple ground state calculations. However, it is worth demonstrating the problems that commonly occur with FSR core hole calculations.

Two questions in particular deserve our attention :
How problematic is supercell size convergence?
And : Which core hole should one use in the *ab initio* calculations?

5.e.1.1 Supercell size converge

First, we give a few examples of successful calculations, where the supercell FSR calculations do not run into problems.

We show *ab initio* WIEN2k calculations of the C K edge of a (7,0) single wall carbon nanotube (SWCNT).²

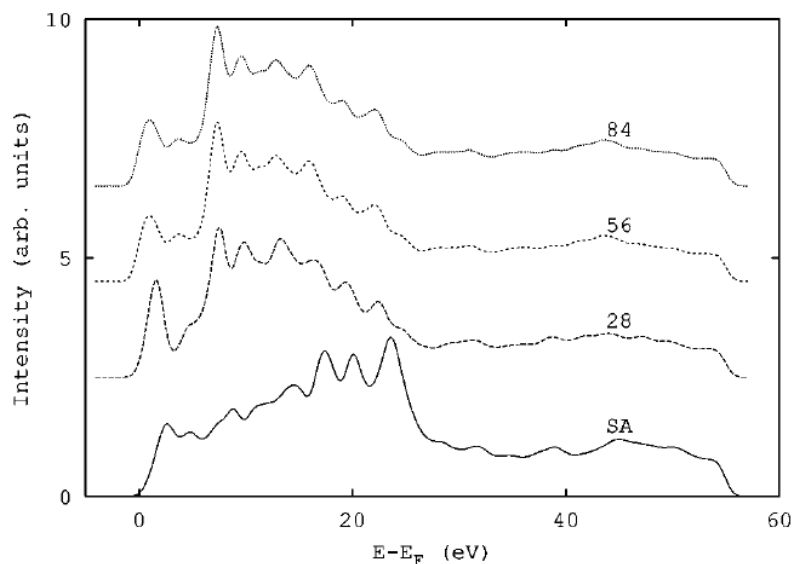


Figure 5-4 C K edge of a (7,0) single wall carbon nanotube calculated using WIEN2k. The beam energy is 300 keV, the collection angle is 3 mrad and the convergence angle is 1.9 mrad. Spectrum calculated without core hole (marked “SA” for Sudden Approximation) is shown together with a series of core hole calculations using super cells of increasing size : 1x (28 atoms), 2x (56 atoms) and 3x (84 atoms) the regular unit cell repeated along the axis of the nanotube.

Figure 5-4 shows a big difference between spectra calculated without core hole (labeled “SA”) and with core hole. The unit cell of the (7,0) SWCNT is a thin section of the tube cut perpendicular to its long axis, containing 28 atoms. Perpendicular to the tube, there is a large distance between the core hole atom in the unit cell and its mirror image in the neighboring cells. Along the axis of the tube, however, the unit cell is quite thin, and successive core hole atoms are only of the order of 2 bond lengths apart. This is close enough to introduce artifacts in the spectrum. Doubling and tripling the unit cell along the axis of the tube, the core hole EELS spectrum can be converged. Figure 5-4 shows clearly that a 28 atom cell is not large enough for convergence, but a 56 atom cell is.

As a second example, we show the O K edge of MnO_2 .²¹

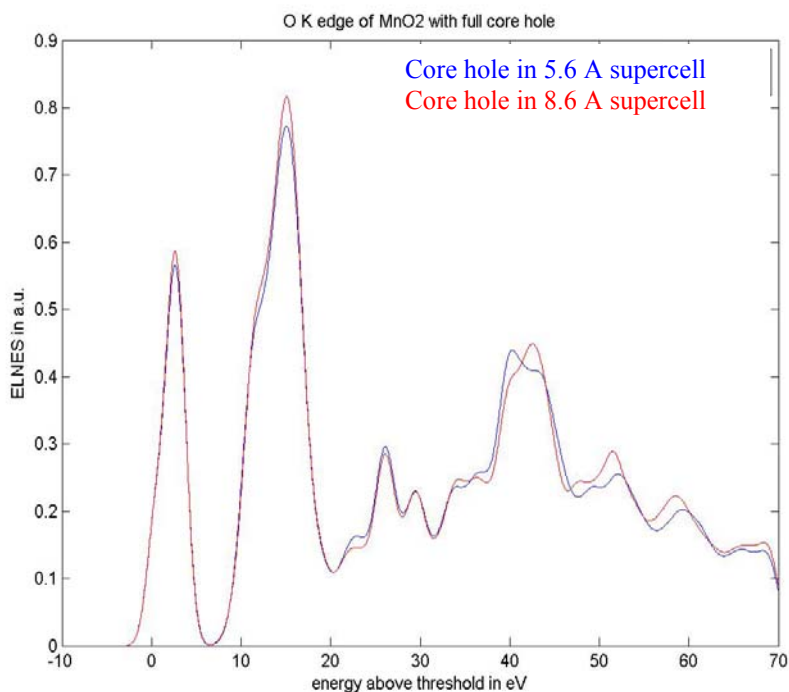


Figure 5-5 Convergence of the O K edge of MnO₂ with supercell size. Full core hole calculations are shown for a core hole - core hole distance of 5.8 Angstrom (blue) and of 8.6 Angstrom (red). The spectrum is already quite well converged for the smaller supercell.

The supercells shown for the O K edge of rutile TiO₂ have core hole – core hole distances of 5.8 Angstrom and 10.5 Angstrom. The supercells shown for the O K edge of MnO₂ have core hole – core hole distances of 5.8 Angstrom and 6.8 Angstrom. In both cases, the differences between the smaller and larger supercell are noticeable but far less dramatic than in the case of the SWCNT above. For many applications, the smaller super cell will suffice here.

However, in some cases convergence is hard or impossible to reach. A notorious case is the C K edge of diamond. Below we cite the work of Taillefer, ⁸³ in which the authors claim to achieve convergence of their calculations in terms of the size of the unit cell.

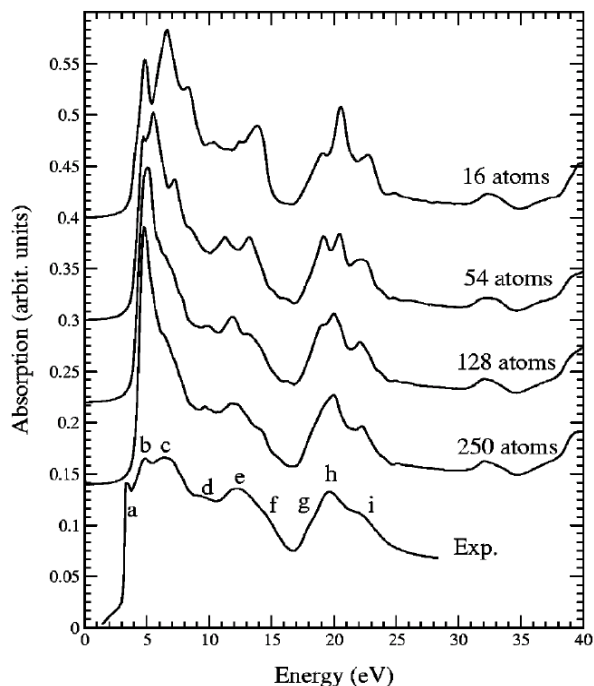


Figure 5-6 Calculated C K edge x-ray absorption spectra in diamond for different supercell sizes, compared with experimental data.¹¹⁸ A 286.1 eV shift was applied to the experimental spectrum.

However, the vertical offsets in Figure 5-6 are misleading. Certainly the *ab initio* results are converging well enough to conclude that they won't match the experimental data. But the strength of the excitonic peak at the threshold keeps increasing with increasing supercell size. In Figure 5-7 we show our own calculations, which reveal the same trend. The calculations were done using WIEN2k, which should be equivalent to the method used in Figure 5-6. One can see clearly, going from the ground state spectrum (black full line) to larger and larger supercells, that the oscillator strength keeps shifting down to the threshold. Clearly, one cannot claim convergence here.

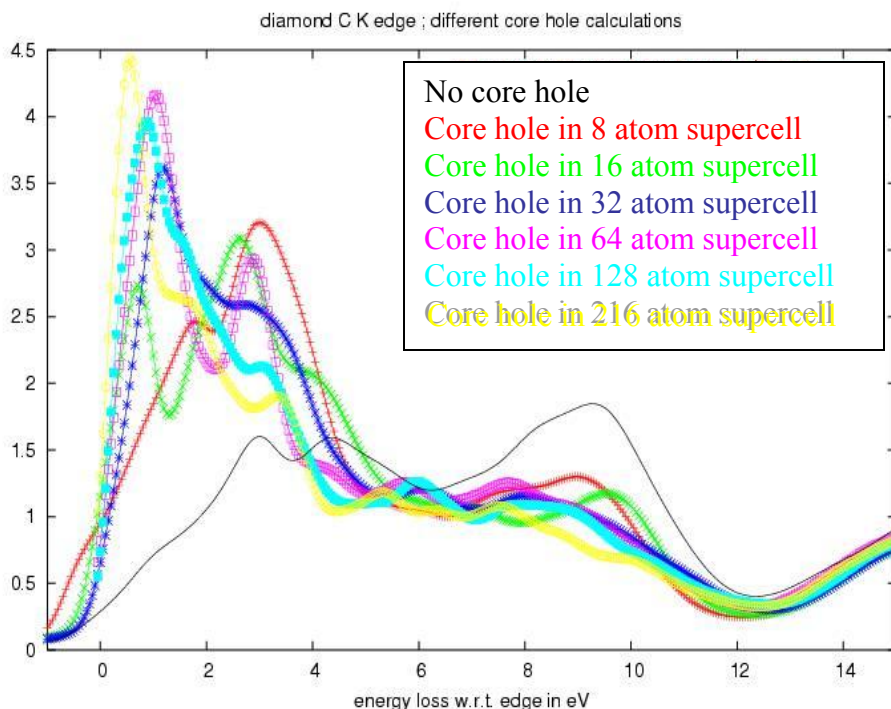


Figure 5-7 C K edge of diamond calculated using WIEN2k+TELNES2. A calculation without core hole (black) is compared with full core hole calculations of different supercell sizes : 8 atoms (red), 16 (green), 32 (dark blue), 64 (pink), 128 (light blue) and 216 atoms (yellow). As the core hole is introduced and the supercell size grows larger, the core hole keeps shifting more and more oscillator strength into the first peak at the threshold.

5.e.1.2 Which core hole should one use?

Generally, in a core hole calculation one removes one electron from the core state whose edge one is measuring. E.g., for the C K edge, one electron is removed from the C 1s orbital, which then has an occupancy of 1.0 in the core hole *ab initio* calculation. However, in principle one can think of the core state occupancy (or, equivalently, the strength of the core hole) as a variable parameter.

Specifically, people have proposed to use half a core hole (e.g., a 1.5 C 1s occupancy for the C K edge), the so-called Slater transition state.¹⁰² This approach ought to give correct transition energies, although it does not guarantee correct transition strength. We illustrate it on the Cu L₂₃ edge.¹¹⁹

The Slater transition state yields excellent agreement with experiment (Figure 5-8). Note also the continuous variation of the spectrum as a function of core hole strength in Figure 5-9.

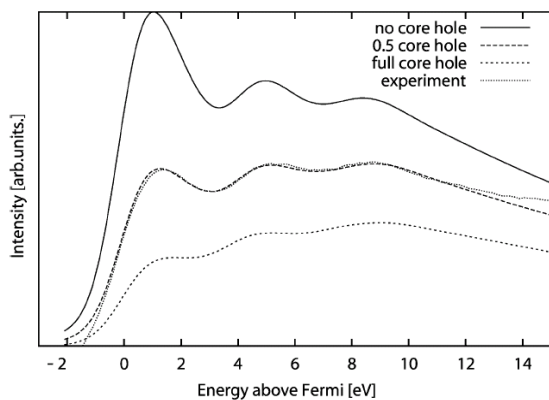


Figure 5-8 Cu L_{23} edge calculated by Luitz et al. using WIEN2k compared to experiment (dots).¹¹⁹ Calculations using a full core hole (short dashes), Slater transition state (long dashes), and no core hole (solid) are compared to experiment (dots).

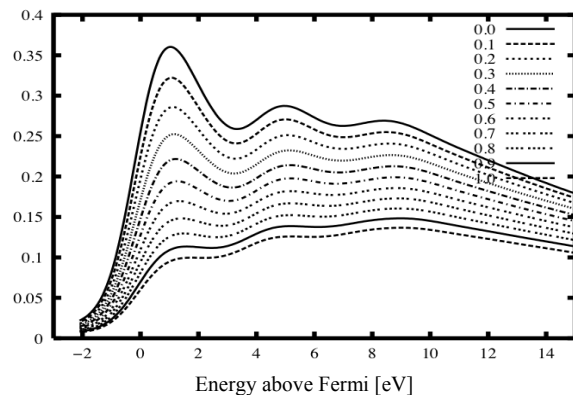


Figure 5-9 Cu L_{23} edge calculated by Luitz et al.⁷ using WIEN2k. The core hole fraction (i.e., the fraction of an electron removed from the initial state) is varied continuously between 0 and 1.

The situation gets more confusing when we look at the N K edge of GaN.⁸⁶ Below we show the N K edge of two different phases of GaN : cubic (or zincblende) in Figure 5-11 and hexagonal (or wurtzite) in Figure 5-10. In both Figures, graph (a) is the experimental result and graph (b) the best matching theoretical WIEN2k+TELNES2 calculation. Surprisingly, a Slater transition state calculation produces much better results for h-GaN, while a full core hole calculation works much better for z-GaN.

One can find a physical interpretation for this remarkable difference in terms of the screening of the core hole working differently in the two structures, leading to a different core hole strength. The optimistic take on this study then is that comparison between experiment and theory can teach us something about the screening of the core hole. The more critical observation is that the core hole is perhaps more of an *ad hoc* parameter than is sometimes admitted.

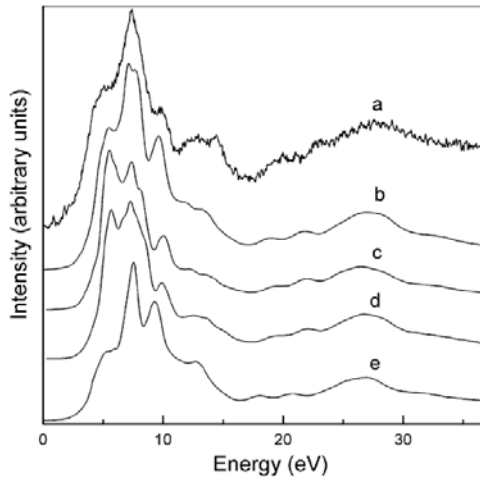


Figure 5-10 Comparison of experimental N-K edge in h-GaN and calculation with various parameter: (a) experiment with 0.2 eV resolution, collection semiangle 4.7 mrad, convergence semiangle, 0.2 mrad, dispersion 0.05 eV/ch; (b) 2x2x2 supercell, 0.5 core hole; (c) 2x2x2 supercell, full core hole; (d) 2x2x1 supercell, full core hole; and (e) without core hole.⁸⁶

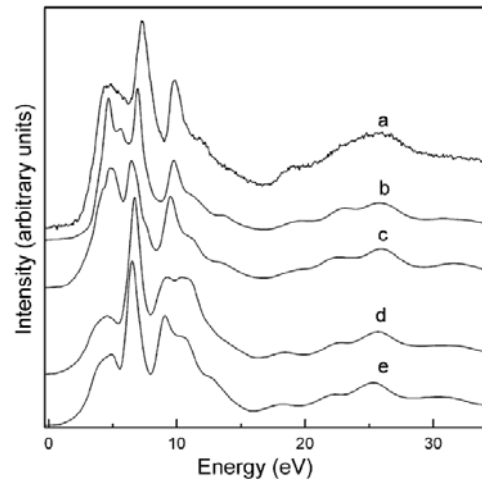


Figure 5-11 Comparison of experimental N-K edge in c-GaN and WIEN2k calculations with various parameters : (a) experiment with 0.2 eV resolution, collection semiangle 0.96 mrad, convergence semiangle, 0.2 mrad, dispersion 0.05 eV/ch; (b) 2x2x2 supercell, full core hole; (c) 2x2x1 supercell, full core hole; (d) 2x2x2 supercell, 0.5 core hole; and (e) without core hole.⁸⁶

I wish to discuss one last study, which in my personal opinion crosses the line between science and fitting. In what I see as a “core hole a la carte” study of the N K edge and B K edge of hexagonal BN, Moreau et al.¹⁰⁰ write: “We show that extremely good agreement [between experiment and theory] can be obtained over a 50 eV region” (Figure 5-12). They achieve this agreement by calculating the π region of the spectrum using a full core hole, and the rest of the spectrum by using a core hole of 0.1 strength (i.e., a 1s occupancy of 1.9 e). The agreement between their simulations and the measurements is indeed quite good.

Physically, there’s no problem with this concept, as screening is related to the dielectric response and is in general frequency (or energy) dependent. However, their approach of using different core hole strengths for different regions of the spectrum is not based on any model for frequency dependent screening, but seems completely *ad hoc*. Perhaps the concept of the core hole supercell Final State Rule model is being dragged beyond its limitations here.

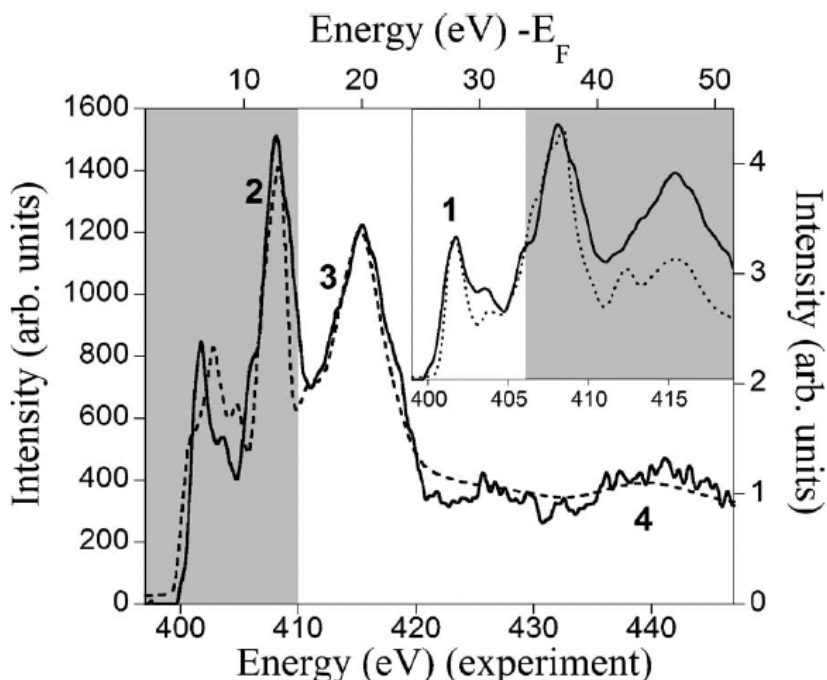


Figure 5-12 Comparison of experimental N K edge in h-BN (full line) with ELNES spectrum calculated using core hole strength 0.1 (dashed line). Inset : comparison of experiment and core hole strength 1.0 calculation in the π^* region.¹⁰⁰

The previously mentioned FSR calculations use a fully screened core hole (i.e., a core hole potential $v_{core\ hole}^{fully\ screened}$ or $0.5 v_{core\ hole}^{fully\ screened}$ or $0.1 v_{core\ hole}^{fully\ screened}$), but other approximations are possible, such as the RPA screened core hole⁸⁰ (i.e., a core hole potential $\epsilon^{-1} v_{core\ hole}^{fully\ screened}$) usually used in BSE calculations.

We cannot reach a general conclusion about how to calculate core hole EELS using a supercell. While good results are often found using a 2x2x2 supercell, there is no guarantee that such a simple prescription will avoid artifacts or convergence problems for any given system. Also, there are no general recommendations for what type of core hole to use (e.g., one or one half fully screened core hole), as even for seemingly similar compounds a different core hole may be required.

5.e.2. Results using k-space FEFF8

In the previous section, we illustrated two problems with the supercell approach to core hole FSR calculations : convergence of the supercell size, and the type of core hole to use. The “core hole without the supercell” approach presented in this dissertation (Sec.

5.a - 5.b), which is a combination of real space and reciprocal space Green's function techniques, addresses the former issue of supercell size convergence.

First of all, as there is no supercell, one does not need to worry about artifacts, and secondly, one does not need to study the computationally expensive convergence of larger and larger cells (cf. the carbon nanotube and the transition metal oxides).

Also, our technique is a solution for materials which are almost impossible to converge with conventional calculations, such as the C K edge of diamond.

However, we do not address the latter issue of which type of core hole to use. Although we do not discuss it in this study, all the possibilities and ambiguities of partial core holes are possible in our new FEFF8 calculations, too. (My personal stance on this is that it is best to keep *ab initio* calculations *ab initio*, and not stray from physics into fitting.)

Below we show results of the “core hole without the supercell” approach for the N K edge of wurtzite (hexagonal) GaN. Measurements were taken from Moreno et al.⁸¹ First, in Figure 5-13 we compare experiment to different types of FEFF calculations. Although the real space calculations are already quite successful for simulation of this particular edge, it is clear that our treatment using reciprocal space and a real space core hole yields the best results, improving in particular the description of the feature at 405 eV loss and the amplitude of the edge onset at 401 eV loss. We also notice that the full reciprocal space calculation (green) gives better results than a hybrid calculation (red) in which the potentials and scattering t-matrices were calculated in real space using a finite cluster, and the FMS calculation was then carried out in reciprocal space using these t-matrices.

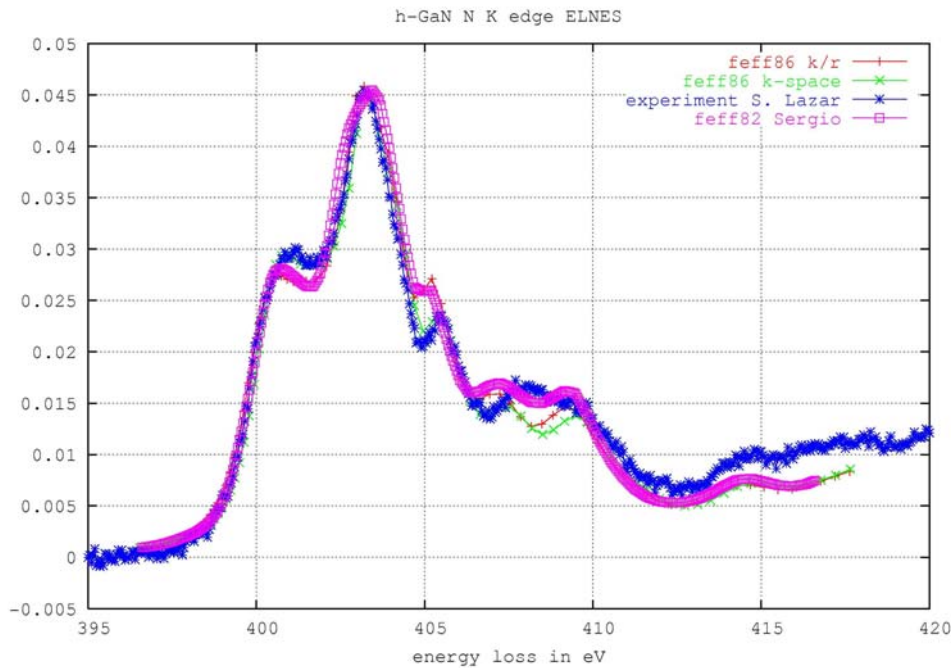


Figure 5-13 N K edge of GaN at 300 keV beam energy and collection angle 0.3 mrad and convergence angle 0.2 mrad, measured in 100 orientation. We compare the experiment (blue) to different FEFF calculations : real space calculation (pink), reciprocal space calculation (green), and a hybrid where the potentials were calculated in real space but the FMS calculation was done in reciprocal space (red). Spectra are aligned by hand and normalized at the second (403 eV) peak. Near the onset of the spectrum, the red and pink curves coincide, and the green and blue curves coincide.

Figure 5-14 shows a comparison of our reciprocal space FEFF calculations to the supercell approach, carried out using the WIEN2k + TELNES2 program. Although the agreement between the WIEN2k and the experimental spectrum is certainly good by common standards, the onset is not described correctly, and it is unclear how precise the feature at 405 eV is reproduced in the calculation. It is of particular interest to study the edge onset. It can be seen that as the supercell grows larger, intensity slowly transfers to the onset, bringing it close to the correct relative amplitude (if not yet position) for the largest supercell we studied (4x4x3). It is interesting to note here how the FEFF calculation might be seen as the convergence point of a series of calculations of increasing supercell size.

Of course, it is not expected that the WIEN2k and FEFF calculations would coincide perfectly, as the physics underlying each method isn't identical. E.g., FEFF uses a complex self energy, while WIEN2k uses a real exchange correlation potential. Also, WIEN2k is full potential, while FEFF uses a muffin tin potential.

Finally, we should mention computational efficiency. Whereas the FEFF spectrum was produced in of the order of 1 hour using 1 modern CPU, the WIEN2k convergence study took several days using multiple CPU's on a computer cluster³, with medium size calculations (e.g., 2x2x2 supercell) taking hours on a dozen of processors, and the largest calculations (4x4x3) taking 1-2 days on half a dozen of processors.

³ Calculations were performed on the Jaws cluster at the University of Antwerp, consisting of 30 dual Intel Xeon and AMD Opteron nodes at 2.4-3.1 GHz clock speed and 3-4 GB of RAM per node.

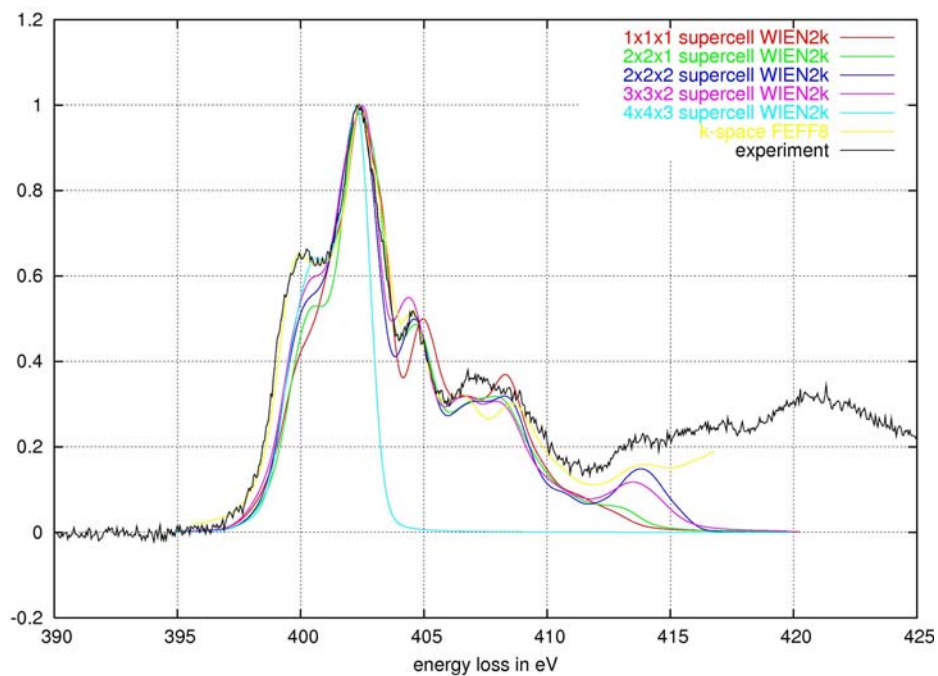


Figure 5-14 N K edge of GaN in the same experimental conditions as . The convergence of WIEN2k supercell size is studied and compared to a FEFF8 calculation (yellow) and experiment (black). Spectra were aligned by hand and normalized to the second peak (403 eV). The 4x4x3 spectrum ends abruptly because of computational limitations encountered in this very large calculation.

6. Conclusions

6.a. ‘State of the simulations’ for TELNES2 and FEFF

In the introduction to this dissertation we stated that improvements in *ab initio* calculations of EELS spectra were needed in two ways :

- * improve the calculation of simple model systems
- * learn how to model more realistic systems.

This dissertation has clearly – and, I believe, successfully – aimed to reduce the former problem. One cannot hope to simulate EELS spectra of any type of material successfully if any important parts of the physics of EELS are missing from the theory or its practical implementation in a software development. While a number of shortcomings remain to be remedied or need further investigation (see Sec. 6.c), I have developed improvements in two fundamental areas of *ab initio* EELS research.

First, it was recently discovered by Jouffrey et al.⁴ that it is necessary to use a relativistic theory for EELS in order to obtain correct scattering properties (*in casu* the magic angle) for anisotropic materials. I have presented the more rigorous derivation of Sorini et al.⁸⁹ of the results of Schattschneider et al.⁵ (Sec. 4.a). Next, instead of making the commonly used small impulse transfer approximation (Sec. 4.b), I derived a full angular momentum based formalism for relativistic ELNES (Sec. 4.c). This allows for arbitrary impulse transfer and arbitrary order of transition (i.e., dipole, quadrupole, etc.) and showed how this formalism connects to the theory of Schattschneider et al. I developed a new and improved “TELNES2” ELNES program (Sec. 4.d) of the benchmark DFT code WIEN2k, based on this relativistic formalism. I also improved the complementary real space multiple scattering program FEFF and implemented the contracted impulse transfer relativistic theory of Schattschneider et al. into it (Sec. 4.e) in terms of a cross section tensor. Thus I generalized two of the most important ELNES codes in the *ab initio* community to a relativistic formalism suitable for accurate calculations of anisotropic materials. WIEN2k describes periodic systems by solving the Schrodinger equation in reciprocal space using DFT, finding orbitals from which to calculate the EELS cross section. FEFF, on the other hand, describes arbitrary but finite systems by calculating the Green’s function in real space using Multiple Scattering theory. FEFF includes a complex self-energy, Debye-Waller factors for thermal effects, and other features that make it particularly well suited for spectroscopy. The two methods complement each other and both are useful for EELS research.

The validity of the relativistic formalism and its implementations was shown in Sec. 4.f, where the magic angle problem is revisited. The magic angle is that value of the collection angle (\sim detector aperture) for which the orientation dependence of the EELS spectrum disappears, greatly simplifying the interpretation of the experiment. The magic

angle is of theoretical interest because it is (in first approximation) material independent and therefore a direct test of the scattering theory. I first present the non-relativistic prediction of the magic angle (Sec. 4.f.1) and show how measured values are vastly different (Sec. 4.f.2), as illustrated on the C K edge of graphite. I rule out remedies within non-relativistic theory (Sec. 4.f.3), and provide analytic-numerical relativistic predictions in Sec. 4.f.4, in much better agreement with experiment. Finally, the magic angle is calculated *ab initio* using TELNES2 with WIEN2k, and using FEFF (Sec. 4.f.5). Both methods find the correct prediction for the magic angle. The full angular momentum resolved TELNES2 calculations give a magic angle almost 10% larger than the small impulse transfer approximated calculations (done by either FEFF or TELNES2), and are even closer to experimental value. The small but quite noticeable shortcomings of the small impulse transfer approximation are thereby illustrated. Also, beyond the somewhat abstract magic angle, we directly calculate the EELS cross section as a function of scattering angle using TELNES2, and compare to experimental measurements, finding very good agreement for the relativistic calculations (and quite bad disagreement for non-relativistic calculations ; see Sec. 4.f.5).

The second problem I worked on is that of core hole calculations. The excitation of the sample is influenced by the core hole that is created as an electron is excited from a core shell into an unoccupied state. As mentioned in the introduction, I work in the Final State Rule, meaning that this dynamic excitation process is modeled by single particle calculations (using either DFT or Green's function theory) of an excited atom with a hole in its core shell, embedded in an otherwise perfect and undisturbed crystal. While the periodic boundary conditions (PBC) of reciprocal space band structure codes make them more efficient and accurate for modeling perfect crystals than real space methods, these PBC become a liability when a core hole is introduced and, analogous to the impurity problem, needs to be treated in a supercell, leading to supercell size convergence problems (Sec. 5.e.1.1). This prevents us from routinely doing DFT core hole calculations, as convergence must always be checked and is sometimes impossible to achieve (e.g., for the C K edge of diamond). Such supercell problems are completely absent from real space methods, as these have no PBC and therefore no supercell. An additional ambiguity, which is not solved in this thesis, is that the amount of core charge that is removed from the core shell in a core hole calculation can be taken as $\frac{1}{2}$ (a Slater transition state) or as a variable *ad hoc* screening parameter, which provides flexibility at the expense of clarity. (It is seldom clear in advance which of these choices will provide the best spectrum.)

We have developed an approach that combines the best of the real and reciprocal world by working out a formalism for the calculation of the Green's function in reciprocal space (Sec. 5.b), very similar to impurity KKR theory. This formalism is added onto the real space multiple scattering code FEFF, making it now capable of switching between real and reciprocal space. Thus the perfect crystal can be treated efficiently and accurately in reciprocal space, and afterwards the core hole is added in real space (Sec. 5.b.1). Combined with the improvements described in the previous paragraph, the result is a new and improved FEFF code for *ab initio* relativistic EELS of crystals within the FSR, avoiding the complications and ambiguity of the supercell.

While more needs to be done before one can with a clear conscience turn *ab initio* EELS into black box tools, I believe that these two steps forward will present clear progress for the computational EELS community. The usefulness of the relativistic formalism is fundamental and will never expire. The final state rule calculations may be superseded by many-body theory calculations at some point, but they will likely remain the method of choice for some time, and the avoidance of the supercell can make FSR calculations more reliable and competitive.

6.b. Key results

Apart from the fundamental and methodological advances summarized in Sec. 6.a, a few results of more applied nature were obtained in this dissertation.

First of all, we succeeded in calculating the magic angle of the graphite C K edge (Sec. 4.f.4 and 4.f.5) and the angular scattering profile of the same edge (Sec. 4.f.5). By avoiding the small impulse transfer approximation of the contracted impulse transfer formalism, we appear to have reproduced experimental results even more accurately.

Using relativistic FEFF in its cross-section tensor formalism (Sec. 4.e), we show that it is in general not sufficient to use only the diagonal components of the tensor. One also needs to take the offdiagonal terms into account to obtain the correct EELS spectrum. These findings mirrored a more general discussion of “cross-terms” in Sec. 4.c.3.

Second, in Sec. 5.d we compared short range (real space) and long range (reciprocal space) calculations of the Si K edge using the new FEFF code. In agreement with the general findings of the electronic structure community, our precise comparison verifies the equivalence expected by Schaich⁶ to high accuracy. Though mostly of theoretical interest, this is a valuable result.

Third, in Sec. 5.e.2 we apply our new “core hole EELS without the supercell” approach using FEFF to the N K edge of wurtzite GaN measured in 100 orientation. Agreement with experiment is clearly improved over older, real space FEFF calculations. We also compare to supercell core hole calculations performed with WIEN2k and TELNES2. Although agreement with experiment and supercell size convergence of the WIEN2k/TELNES2 calculations are quite good for this application, they are not as good as the much simpler and faster FEFF calculations. Furthermore, the shoulder of the N K edge onset appears to slowly rise with increasing supercell size, allowing the interpretation of the “core hole without the supercell” FEFF calculations as the convergence point of a series of ever larger supercell calculations, where the FEFF result corresponds to a supercell of infinite size.

6.c. Outlook

It's an exciting time to be in the *ab initio* EELS field. Both the theory of EELS, computational power, and EELS experiments have now developed sufficiently to allow interesting and quantitative materials science. On the other hand, some challenges still remain.

Much attention has been paid to many body effects in the absorption spectrum. Time dependent density functional theory, Bethe-Salpeter theory, and multiplet theory have all produced promising results. Which theory or combination of theories will emerge as most useful, and in what form, is a question that still remains to be answered, as is the quality that we will in the end be able to achieve using these formalisms. It is also not clear how much many body theory, which is formally superior to but practically so much more demanding than one-particle models, is needed to improve on standard final state rule calculations (seeing, e.g., good results of final state rule calculations simply combined with multiplet calculations for some systems³⁰).

Closer to home, it will be interesting to develop more applications of the relativistic theory, including angle-resolved EELS measurements and the extension of the calculations to the low-loss regime.

All this still leaves the second goal of calculating more realistic samples unaddressed. Increasing computational power, allowing larger basis sets and more complex arrangements of atoms in the calculations, are one part of the answer. The other part must come from considering additional physical mechanisms present in real-life samples in a real microscope, ranging from finite temperature effects to considering structural defects, impurities and surface or sample shape effects on the spectrum ; from incorporating the microscope's beam, lenses and filters into the calculations to considering the interplay of elastic and inelastic scattering in crystals, which would require an approach based on the Mixed Dynamic Form Factor (MDFF).³³ The author's personal outlook is the development of a code that combines electron diffraction and EELS, currently a topic of interest in the community, as a next step to make *ab initio* EELS more realistic.

7. Acknowledgments.

There are some people in science who have, by themselves, revolutionized a whole field of science. They are very, very smart. Some of them have very messy hair. And they get the proverbial call from Stockholm, in recognition of the extraordinariness of their achievements.

Normal science isn't like that. It's teamwork, and the teams usually extend so far that the sun never sets on them.

This dissertation doesn't declare any sort of revolution, and it certainly isn't expecting any phone calls. (Let's ignore the messy hair for a moment, please.) However, many people have contributed to my five year odyssey in physics. Some of their guidance and contributions were vital to my work, and deserve being included in this thesis.

Where some people are fortunate enough to have one good supervisor for guidance, I've had the extravagant pleasure of having three. I wish to thank Prof. Dirk van Dyck for initiating my doctoral work, for providing long term vision at the beginning of my project, and for continued vital support later on. I wish to thank Prof. Dirk Lamoen for being my supervisor during the first 2 ½ years of my doctoral work, which I spent in Antwerp, and for coaching me into the sometimes complicated and confusing world of computational physics. And I wish to thank Prof. John J. Rehr for making me a part of his research group in the last half of my doctoral work, which I spent in the U.S.A., and for being a truly excellent source of guidance and inspiration.

There have been other important influences that I wish to acknowledge. Early on, when I was mostly working with the WIEN2k code, I found a warm "second home" in the WIEN family. I wish to thank especially Cecile Hébert and Joachim Luitz (and Anne Sophie and Joseph Andre) for their extraordinary kindness and their invaluable scientific input. I don't think any other program was ever so much fun to develop as TELNES2, and DFTEM was simply wonderful. I also want to thank Prof. Peter Schattschneider for his hospitality and generous sharing of his deep insights in EELS. Finally, Prof. Peter Blaha should not go unmentioned here, as he so kindly guided me into the family of "WIEN experts" ; and nor should Prof. Jorge Sofu, who shared early morning runs with me in the Wiener Wald, and invited me to a delightful WIEN2007 workshop.

From my U.S.A. / FEFF8 period, a big "thank you" goes out to Zachary Levine for a rich supply of intellectual stimulation. Thanks also to Micah Prange, Josh Kas, Adam Sorini, Joshi Takimoto, Fernando Vila, Hadley Lawler, and Alexei Ankudinov of the FEFF group at the University of Washington, for all the experiences of being in a great research group.

Thanks also to the many people in Antwerp who've been great colleagues to me. Most of all, to John Tatini Titantah, for being a good friend and fellow WIEN97/2k pioneer. Thanks also to Sorin Cucu for being on the TSM team. Thanks to Wim Tirry, Prof. Nick

Schryvers, and Pavel Potapov for fun EMAT collaborations. Thank you to everyone at EMAT and TSM.

At the end of this long list, I wish to make special mention of two people, Jo Verbeeck and Stefaan Cottenier. I haven't interacted with you nearly as much as I would have liked to, but even as friends in the background, you have been tremendously important. You both possess that precious sense of integrity that defines a true scientist more than anything else. I do not know if today's citatocracy will ever honor you with that phone call from Sweden, but you can count on hearing from me (if, perhaps, from less reputable places).

Finally, there are those who have chosen to be in my life irrespective of physics, perhaps in spite of physics. It would be rather silly to dedicate this dissertation to you, now wouldn't it? Rest assured, I have bigger things in mind for us.

8. Appendices

8.a. Bibliography

Publications in refereed journals :

- 1./ Density functional theory calculations of energy-loss carbon near-edge spectra of small diameter armchair and zigzag nanotubes: Core-hole, curvature and momentum-transfer orientation effects, J.T. Titantah, K. Jorissen, D. Lamoen. Phys. Rev.B 69 125406 (2004).
- 2./ Effect of charge transfer on EELS cross sections in Mn and Ti oxides, P. Potapov, K. Jorissen, D. Lamoen, D. Schryvers. Phys. Rev. B 70, 045106 (2004).
- 3./ Quantitative determination of the crystal structure of Ni₄Ti₃ precipitates, W. Tirry, D. Schryvers, K. Jorissen, D. Lamoen. Material Science and Engineering A 438, 517 (2006).
- 4./ Electron diffraction structure refinement of Ni₄Ti₃ precipitates in Ni₅₂Ti₄₈, W. Tirry, D. Schryvers, K. Jorissen, D. Lamoen. Acta Crystallographica Section B 62, 966 (2006).
- 5./ Practical aspects of electron energy-loss spectroscopy (EELS) calculations using FEFF8, M.S. Moreno, K. Jorissen, J.J. Rehr. Micron 38 (1), 1-11 (2007).
- 6./ Real Space Multiple Scattering Calculations of Relativistic Electron Energy Loss Spectra, K. Jorissen and J.J. Rehr., submitted to Phys. Rev. B. (2007).
- 7./ Ab initio relativistic calculations of Electron Energy Loss Near Edge Structure - the new and improved TELNES2 program, K. Jorissen, J. Luitz, A. Sorini, and C. Hébert, in preparation, (2007).
- 8./ Relativistic core hole EELS calculations without the supercell, K. Jorissen and J.J. Rehr, in preparation (2007).

8.b.Glossary

APW	Augmented Plane Waves
BSE	Bethe-Salpeter equation
(I)BZ	(Irreducible part of the) Brillouin Zone
(M)DFF	(Mixed) Dynamic Form Factor
DDSCS	Double Differential Scattering Cross Section
DFT	Density Functional Theory
(J,L)DOS	(Joint, Local)Density Of States
EDX	Energy Dispersive X-rays
EELS	Electron Energy Loss Spectroscopy
ELNES	Energy Loss Near Edge Structure
(k,...)eV	(kilo,...) electron-Volt
EXAFS	Extended Absorption Fine Structure
EXELFS	EXtended Energy Loss Fine Structure
FEG	Field Emission Gun
FMS	Full Multiple Scattering
FFT	Fast Fourier Transform
GGA	Generalized Gradient Approximation
HF(R)	Hartree-Fock(-Roothaan)
KKR	Korringa-Kohn-Rostoker
KS	Kohn-Sham
LAPW	Linearized Augmented Plane Waves
LCAO	Linear Combination of Atomic Orbitals
LDA	Local Density Approximation
LMTO	Linearized Muffin Tin Orbitals
LO	Local Orbital
MFP	Mean Free Path
MS	Multiple Scattering
PBC	Periodic Boundary Conditions
PBE(96)	Perdew, Burke, Ernzerhof (-EXCHANGE-CORRELATION-functional)
PE	Path Expansion
PP	PseudoPotential
PW	Plane Wave
STM	Scanning Tunnelling Microscope
SWNT/MWNT	Single/MultiWalled NanoTube
TDDFT	Time-dependent Density Functional Theory
TEM	Transmission Electron Microscope
UPS	Ultraviolet Photoelectron Spectroscopy
XANES	X-ray Absorption Near Edge Structure
XAS	X-ray Absorption Spectroscopy
EXCHANGE-CORRELATION	Exchange-Correlation
XPS	X-ray Photoelectron Spectroscopy
ZLP	Zero Loss Peak

8.c.The WIEN2k program TELNES2

8.c.1. Introduction.

TELNES2 is a program that calculates theoretical Electron Energy Loss Near Edge Spectra, taking calculated electronic structure information as input. The central calculated quantity is the double differential scattering cross section (DDSCS), which is essentially determined by the dynamic form factor (DFF).

The formalism implemented in the program is described in [Nelhiebel], apart from relativistic corrections implemented only as of the present version (11/2004).

The current version only works as a part of the WIEN2k [ref.] package, but modifications to input routines will enable us to use it with other electronic structure software as well.

History.

In the beginning, there was TXSPEC (written by Joachim Luitz in 1996), which is a WIEN-program that calculates X-ray absorption and emission spectra.

In 1997-1998 Pierre-Henri Louf (Inst. f. Angew. u. Techn. Physik, TU Wien) developed the TELNES program, meant for the calculation of core loss EELS spectra in WIEN97, and based on TXSPEC.

In 1998-1999, the TELNES program was modified by Michael Nelhiebel (of the same group).

The implementation of TELNES into the WIEN code and its graphical interface was done by Joachim Luitz.

In 2004 Kevin Jorissen (EMAT, University of Antwerp, Belgium), J. Luitz and C. Hébert modified the program, added the relativistic corrections and other features, and changed the name to TELNES2.

Contact Information.

You are welcome to ask questions about the ELNES programs on the WIEN2k Mailing List (see www.wien2k.at for more information on the WIEN2k Mailing List).

If necessary, you can contact K. Jorissen at kevin.jorissen@ua.ac.be.

This document.

This text is meant to help users understand and use the ELNES program.

Comments, questions and error reports may be addressed to the author directly at kevin.jorissen@ua.ac.be.

The TELNES2 documentation contains two parts :

- The first part (user's manual – this document) is aimed at users who wish to understand the usage, merits and shortcomings of the program, but are not interested in technicalities or in changing the source code ;
- The second part (programmer's manual) is aimed at users who wish to adapt the program to their needs, or wish to understand it at a technical level.

If you are simply a user, please help save some trees and don't print the programmer's manual (you can omit this page, too ;-)).

Notations.

In this text, the following notations will be used :

- E_0 energy of the electron beam before interaction
- E energy loss (energy transferred from beam electron to sample)
- \mathbf{k}_0 wave vector of the beam electron before scattering
- \mathbf{k} wave vector of the beam electron after scattering
- \mathbf{Q} the impulse transfer $\mathbf{Q} = \mathbf{k}_0 - \mathbf{k}$
- α the microscope convergence semi-angle
- β the detector collection semi-angle

Bold symbols are vectors; their length is denoted by the same symbol (but not bold).

8.c.2. What is calculated?

The TELNES2 program calculates the double differential scattering cross section on a grid of energy loss values and scattering impulse vectors.

This double differential cross section is integrated to yield a (single) differential cross section, which is written to file. The cross section may be differential with respect to energy (TELNES2 integrates over \mathbf{Q}) or with respect to impulse transfer (ELNES integrates over E). The latter case allows to study the angular behaviour of scattering.

Generally, the DDSCS is given by [Nelhiebel]

This formula takes into account the relative orientation between sample and beam. If this is not necessary (because the crystal is isotropic, or the sample is polycrystalline), the formula may be averaged over 4π , giving a much simpler equation :

Both equations are implemented in TELNES2.

8.c.3. Using the program.

You need to do the following things :

* Edit case.innes and make sure all of its options are set to produce the spectrum you want.

* Make sure all necessary input files are ready. (In the following description, ‘case’ should always be replaced by the name of your working directory.)

Case.struct and case.innes are always required.

Depending on your input settings, you will require at least one of case.dos, case.xdos and case.qtl.

Depending on your input settings, you may require also case.qtl, case.rotij, case.vsp, or additional files of which you have specified the name in case.innes

* If you are working on the command line : run ‘x elnes’.

If you are working in the web browser w2web, select Tasks/ TELNES2, and click the corresponding button.

* Check elnes.error and case.outputelnes to make sure that nothing unexpected has prevented the calculation from finishing successfully.

* Analyze the results. You will certainly want to look at the spectrum in case.elnes, and perhaps also at the partial spectra in case.sdlm and the cross term contributions in case.ctr.

8.c.4. The master input file case.innes.

TELNES2 needs one input file that tells it what to do. This is the case.innes – file.

The innes-file consists of two parts : a first block with required input, and a second block with optional input. In fact, the second part may be omitted altogether.

The simplest input file contains only the first block, and looks like this :

```
Graphite C K edge of first atom.
1          (atom)
1, 0      (n, l core)
285       (E-Loss of 1st edge in eV)
300       (energy of the incident electrons in keV)
5.0  1.87 (collection semi-angle, convergence semi-angle, both in
mrad)
5 3       (NR, NT, defining the integration mesh in the detector
plane)
END
```

This part of the file is not formatted. This short file is sufficient to run ELNES. Let's have a look at its contents :

Line number	value	explanation
1	‘Graphite ...’	Title (of no consequence for the calculation)
2	1	Atom number as given in case.struct (the index which numbers inequivalent atoms)
3	1 0	main and orbital quantum number n and l of the core state; e.g. 1 0 stands for 1 s
4	285	energy of the edge onset in eV (here for the C K edge)

```

5      300      beam energy in keV
6      5.0 1.87  detector collection semi-angle and microscope convergence semi-
angle in mrad
7      5 3      parameters NR and NT which determine the mesh used for
sampling the distribution of Q-vectors allowed by collection and convergence angles
8      END      keyword telling the program that there is no more input to read

```

In fact there are many more parameters that specify the calculation. In the previous example, default settings were used for these parameters. They can be set by specifying a keyword and the corresponding value of the parameter.

Our input routine is not very intelligent, so please obey the following rules :

- * start every line at the first position.
- * use only capitals for the keywords.
- * blank lines are allowed, but not lines starting with !, *, or whatever. (As a matter of fact, you can insert comment lines, but only between two keys, and starting from the fifth column.)
- * though only the first four characters of the keyword are considered, I recommend using the full keyword for clarity.
- * end your input with the END keyword.

Allowed keywords are :

OUTPUT

n e.g. : 1 (default : 0)

Specifies how much output you'll get. n is an integer of value 0 (only basic output; default), 1 (medium output) or 2 (full output, including less useful and more technical information).

ATOMS

n1 n2 e.g. : 1 3

In case.struct, the inequivalent atom number corresponds to a class of equivalent atoms. Equivalent positions n1 to n2 will contribute to the spectrum (default : sum over all atoms in the equivalency class). Since all equivalent atoms have identical electronic structure up to a symmetry operation, this will simply yield a prefactor *(n2-n1) for the orientation averaged spectrum, but as each equivalent atom has a different orientation with respect to the beam, this will change the shape of an orientation sensitive spectrum.

ENERGY GRID

emin estep emax e.g. : 0.0 0.02 25.0 (default : 0 0.05 15)

The energy grid on which the spectrum is evaluated, starting from emin and going to emax in steps of estep. All values are in eV and are with respect to the Fermi energy == the threshold.

DETECTOR POSITION

θx θy e.g. : 0.5 0.5 (default : 0 0)

It is possible to place the detector not in the 000 direction but move it away from the incoming beam. Consider the centre of the detector aperture as a point in a plane with the 000 spot as its origin; then θ_x , θ_y are the Cartesian coordinates in mrad of this point.

MODUS

m e.g. : a (default is e)

The SCS is differential with respect to energy if m=e ('energy') and with respect to impulse transfer/scattering angle if m=a ('angles').

SPLIT

splitting energy e.g. : 2.7

branching ratio e.g. : 1.4

If the initial state has an orbital quantum number larger than 0, it will generate two superposed edges : one corresponding to $j=l-1/2$, and one corresponding to $j=l+1/2$ (e.g., for the 2p initial state we have a L3 and a L2 edge). The splitting energy sets the energy separation of the two edges and should be given in eV (here, L3 is at the energy specified in the beginning of case.innes, and L2 is 2.7 eV higher). The branching ratio is a scaling factor (e.g., here the ratio of intensities L3/L2 would be set to 1.4). By default, the splitting energy is calculated by the program, and the branching ratio is set to its statistical value of $(2l+2)/2l$.

Specifying a negative value for either of the parameters restores the default behaviour.

WRONG

This key tells the program not to use the relativistic corrections to the scattering cross section. This option allows to generate spectra identical to output of the TELNES program. By default (much recommended!!), the relativistic corrections are used.

INITIALIZATION

make_dos write_dos e.g. F F (default : T T) (F for false, T for true)

make_rotation_matrices write_r_m e.g. T F (default : T T)

Elnes needs many ingredients for its calculations, and this key defines how it gets two ingredients : the (cross) density of states, and the rotation matrices (used for transforming Q-vectors from one atom to an equivalent atom). On each line, the first entry says whether or not the ingredient has to be calculated (T : calculate; F : read from file), and the second entry says whether or not the ingredient has to be written to file (T : write; F : don't write).

If makedos=T, a file case.qtl must be present from which the dos will be calculated.

If makedos=F, then either a file case.dos or a file case.xdos containing the (x)dos must be present.

if make_r_m=T, rotation matrices will be calculated from the data in case.struct.

If make_r_m=F, a file case.rotij containing the rotation matrices must be present.

If write_r_m=T, a file case.rotij is written.

If write_dos=T, a file case.dos or case.xdos will be written.

The calculation of the rotation matrices is computationally negligible, but if orientation sensitive spectra are calculated, it is recommended to write the xdos to file and not calculate it over and over again.

QGRID

qmodus e.g. L (U by default)

(θ_0 e.g. 0.05 (no default value))

A collection and convergence angle α and β allow scattering angles up to $\alpha+\beta$ and a corresponding set of \mathbf{Q} -vectors ($\mathbf{Q}=\mathbf{k}_0-\mathbf{k}$). This set (a circle of radius $\alpha+\beta$) is sampled with a discrete mesh. Three types of mesh are implemented :

U a uniform grid, where each \mathbf{Q} -vector samples an equally large part of the circle. Sampling is performed by drawing NR circles inside the big circle, and choosing $(2i-1)$ NT points on circle i , giving $\text{NR}*\text{NR}*\text{NT}$ points in total.

L a logarithmic grid, with also NR circles; but now the distance between each circle increases exponentially. There are $(2i-1)$ NT points on circle i , and $\text{NR}*\text{NR}*\text{NT}$ points in total. Circle i is at radius $\theta_0 \exp((i-1) dx)$, where dx depends on NR, α and β .

l a one dimensional logarithmic mesh; there are NR circles at exponential positions, and only one point on each circle (so NR points in total). This means we sample a line in the detector*beam plane. An economic way of getting spectra as a function of scattering angle in cases with symmetric scattering.

The line specifying θ_0 is to be omitted for the U grid.

ORIENTATION SENSITIVE

$\gamma_1 \gamma_2 \gamma_3$ (e.g. 0.0 40.0 0.0) (no default value)

This key tells the program not to average over sample to beam orientations, but to use the particular sample to beam orientation defined by the three Euler angles (to be given in degrees). If the ORIENTATION SENSITIVE key is not set, the program will average over all orientations (this is the default behaviour).

SELECTION RULE

type (e.g. : q) (default : d)

The formula for the DDSCS contains an exponential factor in Q , which we expand using the Rayleigh expansion, and labelling the order of each term as lambda. This key allows to keep some terms and discard others. Possible settings for 'type' are :

m : calculate monopole contribution only

d : dipole only (this is default)

q : quadrupole only

o : octopole only

n : no selection rule, calculate all terms

0-9 : all terms up to the specified value (e.g., 1 means monopole + dipole)

Be aware that sometimes not all these terms will be available ; e.g., for a M45 edge the quadrupole term $l=|c+2|=4$ is not given by the wien2k code (wien2k gives us the DOS only up to $l=3$).

LSELECTION RULE

type (e.g. : q) (default : d)

This key does not restrict the terms in the expansion of the exponential; it limits the l -character of the final state that is used. E.g., for a K edge with type=d, only final states with p character are allowed. There is a subtle difference between this situation and the common dipole approximation, though it is not expected to make much of a difference.

Below is an example of a case.innes file containing all listed options :

```

Graphite C K edge of first atom.
1          (atom)
1, 0      (n, 1 core)
285       (E-Loss of 1st edge in eV)
300       (energy of the incident electrons in keV)
5.0 1.87  (collection semi-angle, convergence semi-angle, both in
mrad)
5 3       (NR, NT, defining the integration mesh in the detector
plane)

OUTPUT
2          (full output)
ATOMS
1 1       (first atom, last atom)
ENERGY GRID
0.0 0.05 10.0 (minimum energy, energy step, maximum energy)
DETECTOR POSITION
0.0 0.0    (thetax, thetay)
MODUS
energy     (DDSCS w.r.t. what?)
SELECTION RULE
n          (selection rule)
LSELECTION RULE
N
SPLIT
3.52      (splitting energy)
0.2       (branching ratio)
INITIALIZATION
F F       (dos and xdos handling)
F F       (handling of rotation matrices)
ORIENTATION SENSITIVE
0.0 40.0 0.0 (alfa, beta, gamma - 3 Euler angles, in degrees)
QGRID
U
END

```

8.c.5. Files used by the TELNES2 program.

For input :

filename	read if	comments
case.innes	always	defines calculation
case.struct	always	defines crystal structure
case.vsp	core wave functions have to be calculated	contains spherical component of the crystal potential
case.rotij	rotation matrices have to be taken from input	contains matrices that transform between equivalent atoms
case.dos	DOS has to be taken from input	contains l-resolved density of states
case.xdos	XDOS has to be taken from input	contains l,m,l',m' resolved cross density of states
case.qtl	DOS or XDOS has to be calculated, or Fermi energy is not specified in case.innes	contains partial 'charge' components, and Fermi energy
case.kgen	DOS or XDOS has to be calculated	contains k-mesh that samples the Brillouin Zone

It is also possible to read core wave functions from file. In that case the name of the input file is specified in case.innes.

For output :

filename	written if	comments
case.outputelnes	always	main log file
case.elnes	always	contains total spectrum
case.sd1m	verbosity > 0	contains partial (l,m) spectra
case.ctr	verbosity > 0 and calculation is orientation sensitive	contains selected (l,m,l',m') cross term contributions to spectrum
elnes.error	always	contains error message
case.corewavef	core wave functions were calculated and verbosity > 1	contains core wave functions
case.final	verbosity > 1	contains APW radial basis functions for final states at selected energies
case.rotij	user has asked to write rotation matrices	contains matrices that transform between equivalent atoms
case.ortho	verbosity > 1	contains scalar products of initial and final states

case.matrx	verbosity > 0 and spectrum is energy-differential	contains proportionality between partial DOS and spectrum for each l-value
case.cdos	calculation is orientation sensitive. verbosity > 1 or user has asked to write DOS	contains selected (l,m,l',m') cross DOS terms (l!=l' or m!=m')
case.dos	calculation is orientation sensitive or DOS is calculated ; furthermore, verbosity > 0 or user has asked to write DOS	contains DOS, depending on context for every l or for every l,m
case.xdos	calculation is orientation sensitive. verbosity > 1 or user has asked to write XDOS	contains all XDOS components (not very suitable for human reading ...)
case.sp2	calculation is orientation sensitive, the spectrum is angular differential, and verbosity > 1	integrated cross sections as a function of collection angle for all l-values (careful : possibly confusing header)
case.angular	calculation is orientation sensitive, the spectrum is angular differential, and verbosity > 1	differential cross section as a function of scattering angle for all l-values (careful : possibly confusing header)

8.c.6. Practical considerations.

Most of the options are self-explanatory, and the user should just pick those that suit his purposes.

Some points are worth making :

* Especially for orientation sensitive calculations, the calculation of the (X)DOS takes a lot of time. Although for safety reasons calculations of the (X)DOS is default, the user can save a lot of time by calculating this once for a sufficient energy range, saving it to file, and from then on use the INITIALIZATION option to read (X)DOS from file.

* I recommend to prepare a suitable dos/xdos file after finishing the self consistency calculation, so that vector files and/or qtl files do not have to be stored (they take a lot of disk space!) or recalculated (this may require several hours for large calculations). Make sure that the energy mesh is fine enough and extends up to sufficiently high energy. The dos-files can be compressed to save even more disk space.

* The parameters NR and NT are the only input variables that do not have a physical meaning. They are simply the number of points used for evaluating an integral numerically. They have to be converged by the user, and we do not provide 'reasonable default values'.

* It is still possible not to use the relativistic corrections. However, this is provided for testing and for compatibility reasons only. This feature should **not** be used for real work.

8.c.7. Compatibility with TELNES.

* The TELNES2 program is incompatible with its predecessor, TELNES. Input files and DOS files for TELNES will not work for TELNES.2 Also the format of input DOS has changed. When switching to TELNES,2 you have to change case.innes and recalculate DOS.

When switching off relativistic corrections and matching input options correctly, TELNES2 spectra should be identical to TELNES spectra.

8.c.8. Major differences with respect to the previous release (i.e., TELNES).

* The old F-option does not exist anymore (it was meant for orientation sensitive edges in high symmetry crystals, and could save some time compared to the current implementation). The current 'averaged' and 'orientation sensitive' modes correspond to old N and H calculations, respectively.

* The limited MDFF-functionality of TELNES has been removed.

* The feature to calculate several spectra for different detector positions with just one call has been removed. The simplest shell script can do the same thing, wasting only a small amount of computing time and producing much better output.

* Relativistic corrections to the scattering cross section are added.

* Spectra can now be given either as a function of energy or as a function of impulse transfer / scattering angle.

* Core wave functions can now be read from file.

* Fermi energy can be specified in case.innes, thus removing the need for case.ctl once the DOS is calculated, which may save considerable disk space.

* Splitting energy between $j=1+1/2$ and $l-1/2$ edge can be calculated by the program.

* Rotation matrices and Bravais matrix can be calculated by the program.

* Selection rules can be imposed in a more straightforward way. Contributions (monopole, dipole, ...) can be separated more easily.

* Branching ratio can be specified in the input.

* New formula for integration over collection and convergence angle which does not consider them to be equivalent anymore (switching them multiplies the complete spectrum by a constant).

* The mesh of Q-vectors can now be chosen in three ways : uniform mesh (as in TELNES), logarithmic mesh, or one-dimensional logarithmic mesh. This gives more

efficient sampling for angular resolved spectra that are to be integrated (most of the intensity is concentrated in the low scattering angle region).

- * XDOS is stored in just one file instead of a hundred messy fort.?? files.

- * DOS is stored in case.dos, not case.dos1 or case.dos1ev. This prevents overwriting of previously calculated density of states using the tetra program.

- * Output has been restructured. A switch allows to control the amount of output. All debugging output has been removed, saving the user several useless MB of disk space. As a rule, all output is useful.

- * Input has been restructured. Use of default values allows for a very compact input file, to which advanced users may add keywords for more advanced options.

- * The calculation of density of states has been integrated into the program. Calls like 'x initelnes, x tetra, x telnes' are no longer necessary. One 'x elnes' will do.

- * Broadening has to be done afterwards by a separate program.

- * Better documentation ;-).

8.c.9. Programmer's Guide.

8.c.9.1 Style.

TELNES2 is programmed in Fortran90.

We use dynamical data allocation. Although most arrays exist are never deallocated, this saves memory because the arrays are not larger than strictly necessary. Also, there is no more need for annoying param.inc files containing compilation time constants for array sizes, which depending on the environment may give errors or rubbish when these sizes are exceeded at runtime.

Variables are grouped into modules (which also contain the corresponding allocation routines) made available by use statements in program units. Contrarily to the common block approach of TELNES, variables are therefore only accessible in the routines where they are necessary, which increases safety.

No implicit type declaration is used (i.e., implicit none statements are used everywhere).

Unnecessary variables and statements have been removed from most parts of the program.

Some parts of the program have escaped these strict rules :

- * old and rather incomprehensible parts, especially some imported lcore routines, which work, and would be very tough to rewrite properly (hfsd and insld have been reworked, though);
- * some imported tetra routines, which have not been touched mainly to make it easy to keep them compatible with the standalone tetra program (which may very well be subject to changes in the future).

Instructions to open files are governed by a definition file (given to the program as command line argument; typically elnes.def). Error messages are passed to an error file (whose name is based on that of the definition file; typically elnes.error).

So far, the program has been compiled and run on only two platforms :

- * MS Windows XP + Compaq Visual Fortran 5.0
- * Linux Redhat 7.3 + Intel Fortran Compiler 7.1-8

In the first configuration I have (in the first executable statements of the main routine in telnes.f) replaced the call to gtfnam by explicit definition of the definition and error file, and increased the stack size.

8.c.9.2 Description of all program units.

(Included in the software distribution.)

8.d. The FEFF8 EELS program.

1. Introduction

In dipole approximation, XAS and EELS are almost the same, so it is only natural to use a code like FEFF for EELS, too. The necessary changes to make this possible were implemented in this version of the FEFF code (FEFF 8.5). More precisely :

- * XAS spectra are converted to EELS spectra (different energy-dependence of the cross-section)
- * Relevant experimental parameters can be used as input – e.g., beam energy, collection angle, etc.
- * We add relativistic effects [Schattschneider] to the cross section, which is currently of much interest in the EELS community.

We stay true to the FEFF tradition of making the calculation easy on the user : one input file (“*feff.inp*”), one command to run the program (“*feff*”). True to the concept of ab initio computation, we want only structural information and experiment parameters as input.

So, FEFF 8.5 calculations of EELS spectra will proceed very much like XAS calculations with older versions. The only difference is that you will use specific input CARDS for EELS (described in section 2) and that you will see new files in your calculation directory (see section 4).

Throughout this document, it is assumed that you are somewhat familiar with the basics of FEFF, and that you have access to a FEFF user’s guide. Together with the program and this document, you should have received an example input file *feff.inp* for the calculation of the C K edge of graphite.

If you are a beginning FEFF user and want to avoid confusion over advanced details, you can start by reading sections 2.1, 2.3 (first paragraph only), 3.1, 4.2, and 8.

2. How to do EELS – input and the EELS cards.

FEFF has a very user-friendly setup. There is one input file, *feff.inp*, in which you specify the system of interest and what you wish to calculate for this system. The FEFF user’s guide explains how to use CARD’s for this purpose. Below we describe the new cards for EELS.

Just like the XAS spectrum is divided into a near-edge region (XANES) and an extended region (EXAFS) for every core edge in the spectrum, EELS spectra have ELNES (near edge structure) and EXELFS (extended structure). The two regions generally need to be computed in a different way, and therefore each has its own input card.

2.1. The ELNES card.

To tell the code to calculate EELS, and give it all relevant parameters, you need to add either the ELNES card or the EXELFS card to your feff.inp input file. The first line of those cards contains the same parameters as the XANES resp. the EXAFS card, and the next lines contain additional information. For ELNES, it looks like this :

```
ELNES [xkmax  xkstep  vixan]
E  [aver [cross [relat]]] # beam energy in keV; optional parameters
[kx ky kz      # beam direction in the crystal frame]
β α           # collection semi-angle, convergence semi-angle (in mrad)
nr na          # q-integration mesh : radial size, angular size
dx dy         # position of the detector (x,y angle in mrad)
```

The parameters between square brackets are optional. For EXELFS, it looks like this :

```
EXELFS xkmax
E  [aver [cross [relat]]] # beam energy in keV; optional parameters
[kx ky kz      # beam direction in the crystal frame]
β α           # collection semi-angle, convergence semi-angle (in mrad)
nr na          # q-integration mesh : radial size, angular size
dx dy         # position of the detector (x,y angle in mrad)
```

Meaning of these parameters :

xkmax maximal k-value for the calculation
xkstep step size of the upper part of the k-mesh
vixan step size of the lower part of the k-mesh
aver 1 to calculate orientation averaged spectrum (e.g. polycrystalline sample, working at magic angle ...); 0 to use specific sample to beam orientation (default);
cross 1 to use cross terms for the cross section (e.g. xy or yx ; default); 0 to use only direct terms (e.g., atom coordinates entered in symmetric coordinate frame ; assumed as default if *aver* is set to 1);
relat 1 to use relativistic formula for the cross-section (default and always recommended) ; 0 to use non-relativistic formula (for checking against old results ; does not save any time!);
E energy of the electron beam in keV (typical values are 100-400 keV);
kx,ky,kz wave vector **k** of the incoming electron in the crystal frame (i.e., the Cartesian coordinate system in which the atom positions of the ATOMS card are given) ; in arbitrary units (only the direction, not the size of **k** is used) and to be omitted if *aver* is set to 1;
β the collection semi-angle of the EELS detector in mrad (typical values are of the order of 1 mrad);
α the convergence semi-angle of the incoming beam in mrad (typical values are of the order of 1 mrad);
nr, na the cross section is integrated over the values of the impulse transfer vector **q** = **k** - **k'** allowed by *α* and *β* ; the integration grid consists of *nr* concentric circles sampling a disc of radius *α* + *β* ; circle *i* contains *na* * (2*i*-1) points, making for *nr***nr***na* points in total (this is a non-physical parameter and should be converged ;

typical would be, e.g., 5,2 ; the integration is quite fast ; only for small values of nr is it necessary to increase na above 1);

dx,dy the position of the detector in the scattering plane, specified by angles in mrad along x and y axis (the same as used in the ATOMS card) (typical values are 0.0, 0.0).

Xkmax, xkstep and vixan are exactly the same parameters as those used for XANES and EXAFS cards, and described in the FEFF user's guide.

The line giving beam orientation (kx,ky,kz) should only be present when an orientation sensitive spectrum is calculated. If an orientation averaged spectrum is to be calculated, that line should be omitted (or commented out).

As an example :

```
ELNES # calculate elnes.
300 # beam energy in keV
0 1 0 # beam direction in the crystal frame
2.4 0.0 # collection semi-angle, convergence semi-angle (in mrad)
5 3 # q-integration mesh : radial size, angular size
0.0 0.0 # position of the detector (x,y angle in mrad)
```

simulates an experiment with a 300 keV beam hitting the sample along the y-axis. The detector is set in the forward direction and has a 2.4 mrad (semi-)opening ; the width of the incoming beam is 0 mrad. To do the integration over the detector aperture, $5*5*3=75$ points are used. The calculation is relativistic and takes sample to beam orientation into account. Default settings are used for the energy/k – mesh.

Another example :

```
EXELFS 25 # calculate exelfs.
200 1 0 # beam energy in keV
0.4 0.5 # collection semi-angle, convergence semi-angle (in mrad)
10 1 # q-integration mesh : radial size, angular size
0.0 0.0 # position of the detector (x,y angle in mrad)
```

simulates an experiment with a 200 keV beam and an orientation averaged calculation (say the sample is isotropic). The detector is set in the forward direction (last line) and has a 0.4 mrad (semi-)opening ; the width of the incoming beam is 0.5 mrad. To do the integration over the detector aperture, $10*10*1=100$ points are used. The calculation is relativistic and averages over sample to beam orientation. No cross terms are calculated (this option – the “0” on the second line could have been omitted, as it is the default for orientation averaged calculations). We use an energy grid up to $k = 25 \text{ \AA}^{-1}$.

2.2 Other EELS related cards.

Currently, there is only one additional new card : the MAGIC card.

```
MAGIC 20 # create a plot that shows the sp2 ratio at 20 eV above
threshold.
```

The MAGIC card makes the code calculate cross sections as a function of collection angle at a particular energy loss. So, in addition to the energy-resolved output produced by the EELS card, the MAGIC card produces angle-resolved output.

The name MAGIC was chosen because the output of this card enables one to find the magic angle for a material very quickly : run the code for two different orientations, and see where the sp^2 - curves cross. This gives you the magic collection angle for the collection angle and EELS edge chosen in *feff.inp*.

2.3 Using traditional FEFF cards for EELS calculations.

* The EELS calculations use the machinery that is at the heart of FEFF to calculate spectra: either full multiple scattering, or path expansion (or both). So, the cards that we reviewed above must be combined with the appropriate card telling FEFF which of its algorithms to use.

For near edge structure (ELNES) we use :

FMS 7.0
ELNES ...

to use the full multiple scattering.

For extended structure (EXELFS) one must use :

RPATH 8.0
EXELFS ...

to use the path expansion.

Of course, the arguments of the FMS and RPATH cards may be set to different values than those given here. Additionally, one can specify other cards in the *feff.inp* file – see the FEFF user’s guide for an exhaustive description.

Here, we only discuss a few issues relevant to EELS calculations in FEFF 8.5.

* For EELS calculations, the polarization vector is an internal variable that is set by the code itself. Therefore, the POLARIZATION card cannot be used. If the card is present, the code should give a warning and ignore it.

Similarly, the beam direction is given by the input parameters of an ELNES/EXELFS card. It is not allowed to use the ELLIPTICITY card when an EELS card is present. Again, if it is used, the code should complain and ignore it.

* One should obviously not combine ELNES or EXELFS with the XANES or EXAFS cards.

* The FPRIME and DANES cards are expected to work in combination with an ELNES/EXELFS card. However, it is not clear what the resulting output in *eels.dat* should mean. The combination of, say, DANES and ELNES could be used as a way of obtaining DANES for all polarizations with a single calculation, though, if one uses the *xmu.dat*-files produced by such a calculation (and ignores the probably meaningless *eels.dat*). (Note : please put the DANES card after the ELNES card, and make sure first lines of both cards are identical.)

* The CONTROL and PRINT cards do not have an additional field for the EELS module. Execution of the EELS module is governed by the presence of an ELNES/EXELFS card in *feff.inp* (or, on a lower level, by the corresponding switch in *eels.inp*). The output level can not be modified at this time, except through the MAGIC card.

3. How to do ELNES – running the code.

3.1 A full run.

Prepare the *feff.inp* file as described in section 2, and run *feff*! If you address the modules individually, then do not forget to add module *eels* to your calling sequence. A full calculation should consist of the steps

rdinp
pot
screen
xsph
ldos
fms
path
genfmt
ff2x
so2conv
eels

Your installation contains a script ‘*feff*’ so that you can run this whole sequence by just giving the command *feff*. The modules *so2conv* and *screen* and *ldos* are optional.

3.2 Changing something.

If you change something in the calculation of the material properties – such as atom positions, or the FMS radius ... - you need to rerun all the traditional modules of FEFF (i.e., the whole sequence described above).

If you change from orientation averaged to orientation sensitive calculation, or from an orientation sensitive calculation without cross terms to one with cross terms, then you need to rerun *rdinp* and the sequence from *fms* until *eels*.

If you only change an experimental parameter – i.e., most of the parameters in the EELS and MAGIC cards – then you only have to rerun module *eels*, which is very fast (fast enough to couple it to fitting software, if you like). To do this, you either :

- * change the ELNES/EXELFS card in *feff.inp*, run *rdinp*, run *eels* ;
- * change the ELNES/EXELFS card and put CONTROL to 0 0 0 0 0 in *feff.inp*, and run *feff*
- * edit *eels.inp* directly – but beware, this is a formatted file! – and run *eels*

4.3 Different behaviour.

When the EELS card is present, certain modules will behave different from what you're used to. Module *fms* will take a little longer, repeat some of its output, and produce a larger output file. Module *path* will take longer and produce more output files. Same goes for module *genfmt* and module *ff2x*.

All in all, the time increase should be quite modest, since most of the time goes into 1/ calculating self-consistent potentials in module 1, which is not affected at all ; and, 2/ inverting the matrix for FMS, which is still done only once – only the post processing in module *fms* takes longer.

A test on an ELNES calculation for a 100 atom FMS cluster in graphite showed negligible computation time increase compared to the corresponding XANES calculation (2 seconds longer on a total of about 9 minutes).

The basic novelty is in the treatment of the polarization. In non-EELS calculations, FEFF takes a polarization from the input (POLARIZATION and ELLIPTICITY cards), sets up a specific polarization matrix for this experimental situation, and calculates one corresponding spectrum. For EELS, however, we calculate a spectrum for every element of the polarization tensor (xx, xy, xz, yz, yy, ..., zz). This gives us the whole absorption tensor (which is symmetric and has six independent components). The main computational effort is in setting up that tensor (modules *rdinp* through *so2conv*). Now, an EELS spectrum can be calculated in a second or less for specific experimental conditions (collection angle, orientation, beam energy, ...).

A standard EELS calculation computes the whole absorption tensor. However, if the user asks for an orientation averaged calculation, only one element (corresponding to the trace) is calculated ; and if the user chooses not to have any cross terms, only xx, yy, and zz elements of the absorption tensor are calculated.

This explains the remarks made in section 4.2.

A last important difference to old calculations is that we disable the normalization of the spectrum at 50 eV above threshold. This was often annoying when several spectra need to be combined.

4. How to do EELS – files.

4.1 Input files.

* The file *feff.inp* contains all parameters related to EELS calculation and is the preferred way for non-expert users to set those parameters. After each change, module *rdinp* must be run to update *eels.inp*.

* The file *eels.inp* is read by the EELS module *eels* and determines what the code will actually do. Expert users can tweak this file directly. Basically, the file contains everything that's in the EELS and MAGIC cards. Of particular interest is the very first parameter, which determines whether *eels* is executed (=1) or not (=0), and also the parameters on the next line, which select the components (1-9) of the sigma tensor that will be calculated.

These parameters are very important because **other modules** will check for the presence of the *eels.inp* file and the values of these parameters to determine their course of action! People who have done EELS and then want to do something else in the same working directory may want to set the execution switch to 0 (or comment the EELS card in *feff.inp* and rerun module *rdinp*, which amounts to the same) to make sure none of the other modules bother about doing something special for EELS.

4.2 Output files.

* The file **eels.dat** contains the EELS spectrum. Its first column contains energy loss in eV, the second column the total spectrum, and the next columns contain the contribution to the total spectrum from each of the nine components of the cross section tensor.

* The file **magic.dat** is only written if the MAGIC card is present in *feff.inp* (and the corresponding switch is set to 1 in *eels.inp*). It contains the collection angle in rad, the pi to sigma ratio, the pi and sigma components of the spectrum, and the total spectrum ; all as a function of collection angle, evaluated at the energy loss set by the MAGIC card. Caution : this has not been tested in the presence of cross terms. E-mail the author in case of doubt.

* The file **logeels.dat** contains reports on the execution of the program. In particular, it contains a summary of the input options used. Most of the information in the file is also written to the screen during program execution.

4.3 Files of other modules.

Modules *xsph*, *fms*, *path*, *genfmt*, *ff2x* and *so2conv* are affected by the presence of an active *eels.inp* file and may behave accordingly :

4.3.1. Module 2 (*ffmod2* or *XSPH*).

If an ELNES/EXELFS card is present, *xsph* sets the polarization tensor to the unit matrix before proceeding. A message is written to *log2.dat*.

4.3.2 Module 3 (*ffmod3* or *FMS*).

If an ELNES/EXELFS card is present, *fms* adds to *fms.bin* all the requested components of the sigma tensor instead of just one. This is fully compatible with non-EELS calculations.

4.3.3 Module 4 (*ffmod4* or *PATH*).

For each polarization component, a separate *list.dat* file is written (i.e., *list.dat*, *list02.dat*, etc.). The format of the files is unchanged.

4.3.4 Module 5 (*ffmod5* or *GENFMT*).

For each polarization component, the corresponding *listnn.dat* is written and a separate *feff.bin* file is written (i.e., *feff.bin*, *feff02.bin*, etc.). The format of the files is unchanged.

4.3.5. Module 6 (*ffmod6* or *FF2X*).

The module reads the large *fms.bin* and all the *feffnn.bin* files, and produces a *xmunn.dat* file containing the corresponding component of the sigma tensor (*xmu.dat*, *xmu02.dat*, ..., *xmu09.dat*). Those files have the traditional *xmu.dat* – format. Similarly, *chinn.dat* – files are produced.

4.3.6 Module 8 (*SO2CONV*).

Again, a loop over all components of the sigma tensor : each *xmu.dat* file is opened and altered individually.

5. Guarantees?

This is a new software development. As such, bugs and various annoying little (or big) problems may occur. Contact the author if necessary.

The code was mostly tested for ELNES calculations on Linux pc's with the Ifort compiler. We believe it should also work on other systems. However, if you experience problems, or if you are unsure about an EXELFS calculation, I encourage you to contact the author.

Compatibility with the use of other input cards and with files from older FEFF versions has been attempted, but may not have been achieved in all cases. Please report problems.

6. Compilation :

- * If you have received a single file, just compile it as you always have.
- * If you have received a small number of files, one for each module, you compile them as usual, but now do one extra module. That is, you'll receive a file *eels_tot.f* that should be compiled to an executable *eels*.
- * If you have received a whole directory tree with lots and lots of files, there should be a Makefile in which you can set compilation parameters (most importantly, the name of your compiler). Do this and run "make".

The source code for the *eels* module contains some fortran90. If you do not have a fortran90 compiler, you can obtain a fortran77 compatible version from us. Alternatively, if you have received the version with the Makefile (item #3 in the above list), you can set the parameter EELSDIR in the Makefile (to 'EELS' for f90, and to 'EELS77' for f77).

If you experience any problems, we'd appreciate your feedback and the opportunity to help you out.

7. Programming details in a nutshell.

A separate Programmer's Guide is available in the documentation of your FEFF 8.5 distribution. Here is a concise summary.

A central quantity in FEFF is the polarization tensor (ptz). In regular FEFF calculations, it is calculated from the polarization vector *e* (*evect* in the code) and the beam direction *k* (*xivect* in the code), and then the spectrum corresponding to that physical situation is calculated. Ptz is processed internally.

For EELS calculations, we want access to all 9 polarizations (6 of which are independent), giving us 9 partial spectra that we can sum, with weights depending on experimental conditions, to very quickly (as sample information is precomputed into those 9 components) assemble a physical EELS spectrum.

The modifications to the code fall into three categories :

- minor things, such as adding new cards, according to FEFF tradition ;
- modifying existing routines that handle the polarization tensor so that the full tensor is preserved ;
- adding a new module, called *eels*, for calculating the spectrum out of the 9 partial spectra.

More details on implementation are available in a separate Programmer's guide.

8. Questions? Remarks? Bugs?

Once more : let me know! kevin.jorissen@ua.ac.be

9. References.

* Relativistic Electron Energy Loss Spectra calculated in the Real Space Multiple Scattering approach, K. Jorissen, J.J. Rehr. In preparation.

This paper will be the official reference for EELS calculations with FEFF.

* Practical aspects of electron energy-loss spectroscopy (EELS) calculations using FEFF8

M.S. Moreno, K. Jorissen and J.J. Rehr, Micron, 2006. (*review article - in print*)

This paper contains practical hints on how to use FEFF8.2 for EELS calculations.

* Real-Space multiple-scattering calculation and interpretation of x-ray-absorption near-edge structure, A.L. Ankudinov, B. Ravel, J.J. Rehr, S.D. Conradson, Phys. Rev. B 58 (12) 7565, 1998.

The main reference for FEFF8.

* Anisotropic relativistic cross sections for inelastic electron scattering, and the magic angle, P. Schattschneider, C. Hébert, H. Franco, B. Jouffrey, Phys. Rev. B 72 045142, 2005.

A good reference for relativistic EELS theory.

Programmer's guide : calculating EELS with feff85.

implementation by Kevin Jorissen

this document by Kevin Jorissen

this version : 05-15-2006

contact me at kevin.jorissen@ua.ac.be

If you are not on the FEFF development team, it is highly unlikely that you will ever need the information contained in this document. Please save a tree and don't print this!

It is assumed throughout this document that the reader is familiar with the contents and notations of the accompanying User's guide and the FEFF User's guide.

1. General comments.

A central quantity in FEFF is the polarization tensor (ptz). In regular FEFF calculations, it is calculated from the polarization vector *e* (evec in the code) and the beam direction *k* (xivec in the code), and then the spectrum corresponding to that physical situation is calculated. Ptz is processed internally.

For EELS calculations, we want access to all 9 polarizations (6 of which are independent), giving us 9 partial spectra that we can sum, with weights depending on experimental conditions, to very quickly (as sample information is precomputed into those 9 components) assemble a physical EELS spectrum. This means that all elements of the code where a specific value for ptz, evec or xivec is used need to be looped over (ptz) or circumvented (evec and xivec).

The modifications to the code fall into three categories :

- minor things, such as adding new cards, according to FEFF tradition ;
- modifying existing routines that handle the polarization tensor so that the full tensor is preserved ;
- adding a new module, called *eels*, for calculating the spectrum out of the 9 partial spectra.

It is important to realize that ***all modules except pot, ldos, and screen have been modified*** and will adapt their behaviour in the presence of active EELS input!! This is because "inner loops" in the code (with substantial changes) allow for much faster calculations than "outer loops" (with no substantial changes).

It is the intention of the author to mention ***every*** modified routine explicitly in this document.

2. Module 0 (RDINP or fmod0).

* This module now accommodates new cards and variables and a new output file. Changing the coordinate system has been disabled in EELS calculations.

* New cards ELNES, EXELFS and MAGIC have been added, with internal codes 54, 56 and 55, respectively. To this purpose, relevant blocks of code were added to *rdinp* and *itoken* (in src/COMMON). Since the ELNES and EXELFS card takes several lines of input from the feff.inp file, a new 'reading mode' mode=4 was added in *rdinp*.

A new common block /elnes/ defined in allinp.h contains the new variables of the ELNES/EXELFS and MAGIC card.

* ELNES is very similar to XANES; the parameters on the first line of the card are exactly the same. Similarly, EXELFS incorporates the EXAFS card. I have 'absorbed' the relevant variables because it seems confusing to have to use both ELNES and

XANES cards in one file – quod non, now. On the other hand, the calculation of ELNES invokes essentially the same routines as that of XANES, so that I have not attributed a new ispec number to elnes and exelfs calculations. Apart from a loop or two, the difference is mainly cosmetic until we reach the *eels* module.

* *Iniall* sets the elnes variables to defaults that essentially mean : don't calculate eels, do traditional x-ray feff.

Rdinp has new card consistency checks : it tries to avoid combinations of ELNES and POLARIZATION or ELLIPTICITY, and it ignores MAGIC if ELNES is not present. It also checks consistency of the control switches aver, cross and elnes, and sets the important parameters ipmin,ipmax,ipstep depending on the control switches. The ip parameters determine which components of the sigma tensor are calculated.

Ffsort has a new input argument : a logical switch doptz which disables the call to mkptz if eels is active. This is because 1/ mkptz is not necessary : the polarization tensor will be set later ; and 2/ because rotation of the atom coordinates in mkptz may interfere with the existence of off-diagonal sigma tensor components and the desired interpretation of the spectrum in terms of its components in a particular basis.

Wrtall writes the eels parameters to the file eels.inp. All other files retain their exact traditional format. Note that global.dat will contain some unset variables (in particular the ptz matrix) in case eels is active.

3. Module POT.

No changes at all.

4. Module SCREEN.

No changes at all.

5. Module XSPH.

* Minor change : explicit setting of the polarization tensor is necessary for EELS calculations for strictly practical reasons.

* *Rexsph* checks for the presence of a eels.inp file with meels=1 (i.e., an active eels.inp file). If it finds this, it sets the polarization matrix ptz – which was read earlier from global.dat – to 1/3. This is necessary, since in case of eels rdinp has not set the polarization matrix, and okay, since for xsph only the trace of ptz matters. A message is written to the log file.

6. Module LDOS.

No changes at all.

7. Module FMS.

* This module has been changed significantly. Instead of summing over the components of the polarization tensor internally, it now calculates a spectrum for each component separately, and outputs all those (9) spectra to its output file fms.bin.

* *Reafms* looks for an active eels.inp file (eels=1). If it finds one, it takes the parameters ipmin, ipstep, ipmax from that file. If not, it sets them all to 1. The variables elnes,ipmin,ipstep,ipmax are returned as output parameters.

Ffmod3 passes them on to fmstot.

Fmstot calls *bcoef* several times to set up the *bmat* matrix for every polarization considered (do *ip=ipmin,ipmax,ipstep*). If (*eels=1*), each call to *bcoef* is preceded by a call to *inipz*, a new routine that sets the polarization matrix and can work either in Cartesian or in spherical coordinates (current settings use a Cartesian representation) ; if (*eels=0*), the value read from *global.dat* in *reafms* is used. The *bmat*'s are stored in a supermatrix *bmat0*, which is one dimension larger. Then inside the big loop over energy, the matrix inversion is done only once (as for *xas*) by calling *fms*. Now there is a loop over the section where *gg* (inverted matrix from *fms*) is formed into *gtr* (the output of *ffmod3*) by applying *bmat*. This loop over polarization tensor components selects the right *bmat* from *bmat0*, calculates, and puts the result in *gtr* – which has an extra dimension in the new code : *gtr(ip, E)*. The MPI instructions for gathering pieces of *gtr* have been modified (but not tested!) to accommodate this extra dimension. The full *gtr* matrix is written to *fms.bin* in a consistent way (i.e., if *ipmin=ipmax=1* it has the exact same format and content as in a *xas* calculation).

8. Module 4 (PATH or ffmod4).

* Most *eels* calculations require the absorption tensor for every polarization component and for every sample to beam orientation. I am not sure how this influences the selection of paths. I fear this may prohibit use of any symmetry and it may be necessary to use *icase=7* for orientation sensitive calculations in *mpprmp* until further testing has been done.

* *Repath* looks for an active *eels.inp*-file (*eels=1*). It passes *eels* on to *ffmod4*, then to *pathsd*, then to *timrep*. If *eels=1*, *timrep* initializes a variable *icase* to 7 ; if *eels=0*, it puts it to -1. This variable is a new input parameter to *mpprmp*, which uses it to override its own decision procedure for *icase* if between 1 and 7.

9. Module GENFMT.

* *Regenf* looks for an active *eels.inp* file (*eels=1*). If it finds one, it takes the parameters *ipmin, ipstep, ipmax* from that file. If not, it sets them all to 1. The variables *elnes, ipmin, ipstep, ipmax* are returned as output parameters.

Ffmod5 passes them on to *genfmt*.

Practically all of *genfmt* (except for the reading of *phase.bin* in *rdxsph*) is contained within a loop over the components of the polarization tensor (do *ip=ipmin,ipmax,ipstep*). For every *ip*-value, a file *feff_ip.bin* and *list_ip.dat* is written – except for *ip=1*, where the filenames are simply *feff.bin* and *list.dat* for compatibility reasons. If (*eels=1*), *inipz* is called (see module 3) to set the polarization tensor *ptz* to the desired value determined by *ip* ; if not, the value read from *global.dat* by *regenf* is used. The polarization tensor is passed on to *mmtr*, which will eventually call *bcoef* to create a *bmat* matrix.

10. Module FF2X.

* This module has been looped over the components of the sigma tensor ; it needs to read input and write output for every component separately.

* *Reff2x* looks for an active *eels.inp* file (*eels=1*). If it finds one, it takes the parameters *ipmin, ipstep, ipmax* from that file. If not, it sets them all to 1. The variables *elnes, ipmin, ipstep, ipmax* are returned as output parameters.

Ffmod6 passes them on to *ff2xmu* (called for *ispec=1* (XANES/ELNES) and *ispec=2* (XES)) or *ff2chi* (called for *ispec=0* (EXAFS/EXE/FS)) or *ff2afs* (called for *ispec=3* (DANES) and *ispec=4* (FPRIME)).

In *ff2xmu*, a new variable *gtrful* (and temporary buffer *gtrtemp*) has been created to enable reading the enlarged *fms.bin* file written by *module3*. The code will work fine for old *fms.bin* files. Much of *ff2xmu* (after reading *xsect.bin*) has been looped over the components of the sigma tensor (do *iip=ipmin,ipmax,ipstep* – the variable *ip* has another meaning in this routine!). The component of *gtrful* corresponding to *iip* is copied into *gtr*, and the corresponding *feff_iip.bin* is read. Because direct components (e.g. *xx*) should have the atomic background, but off-diagonal components (e.g. *xy*) should not, instead of *xsec* (read from *xsect.bin*) I use the variable *kxsec* which is equal to *xsec* for diagonal components and is 0 for offdiagonal components. The resulting spectrum – a x-ray spectrum! – is written to *xmu_iip.dat* (for *iip=1*, we use ‘*xmu.dat*’ for compatibility reasons).

In *ff2chi*, a similar approach is followed. Since *fms.bin* is not read in this routine, we do not need new *gtr*-related variables. Again, most of the code is looped over. We now need to read *list_iip.dat* in addition to the files mentioned earlier. As the variable *omega* (read from *xsect.bin*) is recycled in the code (why keep things clear?), I read it again in each cycle. The same trick with *kxsec* and *xsec* is performed. An additional output file *chi_iip.dat* is written.

In *ff2afs*, again the same thing is done.

10. Module SO2CONV.

* Checks for active *eels.inp* file. If present, the whole code loops over the polarization tensor (do *ip=ipmin,ipstep,ipmax*). Each *xmu.dat* file is read and overwritten individually.

11. Module EELS.

* Completely new module, separate from existing code.

* Description to be provided later.

12. Other source directories.

COMMON : function *itoken* is adapted to accommodate the new cards ELNES, EXELFS and MAGIC.

ATOM, DEBYE, EXCH, FOVRG, HEADERS, LIB, MATH, PAR, SCREEN, TDLDA,
Utility : No changes at all.

13. Programming conventions.

* In existing routines, my aim has been to make as little conceptual modifications as possible. This means that sometimes a routine will not be the shortest possible, or there may be some redundancy in variables ; but its ‘spirit’ will be conserved as much as possible, so that someone who knew the old version of the routine won’t have too much trouble getting used to the new version.

* In existing routines, every line that I change bears my initials in a comment !KJ , sometimes followed by an explanation. When a block of new code is inserted, it will be

preceded and followed by !KJ. If significant changes are made to an instruction, the old version is often preserved as a comment.

* In new routines, the implicit none statement is always used. In existing routines, all new variables (including the index i etc.) are declared explicitly. Always.

* No old-fashioned coding! This means avoiding line numbers, goto statements, and other encryption techniques.

* In the new module *eels*, some f90 is used. We also have a f77 version.

situation	eels	aver	cross	ipmin	ipstep	ipmax	ip	ptz
XAS	0	/	/	1	1	1	1	as given by POLA and ELLI cards
EELS, orientation averaged	1	1	0	10	1	10	10	1/3 * I
EELS, orientation averaged, symmetric coordinates	1	0	0	1	4	9	1, 5, 9	xx, yy, zz
EELS, orientation averaged, general coordinates	1	0	1	1	1	9	1, 2, 3, 4, 5, 6, 7, 8, 9	xx, yy, zz, xy, yx, xz, zx, yz, zy

Table 1 : values of some important EELS variables for several physical situations.

ip	Carth. name	polarization tensor
1	xx	1 0 -1 0 0 0 * 1/2 -1 0 1
2	xy	-1 0 -1 0 0 0 * i/2 1 0 1
3	xz	0 1 0 0 0 0 * 1/sqrt(2) 0 -1 0
4	yx	1 0 -1 0 0 0 * i/2 1 0 -1
5	yy	1 0 1 0 0 0 * 1/2 1 0 1
6	yz	0 -1 0 0 0 0 * i/sqrt(2) 0 -1 0
7	zx	0 0 0

		1 0 -1 * 1/sqrt(2) 0 0 0
8	zy	0 0 0 1 0 1 * i/sqrt(2) 0 0 0
9	zz	0 0 0 0 1 0 0 0 0
10	average	1 0 0 0 1 0 * 1/3 0 0 1

Table 2 : Cartesian components of the polarization tensor expressed in FEFF's spherical basis, as implemented in routine *inipz*.

8.e. The FEFF8 k-space program.

The reciprocal space, impurity-KKR-like FEFF8.6 code works just like regular FEFF : i.e., there's a single input file *feff.inp* that contains all input variables, and it's sufficient to run a single command 'feff' to run the program. All the new functionality is implemented through a handful of new input CARD's, consisting of a keyword and some numerical values, which are briefly described below. The main difference, from the point of view of the user, is that in order to use the reciprocal space calculations, the system is specified in terms of a unit cell with lattice vectors and a basis of atoms in the unit cell, instead of a real space cluster. We will describe how to do this below.

If the RECIPROCAL card is used, then the LATTICE, ATOMS, KMESH and MARKER cards are mandatory. All others are optional.

RECIPROCAL

This card tells FEFF to work in reciprocal space. It affects modules *pot*, *xsph*, *fms* and *ldos*.

REAL

This card tells FEFF to work in real space.

KMESH *nkp usesym symfile*

This card specifies the mesh of k-vectors used to sample the full Brillouin Zone for the evaluation of Brillouin Zone integrals. Nkp is the number of points used in the full zone. If usesym = 1, the zone is reduced to its irreducible wedge using the symmetry options specified in file symfile, which must be present in the working directory. The k-mesh is constructed using the tetrahedron of Bloechl et al., Phys. Rev. B, 1990.

LATTICE type scale

Ax ay az

Bx by bz

Cx cy cz

This card specifies the lattice. First, its type must be specified using a single letter : P for primitive, F for face centered cubic, I for body centered cubic, H for hexagonal. The following three lines give the three basis vectors in Cartesian Angstrom coordinates. They are multiplied by scale (e.g., 0.529 to convert from bohr to Angstrom)

ATOMS n

X1 y1 z1 pot1

....

xn yn zn potn

This card specifies the real space cluster if one uses real space calculations. However, it specifies the atoms in the unit cell if one uses reciprocal space calculations. The unit cell itself was defined in the LATTICE card. Here, each atom is defined by three coordinates and its potential index. (The POTENTIALS card works just the same for real and reciprocal space calculations.) There are n atoms in the unit cell. One can use the COORDINATES card to specify the units in which the coordinates are given.

COORDINATES i

i must be an integer from 1 through 6. It specifies the units of the atoms of the unit cell given in the ATOMS card for reciprocal space calculations. If the card is omitted, the default is assumed.

1 : Cartesian coordinates, Angstrom units. Like FEFF – you can copy from a real space feff.inp file provided that your LATTICE vectors coincide with atoms in that feff.inp file.

2 : Cartesian coordinates, fractional units (i.e., fractions of the lattice vectors ; should be numbers between 0 and 1). Similar to FEFF.

3 : Cartesian coordinates, units are fractional with respect to FIRST lattice vector. Like SPRKKR.

4 : Given in lattice coordinates, in fractional units. Like WIEN2k (but beware of some ‘funny’ lattice types, e.g. rhombohedral, in WIEN2k case.struct in case you’re copy-pasting ...)

5 : Given in lattice coordinates, units are fractional with respect to FIRST lattice vector.

6 : Given in lattice coordinates, Angstrom units.

E.g., say that you have entered a diamond system as :

LATTICE P 6.0

0.0 0.5 0.5

0.5 0.0 0.5

0.5 0.5 0.0

Now you want to enter the atoms :

ATOMS 2

0.0 0.0 0.0 (always right – COORDINATES 1 through 6)

1.5 1.5 1.5 (COORDINATES 1 or 6)

0.25 0.25 0.25 (COORDINATES 2, 3, 4, or 5)

MARKER ic

Specifies the location of the absorber atom for reciprocal space calculations – it's entry ic of the ATOMS card. The marker needs to be specified also for NOHOLE calculations.

NOHOLE ih

This card works the same for real and reciprocal space calculations. One can use either ih = 0 (no core hole) or ih=2 (Yoshi's screened core hole), or omit the NOHOLE card (regular core hole). However, if one uses a reciprocal space calculation, then the recommended way to do a core hole calculation is to use NOHOLE 2, as it is best not to have a core hole in the pot module!

Alternatively, one can use a regular core hole (no NOHOLE card) and run the pot module with reci set to 0 in reciprocal.inp, and afterwards (i.e., before running fms) reset reci to 1 to do that part of the code in reciprocal space. For the test case of GaN, better results were obtained using NOHOLE 2, though.

SGROUP ngroup

This card specifies the space group of the crystal (number from 1 through 230).
Currently not active.

STRFAC eta gmax rmax

This card gives three non-physical internal parameters for the calculation of the KKR structure factors : the Ewald parameter and a multiplicative cutoff factor for sums over reciprocal (gmax) and real space (rmax) sums. Multiplicative means the code makes a 'smart' guess of a cutoff radius, but if one suspects something fishy is going on, one can here e.g. use gmax=2 to multiply this guess by 2. Eta is an absolute number.

In the cases tested so far, it was not necessary to use this card. Its use is not recommended.

BANDSTRUCTURE

This card activates the module that calculates and prints out bandstructure. Not active yet since the bandstructure module isn't ready!

THE FILE RECIPROCAL.INP

This file contains all the parameters described in the abovementioned cards, plus one or two extra that are experimental and not described here. It can always be edited by hand. It affects modules pot, xsph, ldos, and fms. Beware of making changes in between modules – it's not always wrong, but one has to know what one's doing.

The main switch is the first parameter (all are clearly labeled in the file) `reci` : if it's set to 0, the calculation will be done in real space and all the parameters following it are ignored. If it's set to 1, the calculation is done in reciprocal space, and all the parameters following it are read and used.

Apart from this, all other `*.inp` files are the same as they were in FEFF8.5 .

OUTPUT

The output of reciprocal space calculations is fairly indistinguishable from real space calculations, except that a file containing the k-mesh is printed, and some minor intermediate output may be present in the log-files.

USING A PARTIAL CORE HOLE

There are some variables in the `reciprocal.inp` file pertaining to partial core hole calculations (e.g., Slater transition state). However, these types of calculations are still experimental, and no-one except developers should touch these options for the moment.

CONVERGING THE K-MESH

Essentially all parameters that need to be entered for reciprocal space calculations are physical parameters, with one important exception : the number of k-points in the k-mesh. This parameter simply needs to be converged. Although it is impossible to give a general guideline, often starting with 1000 k-points is a good idea for fairly simple and small unit cells. Generally, the number of points scales inversely with the volume of the unit cell. Some systems require more points than others – one always needs to check. Also, the more broadened the property of interest (e.g. ELNES as opposed to DOS), the less points are necessary. Also, the near edge structure requires more points, whereas more extended structure (e.g., 50-70 eV above threshold) is often converged with even just a few k-points.

EXELFS

For extended loss structure (i.e., upwards from 50-100 eV), the real space Path Expansion method is so well tested and efficient that I do not see the point in trying to reformulate it in reciprocal space. Therefore, it is always done in real space.

If the `RECIPROCAL` card is active (and the crystal is specified using `LATTICE` and unit cell `ATOMS` card), then the `rdinp` module will generate a real-space cluster based on the information of the `LATTICE` and `ATOMS` cards, and the value of the `RPATH` value. This cluster will be written to the `atoms.dat` file. The spectrum will then be calculated using the `path` and `genfmt` modules, which haven't been reprogrammed and work in real space.

PROGRAM STRUCTURE

Much of the new programming is contained in a separate source folder “`KSPACE`” that compiles into a `kpace` library included in the Makefile of other source folders. However, several other source folders also contain a few files that are used only for reciprocal space calculations. The new routines are all programmed using `f90` syntax, and the relevant variables are organized in modules. It may be instructive for the FEFF developer to

check out these `src/KSPACE/modules*.f` files, which have comment lines describing almost all variables.

Also, existing routines have been modified. Usually, these modifications were minimal and the original structure of the routines have been preserved as much as possible.

Generally, a module will open the `reciprocal.inp` file in its “read input” routine to figure out which space we’re in. If that’s real space, the calculation will proceed exactly as it always has.

Next, the initialization routines will call a dedicated `kspace` initialization routine if necessary (e.g., routine `kprep`), which sets up the `k`-mesh and prepares objects for the calculation of KKR structure constants.

Then, inside the main energy loop of `pot`, `ldos`, `xsph` and `fms`, the following structure is found :

```
If (reciprocal space)
```

```
  Call fmskspace
```

```
Else (i.e., real space)
```

```
  Call fms
```

```
Endif
```

Where `fms` and `fmskspace` produce equivalent output, e.g. a Green’s function in real space. All the `k`-space is hidden inside `fmskspace`.

The main outputs of all modules – `pot.bin`, `xsect.bin`, `ldos.dat`, `fms.bin` – has not been changed since FEFF8.5.

USING CRYSTAL SYMMETRY

Symmetry could be used in two ways :

- reduce the `k`-mesh
- reduce the Green’s function L, L' matrix

The first of these is currently implemented, HOWEVER! The extent to which symmetry can be used depends on what one is calculating. E.g., to calculate the diagonal parts of $G_{LL'}$, one can reduce the `k`-mesh and just sum all the contributions from inequivalent `k`-vectors. BUT for the offdiagonal components (which are needed in order to add the core hole, if any), symmetry is more subtle and one needs to add all the equivalent ones, which can be somewhat shortcut by reconstructing them from the inequivalent ones through unitary transformations dictated by symmetry elements of the crystal. Whereas the first strategy would yield a speedup ~ 48 for diamond, the gain for the latter strategy is much more modest (~ 5 ?) and dependent on the size of the matrices, i.e. the number of atoms in the unit cell.

So, while a number of symmetry strategies are implemented in the code, it is currently recommended to test these cautiously on a smaller `k`-mesh before relying on them. Contact the author in case of doubt.

The second item – LL' symmetry within the `G` matrix – has not been implemented in any way.

SPEED

Generally, fms is the module that takes longest.

In real space, for every energy point one matrix inversion of order

$n_{clus} * (l_{max} + 1) ** 2 * n_{sp}$

In reciprocal space, for every energy point n_{kp} matrix inversions of order

$nu * (l_{max} + 1) ** 2 * n_{sp}$

Where nu is the number of atoms in the unit cell, n_{kp} the number of k-vectors in the mesh, n_{clus} the number of atoms in the real space cluster, l_{max} the angular momentum cutoff, n_{sp} the number of spins (1 or 2).

So, the relative speed is something like $(nu/n_{clus})^a * n_{kp}$, where a is the scaling of matrix inversion.

In general, unit cells with more atoms (nu) are larger and therefore require less k-vectors (n_{kp}). However, I don't have a general idea of speed. Obviously, for very small systems (1-5 atoms in the unit cell), RECIPROCAL is faster. For larger systems, more study is needed.

Also, it's worth noting that pot sometimes seems to get quite slow in reciprocal space.

9. References

1. Feynman, R. P., Leighton, R. B., and Sands, M. The Feynman lectures on Physics . Addison Wesley, 1970. ISBN 0-201-02115-3
2. Titantah, J. T., Jorissen, K., and Lamoen, D. Density functional theory calculations of energy-loss carbon near-edge spectra of small diameter armchair and zigzag nanotubes: Core-hole, curvature, and momentum-transfer orientation effects . Physical Review B 69 (12), 125406 , 2004.
3. Nicholls, R. J. Electron energy loss spectroscopy of fullerene materials (Ph.D. thesis) . 2006.
4. Jouffrey, B., Schattschneider, P., and Hebert, C. The magic angle: a solved mystery . Ultramicroscopy 102 (1), 61 , 2004.
5. Schattschneider, P., Hebert, C., Franco, H., and Jouffrey, B. Anisotropic relativistic cross sections for inelastic electron scattering, and the magic angle . Physical Review B 72 (4), 045142 , 2005.
6. Schaich, W. L. Comment on the theory of extended x-ray absorption fine structure . Physical Review B 8 (8), 4028 , 1973.
7. Blaha P., Schwarz, K., Madsen, G. K. H., Kvasnicka, D., and Luitz, J. WIEN2k, An Augmented Plane Wave + Local Orbitals Program for Calculating Crystal Properties . 2001. ISBN ISBN 3-9501031-1-2 <http://www.wien2k.at>
8. Ankudinov, A. L., Ravel, B., Rehr, J. J., and Conradson, S. D. Real-space multiple-scattering calculation and interpretation of x-ray-absorption near-edge structure . Physical Review B 58 (12), 7565 , 1998.
9. Moreno, M. S., Jorissen, K., and Rehr, J. J. Practical aspects of electron energy-loss spectroscopy (EELS) calculations using FEFF8 . Micron 38 (1), 1 , 2007.
10. Hebert C. Practical aspects of running the WIEN2k code for electron spectroscopy . Micron 38 (1), 12 , 2007.
11. Keast, V. J., Scott, A. J., Brydson, R., Williams, D. B., and Bruley, J. Electron energy-loss near-edge structure - a tool for the investigation of electronic structure on the nanometer scale . Journal of Microscopy-Oxford 203 135 , 2001.
12. Jouffrey, B., Schattschneider, P., and Hebert, C. Ionization edges: Some underlying physics and their use in electron microscopy . Advances in Imaging and Electron Physics 123 413 , 2002.
13. Schattschneider, P. Fundamentals of Inelastic Electron Scattering . Springer-Verlag, 1986. ISBN 3211819371
14. Ahn, C. C. Transmission Electron Energy Loss Spectrometry in Materials Science and the EELS Atlas . Wiley-VCH, 2005. ISBN 3527405658
15. Egerton, R. F. Electron Energy-Loss Spectroscopy in the Electron Microscope . Plenum Press, New York, 1996. ISBN 0306452235

16. Brydson, R. Electron energy loss spectroscopy . BIOS Scientific Publishers Limited, 2001. ISBN 1859961346
17. Ibach, H. and Mills, D. L. Electron energy loss spectroscopy and surface vibrations . Academic Press, New York, 1982. ISBN 0123693500
18. Fuggle, J. C. and Inglesfield, J. E. Unoccupied electronic states : fundamentals for XANES, EELS, IPS and BIS . Springer Verlag, Berlin, 1992. ISBN 0387541624
19. Suenaga, K., Iijima, S., Kato, H., and Shinohara, H. Fine-structure analysis of Gd M-45 near-edge EELS on the valence state of Gd@C-82 microcrystals . Physical Review B 62 (3), 1627 , 2000.
20. Lazar, S., Botton, G. A., Wu, M. Y., Tichelaar, F. D., and Zandbergen, H. W. Materials science applications of HREELS in near edge structure analysis and low-energy loss spectroscopy . Ultramicroscopy 96 (3-4), 535 , 2003.
21. Potapov, P. L., Jorissen, K., Schryvers, D., and Lamoen, D. Effect of charge transfer on EELS integrated cross sections in Mn and Ti oxides . Physical Review B 70 (4), 045106 , 2004.
22. Egerton, R. F. and Wang, Z. L. Plural-Scattering Deconvolution of Electron Energy-Loss Spectra Recorded with An Angle-Limiting Aperture . Ultramicroscopy 32 (2), 137 , 1990.
23. Egerton, R. F., Williams, B. G., and Sparrow, T. G. Fourier Deconvolution of Electron Energy-Loss Spectra . Proceedings of the Royal Society of London Series A-Mathematical Physical and Engineering Sciences 398 (1815), 395 , 1985.
24. Rehr, J. J., Kozdon, J., Kas, J., Krappe, H. J., and Rossner, H. H. Bayes-Turchin approach to XAS analysis . Journal of Synchrotron Radiation 12 70 , 2005.
25. Verbeeck, J. and Van Aert, S. Model based quantification of EELS spectra . Ultramicroscopy 101 (2-4), 207 , 2004.
26. Verbeeck, J., Van Aert, S., and Bertoni, G. Model-based quantification of EELS spectra: Including the fine structure . Ultramicroscopy 106 (11-12), 976 , 2006.
27. Serin, V., Zanchi, G., and Sevely, J. EXELFS As A Structural Tool for Studies of Low Z-Elements . Microscopy Microanalysis Microstructures 3 (2-3), 201 , 1992.
28. Sikora, T., Hug, G., Jaouen, M., and Rehr, J. J. Multiple-scattering EXAFS and EXELFS of titanium aluminum alloys . Physical Review B 62 (3), 1723 , 2000.
29. Sikora, T., Hug, G., Jaouen, M., and Rehr, J. J. Multiple scattering EXAFS and EXELFS study of Al₃Ti and Ti₃Al alloys . Journal de Physique Iv 7 (C2), 231 , 1997.
30. Tanaka, I., Mizoguchi, T., and Yamamoto, T. XANES and ELNES in ceramic science . Journal of the American Ceramic Society 88 (8), 2013 , 2005.
31. Nelhiebel, M. Effects of crystal orientation and interferometry in electron energy loss spectroscopy (Ph.D. thesis) . 1999.
32. Menon, N. K. and Yuan, J. Quantitative analysis of the effect of probe convergence on electron energy loss spectra of anisotropic materials . Ultramicroscopy 74 (1-2), 83 , 1998.

33. Schattschneider, P., Nelhiebel, M., Souchay, H., and Jouffrey, B. The physical significance of the mixed dynamic form factor . *Micron* 31 (4), 333 , 2000.
34. Nelhiebel, M., Louf, P. H., Schattschneider, P., Blaha, P., Schwarz, K., and Jouffrey, B. Theory of orientation-sensitive near-edge fine-structure core-level spectroscopy . *Physical Review B* 59 (20), 12807 , 1999.
35. Nufer, S., Gemming, T., Kostlmeier, S., and Ruhle, M. Validity of the dipole-selection rule for the Al-L-2,L-3 edge of alpha-Al₂O₃ under channeling conditions . *Ultramicroscopy* 88 (4), 253 , 2001.
36. Weng, X., Rez, P., and Batson, P. E. Single electron calculations for the Si L₂₃ near edge structure . *Solid State Communications* 74 1013 , 1990.
37. Stohr, J., Jaeger, R., and Rehr, J. J. Transition from Adiabatic to Sudden Core-Electron Excitation - N-2 on Ni(100) . *Physical Review Letters* 51 (9), 821 , 1983.
38. Muller, J. E. and Wilkins, J. W. Band-Structure Approach to the X-Ray-Spectra of Metals . *Physical Review B* 29 (8), 4331 , 1984.
39. Hebert, C., Luitz, J., and Schattschneider, P. Improvement of energy loss near edge structure calculation using Wien2k . *Micron* 34 (3-5), 219 , 2003.
40. Rehr, J. J. Theory and calculations of X-ray spectra: XAS, XES, XRS, and NRIXS . *Radiation Physics and Chemistry* 75 (11), 1547 , 2006.
41. Rez, P., Alvarez, J. R., and Pickard, C. Calculation of near edge structure . *Ultramicroscopy* 78 (1-4), 175 , 1999.
42. Rez, P., Bruley, J., Brohan, P., Payne, M., and Garvie, L. A. J. Review of Methods for Calculating Near-Edge Structure . *Ultramicroscopy* 59 (1-4), 159 , 1995.
43. Rehr, J. J. and Albers, R. C. Theoretical approaches to x-ray absorption fine structure . *Reviews of Modern Physics* 72 (3), 621 , 2000.
44. Faulkner, J. S. Multiple-Scattering Approach to Band Theory . *Physical Review B* 19 (12), 6186 , 1979.
45. Stern, E. A. Theory of Extended X-Ray-Absorption Fine-Structure . *Physical Review B* 10 (8), 3027 , 1974.
46. Korringa, J. On the calculation of the energy of a Bloch wave in a metal . *Physica* 13 392 , 1947.
47. Kohn, W. and Rostoker, N. Solution of the Schrodinger equation in Periodic Lattices with an Application to Metallic Lithium . *Physical Review* 94 1111 , 1954.
48. Payne, M. C., Teter, M. P., Allan, D. C., Arias, T. A., and Joannopoulos, J. D. Iterative Minimization Techniques for Abinitio Total-Energy Calculations - Molecular-Dynamics and Conjugate Gradients . *Reviews of Modern Physics* 64 (4), 1045 , 1992.
49. Singh, D. J. Planewaves, pseudopotentials and the LAPW method . Springer, 2005. ISBN 0387287809
50. de Groot, F. Multiplet effects in X-ray spectroscopy . *Coordination Chemistry Reviews* 249 (1-2), 31 , 2005.
51. Shirley, E. L. Ab initio inclusion of electron-hole attraction : Application to X-Ray Absorption and Resonant Inelastic X-Ray Scattering . *Physical Review Letters* 80 (4), 794 , 1997.

52. Onida, G., Reining, L., and Rubio, A. Electronic excitations: density-functional versus many-body Green's-function approaches . *Reviews of Modern Physics* 74 (2), 601 , 2002.
53. Marques, M. A. L., Ullrich, C. A., Nogueira, F., Rubio, A., Burke, K., and Gross, E. K. U. *Time-dependent density functional theory* . Springer-Verlag, 2006. ISBN 978-3-540-35422-2
54. Nesvizhskii, A. I. and Rehr, J. J. L-edge XANES of 3d-transition metals . *Journal of Synchrotron Radiation* 6 315 , 1999.
55. Zaluzec, N. J. An Electron-Energy Loss Spectral Library and Its Application to Materials Science . *Journal de Physique* 45 (NC-2), 429 , 1984.
56. Dreizler, R. M. and Gross, E. K. U. *Density Functional Theory, an approach to the quantum many-body problem* . Springer-Verlag, New York, 1991. ISBN 0387519939
57. Hohenberg, P. C., Kohn, W., and Sham, L. J. The beginnings and some thoughts on the future . *Journal of Advanced Quantum Chemistry* 21 7 , 1990.
58. Kohn, W. and Sham, L. J. Self-consistent equations including exchange and correlation effects . *Physical Review* 140 A1133 , 1965.
59. Ceperley, D. M. and Alder, B. J. Ground-State of the Electron-Gas by A Stochastic Method . *Physical Review Letters* 45 (7), 566 , 1980.
60. Perdew, J. P. and Wang, Y. Accurate and Simple Analytic Representation of the Electron-Gas Correlation-Energy . *Physical Review B* 45 (23), 13244 , 1992.
61. Burke, K. *The ABC of DFT* . 2001. ISBN n/a <http://dft.rutgers.edu/kieron/beta>
62. Perdew, J. P., Ernzerhof, M., Zupan, A., and Burke, K. Nonlocality of the density functional for exchange and correlation: Physical origins and chemical consequences . *Journal of Chemical Physics* 108 (4), 1522 , 1998.
63. Kostlmeier, S. Success and limits of common final-state approximations . *Ultramicroscopy* 86 (3-4), 319 , 2001.
64. de Groot, F. Private communication . 2007.
65. Scott, A., Brydson, R., Craven, A. J., and MacKenzie, M. Comparison of the relative merits of techniques for the modelling of electron energy loss near edge structure (ELNES) . *Electron Microscopy and Analysis 1999* 161 , 1999.
66. Cottenier, S. *Density Functional Theory and the family of (L)APW methods : a step-by-step introduction* . 2002. ISBN 90-807215-1-4 http://www.wien2k.at/reg_user/textbooks
67. Pickard, C. J., Payne, M. C., Brown, L. M., and Gibbs, M. N. Ab initio EELS with a plane wave basis set . *Electron Microscopy and Analysis 1995* 147 211 , 1995.
68. Pickard, C. J. and Payne, M. C. Ab initio EELS: beyond the fingerprint . *Electron Microscopy and Analysis 1997* (153), 179 , 1997.
69. Perdew, J. P., Burke, K., and Ernzerhof, M. Generalized gradient approximation made simple . *Physical Review Letters* 77 (18), 3865 , 1996.
70. Jorissen, K., Luitz, J., Sorini, A., and Hebert, C. Ab initio relativistic calculations of Electron Energy Loss Near Edge Structure - the new and improved TELNES2 program . (in preparation) , 2007.
71. Ankudinov, A. L. *Relativistic Spin-dependent X-ray absorption theory* (Ph.D. thesis) . 1996.

72. Rehr, J. J., Albers, R. C., and Zabinsky, S. I. High-Order Multiple-Scattering Calculations of X-Ray-Absorption Fine-Structure . *Physical Review Letters* 69 (23), 3397 , 1992.
73. Rehr, J. J. and Albers, R. C. Scattering-Matrix Formulation of Curved-Wave Multiple-Scattering Theory - Application to X-Ray-Absorption Fine-Structure . *Physical Review B* 41 (12), 8139 , 1990.
74. Manson, S. T. Inelastic collisions of fast charged particles with atoms : ionization of the Aluminum L shell . *Physical Review A* 6 (3), 1013 , 1972.
75. Jorissen, K. and Rehr, J. J. Real-space multiple scattering calculations of relativistic electron energy loss spectra (submitted) . 2007.
76. Rehr, J. J., Soinenen, J. A., and Shirley, E. L. Final-state rule vs. the Bethe-Salpeter equation for deep-core x-ray absorption spectra . *Physica Scripta* T115 207 , 2005.
77. Rehr, J. J. Lars Hedin and the quest for a theory of excited states . *Physica Scripta* T115 19 , 2005.
78. Hedin, L. and Lundqvist, S. Effects of electron-electron and electron-phonon interactions on the one-electron states of solids . *Solid State Physics* 23 1 , 1969.
79. Dirac, P. A. M. Note on exchange phenomena in the Thomas atom . *Proceedings of the Cambridge Philosophical Society* 26 376 , 1930.
80. Ankudinov, A. L., Takimoto, Y., and Rehr, J. J. Combined Bethe-Salpeter equations and time-dependent density-functional theory approach for x-ray absorption calculations . *Physical Review B* 71 (16), 165110 , 2005.
81. Moreno, M. S., Lazar, S., Zandbergen, H. W., and Egerton, R. F. Accuracy of the calculated unoccupied states in GaN phases as tested by high-resolution electron energy-loss spectroscopy . *Physical Review B* 73 (7), 073308 , 2006.
82. Ankudinov, A. L., Nesvizhskii, A. I., and Rehr, J. J. Dynamic screening effects in x-ray absorption spectra . *Physical Review B* 67 (11), 115120 , 2003.
83. Taillefumier, M., Cabaret, D., Flank, A. M., and Mauri, F. X-ray absorption near-edge structure calculations with the pseudopotentials: Application to the K edge in diamond and alpha-quartz . *Physical Review B* 66 (19), 195107 , 2002.
84. Muller, D. A., Singh, D. J., and Silcox, J. Connections between the electron-energy-loss spectra, the local electronic structure, and the physical properties of a material: A study of nickel aluminum alloys . *Physical Review B* 57 (14), 8181 , 1998.
85. Rahkonen, K. and Krause, K. Total and partial atomic level widths . *Atomic Data and Nuclear Data Tables* 14 (2), 139 , 1974.
86. Lazar, S., Hebert, C., and Zandbergen, H. W. Investigation of hexagonal and cubic GaN by high-resolution electron energy-loss spectroscopy and density functional theory . *Ultramicroscopy* 98 (2-4), 249 , 2004.
87. Knippelmeyer, R., Wahlbring, P., and Kohl, H. Relativistic ionisation cross sections for use in microanalysis . *Ultramicroscopy* 68 (1), 25 , 1997.
88. Dwyer, C. Relativistic effects in atomic inner-shell ionization by a focused electron probe . *Physical Review B* 72 144102 , 2005.

89. Sorini, A., Rehr, J. J., and Levine, Z. H. The magic angle "mystery" in electron energy loss spectra : relativistic and dielectric corrections . (in preparation) , 2007.
90. Moller, C. M. Zur Theorie des Durchgangs schneller Elektronen durch Materie . Ann. Phys. 14 531 , 1932.
91. Bethe, H. A. Theory of the passage of fast corpuscular rays through matter . Ann. Phys. 5 325 , 1930.
92. Fano, U. Differential inelastic scattering of relativistic charged particles . Physical Review 102 385 , 1956.
93. Fano, U. Penetration of protons, alpha particles and mesons . Ann. Rev. Nucl. Sci. 13 1 , 1963.
94. Heitler, W. The quantum theory of radiation . Dover Publications, 1984. ISBN 0486645584
95. Peskin, M. E. and Schroeder, D. V. An introduction to quantum field theory . HarperCollins Publishers, 1995. ISBN 0201503972
96. Landau, L. D. and Lifschitz, E. M. Quantum Mechanics, non-relativistic theory . Butterworth-Heinemann, 1981. ISBN 0080291406
97. Yamamoto, T., Mizoguchi, T., and Tanaka, I. Core-hole effect on dipolar and quadrupolar transitions of SrTiO₃ and BaTiO₃ at TiK edge . Physical Review B 71 (24), 2005.
98. Matthew, J. A. D., Netzer, F. P., Clard, C. W., and Morar, J. F. Giant 4p-quadrupole resonances in the rare earths . Europhysics Letters 4 (6), 677 , 1987.
99. Liberman, D. and Zangwill, A. Quadrupole resonances in the rare-earth metals . Physical Review A 39 (1), 415 , 1989.
100. Moreau, P., Boucher, F., Goglio, G., Foy, D., Mauchamp, V., and Ouvrard, G. Electron energy-loss spectra calculations and experiments as a tool for the identification of a lamellar C₃N₄ compound . Physical Review B 73 195111 , 2006.
101. Hebert-Souche, C., Louf, P. H., Blaha, P., Nelheibel, M., Luitz, J., Schattschneider, P., Schwarz, K., and Jouffrey, B. The orientation-dependent simulation of ELNES . Ultramicroscopy 83 (1-2), 9 , 2000.
102. Paxton, A. T., Craven, A. J., Gregg, J. M., and McComb, D. W. Bandstructure approach to near edge structure . Journal of Microscopy-Oxford 210 35 , 2003.
103. Daniels, H., Brown, A., Scott, A., Nichells, T., Rand, B., and Brydson, R. Experimental and theoretical evidence for the magic angle in transmission electron energy loss spectroscopy . Ultramicroscopy 96 (3-4), 523 , 2003.
104. Hebert, C. private communication . 2007.
105. Radtke, G., Botton, G. A., and Verbeeck, J. Electron inelastic, scattering and anisotropy: The two-dimensional point of view . Ultramicroscopy 106 (11-12), 1082 , 2006.
106. Titantah, J. T. and Lamoen, D. sp(2)/sp(3) characterization of carbon materials from first-principles calculations: X-ray photoelectron versus high energy electron energy-loss spectroscopy techniques . Carbon 43 (6), 1311 , 2005.

107. Prodan, E. and Kohn, W. Nearsightedness of electronic matter . Proceedings of the National Academy of Sciences of the United States of America 102 (33), 11635 , 2005.
108. Ravel, B. and Rehr, J. J. Full multiple scattering XANES calculations . Journal de Physique Iv 7 (C2), 229 , 1997.
109. Beeby, J. L. The Density of Electrons in a Perfect or Imperfect Lattice . Proceedings of the Royal Society of London. Series A, Mathematical and Physical Sciences 302 (1468), 113 , 1967.
110. Beeby, J. L. The Electronic Structure of Disordered Systems . Proceedings of the Royal Society of London. Series A, Mathematical and Physical Sciences 279 (1376), 82 , 1964.
111. Ewald, P. Die Berechnung optischer und elektrostatischer Gitterpotentiale . Ann. Phys. 64 253 , 1921.
112. Faulkner, J. S., Davis, H. L., and Joy, H. W. Calculation of Constant-Energy Surfaces for Copper by the Korringa-Kohn-Rostoker Method . Physical Review 161 (3), 656 , 1967.
113. Ham, F. S. and Segall, B. Energy Bands in Periodic Lattices - Green's Function Method . Physical Review 124 (6), 1786 , 1961.
114. Jorissen, K. and Rehr, J. J. Relativistic core hole EELS without the supercell . (in preparation) , 2007.
115. Monkhorst, H. J. and Pack, J. D. Special points for Brillouin-zone integrations . Physical Review B 13 (12), 5188 , 1967.
116. Enders, P. Special-lines approximation to Brillouin zone integration . Semicond. Sci. Technol. 11 187 , 1996.
117. Blochl, P. E., Jepsen, O., and Andersen, O. K. Improved Tetrahedron Method for Brillouin-Zone Integrations . Physical Review B 49 (23), 16223 , 1994.
118. Ma, Y., Wassdahl, N., Skytt, P., Guo, J. D., Nordgren, J., Johnson, P., Rubensson, J. E., Boske, T., Eberhardt, W., and Kevan, S. D. Soft-x-ray resonant inelastic scattering at the C K edge of diamond . Physical Review Letters 69 2598 , 1992.
119. Luitz, J., Maier, M., Hebert, C., Schattschneider, P., Blaha, P., Schwarz, K., and Joffrey, B. Partial core hole screening in the Cu L-3 edge . European Physical Journal B 21 (3), 363 , 2001.